

HIGH-PERFORMANCE COMPACT GAS FILLED SPARK SWITCHES

A thesis presented in fulfilment of the requirement for
the degree of

Doctor of Philosophy

Michael G. Hogg, B.Eng(Honours), M.Res

2015

Department of Electronic and Electrical Engineering

University of Strathclyde

Glasgow, UK

Declaration of Authenticity and Author's Rights

'This thesis is the result of the author's original research. It has been composed by the author and has not been previously submitted for examination which has led to the award of a degree.'

'The copyright of this thesis belongs to the author under the terms of the United Kingdom Copyright Acts as qualified by University of Strathclyde Regulation 3.50. Due acknowledgement must always be made of the use of any material contained in, or derived from, this thesis.'

Signed:

Date:

ACKNOWLEDGEMENTS

I would like to acknowledge a few people who have been invaluable to me throughout the last 3.5 years in the completion of this thesis. Firstly, I would like to acknowledge Dr. Igor Timoshkin for his supervision, guidance and help without whom this thesis would never have started or finished.

I would also like to thank Prof. Scott MacGregor and the whole HVT Research Group for the opportunities and support. In particular, Dr. Mark Wilson who was always willing to take the time to help and support me in the lab, publishing and with teaching opportunities. I would also like to thank Dr. Martin Given for his continual help with technical discussions and writing.

Thanks to all the guys in the High-Voltage Mechanical Workshop: Sean Doak, Andy Carlin, Frank May, and David Griffin for all their help with designing and machining many switches and pieces of equipment.

Thanks to Maureen Cooper for all of her help over the years, particularly organising conference trips.

This work has been part-funded by a UK MoD Research Programme.

I would also like to thank my family and friends, and in particular Karen for all her support and understanding.

ABSTRACT

Gas filled spark switches are used extensively in pulsed power systems for their high rate of dV/dt , dI/dt , fast closing times with low jitter, and their high voltage and current capability. Recently there has been a renewed interest in designing spark switches that can operate with environmentally friendly gases such as air. This thesis presents an investigation into gas filled plasma closing (spark) switches. Investigating the utilisation of pre-breakdown corona discharge to increase the performance of spark switches operating in environmentally friendly gases is a re-occurring novelty throughout this study.

To achieve the aim of this thesis, a number of separate approaches were adopted. In **Chapter 2** a comprehensive literature review of pulsed power and plasma switches is presented. Breakdown voltage, time delay to breakdown and its jitter are compared as are different electrode topologies and triggering mechanisms. **Chapter 3** describes the experimental systems that were specially designed and built, including the design of a computer (LabVIEW) controlled high voltage system and a precision pneumatic control system. **Chapter 4** presents a comprehensive unique investigation into a range of topologies: plane-plane, sphere-sphere, and cone-plane filled with air, nitrogen, and a 60%/40% nitrogen/oxygen mixture. Building on Chapter 4, **Chapter 5** presents an investigation of the breakdown voltage of point-plane topologies with varying point radii and for the first time a new parameter “critical electrode separation”, d_{crit} , was identified where positive and negative have equal breakdown voltages. A standalone investigation into the corona discharge in point-plane topology is analysed in **Chapter 6** to explain the effects of corona discharge on the self-breakdown voltage.

Triggered switches are used extensively in pulsed power systems such as high-voltage pulse generators. A new approach to triggering a switch is investigated in **Chapter 7**, where a triggering impulse is superimposed on to a DC energised spark switch to initiate breakdown, with breakdown time delays of ~ 20 ns and jitter of $\sim 1-2$ ns. In **Chapter 8**, a multi-stage spark switch was designed with point-plane topology from the results in Chapter 5, to investigate the impact of multi-stages on the breakdown voltage, corona discharge, time delay, and its jitter. It was established that, with negative energisation, a range of DC energisation levels could be identified that would allow the switches to operate with jitter of $\sim 1-2$ ns in a corona stabilised region with increased breakdown voltage.

The final section of this thesis in **Chapter 9** introduces post-breakdown plasma resistance and inductance consideration. A new method of simulating transient plasma resistance and inductance of plasma channel using PSpice software is presented. This new approach to simulating plasma resistance and inductance can lead to the development of much more accurate plasma resistance models and more accurate modelling of pulsed power systems with multiple spark switches such as pulse generators.

CONTENTS

1. INTRODUCTION	11
2. LITERATURE REVIEW	16
2.1 Pulsed Power: Basic Processes, Pulse Generator Systems and Approaches.....	16
2.1.1 Pulse forming line and Blumlein Impulse Generators	18
2.1.2 Spark Switch Topologies	21
2.1.3 Triggering Approaches	25
2.1.4 Multi-Stage Switches	28
2.2 Dynamic Resistance of Sparks.....	32
2.3 Conclusions.....	41
3. EXPERIMENTAL SYSTEMS AND PROCEDURES	43
3.1 Pneumatic Control System.....	43
3.2 Methodology of Measurement of Self-Breakdown Voltage.....	45
3.3 Methodology of Observation of Pre-Breakdown Corona Discharge.....	49
3.4 Novel Approach to Plasma Triggering: Superimposed Trigger.....	50
3.5 Methodology of Triggering of Multi-Spark Switch.....	52
4. SELF-BREAKDOWN CHARACTERISTICS OF RAMPED VOLTAGE STRESSED SWITCHES FILLED WITH AIR, NITROGEN AND AIR/NITROGEN MIXTURE	55
4.1 Development of Spark Switch Topologies	56
4.2 Electrostatic Analysis of Electric Field in Spark Switch Topologies	62
4.3 Open Shutter Images of Spark Discharges.....	64
4.4 Self-Breakdown Voltages of Environmentally Friendly Gases in Different Topologies.....	66
4.4.1 Self-Breakdown Voltages of Atmospheric Air	66
4.4.2 Self-Breakdown Voltages of Nitrogen and 60%/40% Nitrogen/Oxygen Mixture	71

4.5	Conclusions.....	78
5.	INVESTIGATION OF RAMPED SELF-BREAKDOWN VOLTAGE OF SPARK SWITCHES WITH POINT-PLANE TOPOLOGY	80
5.1.1	Point Electrodes	81
5.1.2	Spark Switch Design.....	82
5.2	Ramped Self-Breakdown Voltage: Results and Analysis.....	86
5.2.1	Ramped Self-Breakdown Voltage of Point-Plane Spark Switch as a Function of Gas Pressure in Air, Nitrogen and Nitrogen/Oxygen Mixture	86
5.2.2	Ramped Self-Breakdown Voltage as a Function of Electrode Separation.....	92
5.2.3	Ramped Self-Breakdown Voltage as a Function of Point Electrode Tip Radius	98
5.2.4	Analysis of Paschen Characteristics of Spark Switches Filled with Air.....	104
5.2.5	Conclusions.....	105
6.	CHARACTERISATION OF CORONA DISCHARGES IN SPARK SWITCHES ...	107
6.1	Corona Discharge Inception Voltage.....	113
6.2	Voltage-Current Relationship in Point-Plane Topology	122
6.3	Mobility of Charge Carriers in Corona Discharges	126
6.4	Electric Field in the Switch Influenced by Space Charge.....	128
6.5	Conclusions.....	130
7.	SUPERIMPOSED TRIGGERING OF SPARK SWITCH FILLED WITH AIR.....	132
7.1	Superimposed Triggering: Time Delay to Breakdown	135
7.2	Superimposed Triggering: Switch Jitter	138
7.3	Pre-Breakdown Ionisation Effect on Time Delay to Breakdown	139
7.4	Pre-Breakdown Ionisation Effect on Switch Miss-Fire Rate (Probability).....	142
7.5	Statistical and Formative Times of Analysis Superimposed Triggered Switch: Laue Analysis	144
7.6	Conclusions.....	148

8.	MULTI-STAGE SPARK SWITCHES	150
8.1	Multi-Stage Spark Switch Topology.....	150
8.2	Self-Breakdown Voltage of Multi-Stage Switch Filled with Air.....	154
8.3	Corona Inception Voltage of Multi-Stage Switch Filled with Air.....	160
8.4	Pre-Breakdown Corona Discharge Voltage-Current Relationship for Multi-Stage Switch Filled with Air.....	161
8.5	Time Delay to Breakdown in Multi-Stage Switch Filled with Air	163
8.6	Conclusions.....	171
9.	ANALYTICAL MODELLING OF SPARK RESISTANCE.....	173
9.1	Dynamic Inductance and Resistance of Spark Switch.....	184
9.2	Conclusions.....	189
10.	GENERAL CONCLUSIONS	191
11.	FUTURE WORK.....	197
12.	REFERENCES	199
13.	LIST OF PUBLICATIONS	215
13.1	Journal Publications	215
13.2	Presentations at International Conferences and Workshops	215
14.	APPENDIX 1: LAUE GRAPHS	217
14.1	Laue Graphs for Discharges Without Coronating Electrodes.....	217
14.2	Laue Graphs for Discharges With Coronating Electrodes.....	224
15.	APPENDIX 2: LABVIEW CODE	231
15.1	Main Body of Code.....	231
15.2	Oscilloscope Trigger Code.....	232
16.	APPENDIX 3: CORONA DISCHARGE <i>V-I</i> CURVES	233
16.1	Corona Discharge <i>V-I</i> Curves for Gramophone Needle Point Electrode in Air ..	233
16.2	Corona Discharge <i>V-I</i> Curves for 0.067 mm Radius Point Electrode in Air	235
16.3	Corona Discharge <i>V-I</i> Curves for 0.8 mm Radius Point Electrode in Air	237

17.	APPENDIX 4.....	239
	Discharges and Electrical Breakdown of Gases	239
	Townsend Electron Avalanche	240
17.1.1	Paschen's Law.....	243
17.1.1	Anode Directed Streamer Discharge.....	245
17.1.2	Discharges in Highly Divergent Electric Fields.....	247
17.1.3	Cathode Directed Streamers Discharge	253
17.1.4	Breakdown in Non-Uniform Electrode Topologies.....	254

List of Symbols

V	Voltage (V)
V_{DC}, V_S	DC voltage supply
R_{CH}	Charging resistor
V_{br}	Breakdown voltage (V)
V_C	Corona inception voltage (V)
V_L	Load Voltage (kV)
I, i	Current (A)
R	Resistance (Ω)
r	Dynamic resistance (Ω), Electrode radius (mm)
Z	Impedance (Ω)
SW	Switch
C	Capacitance (F), fitting coefficient and constant
C'	Capacitance per meter (F/m)
L	Inductance (H)
L'	Inductance per meter (H/m)
μ_r	Relative permeability
ϵ_r	Relative permittivity
ϵ_0	Permittivity of free space , 8.854×10^{-12} (F/m)
η	Field enhancement factor
E	Electric field (V/m)
E_P	Peak electric field (V/m)
d	Electrode spacing (m)
x	Distance (m)
v	Normalised distance, velocity (m/s)
a	Point electrode radius (m)
σ	Jitter (s), and conductivity ($1/(\Omega \cdot m)$) or (S/m)
σ_C	Jitter (s) with coronating electrodes
p	Pressure (Pa)
α	Townsend's 1 st ionization coefficient
α_{eff}	Effective ionization coefficient
β	Attachment coefficient
n	Particle density

A, B	Constants
γ	Townsend's 2 nd ionization coefficient
μ	Mobility ($\text{m}^2/(\text{Vs})$)
X_C	Electron avalanche length (m)
ρ	Resistivity ($\Omega\cdot\text{m}$)
l	Length of plasma channel (m)
A	Cross-sectional area of plasma channel (m^2)
ζ	Gas constant
t	Time (s)
C	Constant
U	Arc channel energy (J/m)
ρ_0	Initial gas density (kg/m^3)
d_{crit}	Critical electrode separation (mm)
V_{crit}	Critical breakdown voltage (V)
m	fitting coefficient (kV/MPa)
V_0	fitting coefficient (kV)
x	DC energisation level with respect to self-breakdown voltage (%)
N_t	Total number of breakdowns
N_0	Number of breakdowns longer than a given time
t_f	Formative time (ns)
t_{st}	Statistical time (ns)
K	Constant

1. INTRODUCTION

Within the power and pulsed power industries, there is a demand for high voltage (HV) systems with a reduced footprint and, as such, it is important to design and characterise compact gas-filled switches. In recent years, there has been a renewed interest in spark gas-filled closing switches (sometimes referred to as a plasma closing switch) with a focus on the development of new systems that are not filled with SF₆ as the insulating gas since it was identified as a greenhouse gas, and is now banned in most applications [Reg 2006]. Spark switches have many advantages which make them perfect for the pulse power industry: they can operate at high voltages, high currents and high rates of change of voltage and current, while achieving fast closing times (10's of ns) with low jitter (1-10 ns) [Woodworth 2010]. The low resistance and inductance of spark plasma of these switches also means they can be used in pulsed power systems that require very high voltage and fast rising current output. Systems such as the most powerful pulsed X-ray generator (Z-R machine) and Linear Transformer Drivers at Sandia National Laboratory in USA use thousands of plasma closing switches capable of outputting mega-volts and mega-amps [Li 2015b][Lehr 2002] [Woodworth 2009a,b 2010, 2011]. Spark switches can have solid, liquid or gas insulation between electrodes [Hogg 2011, 2012a,b] [Mesyats 2005].

A gas filled spark switch at its simplest is two electrodes, separated by a gaseous dielectric. When a sufficiently high voltage is applied to the HV electrode of the switch, electrical breakdown develops in the gas resulting in establishment of a highly conductive plasma channel between the electrodes. Thus, the switch which was open before breakdown becomes closed as the spark channel connects both electrodes and current passes through the switch.

The present work looks at novel approaches to the design and operation of spark switches filled with environmentally friendly gases operating in single shot regime. In order to improve operational characteristics of the switches developed and characterised in the present work, switch topologies were equipped with coronating electrodes in order to create pre-breakdown corona discharge in the switch. Corona discharge is known to improve the

stability of high-frequency repetitive operation of SF₆ filled switches [Beveridge 2008]. While corona is known to improve the performance of high-repetition spark switches, it has not been thoroughly investigated in the single shot regime. This research is focused only on single shot regime and investigates the use of corona and coronating electrodes to improve breakdown performance.

To minimise the use of SF₆ in pulsed power systems, it is important to develop switches which are filled with alternative gases such as air, nitrogen, oxygen and their mixtures. This research is focused on investigation of operational characteristics of compact spark switches filled with air, nitrogen and a nitrogen/oxygen mixture. In particular, attention was paid to how corona discharges in different switch topologies can improve the performance and operational characteristics of ramped voltage and impulse triggered spark switches (single stage and multi-stage/multi-gap topologies).

In Chapter 2, the literature section of this work introduces and discusses the principles of pulsed power, explaining the concepts of energy storage, and spark switch designs and their topologies. The different methods of triggering of spark switches are discussed along with typical topologies, and their merits are analysed. The concept of multi-stage (multi-gap) spark switches is important in the pulsed power industry, and much recent literature in high performance plasma closing switches is based around multi-stage switches for use in Linear Transformer Drivers (LTD) [Woodworth 2009a,b 2010, 2011]. The design of multi-stage switches is discussed, including the Rimfire switch developed in 1980's and more recent multi-stage switches used in LTDs [Bluhm 2006]. The performance of compact switches designed in the course of this project is important for comparison with the LTD and other switches described in the literature. The triggering of plasma closing switches requires high-voltage, fast rising impulses which are created using coaxial cable pulse generators, in this research a Blumlein generator is used for triggering of spark switches and the theory of this transmission-line based system is discussed in the literature review.

Modelling and simulation of transient plasma processes in spark switches has been of interest to the pulsed power community as these models help to predict operational characteristics of the switches such as transient plasma resistance and inductance, energy dissipation in the switch, switch closure time and others. These parameters are important for design of plasma closing switches and optimisation of their performance. For example, resistance and inductance of plasma (spark) discharge define the current through the switch, the current rise time and the energy dissipated in the switch. Simulating transient plasma

resistance requires a self-consistent model with multiple factors which are required as initial conditions. The transient models for simulating of plasma resistance are discussed in the literature review, including assumptions and initial conditions, and comparison between different models and approaches are made.

Chapter 3 discusses the experimental designs created and developed throughout the course of this project. Specifically designed computer programs were developed, interfacing with high voltage and measurement equipment, to control and measure breakdown voltage, corona discharge inception voltage, pre-breakdown voltage-current relationships, and time delay to breakdown measurements.

The original results obtained during the course of this research project and presented in this thesis in Chapter 4 to Chapter 9: experimental investigation of ramped self-breakdown voltage of spark switches; experimental investigation of corona discharge characteristics in different gases (air, nitrogen, and oxygen/nitrogen mixture); design, development and investigation of operational characteristics of high-performance triggered spark switches (single stage and multi-stage design); simulation of post-breakdown transient plasma resistance and inductance in plasma closing switches.

Ramped and DC energised self-breakdown switches are used extensively in pulsed power systems including pulse generators (Marx generators and Blumlein topologies, single state generators, LTD's, and others) [Woodworth 2010] [Mesyats 2005]. It is vitally important to have accurate and consistent information on breakdown voltage and its spread in gases and switch topologies which are used in the pulsed power systems. Chapter 4 presents the results of systematic investigation into ramped and DC self-breakdown characteristics of 3 different switch topologies filled with compressed air, nitrogen and a 60%/40% nitrogen/oxygen mixture; gas pressure was varied from 0.1-0.35 MPa. The sphere-sphere, cone-plane and plane-plane topologies were used in this study with and without coronating electrodes energised by positive and negative ramped voltage. In Chapter 5, the point-plane topology creates a highly non-uniform field which was investigated extensively at a range of point radii, and electrode separation. A computer controlled high-voltage test bed was used to control the voltage across the electrodes at a steady rate to ensure consistency between tests. A new relationship between breakdown voltage for positive and negative energisation was derived from the obtained experimental results and can be of use to develop optimal topologies of spark switches or can help in coordination of gaseous insulation for compact high-voltage systems.

Corona discharge and its effects on operational performance of spark switches is a theme and novelty of this research and, as such, it is necessary to investigate corona discharge in its own right. In Chapter 6, corona discharge is investigated using a computer controlled HV test system specifically developed and used to compare tests with consistency. The point-plane topology, creating the optimal conditions for corona [Loeb 1939], was used and the inception voltage, voltage-current relationship were measured in air. From $V-I$ curves, it was possible to determine the mobility of charge carriers which can be used to estimate space charge effects. The space charge limited electric field in the switch with point-plane topology was investigated using the obtained mobility of charge carriers, showing significant field changes for negative energisation as compared with the electrostatic (Laplacian) electric field. Positive energisation resulted in less pronounced space charge effects.

In Chapter 7, a new method of triggering switches is proposed and investigated. In this method, a triggering pulse superimposed on a DC stress is used to energise the main switch electrode. Thus, in this approach, there is no need for an additional trigger electrode as the main HV electrode is used for both purposes, switch triggering and for passing the current through the switch in its closed state. It was found that using compressed air, the jitter of such a switch which is operated in the superimposed DC + trigger impulse mode could be as low as ~ 1 ns. Using a sphere-sphere topology with and without coronating electrodes, the time delay to breakdown and jitter were measured in bottled air using the super-imposed triggering method. The results were analysed using Laue statistical analysis method.

Multi-stage spark switches have been the focus of much of the latest investigation in the field of spark switches for their use in LTDs [Woodworth 2009a,b 2010, 2011]. During the course of this research project, compact single and multi-stage switches with highly non-uniform field topologies energised to 10's kV were designed and their operational characteristics investigated. The breakdown voltage, time delay to breakdown, jitter and voltage-current relationship of two and three point-plane stage switches were obtained using positive and negative ramped energisation. The multi-stage switch which is described in Chapter 8 was designed and developed based on the characteristics of the corona discharges and DC breakdown voltages obtained early in the project and presented in Chapters 5 and 6.

A new approach to simulation of transient spark resistance and inductance using PSpice software is introduced (Chapter 9). This approach is based on the transient plasma resistance models available in literature, these models are discussed and analysed in Section 2.2. The transient resistance models were used to simulate the plasma resistance in the plasma closing switch. A new advance model which includes dynamic plasma resistance and dynamic

inductance of the spark plasma in the switch was developed using PSpice software and the results obtained using this original model compared with the experimental data available in literature. The PSpice approach allowed both dynamic resistance and inductance to be simulated simultaneously. It is shown that the resistance of the plasma obtained from hydrodynamic models is closer to the measured values when both transient inductance and resistance of plasma channel are included in the analysis. The PSpice approach allows simulation of complex circuits with plasma switches to be conducted.

The novel approaches to the design of spark gaps switches introducing corona discharge and coronating electrodes revealed that compact plasma closing switches with advanced operational characteristics can be designed, built and used in pulsed power systems, which opens a new and exciting perspective in further development of pulsed power systems with minimal footprint. Also, it shows that environmentally friendly gases can be successfully used in plasma closing switches developed in the present work, thus eliminating necessity to employ gaseous SF₆. A new relationship, the critical gap, for non-uniform topologies has been established and investigated in the present work. This distance is important for development of switches and compact systems which have similar breakdown voltages for positive and negative energisation. It was shown, that using the new method of triggering of plasma closing switches proposed in the present work, it was possible to achieve excellent switch performance comparable to the performance of plasma closing switches used in LTDs. A novel approach to modelling of transient plasmas resistance and inductance using PSpice software which has been developed in this work simplifies and improves the simulation of transient plasma resistance and inductance in complex gas switch circuits.

2. LITERATURE REVIEW

This chapter presents a review of the relevant literature focusing on the basic concepts of pulsed power, gas discharge, breakdown mechanisms in spark switches, switch topologies and their operational characteristics, and the application of plasma closing switches in the pulsed power industry. First, a brief discussion of pulsed power is provided including the principle of operation of a pulse forming line and Blumlein impulse generator. Within the pulsed power section, a comprehensive discussion of spark switches includes the basic switching topologies and a review of (plasma closing) spark switches focusing on topology and triggering mechanisms. Spark switches operate by the development of a highly conductive spark discharge (plasma channel) between two electrodes. The theory of gas discharges is discussed with focus on difference between uniform and non-uniform electrode topologies. Lastly, this chapter discusses post breakdown transient plasma resistance. Dynamic plasma resistance models available in literature are discussed and reviewed, operating parameters of the plasma closing switches are also analysed.

2.1 PULSED POWER: BASIC PROCESSES, PULSE GENERATOR SYSTEMS AND APPROACHES

Pulsed power technology refers to the accumulation, compression and release of energy. Low energy collected over a relatively long period of time is compressed and then released quickly (ps- μ s). In doing so, the instantaneous power can be extremely high (GW) from a relatively low average power (<kW) source.

Energy compression is achieved by storing the energy in either a capacitive element or inductive element. In the pulsed power systems used in this project, a capacitive energy storage was used in order to produce an impulsive output voltage. While the energy density achievable from inductive storage (50 J/cm^3) can be larger than capacitive storage (up to 3 J/cm^3) [MacDonald 2009], the self-discharge time of the inductive storage elements can be very short and would need to be charged and discharged rapidly [Kind 2001]. The use of inductive energy storage requires plasma opening switches which are not subject of the

current work. The key components of a pulsed power system based on capacitive energy storage are shown in Figure 2.1.

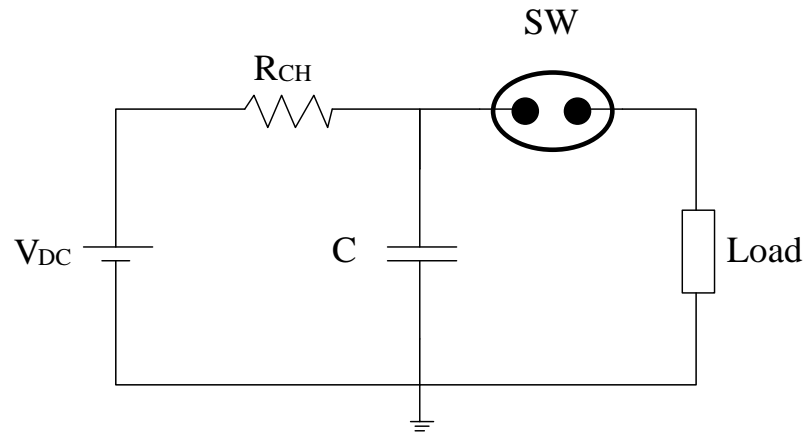


Figure 2.1 Capacitive storage pulse former. V_{DC} - DC charging voltage supply, R_{CH} - charging resistor, C - capacitor storage element, SW - spark switch.

The capacitor, C , is charged by a DC voltage supply, V_{DC} , through a charging resistor, R_{CH} , before switch, SW , is closed. The switch is operated by either a self-breakdown (self-close) or triggered breakdown regime, and the capacitor discharges through the load providing an impulse voltage across the load and impulsive current through the load. Figure 2.1 shows a DC voltage supply creating a voltage impulse of the same polarity as the supply DC charging voltage using a capacitor, C , and a spark switch, SW . Using the same principle as Figure 2.1, an impulse of opposite polarity can be formed. Swapping the capacitor and switch also creates a voltage impulse, shown in Figure 2.2. When the switch closes, the capacitor is connected to ground, so a voltage impulse of the opposite polarity is produced across the load.

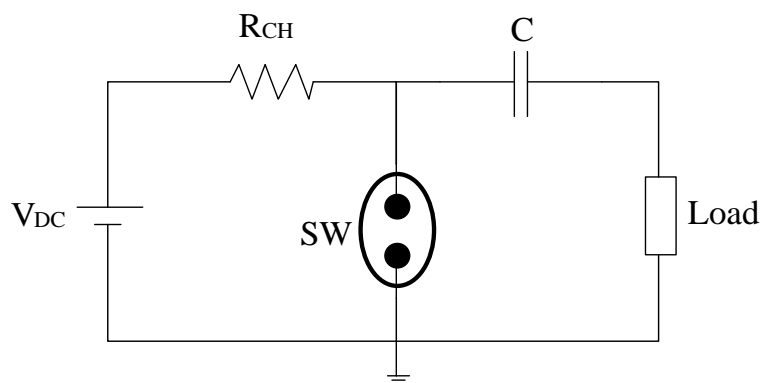


Figure 2.2 Inverting capacitive storage pulse forming circuit. V_{DC} - DC charging voltage supply, R_{CH} - charging resistor, C - capacitor storage element, SW - spark switch.

During operation of the pulsed power system, reverse voltage can cause damage in the storage capacitors and/or in the DC power supplies if there is not proper protection. Therefore, capacitors should be selected in such a way that they will be able to withstand the maximum reverse voltage which would potentially appear across their terminals during operation of the pulsed power system. Also, transient voltages during operation of the pulsed power system may harm the DC power supply, the use of inverting topology helps to decouple the DC power supply from the fast transient pulsed power part of the circuit (switch, energy storage, transmission cables and the load) during switch operation.

The circuits discussed in Figure 2.1 and Figure 2.2 form impulses from DC supplies by using capacitive storage elements where peak output voltage of the impulse is equal to the charging voltage from the power supply. To multiply the voltage from the power supply, multiple capacitors can be charged in parallel and discharged in series. Within the pulsed-power industry, there is a requirement for DC and impulse energised self-closing and triggered switches that operate consistently at high voltage.

Section 2.1.1 discusses the operation of a Blumlein impulse generator, an impulse generator in which co-axial cables are used to store energy and to form a HV impulse with a specific duration.

2.1.1 Pulse forming line and Blumlein Impulse Generators

Common coaxial cable based HV generators include simple pulse forming topologies and Blumlein generators. In order to create impulses with very fast rise and fall times (as short as 10's of pico-seconds) and well-defined shape and duration, coaxial transmission line topology is often used. The length of coaxial cables, which behave like transmission lines, defines the duration of the output voltage impulses, stacked transmission lines also allow multiplication of voltage to be achieved.

A direct polarity pulse forming line is shown in Figure 2.3 with a matched load impedance, Z_0 . This simple coaxial pulse forming line is charged to voltage V_S by the high-voltage DC generator via a charging resistor, R_{ch} . The charged line is then connected to the load via a closing switch, SW_{close} and if the load impedance matches the cable impedance, a single rectangular voltage impulse with magnitude equal to half of the supply voltage, $V_L = 0.5 V_S$, is across the load.

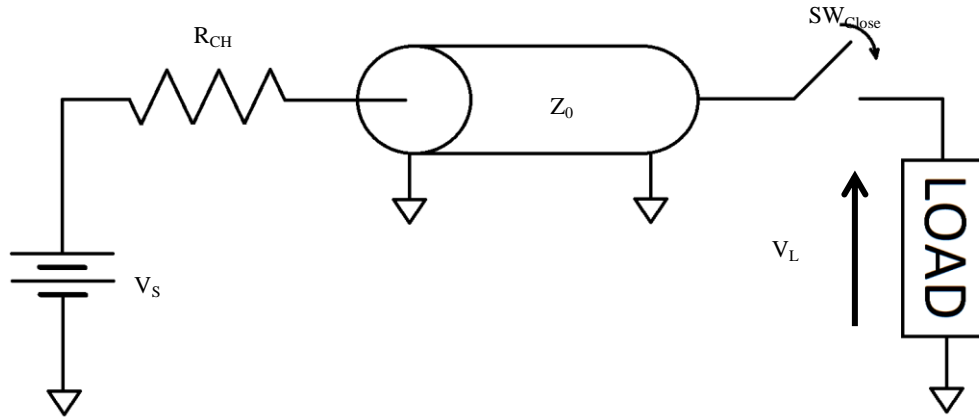


Figure 2.3 Pulse forming line circuit.

For maximum power transfer, the impedance of the load and cables should be the same. The voltage across the load of a pulse forming line, V_L , Figure 2.3, can be calculated by:

$$V_L = V_S \frac{Z_L}{Z_0 + Z_L} \quad (2.1)$$

where V_S is the voltage from the DC source, Z_L is the impedance of the load and Z_0 is the characteristic impedance of the coaxial cables.

In 1941, Alan Blumlein patented a pulse forming network that outputted an impulse with magnitude equal to the supply voltage [Blumlein 1941]. The Blumlein generator places the load in the middle of the transmission line/between two transmission cables.

Figure 2.4 shows a Blumlein generator configuration with the load placed between two transmission lines. If the load impedance is twice the characteristic impedance of the coaxial cables, Z_0 , the Blumlein generators outputs a voltage impulse, V_L , equal to the supply DC voltage, $V_L = V_s$.

The performance of Blumlein generator and pulse forming lines depends heavily on matching the impedance of the coaxial cables and the load.

From Equation (2.1), it can be seen that the maximum output of a pulse forming line with matched impedance is exactly half of the supply voltage, V_s . When the load impedance Z_L and coaxial characteristic impedance, Z_0 , are not matched, the peak voltage across the load can be higher than the supply voltage, V_s .

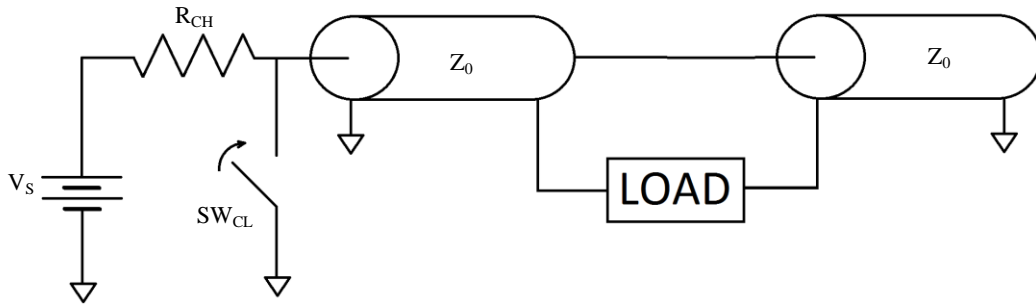


Figure 2.4 Blumlein generator circuit.

Voltage impulses propagate along a transmission line from one end to the other and, at the terminus, the impulse can either reflect back, transmit out of the line, or a combination of both. If the load at the terminus is matched to the characteristic impedance of the transmission line there are no reflections. If there is a mismatch, some or all of the impulse is reflected back. The reflected voltage superimposes onto the original impulse amplifying the voltage. The voltage can keep bouncing along the transmission line superimposing up to voltages close to the supply voltage. The reflections create an impulse that is not square and will have oscillations.

To achieve voltage multiplication, several Blumleins can be stacked to create double, triple Blumleins which output voltage equal to the number of stages times the supply voltage [Somerville 1990].

The output of the coaxial transmission lines is strongly dependent on matching the impedance of the load and the cables. In pulse power applications with short, fast pulses the characteristic impedance can be calculated using:

$$Z_0 = \sqrt{\frac{L'}{C'}} \quad (2.2)$$

where L' and C' are the cable inductance (H/m) and capacitance (F/m) per unit length respectively. Transmission line characteristic impedance is commonly either 50 Ω or 75 Ω , URM67 coaxial cable used in many pulsed power generators has a capacitance, $C'=100$ pF/m and inductance $L'=250$ nH/m which results in a 50 Ω characteristic impedance [Wilson 2011].

The duration of the voltage impulse is dependent on the coaxial cable properties and the length of the cable. The velocity of impulse propagation can be calculated by:

$$v = \frac{c}{\sqrt{\mu_r \epsilon_r}} \quad (2.3)$$

where c is the speed of light in vacuum ($\sim 2.98 \times 10^8$ m/s), μ_r is the relative permeability and ϵ_r is the relative permittivity of the coaxial cable insulation. In the case of URM67, the polyethylene dielectric insulator has a relative permeability of, $\mu_r \sim 1$ and a relative permittivity of, $\epsilon_r \sim 2.2$, and using Equation (2.2), the propagation velocity can be calculated as $\sim 2 \times 10^8$ m/s [Wilson 2011].

With the velocity of propagation and knowing the length of the transmission line, the duration of the impulse can be calculated. For a single pulse forming line using URM 67 each meter of cable adds ~ 5 ns to the period of the impulse. A Blumlein has two way transmission, as such, each meter of URM67 add ~ 10 ns to the impulse period [Wilson 2011].

Coaxial cable generators like Blumlein generators can provide very fast, ps, rising and falling rectangular voltage impulses across the matched load which can be advantageous in the pulsed power industry and, as such, they are used extensively. However, there are many limitations to using coaxial cable including, but not limited to, the maximum charging voltage. URM67 was rated at 40 kV above which breakdown and partial discharges could occur in the insulation. In addition, the maximum energy-storage of coaxial cables is very small, 8 J for 100 m reel of URM67 [Wilson 2011].

In this research, the Blumlein pulsed generator is used for creating triggering voltage impulses and with a mismatched load, sufficient voltage multiplication can be achieved.

The next section of the pulsed power part of the literature review discusses spark switches, starting with the basics of spark switch topologies and then triggering mechanisms. Lastly, multi-spark switches are discussed with reference to current switches presented in literature.

2.1.2 Spark Switch Topologies

Plasma closing switches commonly operate with quasi-uniform electric field or highly non-uniform electric fields. Uniform electric field topologies create predictable switches where the breakdown voltage level can be predicted or set using Paschen's law. Paschen's law describes the breakdown voltage as a function of electrode gap and gas pressure for uniform-field electrode topologies. Non-uniform topologies are used in switches to utilise pre-spark-breakdown activity such as corona discharge to stabilise the switch performance. Pre-spark

corona discharge increases the performance of repetitive closing switches, where corona discharge can reduce the pre-fire rate [Beveridge 2008].

Topologies used in the pulsed-power and high voltage industries include: plane-plane, sphere-sphere and point-plane (cone-plane), shown in Figure 2.5. The plane-plane topology creates a uniform electric field with slight enhancements at the electrode corners. For practical applications, it is often assumed uniform between the electrodes. A small radius was added to the parallel-plane electrodes to reduce the fringing effects. To remove fringing effects completely, a specialist electrode profile such as a Rogowski profile is required [Rogowski 1923].

Sphere-sphere topology is commonly used and much research has been done on the breakdown voltage. There are small localised high-field regions at the tip of the spheres but it is not usually strong enough to cause significant localised corona discharge. Point-plane topologies create highly non-uniform electric fields, with very high fields at the tip of the point electrode. The radius of the point electrode defines the field enhancement; a smaller radius tip results in higher fields. The field rapidly reduces with distance from the tip of the point to an average field, sometimes many orders of magnitude lower than the field at the tip. Figure 2.5 shows typical (a) plane-plane, (b) sphere-sphere and (c) point-plane topologies.

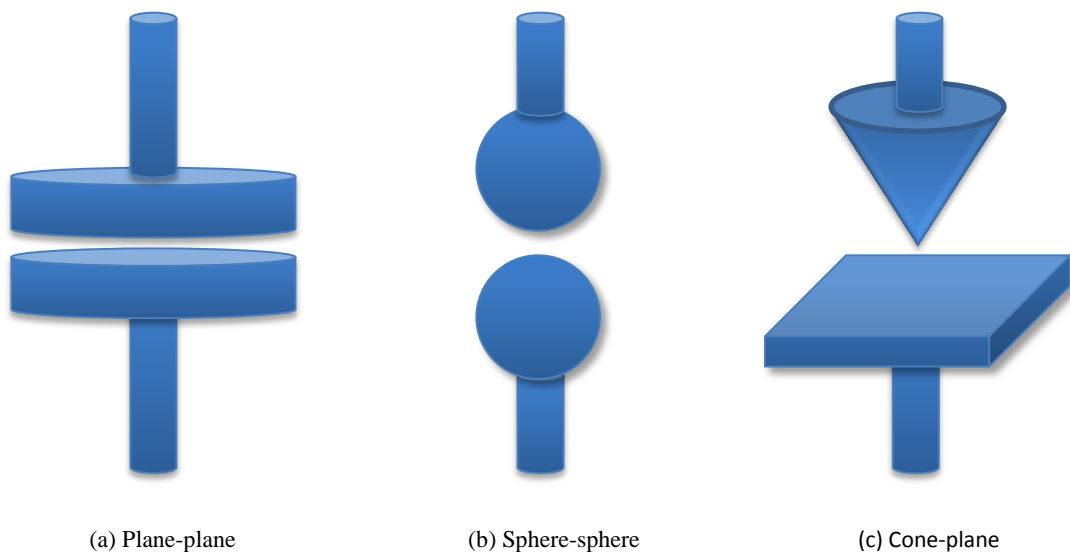


Figure 2.5 Typical spark switch electrode topologies.

Localised high electric field regions are often compared against a uniform topology as a method of standardising the discussion of non-uniform fields. The ratio of peak field to the uniform topology is the field enhancement factor, η :

$$\eta = \frac{\text{Peak field}}{\text{Uniform field}} \quad (2.4)$$

where the uniform field is calculated by Equation (2.5). The uniform field in the plane parallel topology (assuming no fringing effects) can be calculated by:

$$E = \frac{V}{d} \quad (2.5)$$

where E is the electric field strength, V is the voltage, and d is the inter-electrode separation.

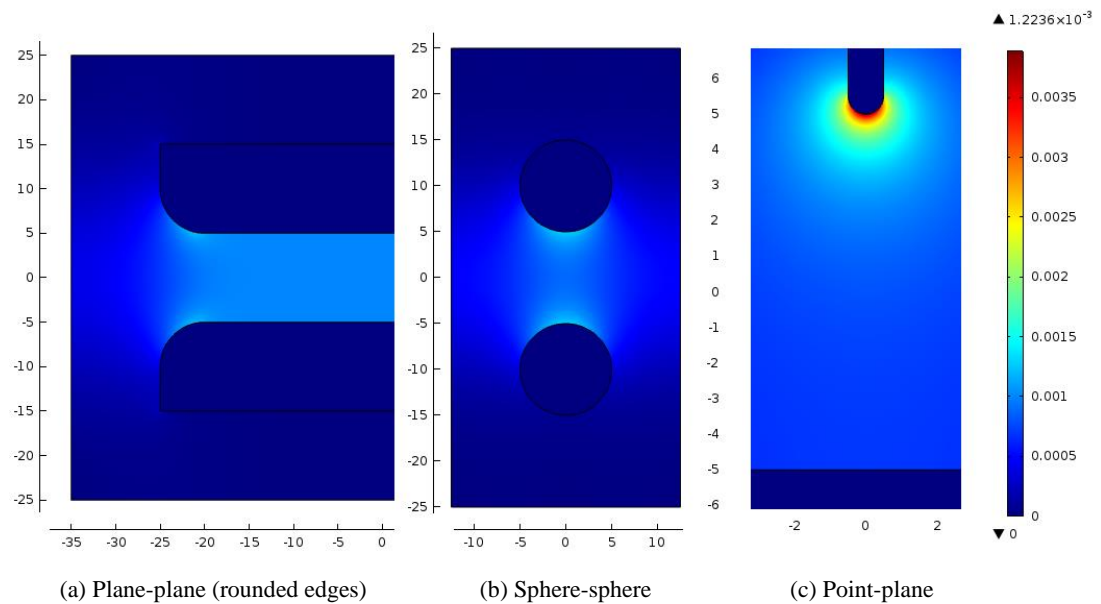


Figure 2.6 Electric field distributions of typical spark switch topologies. Simulated using Comsol Multiphysics electrostatic software with a 10 mm gap between electrodes and a 1 V energisation. Electric field is given in kV/cm.

Figure 2.6 shows the difference between plane parallel, sphere-sphere and point-plane topologies field distributions. Plane parallel topology, Figure 2.6(a), produces a uniform electric field between the electrodes (excluding enhancement fringing effects at the edges), the two other topologies generate non-uniform electric field with different degree of non-uniformity.

Equation (2.5) calculates the electric field assuming an ideal case of complete uniformity. It is often used as a bench mark for comparison, as in the case of Equation (2.4) for the uniform field.

When it is desired to have highly non-uniform field, the point-plane topology can provide the strongest local enhancement. The field in the point-plane topology is not symmetrical along the vertical inter-electrode axis, an analytical expression for the field along this vertical axis is given by Coelho and Debeau assuming the point electrode to be two confocal hyperboloids [Coelho and Debeau 1971]:

$$E(v) = \frac{\sqrt{[\rho^2(2 - \rho)^2 E_p^2]}}{(v + \rho)(2 - v - \rho)} \quad (2.6)$$

where:

$$\rho = \frac{r}{2d}$$

$$v = \frac{x}{d}$$

and r is the radius of the tip of the point electrode, d is the inter-electrode gap, x is the point along the inter-electrode gap, v is the normalised point along the inter-electrode gap and E_p is the peak electric field. E_p can be calculated similarly [Coelho and Debeau 1971] by:

$$E_p = \frac{2V}{a \ln\left(\frac{4d}{a}\right)} \quad (2.7)$$

where V is the voltage applied to the point electrode, and a is the electrode radius.

Equation (2.7) gives the peak field at the tip of a sharp point electrode. Coelho and Debeau made the assumption that the point can be modelled by two confocal hyperboloids, but it is reasonable to use for most sharp point electrodes in point-plane topologies.

The topologies discussed are general forms that are common in the pulsed power systems for switching and other applications. Most self-closing switches are very similar or slight variations on these general topologies. Triggered switches will have more complex

variations to allow for a trigger electrode or triggering ionisation sources. The triggering mechanisms of spark switches are discussed in the next section.

2.1.3 Triggering Approaches

Spark switches are used in the high-voltage, pulsed-power industry because they are capable of operating with: high voltage (100's V-100's kV), high current (kA), high dV/dt and dI/dt can provide fast closing times (10's of ns) with low jitter (few ns). They consist of 2 or more electrodes separated by an insulator, when a spark forms between the two electrodes through the insulator, the switch closes. This chapter will discuss the different methods of triggering the closure of spark switches and the switches currently used in the pulsed-power industry. Plasma closing switches can be sub-divided by means of their triggering mechanism. There are different methods by which a plasma closing switch can be triggered, some common methods are discussed: self-closing, trigatrons, and field-distortion triggering. This section discusses each of these triggering mechanisms and their advantages and disadvantages.

Self-breakdown closing switches are one of the most basic plasma closing switches, the simplest topology includes just 2 electrodes separated by a gas or liquid[Mesyats 2005]. Switch closure occurs when the applied field exceeds the critical value resulting in dielectric breakdown between the switch electrodes. Self-closing switches are popular in pulsed power systems as they are robust, reliable and cost-effective. Topologies of such switches can be optimised to minimise switch inductance. To operate the self-breakdown switch, voltage should be raised above the breakdown level or the breakdown threshold voltage can be reduced. There are two ways a breakdown voltage level could be reduced in a basic self-breakdown switch: reduction of electrode gap or reduction of the gas pressure in the switch. To reduce the electrode gap would require moving electrodes [Zou 2015] which makes switches more complex and less reliable. Therefore, once set, the electrode gap is normally fixed and the threshold breakdown level is controlled by changing the gas pressure (pneumatically operated switch). Self-closing switches are used extensively in the pulsed-power industry in high voltage generators such as the Marx generators [Marx 1923][Marx 1928].

Trigatron is a type of plasma closing switches which is equipped with a trigger electrode and is triggered via an electrical signal applied to this electrode. A trigger (pin) electrode can be inserted into one of the main electrodes. With 2 main electrodes energised to below the breakdown voltage level, a trigger pulse is applied to the trigger electrode which creates a

small spark between the trigger pin and main electrode. This trigger discharge results in the development of the breakdown in the main gap between the HV and ground electrodes.

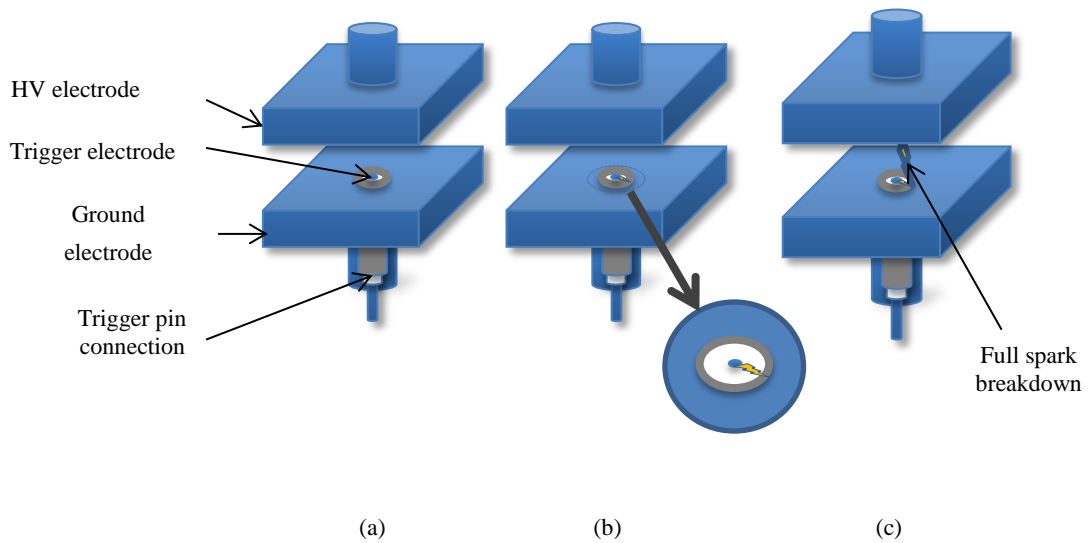


Figure 2.7 Trigratron switch operation. (a) no trigger pulse, (b) initiating spark, (c) full spark breakdown between main electrodes.

Trigratrons are popular switches because they are reliable and relatively simple switches that can be conveniently triggered by an electrical signal. The principle of operations of trigratron switches is depicted in Figure 2.7.

Field distortion triggering is commonly used when high-performance and consistency is required. In the simplest form, field distortion triggering has a trigger electrode located between the main electrodes. Usually positioned on the equipotential surfaces to have minimal impact on the field distortion before triggering, the trigger electrode is ‘floating’ and the main electrodes are pre-energised below the self-breakdown voltage level. Figure 2.8 shows an example of a field distortion switch with a trigger electrode placed between the main electrodes.

The electrodes are arranged such that DC pre-energisation does not cause electric breakdown between the main electrodes and trigger electrode when there is no trigger pulse. Also, the trigger pulse isn’t sufficient to cause breakdown without DC pre-energisation.

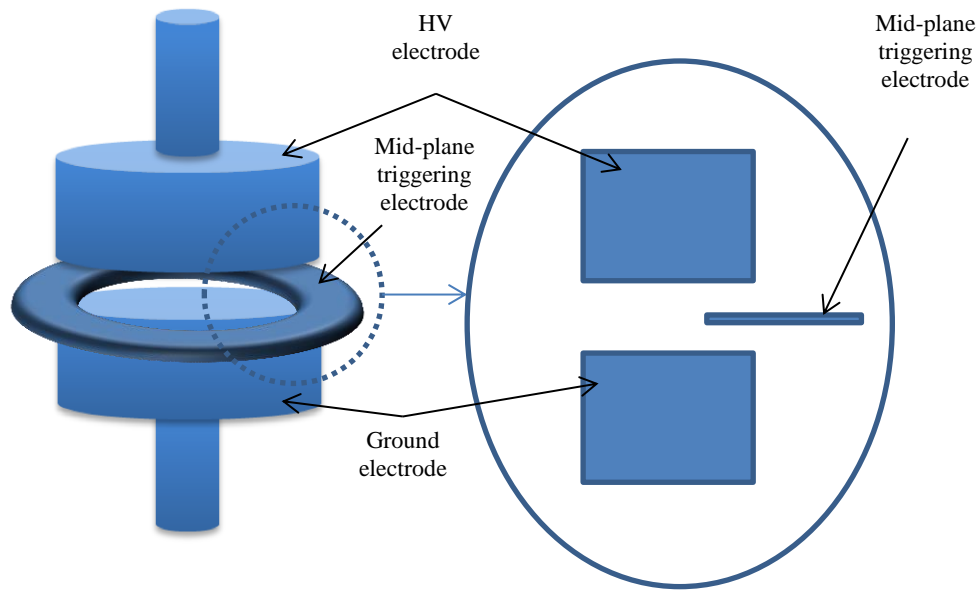


Figure 2.8 Field distortion triggered switch.

When a triggering pulse is applied (usually of opposite polarity to applied voltage), the local field between the trigger electrode and one of the main electrodes is very large, initiating a discharge. The discharge then expands to breakdown the gap between the main electrodes. Figure 2.9 shows the progression of the field distortion triggering switch.

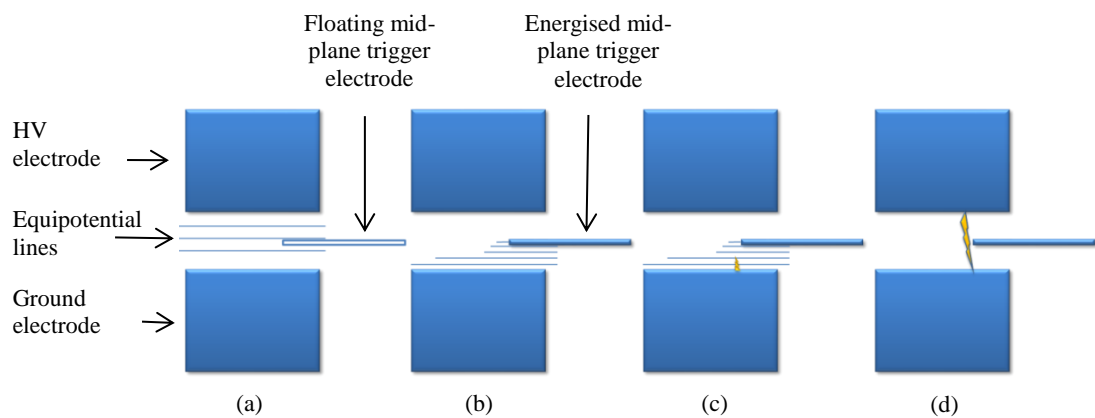


Figure 2.9 Progression of the field distortion triggered switch. (a) DC energised with no trigger voltage, (b) trigger voltage applied with enhanced field between trigger and main electrode, (c) discharge initiated in high field region, (d) complete breakdown between main electrodes.

Field distortion triggered switches can operate at wide range of voltages (~10-100s kV) with low jitter (~2 ns) and good reliability [Mercer 1976]. They are used in many large pulsed power systems that operate with very high voltage and could, in theoretically proposed generators, require up to 100,000 switches to operate at the same time [Woodworth 2009b] [Stygar 2007]. Field distortion triggering performance is dependent on the level of DC pre-

energisation, rate of rise and magnitude of applied trigger pulse. Higher over-voltage tends to reduce closing time and jitter.

Other triggering mechanisms used in plasma closing switches include UV ionisations, electrons beam, and laser triggering. These triggering mechanisms use a source of external radiation to inject seed electrons to cause ionisations and initiate a discharge. These methods can be highly controllable with fast (~ 10 ns), consistent closing times (jitter ~ 1 ns) [Mesyats 2005]. These external triggering methods are out with the scope of this research.

Many high-energy systems requiring very high hold-off voltages such as those used in linear transformer drivers use switches with multiple gaps, stacking three or more electrodes to increase the breakdown strength and improve switching performance. Multi-gap switches are discussed in Section 2.1.4.

2.1.4 Multi-Stage Switches

Multi-stage spark switches have two or more spark gap that must breakdown to close the switch. By increasing the number of stages (spark gaps) the breakdown strength of the switch can be increased while keeping reasonably low pressure in the switch. The switch remains compact and its performance satisfies the operational requirements. Multi-stage switches are normally used in high-energy, high-voltage pulsed power systems such as Sandia's Z accelerator or linear transformer drivers. Multi-stage switches are not new, Gardner and Vorob'ev suggested multi gap switches in 1953 and 1959 respectively [Gardner 1953] [Vorob'ev 1959]. The early development of multi-stage switches demonstrated that there was the possibility to achieve fast closing switches, ~ 10 ns, with nano-second jitter [Mesyats 1960, 1974]. In recent years, there has been renewed interest in multi-stage switches with publications comparing switches from Sandia National Laboratories, Kintech Ltd (USA), and the Institute of High Current Electronics (IHCE), Tomsk, Russia [Kim 2006, 2009] [Woodworth 2009a,b, 2011, 2012].

Multi-stage switches distribute the charge across all of the stages with reduced electric field across each gap in the switch, resulting in increased overall breakdown strength. The voltage is graded across the stages of the switch, achieved by either fixed resistors between the stages or by sharp point protrusions on the electrodes creating corona discharge [Mesyats 2005] [Given 2011]. The early development of multi-stage switches were used in megavolt systems such as the 6 MV PBFA II and Hermes III at Sandia National Laboratories

in America, which used the Rimfire switch [Humphreys 1985] [Turman 1983][LeChien 2010]. The Rimfire switch and variations of it were used in many megavolt systems claiming that it could promote multichannel breakdown, therefore reducing the switch inductance [Kemp 2005][Kemp 2006]. The 6 MV Rimfire switch has 26 8.4 mm cascading spark gaps and a UV laser (KrF, 25 mJ) triggered first gap, Figure 2.10, [Bluhm 2006]. The Rimfire switch electrodes are toroidal rings, which are stacked, separated by small plastic insulators was also created for 4 MV operation with just 15 stages [Bluhm 2006].

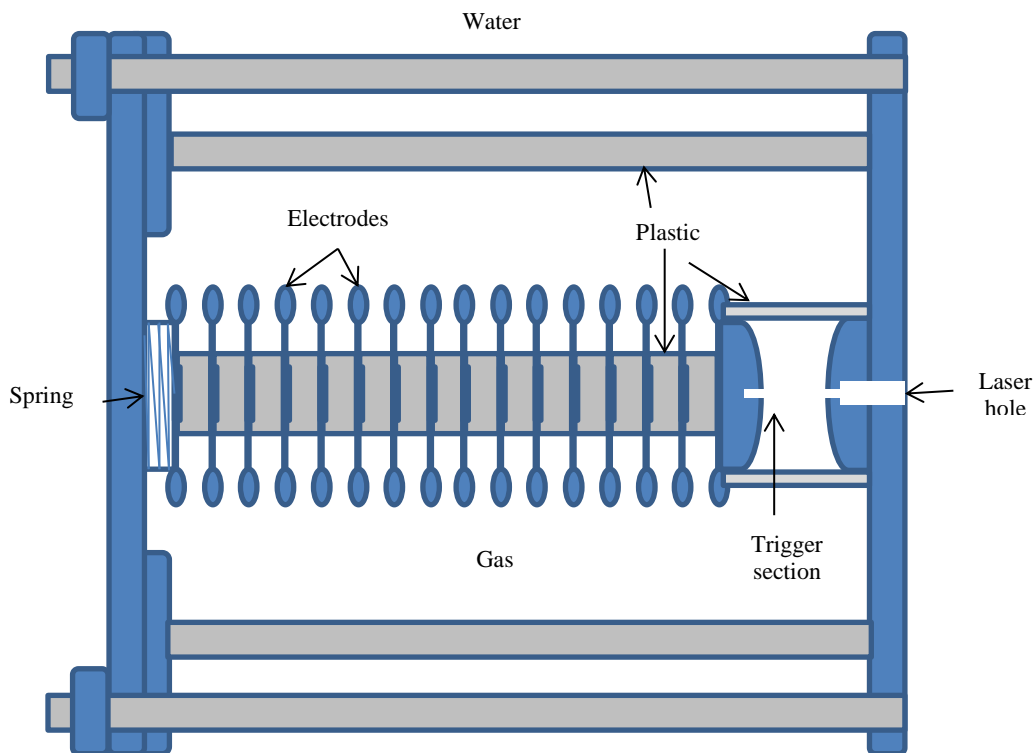


Figure 2.10 Toroidal electrodes used in Rimfire switch.

The Rimfire switch was later adjusted to replace the laser triggering in the HYBRID switch that used another multi-electrode triggering switch to trigger [Volkov 1999]. The HYBRID switch is used in the APPRM system in Sandia National Laboratories [Mesyats 2005]. The laser triggered 6 MV Rimfire switch has a delay of ~20 ns and jitter of less than 0.4 ns [Bluhm 2006].

The Rimfire switch and its variations were filled with SF₆ at 0.6 MPa and were then immersed in transformer oil. SF₆ was used due to its high breakdown strength, but it has since been identified as a greenhouse gas hence renewed interest to find environmentally friendly alternatives. The most recent literature focusing on replacing SF₆ in megavolt

systems focuses on newer switch designs, including multi-electrode designs. With the advancements in linear transformer drivers (LTD), the demands of their switches require hold-off voltage of 100-200 kV.

The 4 main switches topologies used in mega-voltage pulsed power are considered in recent literature [Woodworth 2009a,b, 2010, 2011]. These switches include the SNL switch from Sandia National Laboratories (USA) and L3 Communications Pulse Sciences Division (USA), the LLC switch developed by Ktech Ltd and Sandia (USA) and the IHCE switch developed by the Institute of High Current Electronics in Tomsk, Russia. While the presented research is not focused on developing a switch topology to compete with the systems mentioned above, it is useful for comparison because LTD switches require the best performance, fast closing times, low jitter and low inductance. Table 2.1 shows a comparison of the air insulated LTD switches, focusing on operating results, inductance and jitter.

Table 2.1: LTD plasma closing switch performance comparison [Woodworth 2009a,b 2010, 2011].

	Voltage (kV)	No. of gaps	Inductance (nH)	Pressure (MPa)	Jitter (ns)
L3	120	2 at 6.4 mm	93	0.69-1	0.47-1.2
IHCE	100	6 at 6 mm	115-120	0.27-0.43	0.98-1.8
LLC	200	2 at 5 mm	69	1.6-1.9	1-2.4
SNL	200	2 at 12 mm	66	0.9	5.7

The best triggering mechanism for high performance switches is debatable and the LTD switches employ varying methods. All of the LTD switches require a triggering impulse to a middle electrode, the triggering voltages depending on the size of the switch and the number of gaps.

The L3 switch developed by Communications Pulse Sciences Division in the USA has just two gaps. The L3 switch has a central pre-illumination gap which a short air arc fills with UV radiation. The switch consists of two flattened, hemispherical electrodes 6.4 mm from a mid-plane trigger electrode. A small hole in the centre of the mid-plane electrode allows for

UV radiation coupling between the gaps [Woodworth 2009b]. Figure 2.11 shows an axisymmetric representation of the switch topology with two main electrodes and a mid-plane electrode with a hole in the middle.

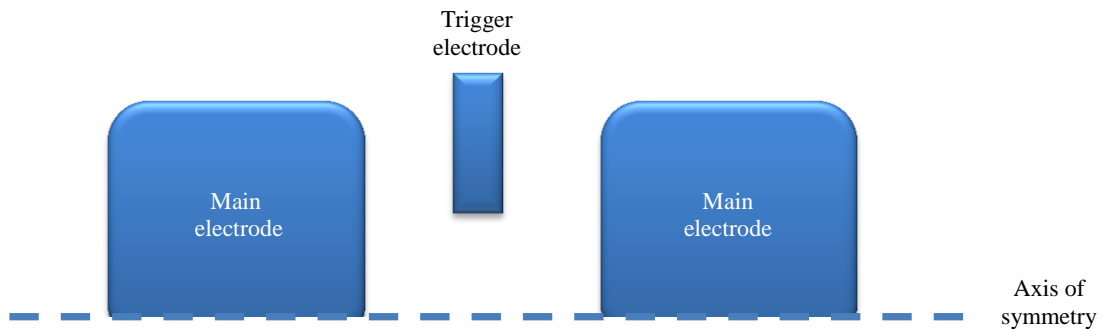


Figure 2.11 Axisymmetric representation of the topology in the L3 switch made by Communications Pulse Sciences Divisions (USA).

Literature publications on the spark switches do not provide detailed description of all the switch topologies. For the L3 switch, Woodworth *et al.* provided a crude drawing and brief explanation of the topology [Woodworth 2010].

The IHCE switch is different to the others considered in this review because it has more than two gaps and a very different topology design. The main switching electrodes are toroidal shaped with a 6 mm gap between the toroids with a total of 6 gaps. The centre of the toroid is a plane parallel to all toroids with a sharp point corona pin which acts to distribute the charge between the stages of the switch. Figure 2.12 shows an axisymmetric representation of a section of the IHCE toroidal electrode topology.

The IHCE switch has a similar toroidal design to that used in the early multi-stage switches such as the Rimfire switch [Mesyats 2005][Kim 2009]. The toroidal design provides a similar field enhancement to a sphere-sphere topology and, being a toroid, it has a larger surface area to reduce electrode erosion which results in a longer life time of the switch. The parallel planes in the middle of the toroid and the corona point electrodes act as a point-plane topology creating intensive electric fields which causes corona discharge between stages that grades the voltage across the switch stages [Mesyats 2005].

The LLC switch from Kintech ltd (USA) has a more simple design with two main identical hemispherical topped copper-tungsten electrodes at each end of the switch. The two stages are made up with 4 trigger pins that are located in the middle of the switch. The trigger pins

are 3 mm diameter hemispherical tipped rods and the gap between the main electrodes and the trigger electrodes is 5mm [Woodworth 2009b].

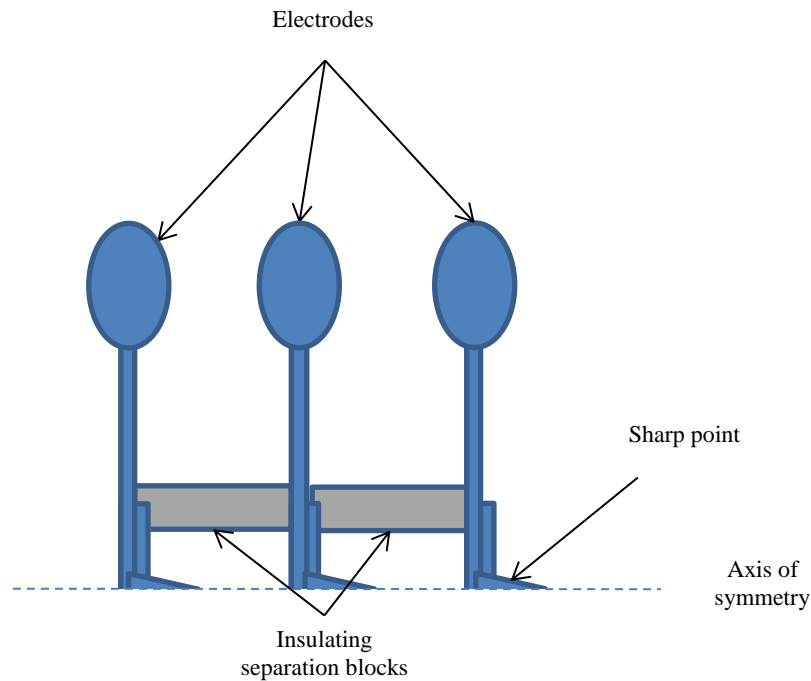


Figure 2.12 Axisymmetric representation of the topology in the IHCE switch (Russia).

This section was focused on pulsed power, introducing the basics of pulsed power theory and discussing spark switches. The triggering of spark switches was discussed and different approaches compared as well as a comparison of multi-gap switches currently in use.

The last section of this literature review concerns the post-breakdown plasma parameters: plasma resistance, and inductance. Post breakdown plasma resistance and inductance are, in some cases, the most important factor when fast-rising high current pulses are required and, therefore, it is the next step for the progression of this work.

2.2 DYNAMIC RESISTANCE OF SPARKS

In this section, the models of dynamic plasma resistance formed by a high voltage discharge in a gaseous dielectric are discussed. A good understanding of the resistance of sparks is necessary for optimisation of energy dissipation in the spark channel in spark switches. Plasma resistance has been investigated by many researchers with the aim of identifying

accurate models of the time varying dynamic resistance of plasma in gases [Li 2014][Oreshkin and Lavrinovich 2014][Engel 1989] [Istemic 2005] [Greason 1997] and liquids [Kudelcik 2010] [Timoshkin 2006]. To date, there are no definitive theoretical models that can predict dynamic resistance with sufficient accuracy. There are different approaches competing to provide the most accurate representation of experimentally measured resistance.

All the proposed models in literature directly relate the current in the plasma channel to its resistance. This is a reasonable assumption since the conductivity of a gas is dependent on the mobility of the charged particles. As electrons become more mobile, their velocities increase and as such the current increases. However, in the simplest form, Ohm's law includes constant resistance, $V=IR$. Therefore, in order to model the transient process accurately, it is necessary to develop a self-consistent model with non-constant resistance: $V(t) = I(t)R(t,I)$. Therefore, this approach will allow simulation of transient parameters in the switch such as transient current, transient resistance and power.

Plasma resistance is not only dependent on current because the plasma channel is not a fixed size, temperature or pressure. Therefore, the models for dynamic plasma resistance have further assumptions and/or coefficients to increase their accuracy. The models discussed here and in literature follow two main approaches: resistance, r , is proportional to the inverse integral of current, i :

$$r_{pl} \propto \frac{1}{\int i dt} \quad (2.8)$$

and resistance is proportional to the inverse exponential of current, i , to the power n :

$$r_{pl} \propto \frac{1}{i^n} \quad (2.9)$$

both of which only account for plasma resistance from open circuit resistance to minimum resistance as the current reaches its maximum.

A radius of plasma channel does not remain at a fixed size as the energy in it is increased. Plasma channels will initially have a very small cross-section which will expand rapidly as the energy in the plasma increases. This has a direct impact on the resistance of the plasma channel, if plasma were assumed to be a conductive wire, its resistance would be expressed as:

$$r = \rho \frac{l}{A} \quad (2.10)$$

where:

- ρ is the resistivity [$\Omega.m$],
- l is the length of conductor (plasma channel) [m],
- and A is the cross-sectional area of the conductor (plasma channel) [m^2].

In the same manner, the available area for charged particles to flow in plasma has a direct impact on the resistance and it is an important factor to consider when simulating plasma resistance. Plasma channel radius can be reasonably evaluated using a hydrodynamic model proposed by Braginskii. This approach has been used in several studies and has been compared with experimental data on plasma resistance by Maas to show reasonably accurate results [Braginskii 1958] [Maas 1985]. Therefore, for the purposes of this investigation Braginskii's model was used for plasma channel simulations. Braginskii's plasma arc radius equation is expressed as [Braginskii 1958]:

$$a^2(t) = \left(\frac{4}{\pi^2 p_0 \zeta \sigma} \right)^{1/3} \int_0^t i^{2/3} dt \text{ } [\mu m] \quad (2.11)$$

where:

- $a(t)$ is the radius of the plasma channel [m],
- i is the current [A],
- p_0 is the initial gas density [kg/m^3],
- ζ is a constant which depends on the gas,
- σ is the conductivity [$1/\Omega.m$],
- and t is time [s].

In the present work, 7 plasma resistance models proposed by Braginskii, Toepler, Rompe and Weizel, Barannik *et al*, Popovic *et al*, Demenik *et al* and Kushner *et al* will be analysed and used for obtaining of the transient plasma channel resistance. The plasma resistance models which are available in the literature will be discussed in terms of the basic theory and assumptions made in each of these model, [Braginskii 1958] [Toepler 1906] [Rompe 1944] [Barannik 1975] [Popovic 1974] [Demenik 1968] [Kushner 1985]. Most of these models are based on the main physical mechanisms (energy balance equation, principles of thermodynamics). However all of them require phenomenological constant(s) in order to fit

analytical data to specific experimental conditions (type of gas, pressure, etc). In the models discussed below, this empirical constant, C , accounts for different spark parameters. The constant C does not have an impact on the functional behaviour of the transient plasma resistance $R(t)$ and, in many cases the authors did not even suggest values for the constants. Rompe and Weizel attempted to analytically calculate C [Rompe 1944]. However, in most models, this constant is usually empirically found using experimental data and some values for these simulations have been suggested for initial pressure of $P_0 = 0.86 \times 10^5$ Pa by Engel *et al* [Engel 1989]. In the present research project, the constants in the resistance models are manipulated to normalise the modelled data for one pressure. When comparing simulated plasma results with the experimental results available in the literature, it may be necessary to adjust the constants to align the resistance curves which may have been taken under different experimental conditions. Each of the models created by the researchers mentioned above will be discussed briefly, their expression for plasma resistance, and some of the assumptions and parameters will be provided.

Toepler first proposed an equation for plasma resistance as proportional to the inverse integral of current in 1906 [Toepler 1906]. This equation was derived empirically from experimental data:

$$r(t) = \frac{Cl}{\int i dt} \quad (2.12)$$

where:

- $r(t)$ is the dynamic plasma resistance [Ω],
- C is the constant for proportionality which characterises the gas,
- l is the arc length [m],
- and i is the current [A].

The empirical data on which this model is based gives a discharge length between, $l = 9 - 10$ mm and was conducted in air with an initial pressure of, $P_0 = 10^5$ Pa. The author provided no recommendations for constant C , however, to present data at a normalised pressure of $P_0 = 0.86 \times 10^5$ Pa, Engel *et al* reports a constant of $C = 4.5 \times 10^{-2}$ [Engel 1989].

Research into plasma resistance by Popovic *et al* presented another empirical relationship to describe plasma resistance via an inverse integral [Popovic 1974]. The relationship between resistance and current is expressed as:

$$r(t) = \frac{Cl}{[\int i^2 dt]^n} \quad (2.13)$$

where the symbols have the same meaning as those in Equation (2.12) and n is a constant. This relationship was based on a different experiment to Toepler in which different gases were used (air, oxygen, argon and xenon) and the initial pressure is given by $P_0 \leq 0.5 \times 10^5$ Pa. The arc length, l was set at 20 mm and a unipolar pulse was used to get the plasma resistance. The author suggests a coefficient for the proportionality of $n = 0.33$ and Engel *et al* have suggested $C = 30$ and $n = 0.33$ [Engel 1989].

There are three other models considered here that have an inverse proportionality with the integral of current. Models proposed by: Braginskii, Rompe and Weizel and Barranik *et al* all derive the plasma resistance equations from the energy balance equation and result in an inverse integral proportionality with current. The energy balance equation is derived from hydrodynamic equations and can be expressed as [Engel 1989]:

$$\frac{dU}{dt} + p \frac{l}{dt} [\pi a^2] = \frac{i^2}{\sigma \pi a^2} \quad (2.14)$$

where:

- U is the arc channel energy per unit length [J/m],
- p is the shock front pressure [Pa],
- a is the channel radius [m],
- and σ is the conductivity [$1/(\Omega \cdot m)$].

In 1944 Rompe and Weizel proposed an equation for plasma resistance derived from the energy balance equation (Equation (2.14)) which expressed resistance as an inverse integral of current [Rompe 1944]:

$$r(t) = \sqrt{\frac{P_0 l^2}{2C \int i^2 dt}} \quad (2.15)$$

where the symbols have the same meaning as those in Equation (2.12). Rompe and Weizel derived this equation to work with an initial pressure, $P_0 = 1.6 \times 10^5$ Pa and valid for arc lengths, $l \leq 35$ mm. This was based around a unipolar pulse of 50 ns and has been experimentally confirmed by Mesyats [Mesyats 1971][Engel 1989]. The limitation of this model is the lack of arc radius consideration or thermal losses. The authors did not suggest

any values for the proportionality constant, C . However, Mesyats confirmed the results and published $C = 11.5$ and Engel suggested $C = 9.7$ for air [Mesyats 1971] [Engel 1989].

Barannik *et al* published a new model for plasma resistance with an inverse integral proportionality with current which includes arc radius effects [Barannik 1975]. This equation was also derived from the energy balance equation (Equation (2.14)) and can be expressed as:

$$r(t) = \frac{Cl\rho_0^{1/3}}{\int i^{2/3} dt} \quad (2.16)$$

where the symbols have the same meaning as those used in Equation (2.12) and ρ_0 is the initial gas density. Barranik's equation was developed to suit experimental testing using a unipolar pulse of 100 ns and current below, $i \leq 10$ kA . The equation was given for arc length of, $l \leq 400$ mm in air, sulphur hexafluoride and nitrogen with initial pressure, $P_0 \leq 12 \times 10^5$ Pa. This model assumes no thermal losses, electron temperature is constant and conductivity is constant. The author suggested a proportionality constant, $C = 1.7 \times 10^{-3}$ for an initial pressure $P_0 = 10^4$ Pa and Engel *et al* suggested $C = 1.7 \times 10^{-3}$ Pa for initial pressure, $P_0 = 0.86 \times 10^5$ Pa [Engel 1989].

Braginskii who developed the hydrodynamic expression for arc channel radius that is primarily used here, gives an expression for plasma resistance as [Braginskii 1958]:

$$r(t) = \frac{l}{\sigma \pi a(t)^2} \quad (2.17)$$

where:

- l is the arc length [m],
- σ is the conductivity of the channel [$(\Omega \cdot m)^{-1}$],
- and $a(t)$ is the plasma arc radius [m].

Braginskii, in the same paper, presents a reduced expression for the channel that is expressed as:

$$r^2(t) = C_{BRAG}^{1/3} \int i^{2/3} dt \quad (2.18)$$

where:

- C_{BRAG} is a constant that depends on initial pressure, conductivity and gas type,

- and i is the current [A].

The constant C_{BRAG} is a function of initial gas density, conductivity and gas type which they expressed as [Martin 1993]:

$$C_{BRAG} = \frac{4}{\pi^2 \rho_0 \zeta \sigma} \quad (2.19)$$

where:

- ρ_0 is the initial density [kg/m^3],
- σ is the conductivity (which is constant) [$(\Omega \cdot \text{m})^{-1}$],
- and ζ is a constant for the gas type.

The Braginskii constant is designed to make allowances for different gases, pressures and conductivities. Martin provides values for ρ_0 and σ for different gases and gives $\zeta = 4.5$ for all gases which was published by Braginskii for hydrogen. For use in air, Martin suggests values for initial density and conductivity, $\rho_0 = 1.293 \times 10^{-3} \text{ g}/\text{cm}^3$ at 14.7 psia and $\sigma = 200 \mu\text{S} \cdot \text{cm}$ Martin gives $C_{BRAG} = 0.091$, Rosenthal *et al* give a conductivity of $160 (\Omega \cdot \text{cm})^{-1}$ [Martin 1993] [Rosenthal 2003].

So far, the models considered have all assumed plasma resistance to have a proportionality inverse to the integral of the current. However, some investigations have identified a close approximation with experimental data using inverse exponential expressions. This investigation considers models with this characteristic by Demanik *et al* and Kushner *et al* [Demanik 1968] [Kushner 1985]. These can provide close approximations for plasma up to peak current and for a short time after, which is not possible in the inverse integral expressions used by Braginskii, Toepler, Barranik, Popovic and Rompe and Wiesel.

Demenik *et al* published a model in 1968 with an inverse exponential current proportionality which also accounts for plasma arc radius expressed as [Demenik 1968]:

$$r(t) = \frac{Cl}{a(t)^{10/11} i(t)^{6/11}} \quad (2.20)$$

where:

- $a(t)$ is the dynamic arc radius [m],
- $i(t)$ is the dynamic current [A],
- l is the length of the arc [m],
- and C is a constant.

Demenik *et al*'s equation is given for xenon at an initial pressure of $P_0 = 0.5 \times 10^5$ Pa and an arc length of $d = 6 - 300$ mm for a unipolar pulse 1.5 m long. This equation assumed conductivity to be proportional to electron temperature: $\sigma \propto T_e^{3/2}$ and electron temperature is given by: $T_e = \frac{i^{4/11}}{r^{2/11}}$. It assumes “weak” ionisation and Demenik *et al* provide no values for constant C . However, Engel *et al.* suggests, $C = 0.3$ for an initial pressure $P_0 = 0.86 \times 10^5$ Pa [Engel 1989]. The equation is valid for current densities ranging from $j = 0.3 \times 10^4 - 15 \times 10^4$ kA/cm².

The final model considered in this research was proposed by Kushner *et al* in 1985, and it has the plasma resistance proportional to the inverse exponent of current [Kushner 1985]:

$$r(t) = Cl \left[\frac{P_0^3}{A^2 i^6} \right]^{1/5} \quad (2.21)$$

where the coefficients are the same as those in Equation (2.20) and which is based on a unipolar pulse of 100 ns in hydrogen, nitrogen, sulphur hexafluoride, methane and xenon with an initial pressure $P_0 = 0.5 \times 10^5$ Pa. Experimentally, this expression was proved reasonable for a gap length $l = 12$ mm with current density 2×10^4 MA/cm². The author did not give any values for the proportionality constant C , however, Engel *et al.* reported $C = 24.7$ for initial gas pressure $P_0 = 0.86 \times 10^5$ Pa in air [Engel 1989].

All of the plasma models that have been discussed here can be grouped into two main theoretical approaches:

- solving the energy balance equation,
- or assuming $r \propto \frac{d}{\sigma A}$ (like a wire conductor).

It was shown that Kemenik *et al*, Kushner *et al* and Rompe and Weizel models can reasonably simulate plasma resistance in the early stages of breakdown (up to the peak current). Engel suggests these models to be more accurate due to the fact they all assume “Spritzer conductivity” where the conductivity is proportional to the electron temperature, $T_e^{3/2}$ and, as such, there is a high degree of ionisation [Engel 1989]. At times after the peak current this may no longer be true and the inverse integral equations do not represent plasma resistance as well as the inverse exponential functions. Engel also says that the empirical formulae proposed by Toepler and Popovic *et al* may not be as accurate as Rompe and Weizel due to less complete models with fewer considerations of gas constants. In Chapter 9,

each of the equations discussed in this section are used in the model which was created using PSpice software in order to obtain transient plasma resistance function for different gases.

All of the models discussed have analytical basis for most of their coefficients. However, Braginskii's model can be derived using hydrodynamics and includes coefficients for different gases, arc lengths, conductivity, and initial pressure. While other models have been developed around multiple gases, arc lengths, etc; Braginskii's model gives the most robust range of configuration with fewest assumptions.

These transient plasma resistance values are compared with the experimental data available in the literature.

2.3 CONCLUSIONS

This chapter discussed the principles of pulsed power, fundamental aspects of the development of discharges in gases and the main topologies and parameters of the plasma closing switches. The main pulsed power systems and topologies were discussed with reference to spark switches and the high voltage pulsed power techniques. A review of spark switch triggering techniques and topologies was conducted. Recently designed and developed spark switches were discussed with reference to their operating parameters and performance of interest to the pulsed power industry.

The main aspects of breakdown mechanisms in uniform and non-uniform electric fields were discussed including: Townsend discharge, Paschen's law, corona and streamer discharges, attention was paid to breakdown behaviour in non-uniform electric fields in the case of positively and negatively stressed electrodes. Special consideration was given to corona discharge theory which occurs in non-uniform electric fields because it is a reoccurring theme investigated in this thesis.

Finally, the main dynamic plasma resistance models proposed in literature were discussed. Plasma resistance is particularly important in the pulsed power industry which requires fast rising high current output, and so much work is focused on modelling dynamic plasma resistance. This thesis presents a new approach to simulating dynamic time varying plasma resistance using PSpice simulation software which would allow dynamic plasma resistance to be included in complex circuit models. Therefore, a review of literature models was conducted and the limitations and advantages were discussed.

In the following chapters, this thesis discusses the experimental techniques used to investigate spark switches. Initially, the ramped self-breakdown voltage and its standard deviation were investigated by considering different commonly used topologies, plane-plane, sphere-sphere and cone-plane. A sharp point-plane topology was then investigated in detail. Corona discharge is discussed throughout this thesis with reference to its impact on switching performance and so it is investigated in its own chapter. Building on from the results obtained, the time delay to breakdown and jitter are investigated and a new method for triggering is presented. From initial work on different topologies, the point-plane geometry was chosen to investigate the multi-stage regimes by stacking 2 and 3 spark gaps. A new approach to modelling of post-breakdown transient spark resistance using PSpice simulation software is developed. Models for plasma resistance from literature are simulated

using the PSpice approach and compared with experimental data taken from literature. An advanced model was created to include both transient dynamic resistance and inductance analysis of performance of pulsed power systems.

3. EXPERIMENTAL SYSTEMS AND PROCEDURES

This research project focuses on development of compact self-breakdown and triggered spark switches with and without corona discharge, investigating the operational characteristics and parameters. Several different experimental systems and switch topologies were developed for the purposes of this research project, each of these systems and experimental procedures are discussed in this chapter. The design and development of the experimental set-ups with improved control and measurement characteristics is one of the major outcomes of this thesis. Initially, a precision pneumatic control system was designed and developed to ensure high degree of control of gas pressure in the test switches. An HV test bed was designed. In order to provide an accurate control of the DC charging voltage (magnitude and rate of rise), a custom written LabVIEW code was used. This HV computer-controlled system was used to study breakdown voltage of spark switches with different topologies. Building on from the DC breakdown experimental facilities, an adaptation to this test bed was made which included a corona viewing shunt resistor for measuring corona voltage. A new experimental HV test bed for investigation of operational characteristics of triggering spark switches was also developed. In this system, superimposed impulse triggering of two electrode switches was implemented. The last experimental system discussed in this chapter was developed to study operational parameters of triggered multi-stage switches. Each of these experimental HV test beds are discussed in the following sections.

3.1 PNEUMATIC CONTROL SYSTEM

The experimental work carried out in the course of this research focused on investigation of operational characteristics of gas filled spark switches filled with different gases where the pressure in the switches ranged from atmospheric pressure (0.1 MPa) up to 0.4 MPa. Special care was taken to ensure the accurate values of the gas pressure inside the switches and

consistency in the gas handling procedure. A specially designed precision pneumatic gas control board was designed to control the gas in the experimental test beds, Figure 3.1.

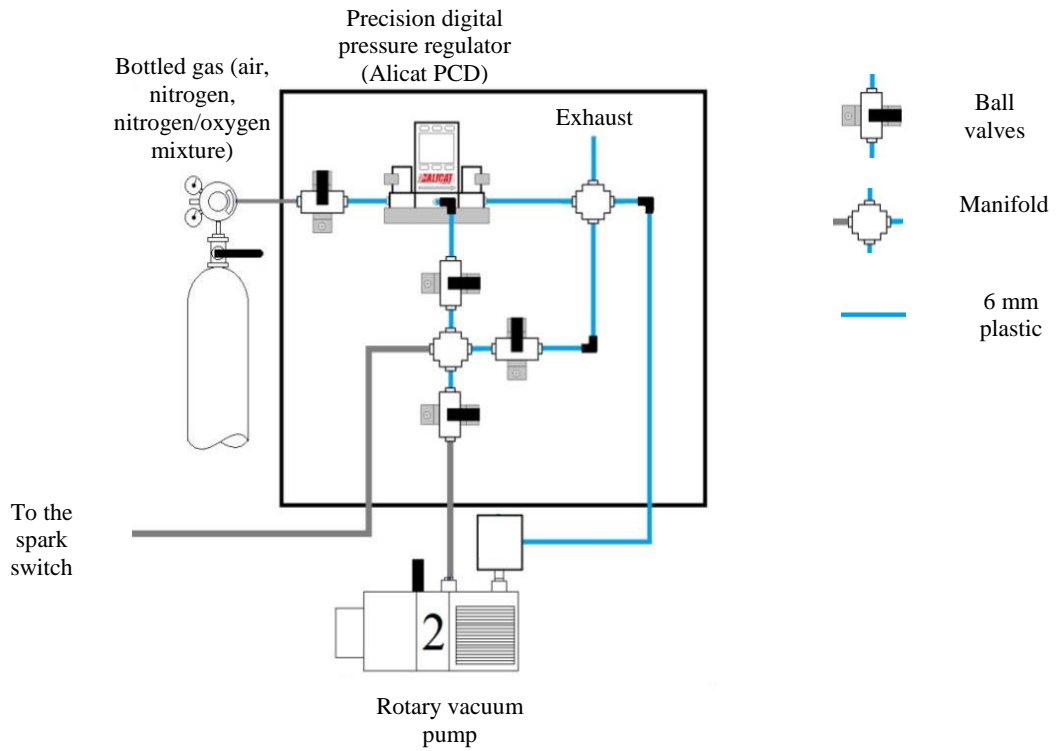


Figure 3.1 Pneumatic pressure control system.

A digital pressure regulator (Alicat PCD) was used to control the gas pressure in the switch. Using the precision pressure regulator, the switches were pressurised with: bottled air, nitrogen, and a 60%/40% nitrogen/oxygen mixture up to 0.4 MPa. The accuracy of the gas pressure measurements was ± 0.00175 MPa. This pneumatic control system was used in all of the experimental set ups in this research project. In further description of the experimental procedures (in the schematics given for each experiment), the gas handling system is indicated as a box without details, all specific details are given in Figure 3.1.

Section 3.2 to Section 3.5 discuss the electrical test bed systems used throughout this research project. The next section discusses the development of the first test system to measure self-breakdown voltage.

3.2 METHODOLOGY OF MEASUREMENT OF SELF-BREAKDOWN VOLTAGE

Measuring the self-breakdown voltage of spark switches that include pre-breakdown corona discharge requires an experimental system which consistently provides repeatable conditions. Pre-breakdown corona discharge can create volumetric negative space charges in electronegative gases that increase the breakdown voltage significantly. Negative self-breakdown voltage of a point-plane electrode topology is 20-30% higher than positive because of space charge screening effects. Therefore, when comparing the self-breakdown voltage of topologies with pre-breakdown corona discharges, it is important that the experimental conditions such as gas pressure, rate of voltage rise are repeatable. Throughout the progress of the research, the experimental system was continually developed. Figure 3.2 shows the test system used in Chapter 4 to measure breakdown voltage, with a computer controlled high-voltage DC power supply.

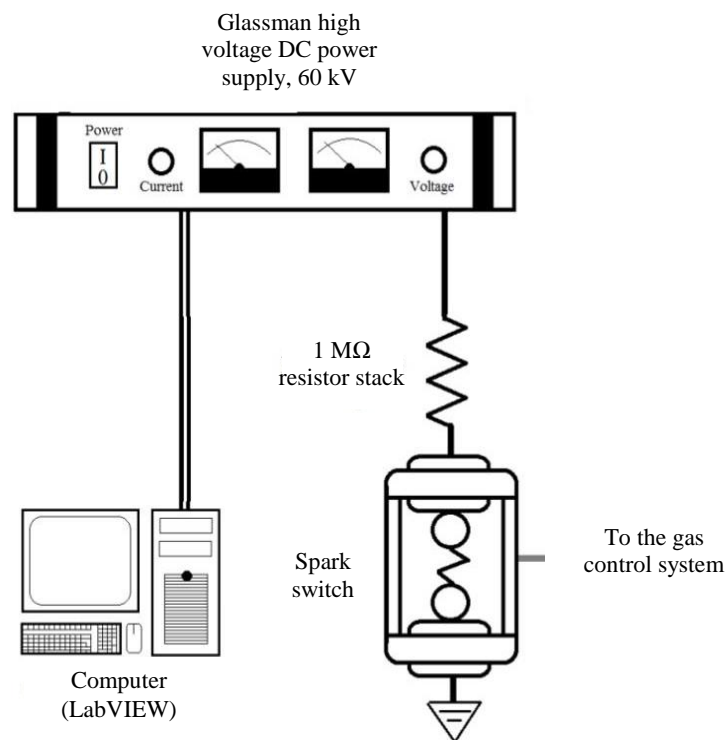


Figure 3.2 DC breakdown voltage initial experimental test system.

A Glassman high voltage DC power supply (EH series, 0-60 kV) was used to stress the spark switches via a charging resistor (1 M Ω). The voltage out of the HV DC power supply was controlled by a LabVIEW program that interfaces with the power supply using a National Instruments DAQmax SCB-68. The DC and ramped voltage across the switch was measured using a TESTEC TT-HVP40 high-voltage probe (1000:1, 40 kV, 300 Hz) and an ISO-TECH IDM91E digital multi-meter. The breakdown voltage was recorded as the highest voltage before voltage collapse due to gas breakdown in the switch.

The laboratory environment was divided into two sections: the control, low-voltage section of the lab was used for control equipment and the DC power supply; another section was a high voltage section in which test beds and HV probes were placed during high-voltage experiments. The experimental control room is shown in Figure 3.3 and the high-voltage test room is shown in Figure 3.4.

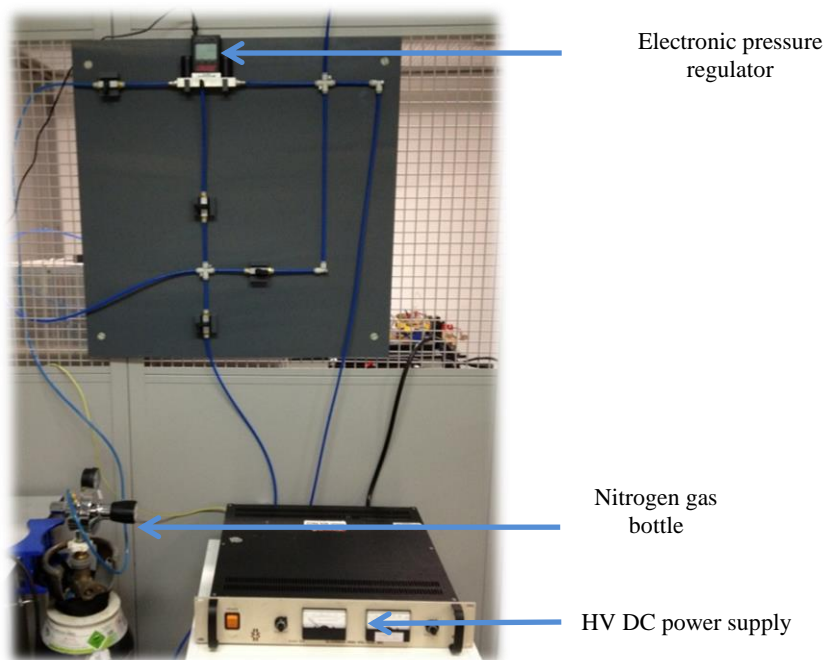


Figure 3.3 Experimental control room.

The LabVIEW code was written to control the voltage across the switch with a stepwise increase of voltage ramping up from 0 V till breakdown occurs. A 0-10 V signal from the digital acquisition board, DAQmax, proportionally outputted a 0-60 kV from the HVDC power supply.



Figure 3.4 Experimental high-voltage room.

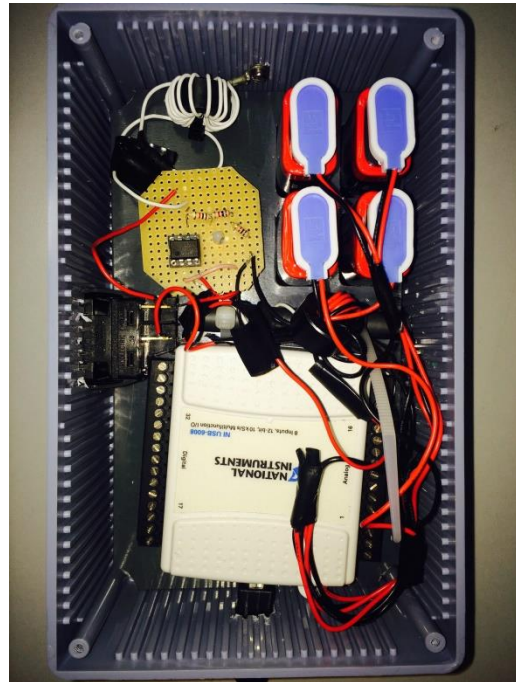
The initial rate of rise used in the tests presented in Chapter 4 increased at a rate of 667 V/s. This rate of rise was chosen such that experimental conditions would remain constant so that data could be compared reliably while ensuring a significant amount of data could be collected in a timely manner. However, this rate of rise is, in the context of pulse power and gas discharge, very slow and can be considered DC for the purpose of measuring breakdown voltage and corona inception voltage. This rate of rise was changed in later experiments and is explained in the relevant chapters. The reference voltage out of the Glassman HVDC supply was monitored by the LabVIEW program which identifies breakdown which then reduces the voltage to 0.

Continuous development of the experimental system improved upon the original system in Figure 3.2. When measuring the breakdown voltage of the point-plane topology, the DAQ interface between the computer with LabVIEW program and HVDC was changed because the National Instruments signal conditioning box SCB-68 stopped working due to electromagnetic interference issues. To overcome this problem, a new National Instruments digital acquisition card, DAQ (USB6008), was used with an amplifier circuit to increase

output from max 5V to 15V, Figure 3.5. Additional steps to mitigate EMC interference included the use of ferrite chokes to reduce transient signals.



(a) Closed box



(b) Open box

Figure 3.5 DAQ and amplifier box for communication with HVDC power supply. (a) closed box, (b) open box with DAQ, batteries, amplifier and inductive loops for EMI mitigation.

Further development of the self-breakdown measurement test system included adding probes capable of measuring higher voltages and improvement on the LabVIEW system. Breakdown voltage was measured using a Northstar PVM-5 high voltage probe (1000:1 division ratio, 80 MHz bandwidth, <0.1% DC accuracy) and a 2024 Tektronix digitising oscilloscope (200 MHz, 2 GS/s). The LabVIEW program was stopped using a signal from the oscilloscope when the voltage dropped below the trigger level which was checked every 150 ms and the voltage supply was reduced to zero. The experimental schematic of the finalised DC self-breakdown voltage tests is given in Figure 3.6.

The oscilloscope was set up with a short time scale and small voltage scale to have high resolution at breakdown. After the oscilloscope triggered on the collapse of voltage, the digital cursor was used to measure the highest voltage before breakdown.

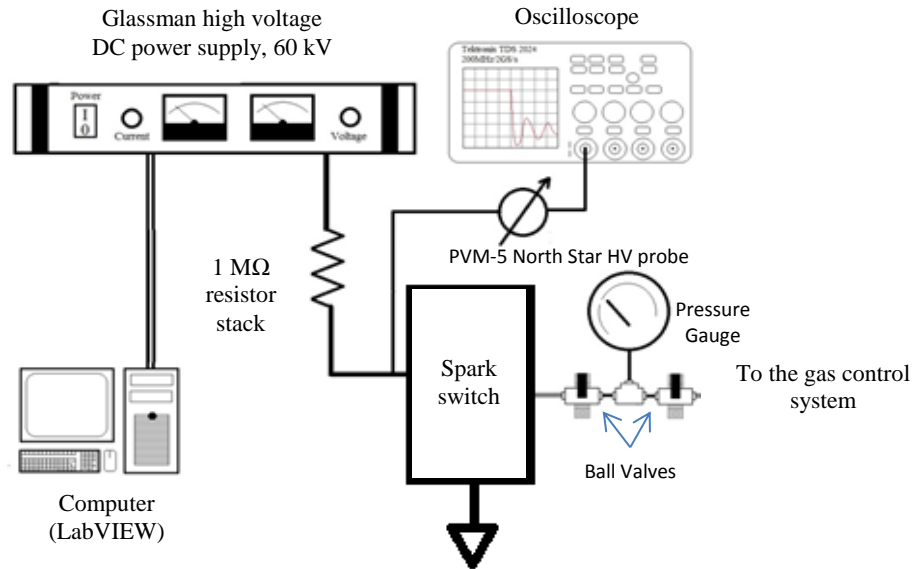


Figure 3.6 Self-breakdown voltage measurement final experimental design.

This voltage was recorded as the breakdown voltage. There were no transients on the voltage signal at the moment of breakdown. The full listing of the LabVIEW code used for this experiment is provided in Appendix 2. The experimental test system in Figure 3.6 was used for measurement of breakdown voltage. In Chapter 5 and Chapter 8, a stepwise increase of voltage was amplified to a rate of 340 V/150 ms.

The next section, Section 3.3, explains the test system developed to observe the pre-breakdown corona discharge activity.

3.3 METHODOLOGY OF OBSERVATION OF PRE-BREAKDOWN CORONA DISCHARGE

To measure corona discharge currents and $V-I$ curves, a designated experimental test bed was developed, Figure 3.7. A 100 kΩ shunt resistor was introduced between the switch and ground of the experimental test system discussed in Figure 3.6. The voltage, $V(t)$, across the shunt resistor was measured using the HV probe Tektronix P6015A (1:1000 division ratio, 75 MHz), then the corona current, $I(t)$ was calculated using the Ohm's law, $V(t) = I(t)R$.

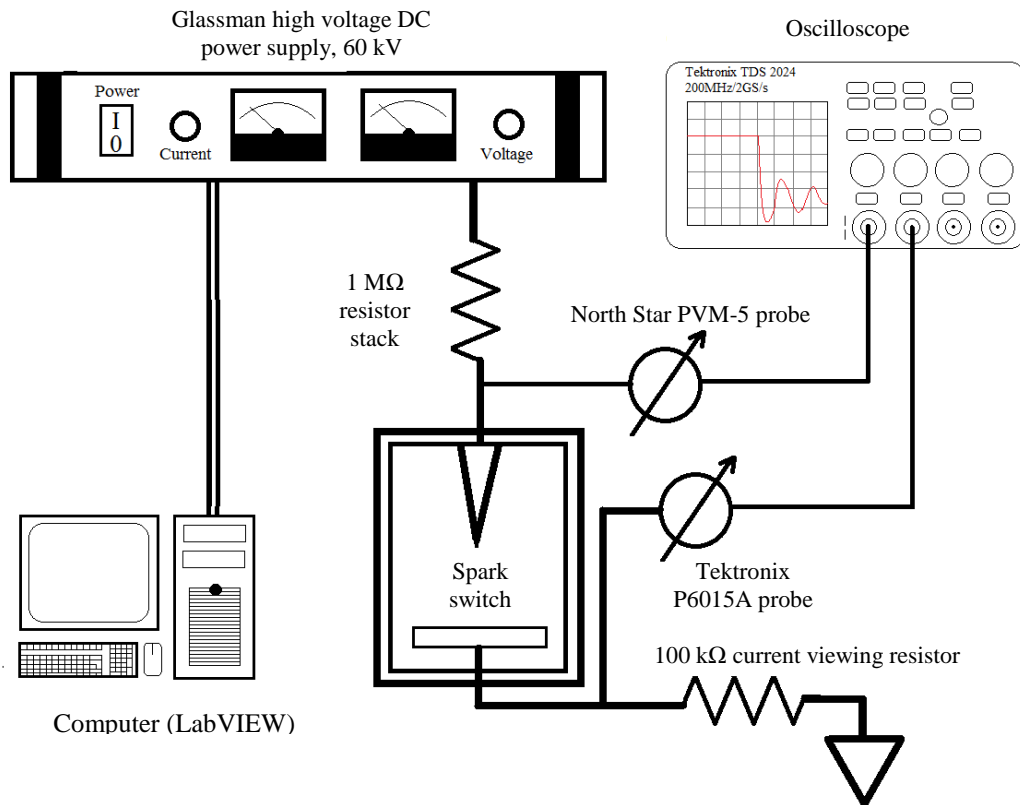


Figure 3.7 Corona discharge current viewing experimental design.

The corona discharge measurement system was used in Chapters 5, Chapter 6 and Chapter 8 to identify corona inception voltage and measure $V-I$ curves.

3.4 NOVEL APPROACH TO PLASMA TRIGGERING: SUPERIMPOSED TRIGGER

In this present research project, a superimposed triggering of plasma switches is proposed and investigated. A triggering impulse superimposed on a DC stress forces a 2 electrode switch to break. In order to investigate the operational parameters of switches triggered using this superimposed approach, a special test bed was developed. In this test bed, fast rise times of sub-50 ns triggering impulses were generated using the Blumlein pulsed power system, these impulses were superimposed on DC stress applied to the switch, the magnitude of the HV impulses was up to 95% self-breakdown voltage in a sphere-sphere switch in pressurised air (0.1-0.4 MPa). Figure 3.8 provide the schematic diagram of the superimposed triggering test bed.

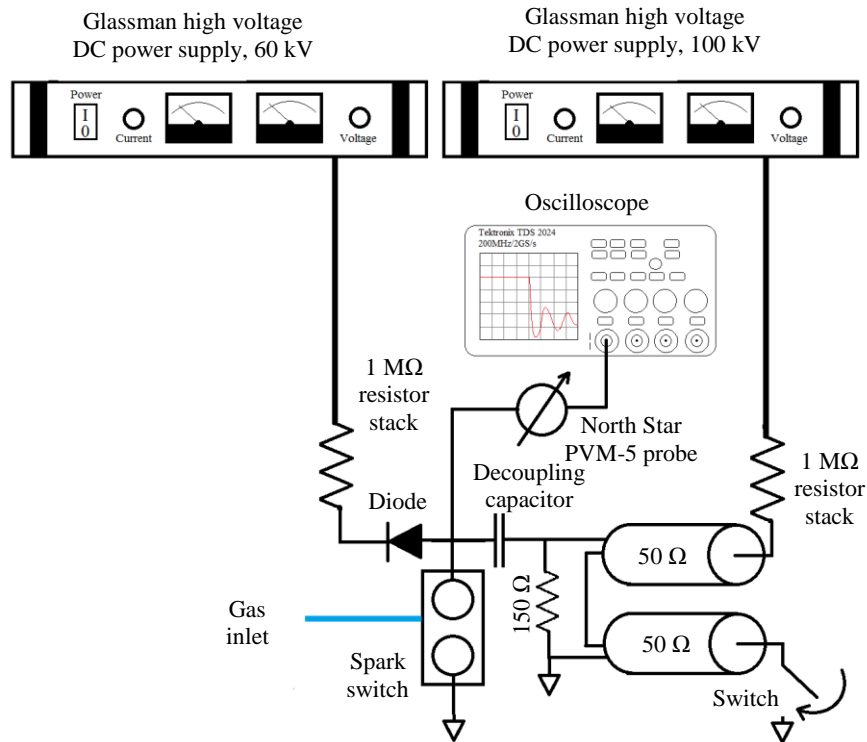


Figure 3.8 Experimental set up for triggering a 2 electrode switch, using a trigger impulse superimposed on a pre-energisation with DC voltage.

The Blumlein was charged to 35 kV to achieve a high output voltage without risking damage to the Blumlein cables. The Blumlein generator outputted approximately a 50 kV voltage pulse rising at about 1 kV/ns to the switch. The Blumlein full pulse waveform (duration 284 ns) oscillates as shown in Figure 3.9 due to the impedance mismatch in the test system. A Glassman HVDC power supply (0-60 kV) pre-energises the switch via a 1 MΩ charging resistor. A decoupling capacitor (2.2 pF) prevents DC pre-energisation impacting on the Blumlein generator and a HV diode protects the DC supply from high voltage impulses from the Blumlein generator. The voltage across the switch was measured using a Northstar PVM-5 high voltage probe (1000:1) and a 3054B Tektronix oscilloscope (500 MHz, 5 GS/s).

A clear acrylic cylinder switch housing a sphere-sphere topology, 19 mm internal in diameter with a 2 mm gap was pressurised to 0.1-0.4 MPa with bottled air (12.5% rh) using a precision Alicat PCD digital pressure regulator. Soft-tone gramophone needles (with a radius of 0.036 mm were used) as pre-breakdown ionisation electrodes at HV potential and were positioned 7.5 mm from the centre and 1 mm back from the tip of the high-voltage sphere electrode. No breakdowns occurred from the gramophone needles.

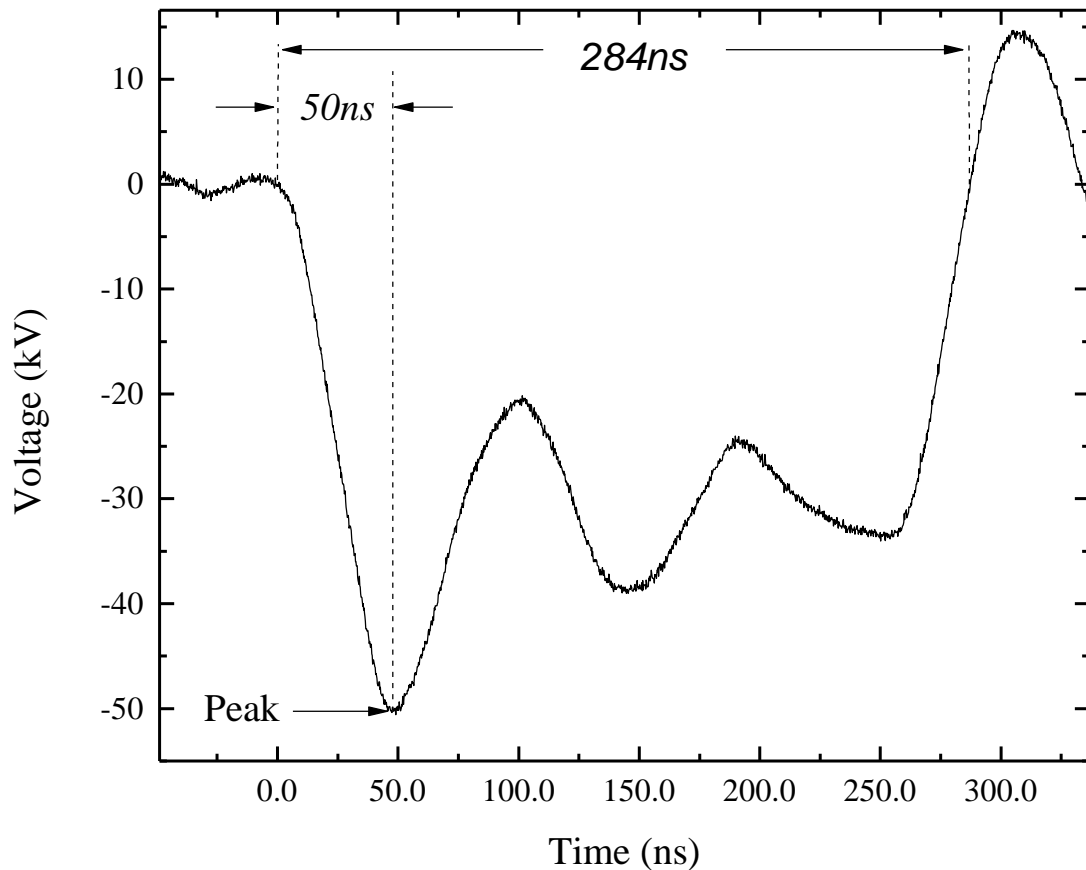


Figure 3.9 Trigger pulse output of the Blumlein generator.

DC pre-energisation of 0 kV to self-breakdown voltage was increased in 2 kV increments. 30 triggered breakdowns were observed, measuring the time delay to breakdown from the start of the impulse until the collapse of voltage.

3.5 METHODOLOGY OF TRIGGERING OF MULTI-SPARK SWITCH

Within the framework of this project, multi-stage switches were designed and their operational characteristics were investigated. Initially, for the self-breakdown and corona discharge current in the multi-stage switches studied, the experimental systems in Sections 3.1 and 3.2 were used. For triggered operation of these switches, it was required that a triggering impulse be applied to one of the electrodes of the switch. Therefore, a new experimental test bed was designed that would pre-energise the multi-stage switches with

DC voltage and could supply a consistent triggering impulse on demand. The schematic diagram of this test bed used in multi-stage switch experiments is shown in Figure 3.10.

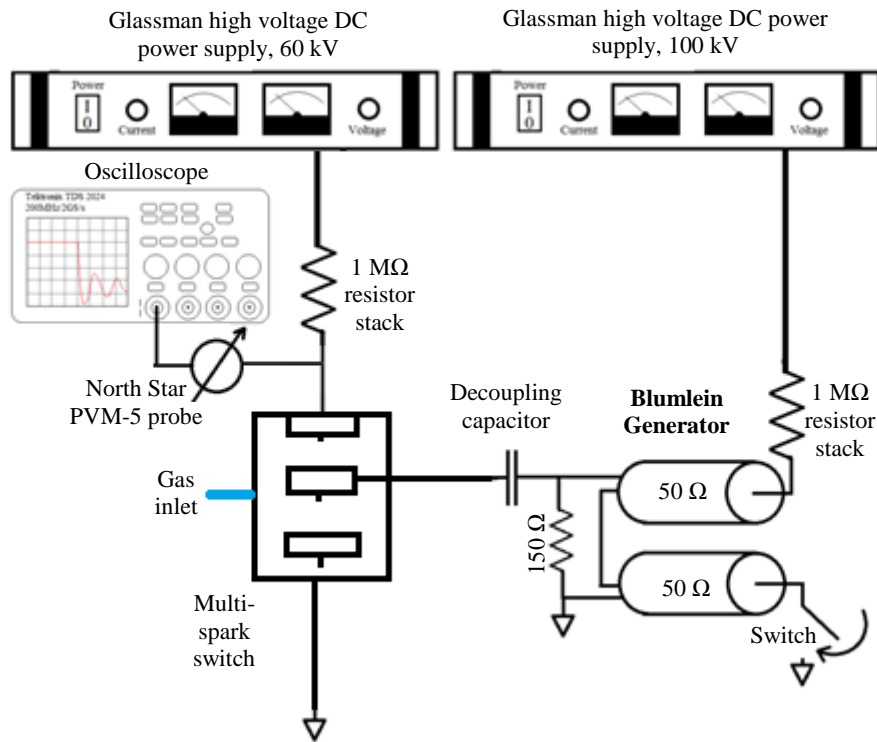


Figure 3.10 Triggered multi-gap switch experimental design.

The Blumlein generator, the same as used in Section 3.3, outputs a 50 kV voltage pulse rising at 1 kV/ns to one of the electrodes on the multi-gap switch over voltaging the top stage of the switch. The trigger pulse waveform is the same as shown in Figure 3.9. The HV impulse has a duration of 284 ns which oscillates as shown in Figure 3.9 due to the mismatch in impedances in the test circuit. A Glassman HVDC power supply (0-60 kV) pre-energises the switch via a 1 MΩ charging resistor. A decoupling capacitor (2.2 pF) prevents DC pre-energisation impacting on the Blumlein.

The voltage across the switch was monitored using a Northstar PVM-5 high-voltage probe (1000:1) and a Tektronix TDS 3000 series oscilloscope (500 MHz, 5 GS/s). Breakdown was identified as the moment at which the DC energisation level reduced to 0 V. A Pearson current monitor (model 6585, 250 MHz) was also used to measure the current on the ground connection as a further indication of a breakdown event.

This section has discussed the different experimental test bed topologies used for investigation of operational characteristics of plasma closing switches such as self-breakdown voltage, corona initiation voltage, voltage-current relationship and time delay to

breakdown. The following chapters present the results of these comprehensive studies, starting with an investigation into the electrode geometry of the DC self-breakdown spark switches (Chapter 4).

4. SELF-BREAKDOWN CHARACTERISTICS OF RAMPED VOLTAGE STRESSED SWITCHES FILLED WITH AIR, NITROGEN AND AIR/NITROGEN MIXTURE

The ability of spark switches to withhold high voltages and be operated with accuracy and consistency means they are used in a range of practical applications from over-voltage protection to pulse power generators. This chapter investigates the breakdown voltage and its standard deviation of spark switches with varying topologies including topologies with corona ionisation electrodes. The switches are filled with gas in the pressure range 0.1-0.35 MPa. The role of corona discharge in triggered spark switches is to improve the performance of spark switches. In the present work, for the first time, an in depth investigation comparing breakdown voltage and its stability with and without corona discharge electrodes using topologies with a significant range of electric field enhancements has been conducted in air, nitrogen and a nitrogen/oxygen mixture. In this chapter, the effect of pre-breakdown corona discharge is investigated to observe its effect on the breakdown voltage and its standard deviation in commonly used spark switch topologies filled with environmentally friendly gases. Previously, corona discharge has been used to improve the performance of spark switch such as reducing the pre-fire in repetitive spark switches allowing for higher frequencies to be reliably achieved [Beveridge 2008]. This chapter investigates the corona discharge effects on the ramped breakdown voltage and its standard deviation.

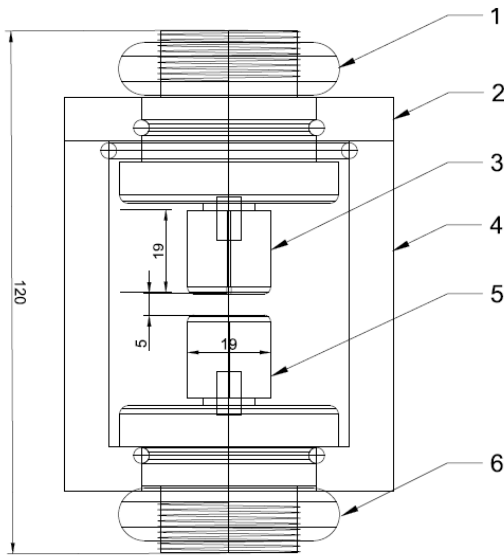
Corona discharge and coronating electrodes are known to improve the operation of repetitive breakdown and multi-stage switches [Beveridge 2008]. However, little work has been published on the effect of corona discharge on the ramped breakdown voltage and its

standard deviation in spark switches. This chapter investigates the breakdown characteristics of three main switch topologies: sphere-sphere, plane-plane, and cone-plane with and without coronating electrodes placed in the vicinity of the main electrodes. Results from this investigation were presented and published in the proceedings of the XIX International Conference on Gas Discharges and Their Applications in 2012 [Hogg 2012c].

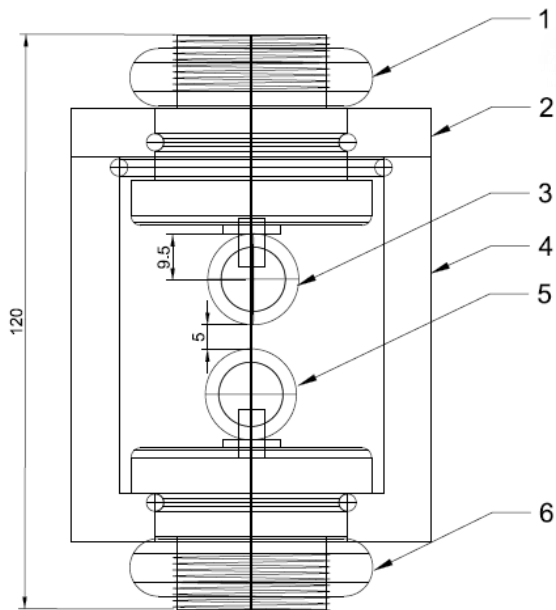
4.1 DEVELOPMENT OF SPARK SWITCH TOPOLOGIES

Initially, three electrode topologies, varying from uniform to highly non-uniform electric fields, were selected for investigation of the DC self-breakdown voltages. Plasma closing switches with plane-plane, sphere-sphere, and cone-plane electrode topologies were designed and developed; these electrode configurations provided varying levels of electric field enhancement. The aim of this investigation was to establish which electrode topology provides the most stable operation characteristics (minimum spread in the self-breakdown voltages) and the highest breakdown voltage when stressed with positive and negative ramped voltage. This investigation required a switch that can take inter-changeable brass electrodes and can be pressurised up to 0.4 MPa.

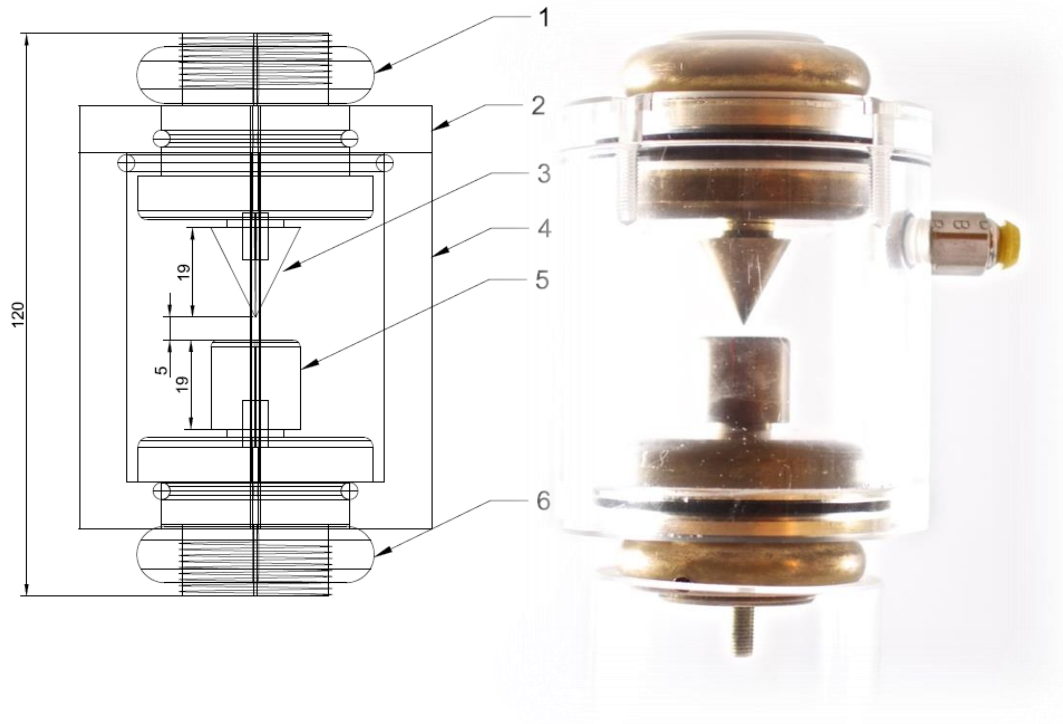
Figure 4.1 shows the switch body designed to house inter-changeable electrodes set with a 5 mm inter-electrode gap. 3 brass electrode topologies were selected for this investigation (plane-plane, sphere-sphere, cone-plane), each of the topologies were created with equal lengths and widths such that when fitted in the switch, the inter-electrode gap is the same (5 mm), Figure 4.1. Brass electrodes were used because brass has a high resistance to erosion and it can be easily machined.



(a) Plane-plane



(b) Sphere-sphere



(c) Cone-plane

Figure 4.1 Inter-changeable brass electrode switch (a) plane-plane, (b) sphere-sphere, and (c) cone-plane. 1 - HV connection, 2 - Clear acrylic top, 3 - HV electrode, 4 - Clear acrylic switch body, 5 - Ground electrode, 6 - ground connection. Dimensions in mm.

Figure 4.1 shows the plane-plane, sphere-sphere, and cone-plane topology designs with key dimensions highlighted and a photograph of the actual topology in the switch. Figure 4.2 shows the tip of cone electrode photographed under a microscope along with a 1000th of an inch spacer.

The machining technique used to make the cone electrode resulted in a tip with a flat top and small imperfection. The cone has a larger radius of 0.28 mm and the smaller bump has a radius of 0.1 mm. Each of the topologies in Figure 4.1 were also tested with coronating electrodes, Figure 4.3.

Figure 4.3 shows the topologies: plane-plane, sphere-sphere, and cone-plane with coronating electrodes, highlighting the important dimensions. The coronating electrodes are used to generate corona discharge prior to breakdown without causing breakdown from the sharp points. The points of the coronating electrodes were photographed under a microscope along with a 1000th of an inch spacer so that the tip radius could be measured.

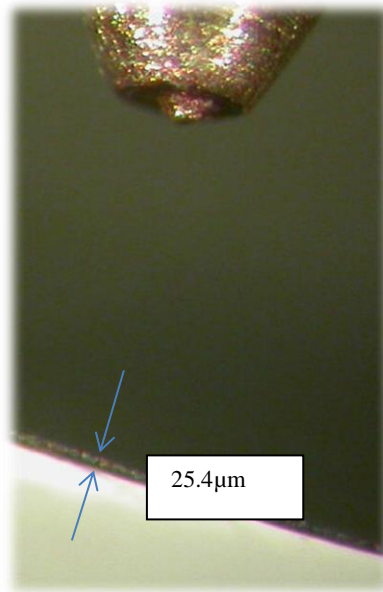
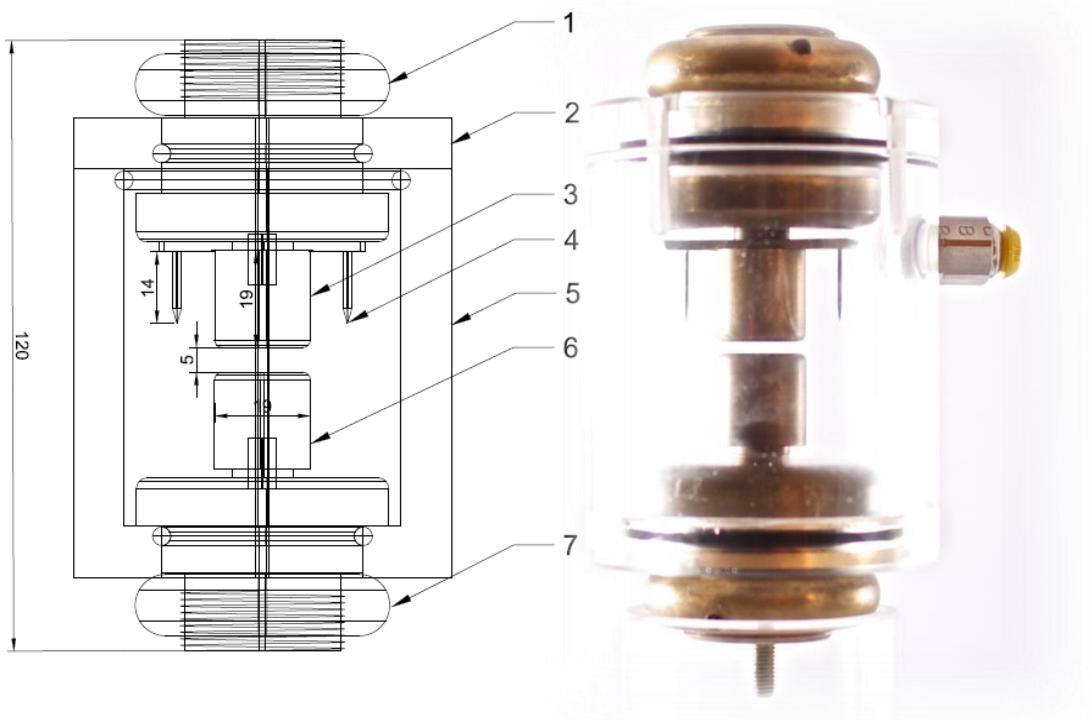
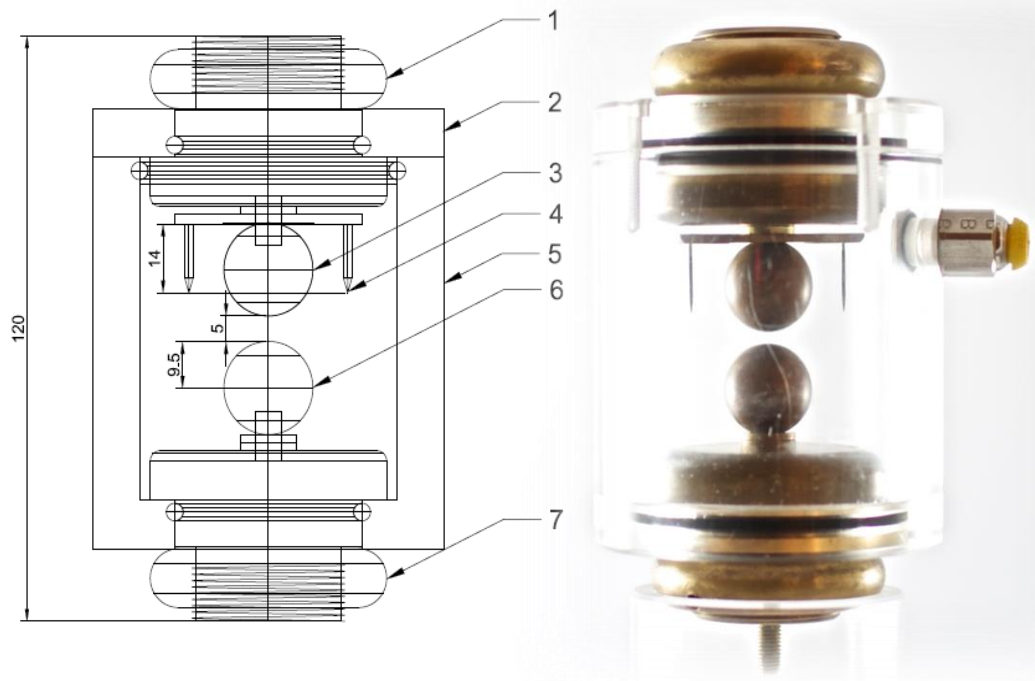


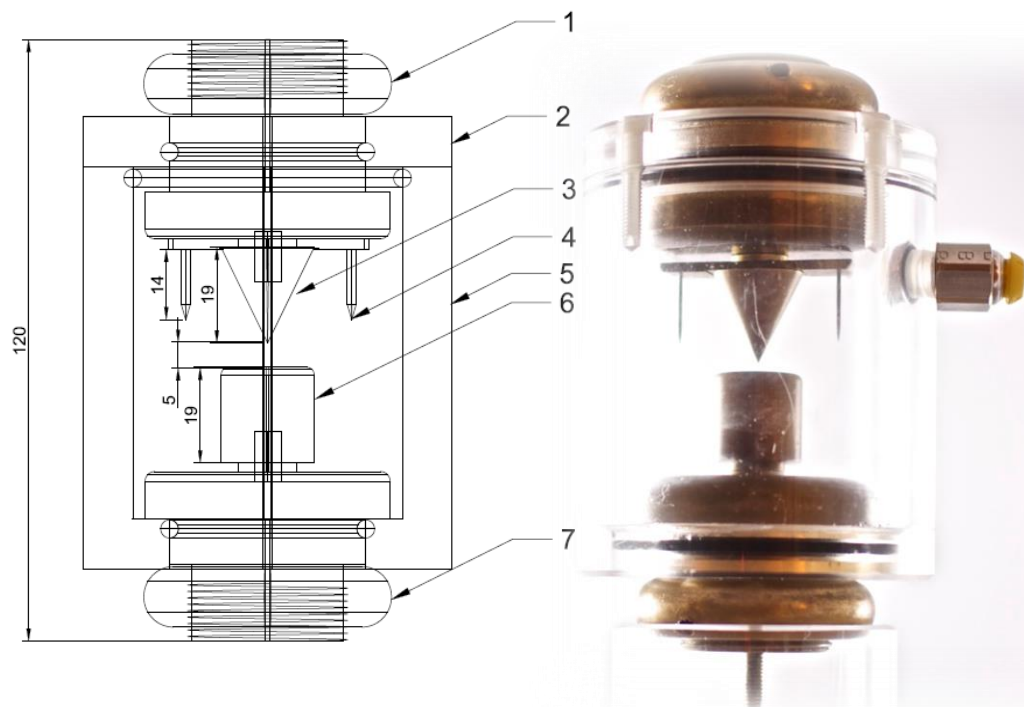
Figure 4.2 Tip of cone electrode photographed under microscope. Tip = 0.275 mm. Protrusion = 0.1 mm.



(a) Plane-plane with coronating electrodes



(b) Sphere-sphere with coronating electrodes



(c) Cone-plane with coronating electrodes

Figure 4.3 Inter-changeable electrode switch with coronating electrodes. 1 – HV connection, 2 – Clear acrylic switch top, 3 – HV electrode, 4 – coronating electrodes, 5 – Clear acrylic switch body, 6 – Ground electrode, 7 – Ground connection. Dimensions in mm.

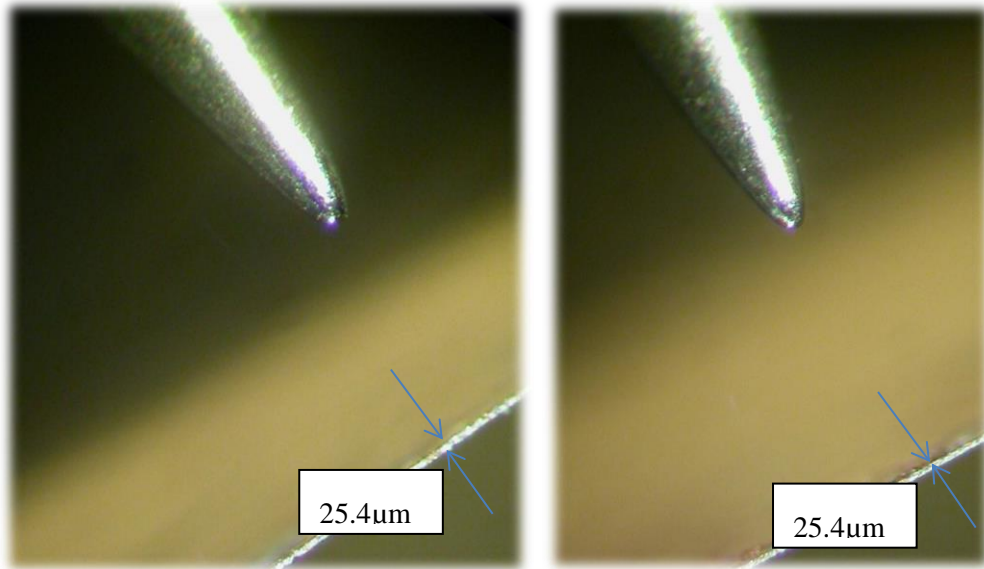


Figure 4.4 Coronating electrodes – Soft-tone gramophone needles photographed under microscope.

The coronating electrodes are soft-tone gramophone needles which provided sharp, consistent and smoothly rounded tips, Figure 4.4. The two gramophone needles were positioned on either side of the high voltage main electrode. Electrostatic field in each of the topologies was modelled using Comsol Multiphysics software package, the results of this modelling are presented in Section 4.2.

4.2 ELECTROSTATIC ANALYSIS OF ELECTRIC FIELD IN SPARK SWITCH TOPOLOGIES

Electrostatic simulation was used to model the switch topologies used in the present research project: plane-plane, sphere-sphere and cone-plane with and without the coronating electrodes. This electrostatic field modelling is required for determining if there were significant fringing effects on the plane electrodes and for determination of the electric field enhancement with the sphere-sphere and cone-plane electrodes, Figure 4.5, Figure 4.6, and Figure 4.7. Based on the result of the electrostatic modelling, the switch topologies were designed in such way as to avoid unwanted spark discharges from the sharper electrodes. Such unwanted spark discharges potentially can be generated from the sharp coronating electrodes which are at the same potential as the main electrode.

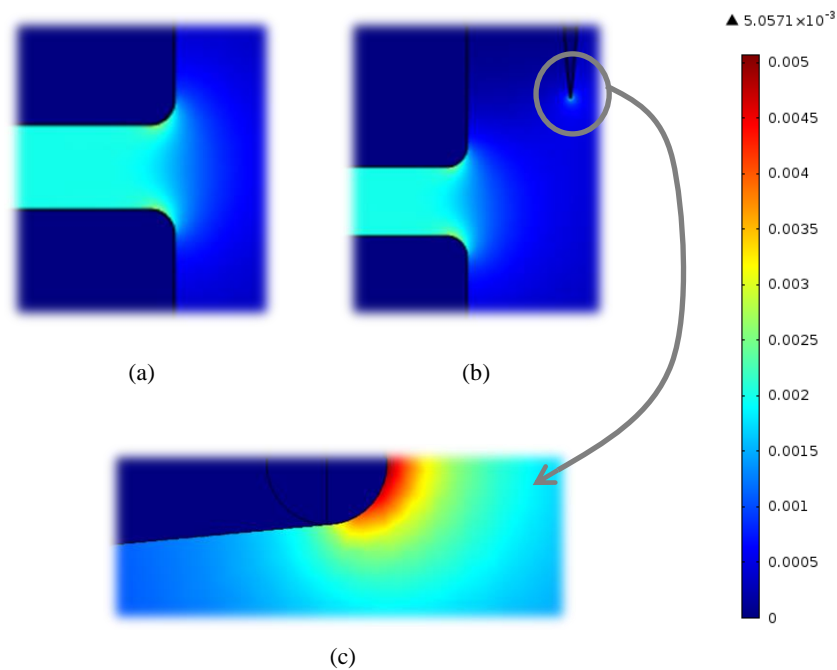


Figure 4.5 Electrostatic simulation: (a) plane-plane, (b) plane-plane with coronating electrodes, and (c) zoomed on point of coronating electrode. 1 V energisation. Electric field is given in kV/cm.

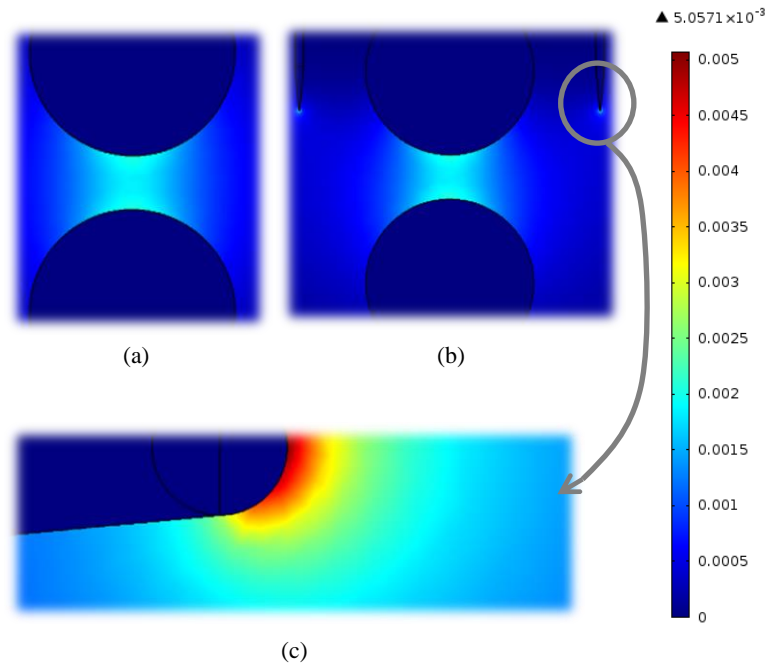


Figure 4.6 Electrostatic simulation: (a) sphere-sphere, (b) sphere-sphere with coronating electrodes, and (c) zoomed on point of coronating electrode. 1 V energisation. Electric field is given in kV/cm.

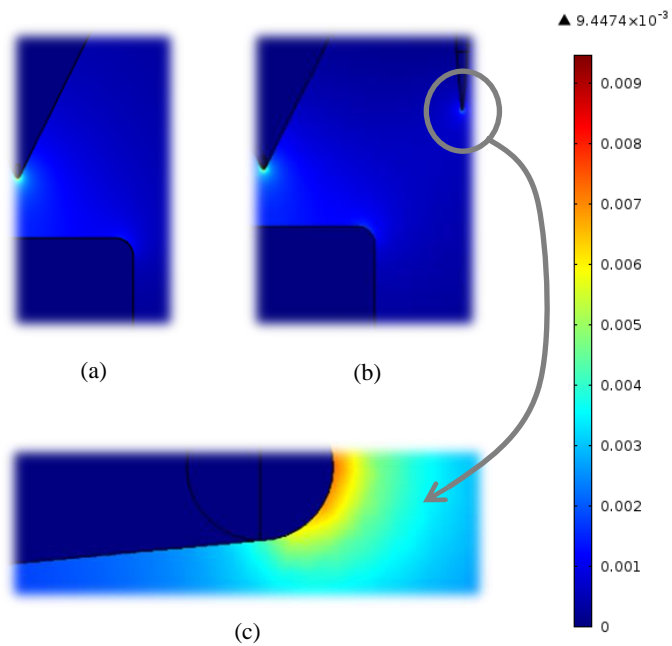


Figure 4.7 Electrostatic simulation: (a) cone-plane, (b) cone-plane with coronating electrodes, and (c) zoomed on point of coronating electrode. 1 V energisation. Electric field is given in kV/cm.

By re-modelling the topologies with the inclusion of the coronating electrodes, it was confirmed that the presence of the sharp electrodes at their location, 17 mm from the central

line, did not have significant impact on the electric field distribution between the primary electrodes. The electrostatic simulations alone are unable to confirm if a spark breakdown would occur between the main electrodes or between the coronating electrodes. However, any conclusions drawn from this investigation could be confirmed to be as a result of space charge effects and not due to Laplacian electric field changes between the primary electrodes.

With non-uniform fields, there is no accurate method of predicting breakdown voltage using electrostatic analysis yet. Therefore, to ensure that spark breakdown occurred between the main electrodes and not originating from the coronating electrodes, open shutter photography was used. The next section discusses the use of open shutter photography for confirmation of spark location.

4.3 OPEN SHUTTER IMAGES OF SPARK DISCHARGES

Adding sharp coronating electrodes (gramophone needles) to the switch topology, energised at the same polarity as a main HV energised electrode could cause unwanted breakdown between the pins and the ground electrode. Therefore, in order to select desirable location of needle electrodes, it was necessary to take photographs of the discharges to confirm the breakdown occurs only between the main electrodes of the switch. In the initial design stage, coronating electrodes were tried at different locations and spark breakdown was identified as originating from the sharp corona electrodes, Figure 4.8.

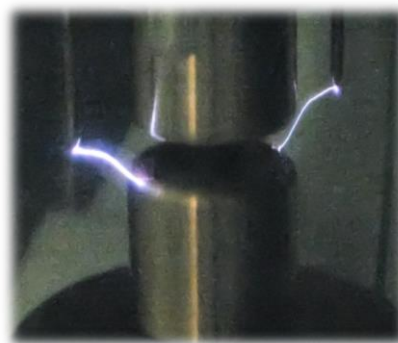


Figure 4.8 Unwanted spark breakdown form coronating electrodes in early prototype switch. Positive energisation, 0.1 MPa.

Through an iterative approach, the location of the coronating electrodes was found whereby corona discharge activity could be initiated and spark breakdowns did not originate from these corona electrodes. Figure 4.9 shows 30 second exposure open shutter photographs of sphere-sphere and plane-plane topologies during breakdown. The switch body was filled with air at atmospheric pressure, room temperature and humidity.

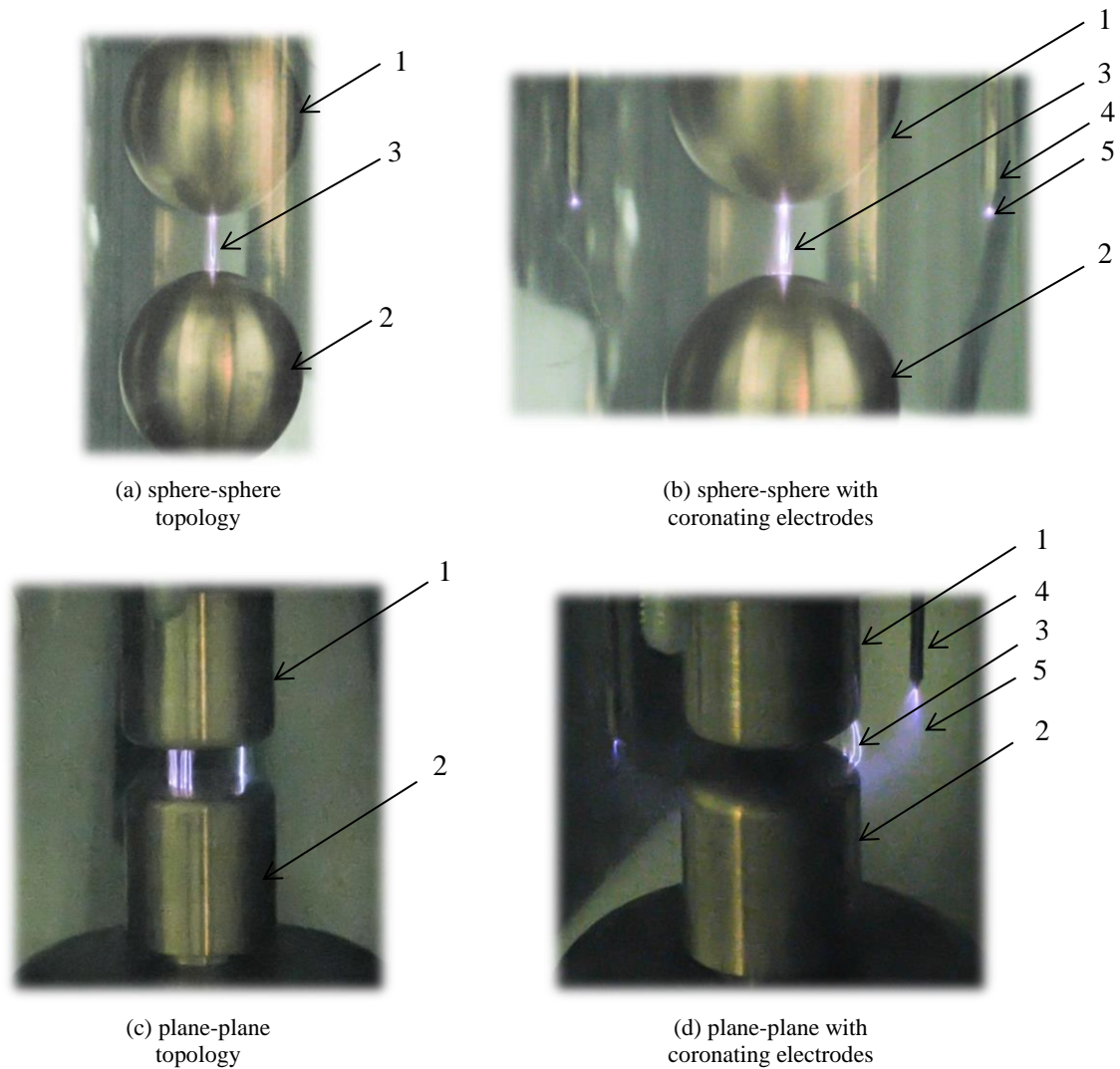


Figure 4.9 Open shutter photographs of spark discharge. Negative energisation in 0.1 MPa bottled air and main electrode gap of 5 mm. 1 – HV electrode, 2 – Ground electrode, 3 – Spark discharge, 4 – Coronating electrode, 5 – Corona discharge.

Open shutter photographs shown in Figure 4.9 confirm that there are not spark breakdowns between the corona electrodes and the opposite ground electrode.

Final dimensions are as shown in Section 4.1. Once the topologies were finalised, the investigation into the breakdown performance of selected switch design was conducted. The

next section discusses the results of an investigation into breakdown voltage with each of the topologies described: plane-plane, sphere-sphere, and cone-plane with and without the coronating electrodes.

4.4 SELF-BREAKDOWN VOLTAGES OF ENVIRONMENTALLY FRIENDLY GASES IN DIFFERENT TOPOLOGIES

This section aims to investigate the breakdown voltage of different electrode topologies in environmentally friendly gases. Spark switches are used in a range of applications from pulsed power generators to over voltage protection where it is vital to reliably know the breakdown voltage of the switches. If breakdown voltage is not known and reliably consistent, unwanted firing of high voltage pulse generators could occur or sensitive equipment may not be protected by overvoltage protection. Breakdown voltage is arguably the most important factor which characterises operational performance of spark switches. In the first instance, the switches were filled with atmospheric bottled air (12% relative humidity); breakdown tests were conducted at room temperature. Then, pure nitrogen (99.9% N₂, BOC Ltd) and a 60%/40% nitrogen/oxygen mixture (mixed by BOC Ltd) were used as gases for filling plasma closing switches and their breakdown performance is also discussed in the present chapter. In the following sections, the results are fitted with empirical fittings for easy comparison. These fittings are only valid for the experimental conditions used in this research.

4.4.1 Self-Breakdown Voltages of Atmospheric Air

The aim of this section is to compare breakdown performance of three of the common topologies that are used in the power and pulsed power industry in order to identify which topology provides the best results for high performance switches. Breakdown voltages in each of the topologies were considered separately at first and then compared against each other. DC breakdown voltage was measured using the procedure and experimental test bed discussed in Section 3.2. The switch was filled with a fresh portion of gas and 30 breakdowns events were observed after which the gas in the switch was changed, the average breakdown voltage and standard deviation were calculated to ensure accurate results. Each

point in Figure 4.10 shows the average breakdown voltage, error bars show standard deviation, the breakdown tests were conducted in the plane-plane topology. Also, an empirical fitting procedure was used to fit the experimental points with linear functions using OriginPro 9.0 software package. The empirical equations, with corresponding coefficients, describe these linear fit lines with breakdown voltage, V_{br} , (kV) as a function of pressure, p (MPa):

$$V_{br} = Ap + B \quad (4.1)$$

where A (kV/MPa) and B (kV) are fitting coefficients and are given in these figures for each combination of polarity of the applied voltage and the presence and absence of the corona electrodes. Figure 4.10 presents the breakdown voltage data for the plane-plane electrode topology.

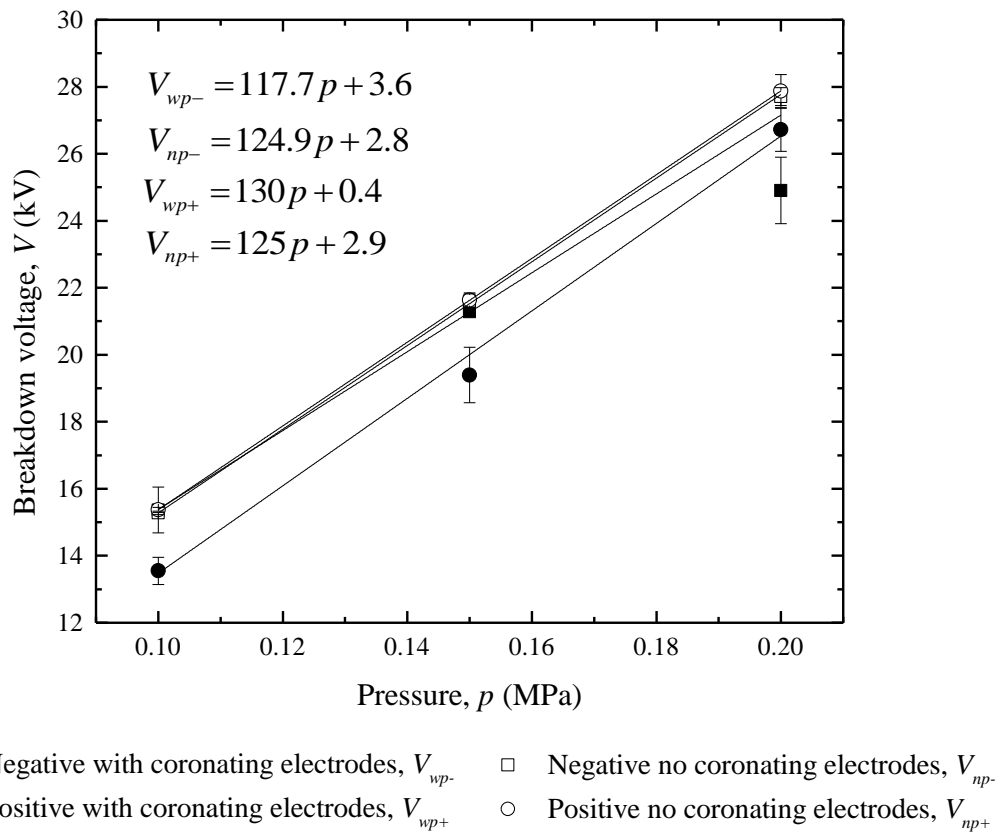


Figure 4.10 Breakdown voltage of plane-plane topology in compressed bottled air. A 5 mm gap was used.

The **plane-plane** topology without corona electrodes is symmetrical in terms of electrostatic field distribution. So when the polarity of HV stress is changed, it is expected that the results will be similar for positive and negative energisation. Figure 4.10 shows the breakdown voltage of the plane-plane topology in compressed air as a function of applied pressure. The

breakdown voltage increases linearly with pressure, and the lines of best fit show the empirical fit lines to be similar with both polarities having a gradient of ~ 125 kV/MPa and extrapolated intersection points at ~ 3.6 kV and ~ 2.8 kV. The negative breakdown voltage with coronating electrodes in 0.2 MPa pressure appeared lower than the trend line from lower pressures. This is likely due to the stochastic nature of gas discharge breakdowns.

Much work has been conducted on plane-plane topologies and published as Paschen curves and a well-established relationship is known for air [Meek 1953]. With a 5 mm gap and pressure of 0.1 - 0.2 MPa, the data collected in this section sits on the right hand side of the Paschen curve where the breakdown voltage is ~ 300 kV/cm/MPa. The slight difference in breakdown voltage between Figure 4.10 and Paschen's curve results reported by Meek 1953 is likely due to fringing effects where localised electric field is increased around the edges of the planes, as discussed in Section 4.2. The standard deviation of breakdown voltage for all pressures and voltage polarities is below 0.7 kV and the best value of the standard deviation occurred with negative energisation at 0.05 kV at 0.1 MPa, though there is no trend to reduce given increase or decrease in pressure.

With the addition of coronating sharp electrodes, there is a reduction in the breakdown voltage. In the case of negative energisation, the breakdown voltage reduces more as pressure is increased and is only significant at 0.2 MPa where the voltage has dropped by ~ 3 kV. Positive energisation produced a more significant drop in the breakdown voltage at lower pressures of 1 - 2 kV but does not reduce this voltage further as the pressure is increased. The breakdown voltage standard deviation was slightly increased with the inclusion of coronating electrodes from 0.7 kV to 1 kV.

Breakdown voltage in the **sphere-sphere** topology is also similar for both positive and negative energisation which is expected because this topology is symmetrical. The localised regions of increased electric field mean sphere-sphere breakdown voltage are not technically suited to the Paschen curve; however, the breakdown voltage is often compared on a Paschen curve. Figure 4.11 shows the breakdown voltage for the sphere-sphere topology, and it can be seen that the breakdown voltage are similar to Figure 4.10.

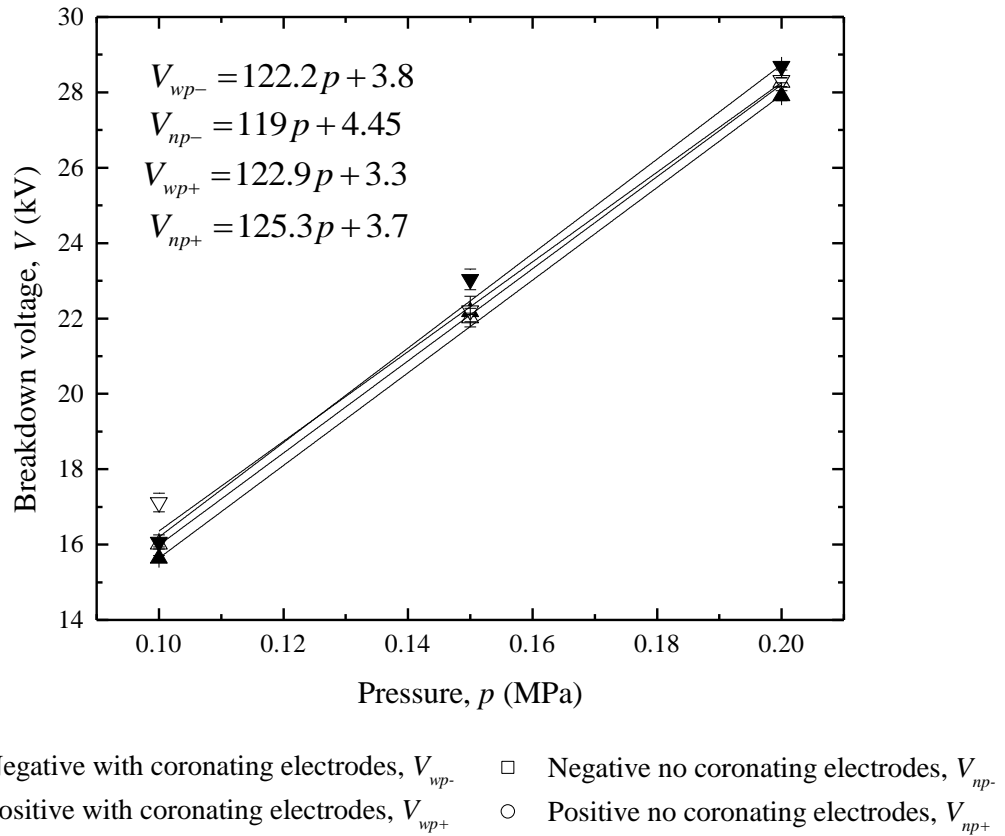
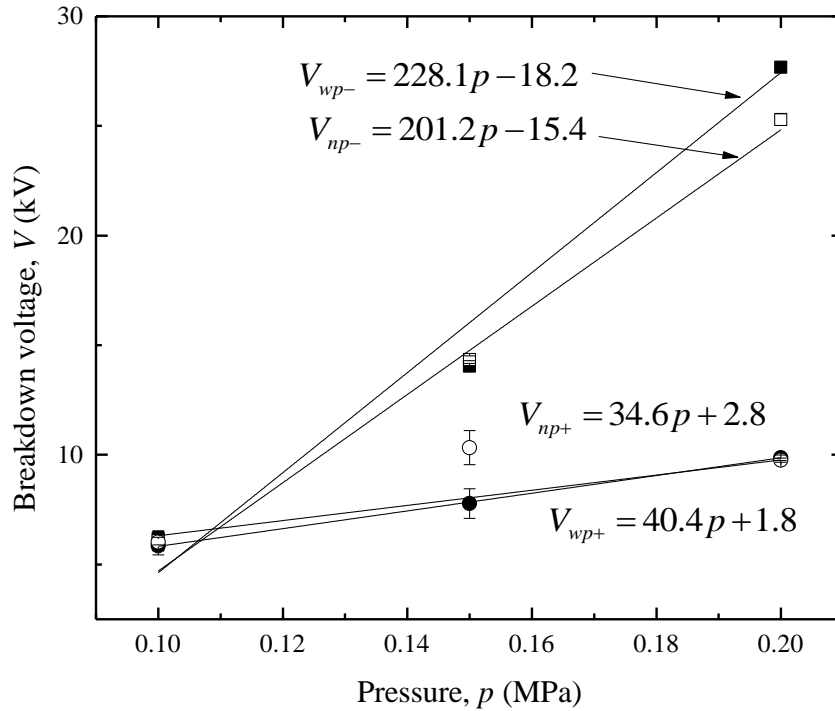


Figure 4.11 Breakdown voltage of sphere-sphere topology in compressed bottled air. A 5 mm gap was used.

The breakdown voltage increases linearly with pressure at a similar rate to the plane-plane topology, $\sim(119-125)$ kV/MPa compared to ~ 125 kV/MPa for plane-plane. Coronating electrodes, the breakdown voltage did not significantly reduce as in the case of plane-plane topology. The standard deviation of breakdown voltage was not reduced except at 0.1 MPa where the standard deviation went from 0.25 kV to 0.08 kV.

The functional behaviour of the breakdown voltage in the **cone-plane** topology is significantly different from the plane-plane and sphere-sphere topologies because there is a significant localised field enhancement ($\eta = 15.7$ using Equation (2.4)) at the tip of the cone and it is not symmetrical. The breakdown voltage for positive and negative energisation are not the same which is due to differing mechanism and space charge effects discussed in Section 2.2.3. Volumetric negative space charge created in front of the cone tip screens the electric field resulting in higher breakdown voltages. This effect is more prominent in the case of negative energisation for electronegative gases, and it can be seen in Figure 4.12 where negative breakdown voltage is ~ 15 kV higher than positive breakdown voltage at 0.2 MPa.



- Negative with coronating electrodes, V_{wp-}
- Negative no coronating electrodes, V_{np-}
- Positive with coronating electrodes, V_{wp+}
- Positive no coronating electrodes, V_{np+}

Figure 4.12 Breakdown voltage of cone-plane topology in compressed bottled air. A 5 mm gap was used.

The breakdown voltage for both positive and negative energisation increase linearly as pressure is increased and they both breakdown at ~6 kV at 0.1 MPa. However, the rate at which they increase is different. Breakdown voltage for negative energisation increases quickly with pressure with a rate of ~201 kV/MPa, where positive energisation only increases with a rate of ~35 kV/MPa. The significant difference between the highly non-uniform fields in the cone-plane and uniform fields mean it is not expected that the breakdown voltage will be similar in these topologies. Although, it is established that in electronegative gas in highly non-uniform fields, negative breakdown voltages are generally higher than positive, in the present study (Figure 4.12) it was shown that there can be similar breakdown voltages in specific switch topologies. At 0.15 MPa, breakdown voltage deviations from the trend lines is due to the stochastic nature of gas discharge.

In this section, the different topologies have been considered for bottled air. The next Section 4.4.2 considers breakdown voltages in the same topologies in a 60%/40% nitrogen/oxygen mixture and in pure nitrogen.

4.4.2 Self-Breakdown Voltages of Nitrogen and 60%/40% Nitrogen/Oxygen Mixture

Breakdown events in nitrogen and a 60%/40% nitrogen/oxygen mixture were investigated using the same topologies and conditions as those in air, Section 4.4.1, Figure 4.10 to Figure 4.12. These two gases were chosen to show the importance of gas electronegativity on the breakdown voltage and its standard deviation. Nitrogen is an electropositive gas and oxygen is an electronegative gas. Therefore, comparison of the breakdown voltage behaviour in atmospheric air (~20% oxygen) and in a nitrogen/oxygen mixture with 40% oxygen helps to establish what gas would have the best breakdown performance and could be used in high performance spark switches. The breakdown voltages of each gas are compared with the breakdown voltages obtained for air. In the first case, the breakdown performance of switches with and without corona electrodes filled with the 60%/40% nitrogen/oxygen mixture was investigated and the results are presented in, Figure 4.13 and Figure 4.14.

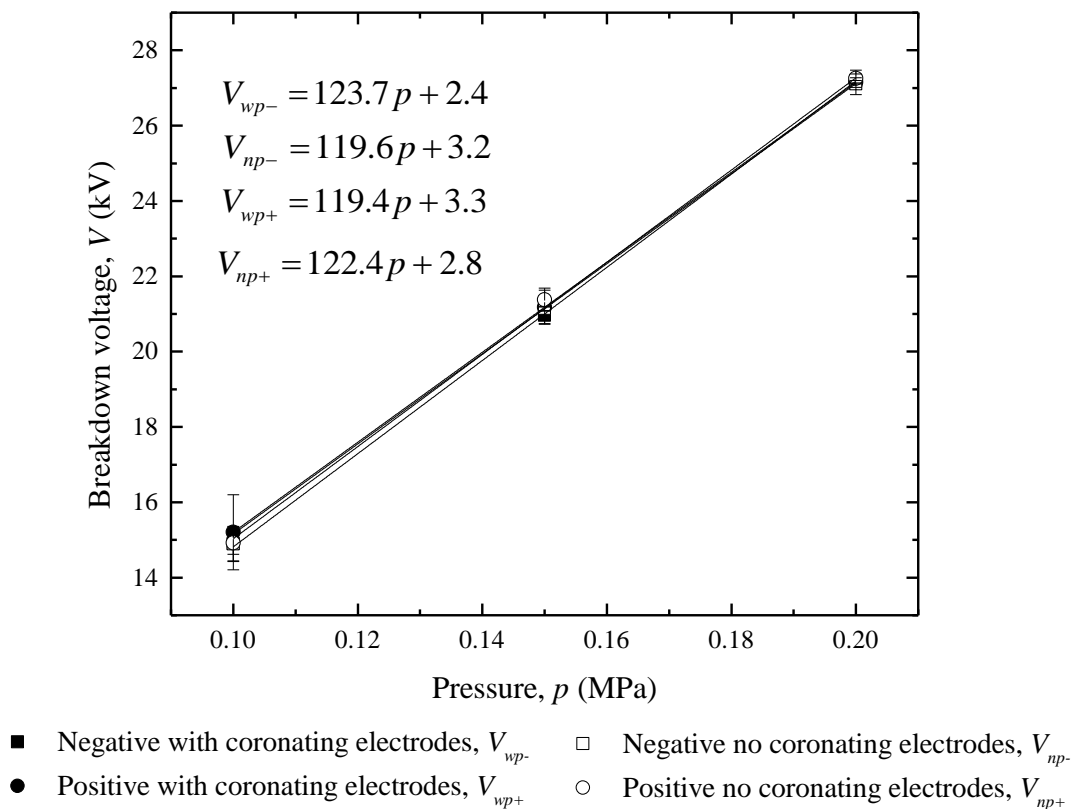


Figure 4.13 Breakdown voltage of plane-plane topology in compressed nitrogen/oxygen mixture (60%/40%). A 5 mm gap was used.

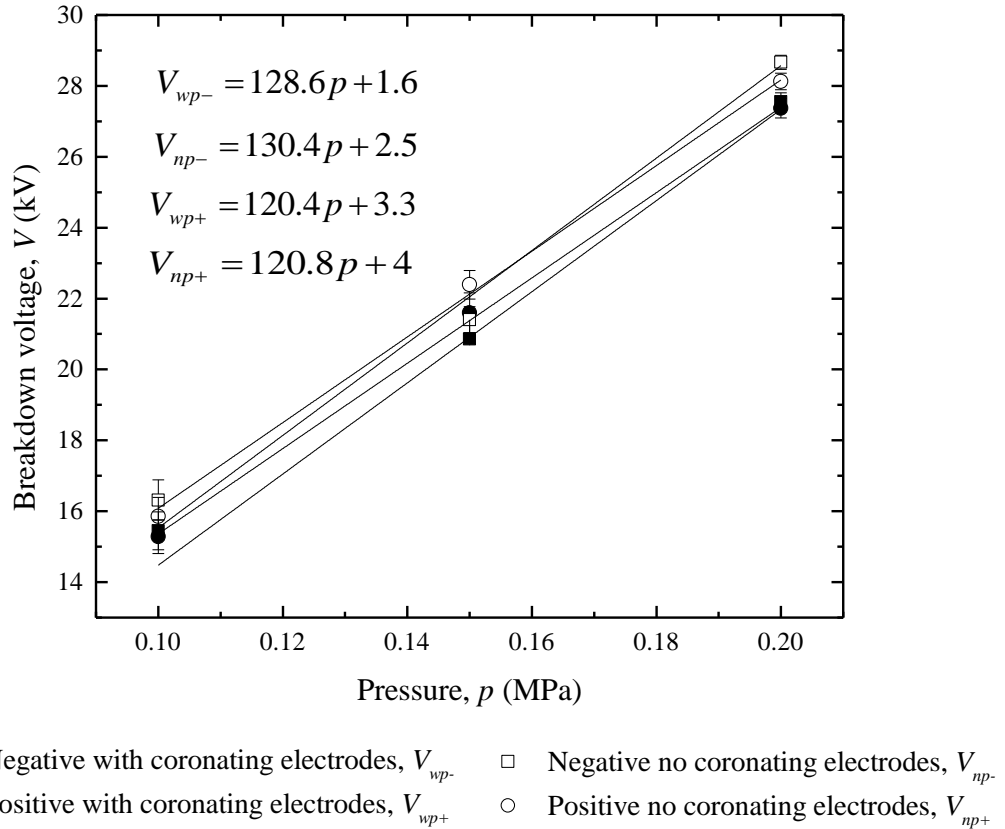


Figure 4.14 Breakdown voltage of sphere-sphere topology in compressed nitrogen/oxygen mixture (60%/40%). A 5 mm gap was used.

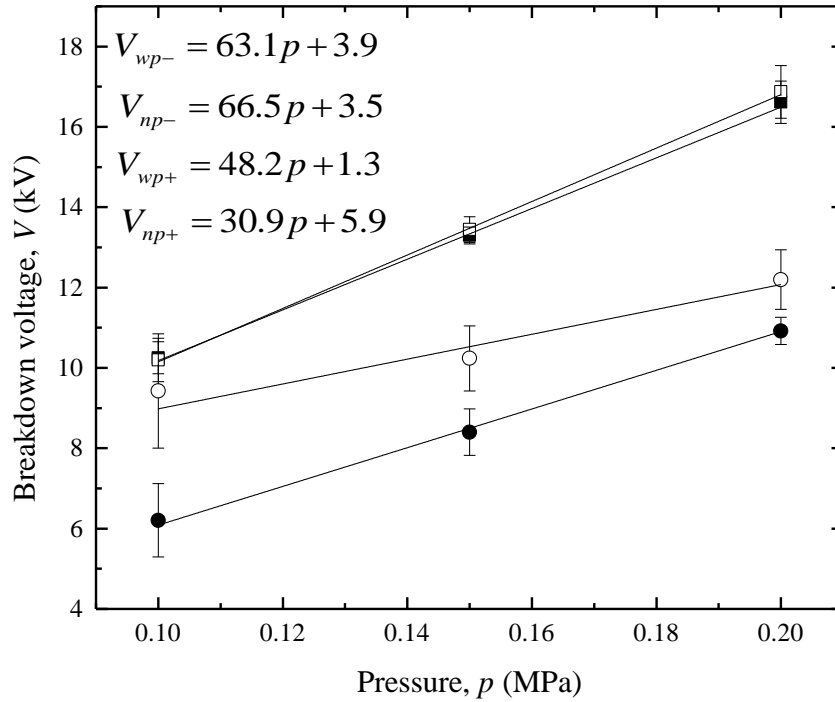
With ~20% more oxygen than in air, the nitrogen/oxygen mixture has higher proportion of electronegative gas. Therefore, the three gases investigated: nitrogen, air, and the nitrogen/oxygen mixture provide a range of concentrations of the same electronegative element, oxygen. The **plane-plane** and **sphere-sphere** topologies, Figure 4.13 and Figure 4.14, show similar functional behaviour of the breakdown voltage with gas pressure to the behaviour $V_{br}(p)$ obtained in air. However, cone-plane showed more significant differences. With little electric field enhancement, breakdown voltages in plane-plane and sphere-sphere topologies are not greatly impacted by increasing the proportion of electronegative component in the gaseous media compared with breakdown voltage in the cone-plane topology. The breakdown voltage for plane-plane and sphere-sphere topologies are similar for the oxygen/nitrogen gas mixture and air: ~15 kV for plane-plane topology and ~16 kV for sphere-sphere topology at 0.1 MPa. The breakdown voltage increases linearly as the pressure is increased, and it is only slightly different from the functional behaviour of breakdown voltage in air: breakdown voltage in air increases with a rate of ~120 kV/MPa compared to ~125 kV/MPa in the case of the plane-plane topology. The only notable

difference for breakdown voltage characteristics in the plane-plane and sphere-sphere topologies is the reduction of the standard deviation of the breakdown voltage as pressure is increased. The standard deviation of the breakdown voltage at 0.1 MPa reduces from 0.45 kV to 0.09 kV as the pressure was increased from 0.1 MPa to 0.2 MPa. With the sphere-sphere topology, the standard deviation of the breakdown voltage reduces from 0.57 kV to 0.2 kV when the pressure was increased from 0.1 MPa to 0.2 MPa.

The inclusion of coronating electrodes has, as in the case of air, little impact on the breakdown voltage magnitude or its standard deviation. In the sphere-sphere topology, there is a consistent reduction in breakdown voltage value of, ~ 0.5 kV, with the addition of coronating electrodes with both positive and negative energisation and across the pressure range.

Higher concentration of electronegative component of the gas has a large impact on space charge development in non-uniform topologies where the breakdown voltage is significantly impacted by space charge effects. Higher attachment coefficients in electronegative gases result in more negative ions and more prominent space charge for negative energisation. The **cone-plane** topology in the 60%/40% nitrogen/oxygen mixture, Figure 4.15, has had the most impact of the increase in concentration of the electronegative component (oxygen) over air.

At 0.1 MPa, the breakdown voltage has increased from ~ 6 kV (Figure 4.12) for both positive and negative energisation to ~ 9.4 kV and ~ 10 kV respectively. The breakdown voltage in the oxygen/nitrogen mixture increases linearly but at a much lower rate than in air, at just 66.5 kV/MPa compared to ~ 201 kV/MPa in air. At 0.2 MPa, the breakdown voltage has reduced by $\sim 32\%$ from 24.8 kV in air to 16.8 kV in the oxygen/nitrogen mixture for negative energisation. Breakdown voltages in the case of positive energisation are less affected by the space charge effects, but by the inclusion of coronating electrodes, they also increase at a reduced rate of ~ 30 kV/MPa compared to air in which V_{br} increases with pressure at a rate of ~ 35 kV/MPa. Breakdown voltage in the case of negative energisation is much more affected by the increase in concentration of the electronegative component of the gas. The increase in the concentration of the electronegative component in the gas has also impacted on the standard deviation of breakdown voltages.



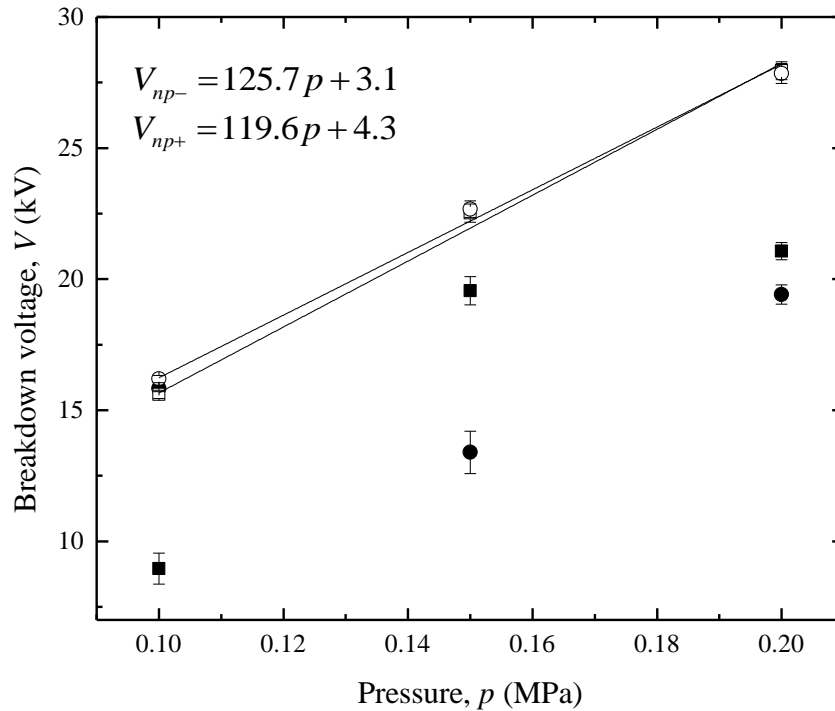
- Negative with coronating electrodes, V_{wp-}
- Negative no coronating electrodes, V_{np-}
- Positive with coronating electrodes, V_{wp+}
- Positive no coronating electrodes, V_{np+}

Figure 4.15 Breakdown voltage of cone-plane topology in compressed nitrogen/oxygen mixture (60%/40%). A 5 mm gap was used.

At 0.2 MPa, the standard deviation of breakdown voltage in air was 0.12 kV for negative energisation; whereas, in the gas mixture it has increased to 0.66 kV. Moreover, unlike breakdown voltage behaviour in plane-plane and sphere-sphere, the breakdown voltage in the cone-plane topology filled with oxygen/nitrogen mixture does not show a strong tendency to reduction of breakdown voltage and its standard deviation as the pressure is increased.

The 60%/40% nitrogen/oxygen mixture has shown the effects of increasing the concentration of the electronegative component of the gas on the breakdown voltage. It is expected that breakdown voltages in topologies filled with nitrogen will be significantly different from the breakdown voltages in air and the nitrogen/oxygen mixture when a highly non-uniform field is produced by cone-plane electrodes or by the inclusion of coronating electrodes.

Breakdown voltages in the plane-plane and sphere-sphere topologies were obtained together because they are significantly different from the breakdown voltages in cone-plane electrode configuration. Figure 4.16 and Figure 4.17 show the breakdown voltages for plane-plane and sphere-sphere topologies respectively.



- Negative with coronating electrodes, V_{wp-}
- Positive with coronating electrodes, V_{wp+}
- Negative no coronating electrodes, V_{np-}
- Positive no coronating electrodes, V_{np+}

Figure 4.16 Breakdown voltage of plane-plane topology in compressed nitrogen. A 5 mm gap was used.

Considering the plane-plane and sphere-sphere topologies without the coronating electrodes, the breakdown voltages as a function of gas pressure behave as expected. The breakdown voltages for positive and negative energisation are similar which is expected given that they both were measured in symmetrical electrode topologies. The breakdown voltage increases linearly as the pressure increases as in the case of air and the oxygen/nitrogen mixture and at similar rates. Breakdown voltages in the plane-plane topology in nitrogen increases at the rate of ~ 125 kV/MPa; whereas breakdown voltages in air and the nitrogen/oxygen mixture increased at the rate of ~ 120 kV/MPa. The breakdown voltage of the plane-plane and sphere-sphere topologies at 0.1 MPa is 16 kV in pure nitrogen and 15 kV in air and the standard deviation in breakdown voltage is 0.1 kV and 1 kV respectively. When the coronating electrodes are introduced the breakdown voltage becomes more unstable. The breakdown voltage did not show a clear linear increase as the pressure is increased and the standard deviations increased in most cases. In the plane-plane topology, the inclusion of coronating electrodes has more than doubled the standard deviation of the breakdown voltage, 0.8 kV, as compared with 0.3 kV for the topology without corona electrodes.

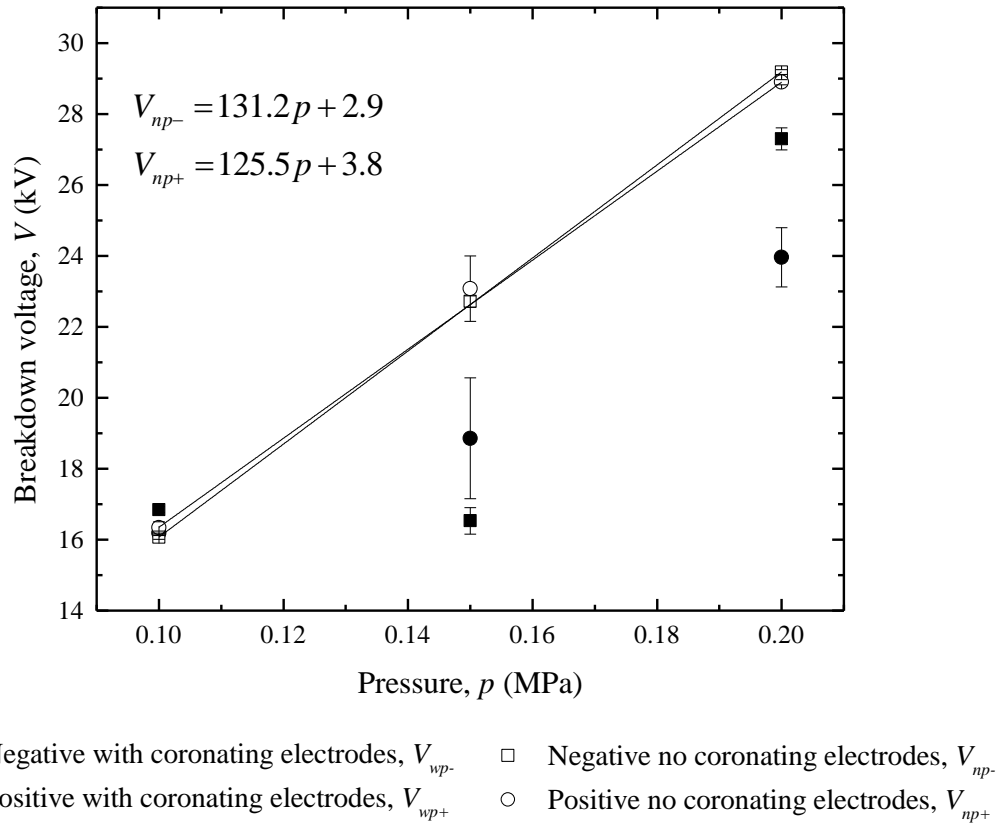


Figure 4.17 Breakdown voltage of sphere-sphere topology in compressed nitrogen. A 5 mm gap was used.

The breakdown voltage has reduced significantly in all cases for pressures above 0.1 MPa. The reduction in breakdown voltage is not consistent or linearly dependent on pressure ranging from ~30% to almost no difference. It is clear that in pure nitrogen, the inclusion of coronating electrodes in the vicinity of the plane-plane and sphere-sphere gap does not improve switch performance.

Next the cone-plane topology was considered which results in highly non-uniform field distribution in the switch and, therefore, the breakdown voltages in this topology were significantly impacted by reducing the concentration of the electronegative component (oxygen) of the fill gas.

The **cone-plane** topology has the largest field enhancement between the main electrodes and, as such, is strongly influenced by space charge. In nitrogen, as it is an electropositive gas, there is very little to no negative space charge and so the breakdown voltage is significantly different to the electronegative air and mixture gases. Figure 4.18 shows the breakdown voltage for the cone-plane topology in pure nitrogen.

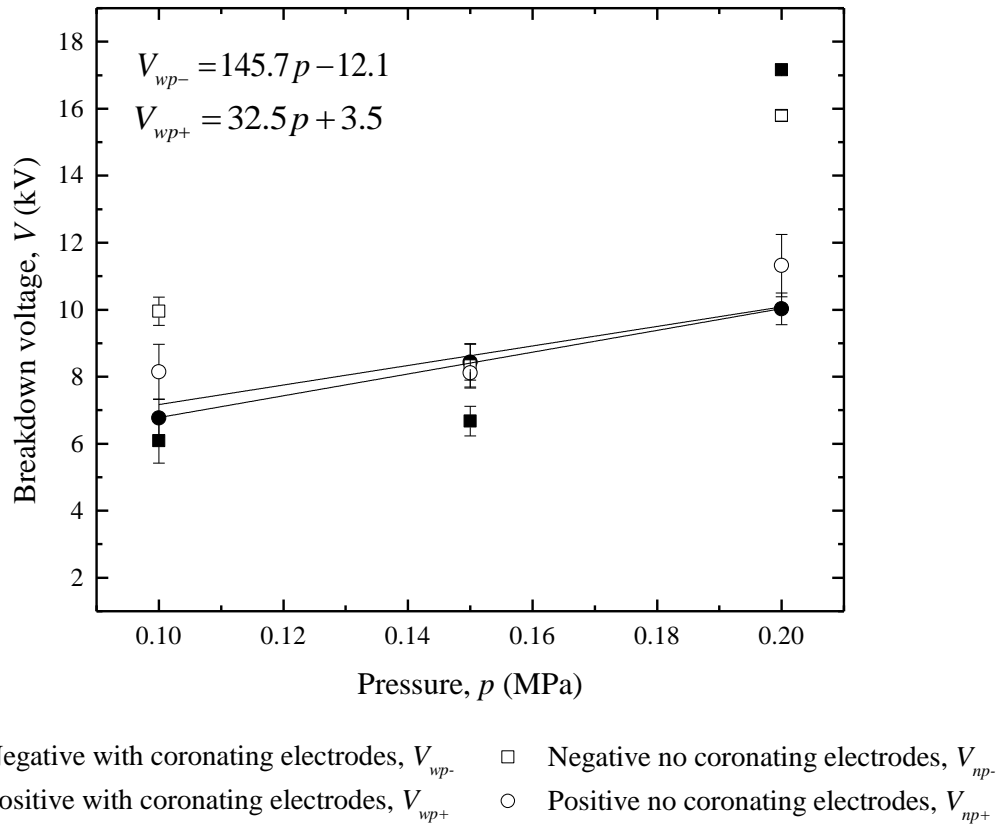


Figure 4.18 Breakdown voltage of cone-plane topology in compressed nitrogen. A 5 mm gap was used.

Where there are no coronating electrodes included, the breakdown voltage does not increase linearly as the pressure is increased in the case of negative energisation. In Figure 4.18, straight lines have been fitted in the same way as all the other graphs discussed in this section but, for the negative voltage, it is clear that a linear line cannot be reasonably fitted to the data. At 0.1 MPa, the breakdown voltages of $\sim(8-10)$ kV are similar to breakdown voltage in air (which is considered as an electronegative gas) and breakdown voltages in nitrogen/oxygen mixture. However, as the pressure is increased to 0.15 MPa, the breakdown voltage decreases by $\sim 37\%$ lower than the breakdown voltage in the electronegative gases for negative energisation. Then, as the pressure is increased to 0.2 MPa, the breakdown voltage increases again back to $\sim(16-17)$ kV, similar to the breakdown voltage behaviour in the electronegative gases. Positive breakdown voltage is more stable and consistent using air and the (N_2/O_2) mixture. The breakdown voltage does not increase linearly, remaining at ~ 8 kV when the pressure is increased from 0.1 MPa to 0.15 MPa, where in air the breakdown voltage increases from 9.5 kV to 10.3 kV. So, the differences are not as significant as they were at negative energisation where there was a 37% drop in the

breakdown voltage in the same pressure range. At 0.2 MPa the breakdown voltage is 11.3 kV which is similar to the breakdown voltage in air, 12.2 kV.

Therefore, it may be concluded that introduction of coronating electrodes to the cone-plane topology in pure nitrogen reduces the breakdown voltage for most gas pressures. Only for 0.2 MPa with negative energisation and 0.15 MPa with positive energisation does the breakdown voltage increase. There is no strong trend for the impact of the breakdown voltage as in the case without coronating electrodes. In the case of positive energisation, the breakdown voltage standard deviation reduced at 0.2 MPa by ~48% from 0.9 kV at 0.1 MPa to 0.47 kV at 0.2 MPa.

4.5 CONCLUSIONS

This experimental investigation into the functional behaviour of breakdown voltage in different topologies for use in high performance spark switches produced some significant findings. Using air as the fill gas, breakdown voltages in plane-plane, sphere-sphere and cone-plane topologies were compared, focusing on the magnitude of breakdown voltage and its standard deviation as a function of pressure. An investigation into the influence of increasing and decreasing the electronegativity of the gas on the behaviour of the breakdown voltage was completed using the same topologies. Nitrogen was used as an electropositive gas and a 60%/40% nitrogen/oxygen mixture was used as a higher concentration electronegative component gas (as compared with air). It was found that using coronating electrodes in the vicinity of the plane-plane, sphere-sphere and cone-plane topologies does not consistently reduce the standard deviation of breakdown voltage. No consistent trend could be determined to predict which configuration would benefit from coronating electrodes in air, nitrogen or the mixture.

Using atmospheric air as a benchmark, the breakdown voltages for nitrogen and the oxygen/nitrogen mixture were investigated. It was found that there was no significant difference between breakdown voltages in air and in gas mixture with 20% more oxygen in the plane-plane and sphere-sphere topologies. The negative energisation of the cone-plane topology resulted in higher initial breakdown voltages as compared with other investigated topologies. However, the breakdown voltage in the cone-plane topology had a significantly reduced rate of increase with pressure leading to overall lower breakdown voltages at 0.2 MPa as compared with other topologies. Breakdown voltages in nitrogen were also similar for plane-plane and sphere-sphere topologies. However, with non-uniform electric

field such as topologies with coronating electrodes or cone-plane topology, the breakdown voltage in nitrogen became difficult to predict for negative energisation and the breakdown voltage standard deviation increased.

It was found that in air, the breakdown voltages of each of the topologies increased linearly as the pressure was increased. Breakdown in the plane-plane and sphere-sphere topologies were not strongly dependent on the polarity of applied voltage which was expected because the electrode geometries are symmetrical. The cone-plane topology with highly non-uniform electric field produced very different breakdown voltages for positive and negative energisation. This is due to space charge screening effects increasing the breakdown strength significantly for negative energisation. However, because the breakdown voltages increased at different rates as the pressure is increased the breakdown voltage around 0.1 MPa was similar.

The intersection point between positive and negative breakdown voltage is an interesting phenomena which could be very useful to the design of compact pulsed power systems and spark switches. Using the electronegative gases, air and the oxygen/nitrogen mixture, it was found that the stability of the breakdown voltage in the cone-plane topology was improved as the pressure was increased. The next section of this thesis will provide results of investigation of self-breakdown voltages in point-plane topologies with varying point electrodes.

5. INVESTIGATION OF RAMPED SELF-BREAKDOWN VOLTAGE OF SPARK SWITCHES WITH POINT-PLANE TOPOLOGY

In Chapter 4, an investigation into ramped self-breakdown voltages in different electrode topologies was conducted using plane-plane, sphere-sphere and cone-plane electrode geometries filled with air, pure nitrogen and a 60%/40% nitrogen/oxygen mixture. This chapter continues investigating breakdown voltage focusing on the point-plane topology only. It was found (in Chapter 4) that the breakdown voltage for positive and negative energisation is different at higher gas pressures with the cone-plane topology but positive and negative breakdown voltage values converge with a decrease in gas pressure to be similar. This chapter investigates the convergence point between positive and negative breakdown voltages in point-plane topologies filled with different point electrodes and gases. These results obtained in this research will aid in the development of compact high-performance spark switches and pulsed power systems where there is a need for systems with small footprint.

Using the results obtained in this research project, and presented in this thesis, it is possible to design a switch with a point-plane topology that will provide equal breakdown voltages for positive and negative energisations. Such switch topology has been developed in the present chapter and was used in the design of the triggered switches and multi-gap switches investigated in other sections of this thesis. Breakdown voltage in electronegative gas is usually expected to be higher with negative energisation than for positive energisation in non-uniform topologies because of negative volumetric space charge effect, i.e. screening of the electric field in the vicinity of the high voltage point electrode, as discussed in Section 2.2.3.

The aims and tasks of this part of the research project are to investigate the functional behaviour of the breakdown voltage in a point-plane topology for both positive and negative applied voltages. Changing the inter-electrode gap and using bottled air at a range of pressures from 0.1 MPa to 0.35 MPa as a filling gas, the breakdown voltages were obtained as a function of pressure and distance in a range of inter-electrode gaps from sub-mm to ~6 mm. Plotting the breakdown voltages for positive and negative energisation, the ranges of parameters (pressure, p , distance, d , and their combination, pd) where positive energisation breakdown voltage is higher than negative energisation have been identified. Also, the pd ranges where positive and negative energisation have similar breakdown voltages have been established and the range of pd where negative energisation resulted in a higher breakdown voltage as compared with positive energisation has been established. The pd value at which the positive and negative breakdown voltages become equal is identified for bottled air at a range of pressures from 0.1 MPa gauge and 0.35 MPa gauge.

This investigation identifies the cross-over point of the positive and negative breakdown voltages as functions of inter-electrode distance which will be called the ‘critical breakdown voltage’, V_{crit} and ‘critical gap’, d_{crit} . For the first time, the critical voltage and gap was investigated with varying electrode diameters, insulating gases and voltage polarities. The following sections describe the design of the spark switches and the topologies and present the results of investigation into critical breakdown voltage and critical gap in bottled air. Results from this, investigations were presented and published in the proceedings of 19th IEEE Pulsed Power Conference in 2013 [Hogg 2013] and in IEEE Transaction on Dielectric and Electrical Insulation [Hogg 2015].

5.1.1 Point Electrodes

Three HV point electrodes were used in this investigation, with radii: 0.038 mm, 0.067 mm, and 0.8 mm. The 0.038 mm radius point was a soft-tone gramophone needle and the 0.067 mm and 0.8 mm radius points were sharpened and hemispherical tipped tungsten rods. The electrodes were examined and photographed under a microscope alongside a 1000th inch spacer for comparison. The microscope pictures of the point electrodes showed the profile and smoothness of the tips as well as allowing the radii to be calculated.

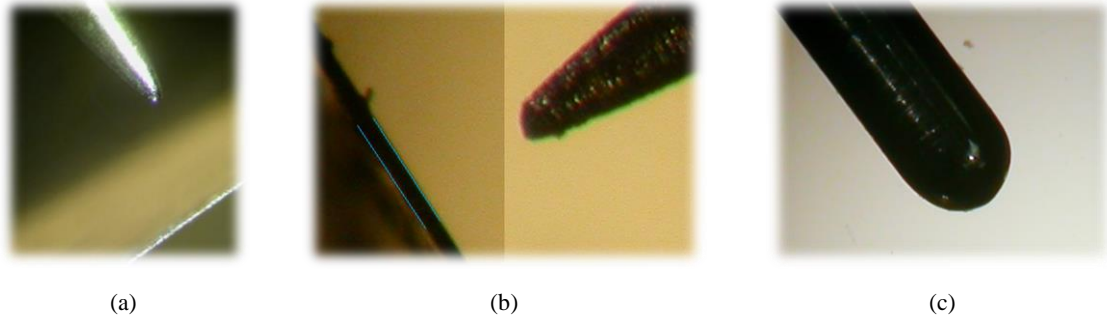


Figure 5.1 Point electrodes photographed with microscope. (a) gramophone needle, $r=0.038$ mm. (b) Sharpened tungsten rod, $r=0.067$ mm. (c) Hemispherical tipped tungsten rod, $r=0.8$ mm. Thin line – filler gauge with 1000^{th} inch thickness.

The ground electrodes were machined brass rings of 40 mm diameter with rounded edges that were polished to reduce rough edges that could cause field enhancement. A 40 mm diameter was chosen because it was planned that the largest gap between the electrodes would be 10 mm. The radius of the electrode should be twice as large as the gap to ensure all current radiating from the HV point is collected and, as such, 40 mm was required. This was important because it then defined the remaining dimensions of the test cell.

The plane electrode was regularly changed throughout the experiments and re-polished to remove any imperfections formed during breakdown tests. This ensured no significant effects from micro protrusions and pits caused by repetitive breakdowns upon the ground electrode.

5.1.2 Spark Switch Design

The point-plane electrode topology described above was housed in a test cell that allowed the gas to be pressurised. The test cell was cylindrical machined glass nylon wide enough to house the plane electrode with a gap of 5 mm all around. The schematic can be seen in Figure 5.2 with all the components labelled and the key dimensions given. The plane electrode sat on the bottom of the test cell with a threaded connection out of the base via a clearance hole. This allowed the ground connection to be easily connected and disconnected. A rubber ‘o’ ring slightly smaller than the plane electrode was compressed between the plane and base of the test cell forming an air tight seal. Figure 5.2 shows the schematic of the test cell.

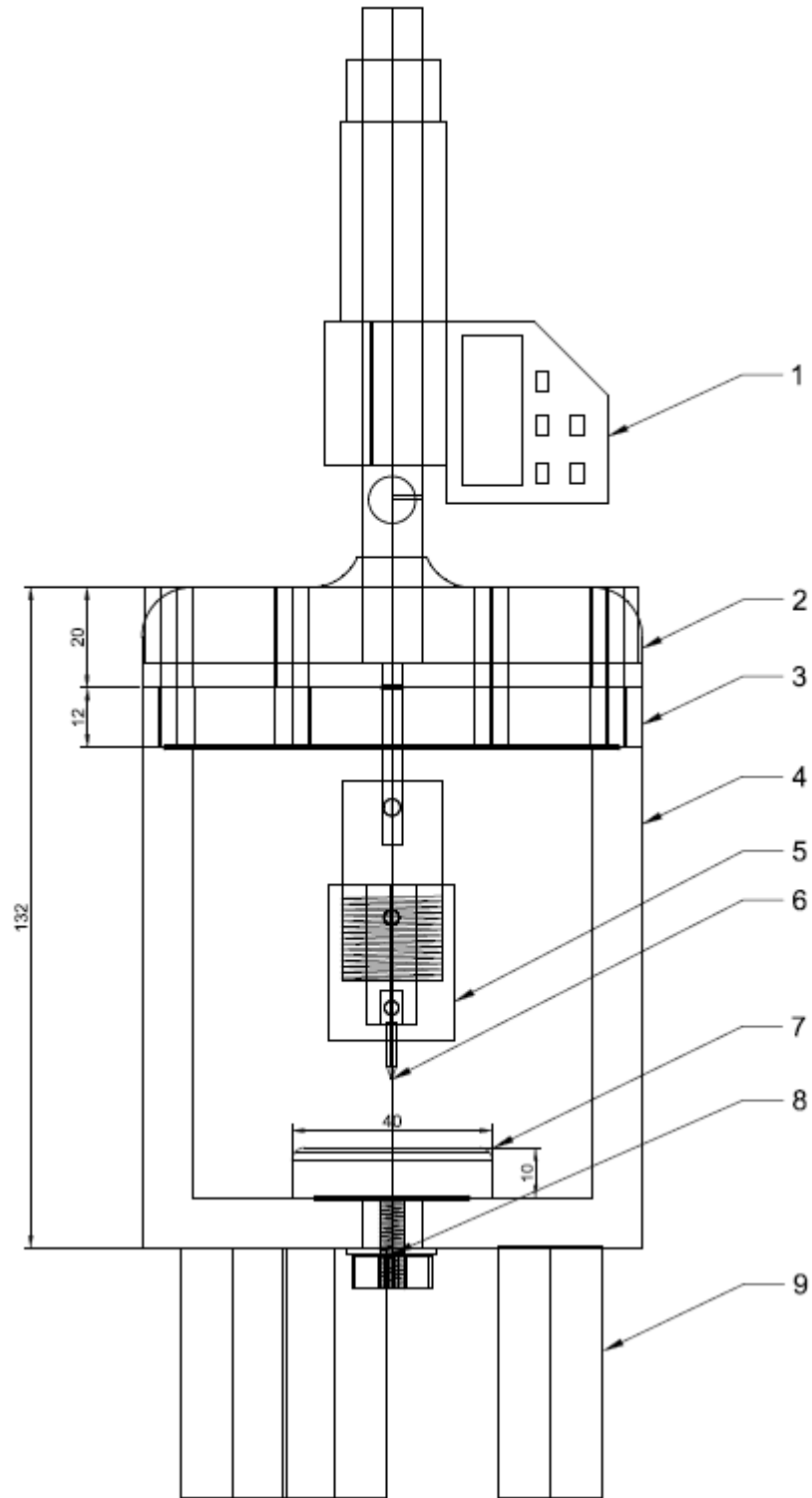


Figure 5.2 Point-plane test cell schematic. 1 - Precision Digital Depth Gauge, 2 – Acrylic top of switch, 3 - Aluminium shielding block, 4 - Acrylic body of test cell, 5 - Point electrode holder, 6 - Point electrode, 7 - Plane electrode, 8 - Ground connection, 9 - Test cell support legs. Dimensions are in mm.

The point electrode is held by a brass connector which is held by a glass nylon flange insulating it from the metal rod. The metal rod is raised and lowered by a digital micrometre depth gauge to set the gap. The depth gauge is capable of setting inter-electrode gaps accurately to ± 0.003 mm and so provides the ability to set sub-mm gaps accurately. The rod goes through an aluminium block, which shielded the digital components in the depth gauge from electromagnetic interference. The rod then passes through a glass nylon top before entering the control and measurement part of the depth gauge. Between the aluminium and glass nylon top a rubber 'o' ring sits around the rod and forms an air tight seal when the top is secured and 'o' ring is compressed. The top is secured by 8 long metallic screws which screw into pre-tapped holes in the walls of the test cell. Once secured properly, the test cell is air tight above 0.35 MPa. The depth gauge sits atop the test cell and is fixed by a grub screw. The point electrode can be raised and lowered once the test cell is closed using the depth gauge controls. The brass connector holds the point electrode by a grub screw and is connected to the HV via a small connector and grub screw.

The brass connector is connected to a push fitting socked on the wall of the test cell via a flexible HV cable. HV from the DC power supply is connected to the other side of the test cell wall and the point can be energised. The pressure inside the test cell is controlled via a push fitting connection on the wall of the test cell. Figure 5.3 shows some photos of the finished test cell.



(a)



(b)

Figure 5.3 Photographs of the point-plane switch with micrometre depth gauge. (a) Whole switch. (b) Depth control and point-electrode holder.

5.2 RAMPED SELF-BREAKDOWN VOLTAGE: RESULTS AND ANALYSIS

The results of the breakdown voltage behaviour in the point-plane topology are considered in three different sections investigating the breakdown voltage dependence on gas pressure, gas type, electrode separation and point electrode radius. In Section 5.2.1, the breakdown voltage as a function of gas pressure has been investigated using three gases: air, pure nitrogen and a nitrogen/oxygen mixture using a single point-plane electrode topology. Section 5.2.2 compares the breakdown voltage in these gases as a function of electrode separation using the single point-plane electrode topology. In Section 5.2.3, the breakdown voltage in the single point-plane electrode topology filled with bottled air has been obtained for different pressures and point electrode radii. In the following sections, the results are fitted with empirical fittings for easy comparison. These fittings are only valid for the experimental conditions used in this research.

5.2.1 Ramped Self-Breakdown Voltage of Point-Plane Spark Switch as a Function of Gas Pressure in Air, Nitrogen and Nitrogen/Oxygen Mixture

In this section, a single point-plane electrode topology was used to obtain breakdown voltage for three gases: bottled atmospheric air, pure nitrogen (BOC Ltd, 99.9% purity) and 60%/40% nitrogen/oxygen mixture (BOC Ltd mix). The sharpened tungsten rod with tip radius of 0.067 mm was used and breakdowns for positive and negative energisation were observed. The inter-electrode gap range was dependent on the results, increasing or decreasing the gap to add information to observe the critical gap and ensure a clear difference between positive and negative breakdown voltage was achieved.

Bottled atmospheric air (12.5% relative humidity) was used as a bench mark for comparison of breakdown voltages in nitrogen and the nitrogen/oxygen gas mixture. The relationship between breakdown voltage and pressure was considered. The switch was filled with a fresh portion of gas before each test, each point on these graphs represent an average value of 30 breakdown measurements which were conducted without changing the gas in the switch; the error bars show the standard deviation. Figure 5.4 shows the breakdown voltage with respect to pressure for 5 inter-electrode separations starting with 0.25 mm up to 6 mm. It can be seen

that for positive and negative energisation breakdown voltage has a linear dependence on the pressure of the air.

As before, and in this chapter, an empirical fitting procedure was used to fit the experimental points with linear empirical functions using OriginPro 9.0 software package. The empirical equations with corresponding coefficients which describe these linear fit lines with breakdown voltage, V_{br} , (kV) as a function of pressure, p (MPa):

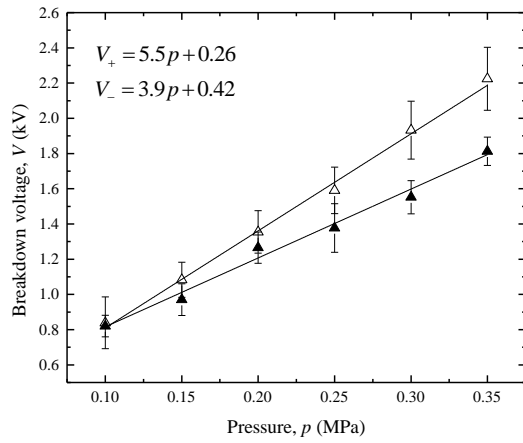
$$V_{br} = Ap + B \quad (5.1)$$

where A (kV/MPa) and B (kV) are fitting coefficients, given in these figures for each combination of polarity of the applied voltage and the presence and absence of the corona electrodes.

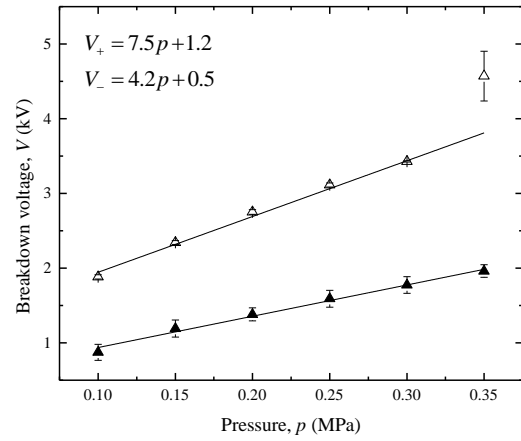
Breakdown voltage for 0.25 mm, 0.5 mm and 1 mm gaps, Figure 5.4(a,b,c), show positive breakdown voltage is ~25% larger than negative energisation at 0.35 MPa. When the gap is increased above 3 mm, Figure 5.4(d,e), the breakdown voltage switches to be larger for negative energisation than for positive energisation. With a 3 mm gap, the breakdown voltage for negative energisation has already surpassed positive energisation and is 28% higher at 0.35 MPa. In Figure 5.4(b), the breakdown voltage in 0.35 MPa was lower than the trend line due to the stochastic nature of gas discharge.

The rate at which breakdown voltage increases with pressure is higher for positive energisation compared with negative energisation at 1 mm gap and below. The rate at which the breakdown voltage increases with pressure is dependent on the electrode spacing, at 0.25 mm positive energisation is 30% higher than negative energisation increasing to 40% higher with a 1 mm gap. With a 3 mm gap, the negative breakdown voltage increases with respect to pressure at a higher rate than positive energisation. At 3 mm, negative energisation is already increasing 37% quicker than positive energisation as pressure is increased.

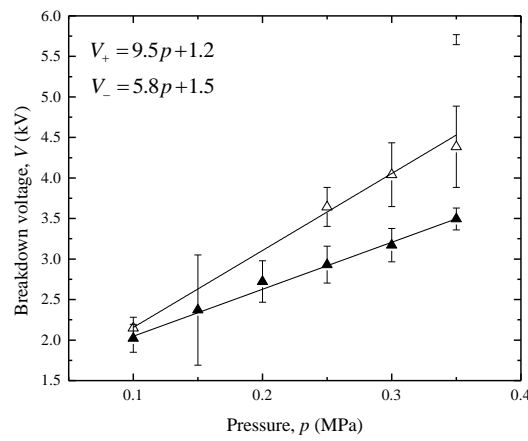
This shows that there is a critical gap between 1 mm and 3 mm, at which the breakdown voltages for positive and negative energisation should be similar. This will be discussed further when the results are considered as a function of electrode separation instead of pressure.



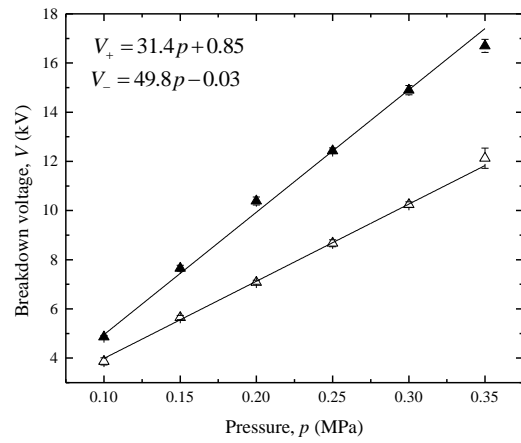
(a) 0.25 mm



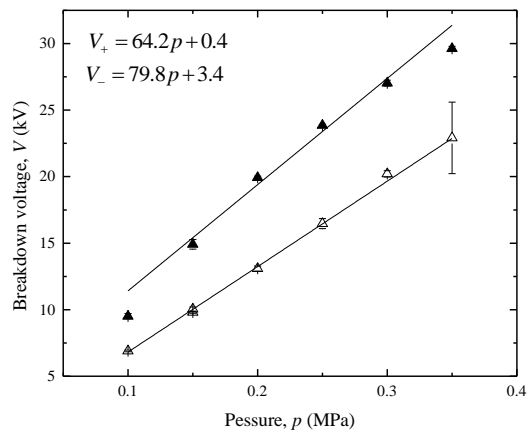
(b) 0.5 mm



(c) 1 mm



(d) 3 mm



(e) 6 mm

\triangle Positive energisation
 \blacktriangle Negative energisation

Point electrode radius – 0.068 mm.

Gas – Bottled air (~20°C, 12.5%rh).

Figure 5.4 Breakdown voltage as a function of gas pressure for a point-plane gap filled with bottled air.

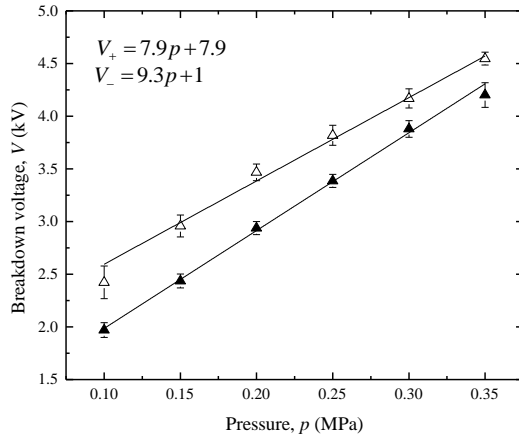
The relationships between breakdown voltage and pressure, for positive and negative energisation, in the more electronegative 60%/40% nitrogen/oxygen mixture (Figure 5.5) are similar to air (Figure 5.4). Figure 5.5 presents the breakdown voltage as a function of air pressure a range of inter-electrode gaps filled with the nitrogen/oxygen mixture.

The breakdown voltage is higher for positive energisation compared to negative energisation in the 0.5 mm gap, Figure 5.5(a). This is similar to 0.5 mm in air, Figure 5.4(b). However, as the inter-electrode gap is increased to just 1 mm, Figure 5.5(b), it can be seen that positive breakdown voltage starts higher at 0.1 MPa but ends up lower as the pressure is increased to 0.35 MPa. This shows that the critical gap where positive and negative energisations have similar breakdown voltages is lower than for air which is between 1 mm and 3 mm.

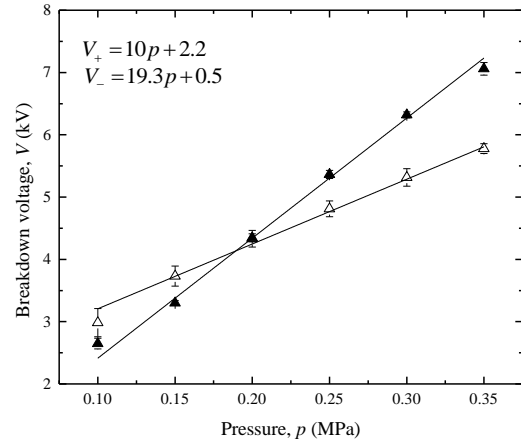
The rate at which the breakdown voltage increases with pressure in the gas mixture is not the same as air. At shorter gaps, below 1 mm, the rate of increase is similar for positive energisation. As the gap is increased to 6 mm the rate breakdown voltage increases, for positive energisation, it is 47% lower at 34.2 kV/MPa compared to 64.2 kV/MPa. Whereas, negative energisation increases at a higher rate, 21% higher than air. This is due to the increase in the negative space charge because of higher concentration of electronegative component (oxygen) of the nitrogen/oxygen mixture producing more negative ions. This leads to the separation between positive and negative energisation breakdown voltages occurring in shorter gaps and at lower pressures as compared with air.

The electropositive nitrogen gas has significantly less pronounced volumetric space charge, and so it was expected that negative breakdown voltage would never be significantly higher than positive breakdown voltage. Figure 5.6 shows the positive and negative breakdown voltages as functions of nitrogen pressure.

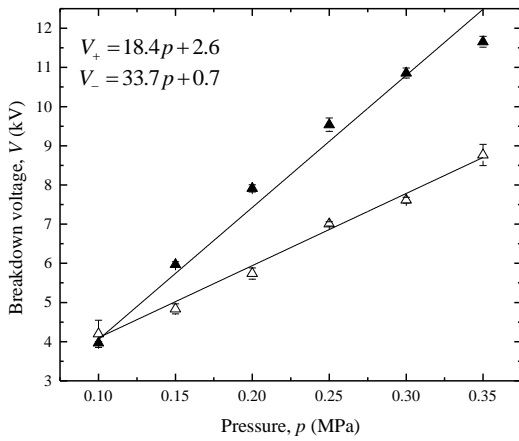
The first observation to make about breakdown voltage in nitrogen is that with negative energisation the breakdown voltage does not significantly surpass positive energisation. Positive breakdown occurred similar to air and the mixture where breakdown voltage increased linearly with gas pressure at similar rates, ~30 kV/MPa for 4 mm gap and ~10 kV/MPa for 1 mm gap. Negative breakdown voltage, on the other hand, behaves significantly differently. Initially, the breakdown voltages for negative and positive energisation are similar, but as the pressure is increased the negative breakdown voltage drops off.



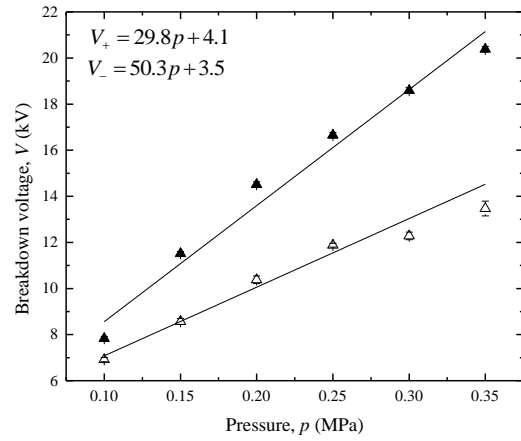
(a) 0.5 mm



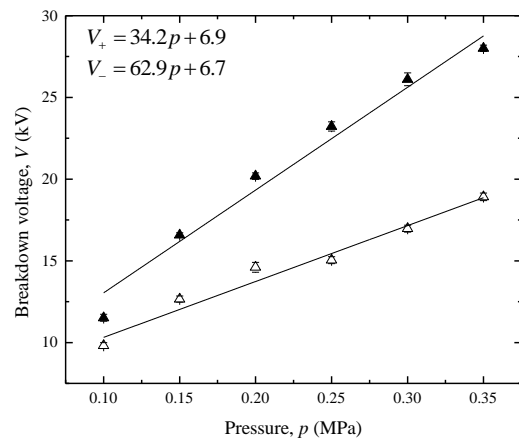
(b) 1 mm



(c) 2 mm



(d) 4 mm



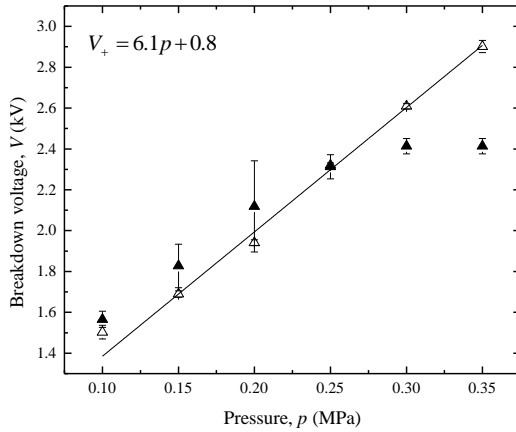
(e) 6 mm

\triangle Positive energisation
 \blacktriangle Negative energisation

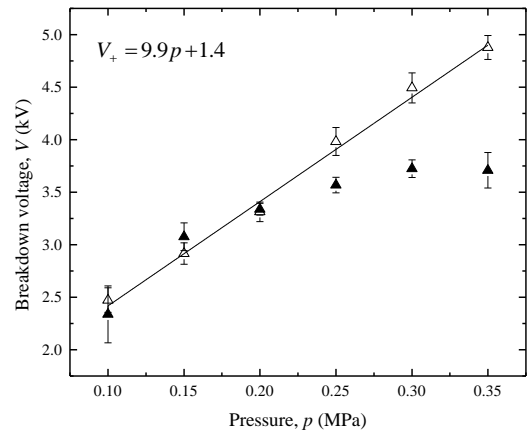
Point electrode radius – 0.068 mm.

Gas – 60% nitrogen/ 40% oxygen.

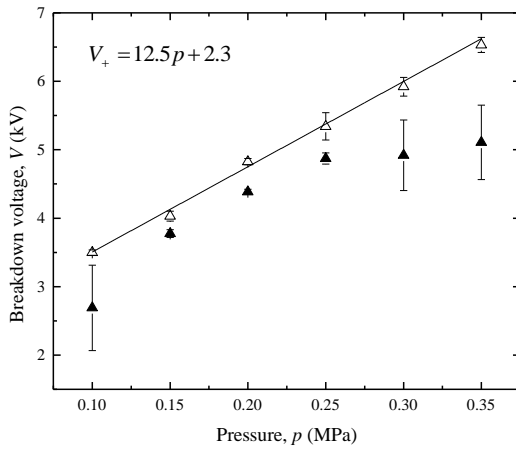
Figure 5.5 Breakdown voltage as a function of gas pressure for a point-plane gap.



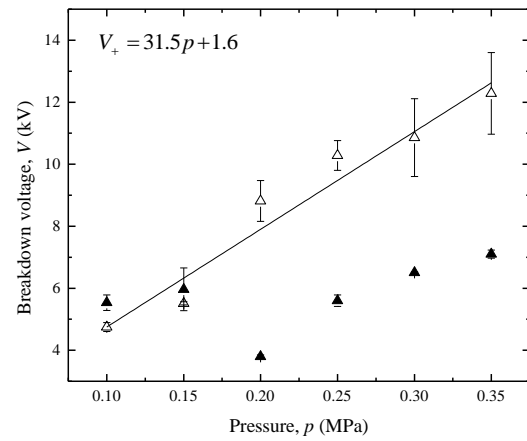
(a) 0.5 mm



(b) 1 mm



(c) 2 mm



(d) 4 mm

△ Positive energisation
 ▲ Negative energisation

Point electrode radius – 0.068 mm.
 Gas – nitrogen.

Figure 5.6 Breakdown voltage as a function of gas pressure for a point-plane gap.

It was found that, in most cases when the negative breakdown voltage reduces below breakdown voltage at positive energisation, negative breakdown did not cause sudden voltage collapse. Using a specialised test cell, discussed in Chapter 6, with a quartz window it was observed that the breakdown gradually initiated a corona and then to arc transition. This occurred much slower than a spark breakdown and visually could be seen to have much less light emission. For this reason, it was not possible to continue with breakdown results in nitrogen at up to 6 mm.

The similarity between nitrogen and the electronegative gases at shorter gaps shows that it is the initiation of corona discharges that can explain the increase in breakdown strength of negative energisation in electronegative gases.

The conclusions of this investigation into varying gas electronegativity and pressure using sharp point-plane topology has shown that with electronegative gas, the breakdown voltage increases linearly as the pressure is increased for both polarities. It also increases linearly for positive energisation in nitrogen but negative energisation breakdown is not always linearly dependent on pressure.

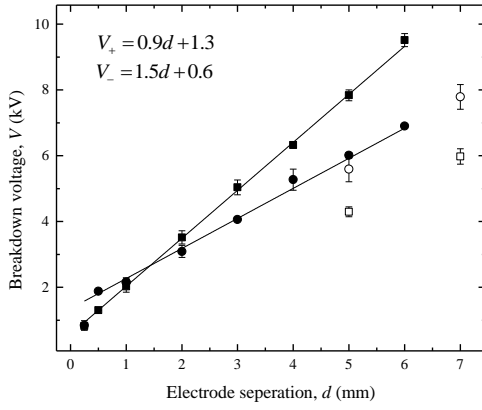
It may be concluded that nitrogen is not a suitable gas to use for spark switches with non-uniform topologies which would be used with negative energisation. The breakdown voltage is unstable and the development of a spark is not as predictable.

Air and the 60%/40% nitrogen/oxygen mixture have similar breakdown voltages with the breakdown voltages in more electronegative gas mixture are slightly more effected by space charge. The positive energisation breakdown voltage is higher at short gaps and, at larger gaps, it is lower than negative energisation. The transition from breakdown voltage for positive energisation being higher than negative energisation is discussed in more detail in the next section where breakdown voltage is considered with respect to electrode separation.

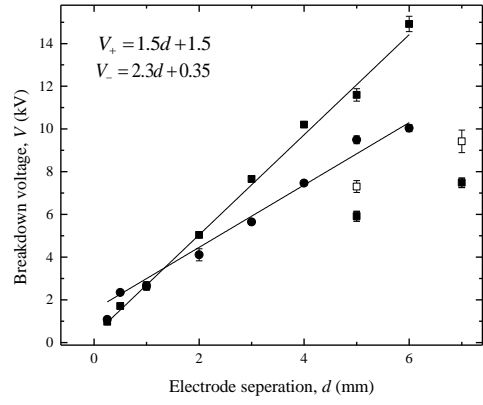
5.2.2 Ramped Self-Breakdown Voltage as a Function of Electrode Separation

It has been observed that breakdown voltage for positive and negative energisation converge at a critical gap, d_{crit} , as pressure and distance change depending on the switching conditions. In the last section, it was observed that the critical gap is dependent on the gas pressure, gas type and electrode spacing. This section identifies the critical gap where the convergence occurs for a range of pressures using the sharpened tungsten rod with tip radius 0.067 mm. Figure 5.7 shows the breakdown voltage for bottled air as a function of electrode spacing for individual fixed pressures.

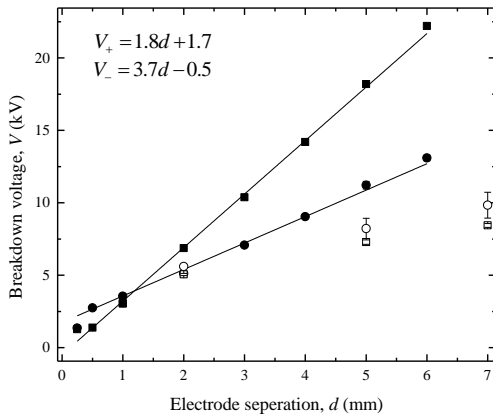
Plotting the breakdown voltage as a function of inter-electrode separation shows the intersection of positive and negative breakdown voltages. The electrode separation where the intersection occurs, referred to as the critical gap, d_{crit} , can be calculated.



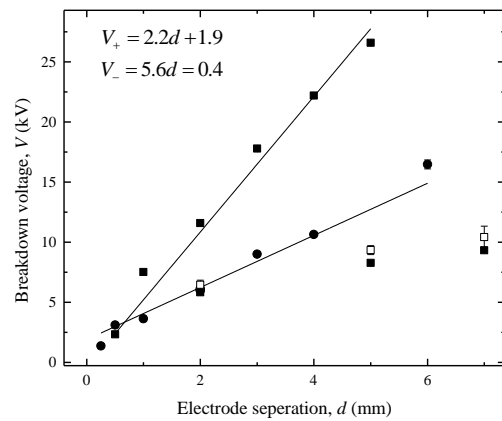
(a) 0.1 MPa



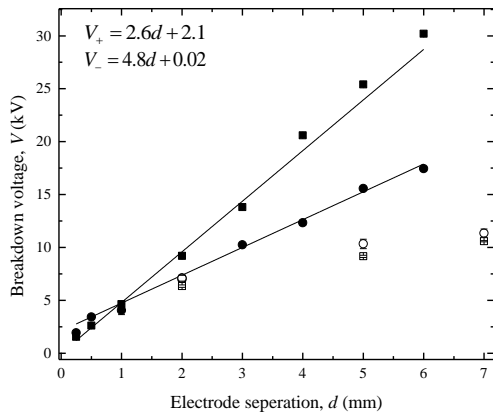
(b) 0.15 MPa



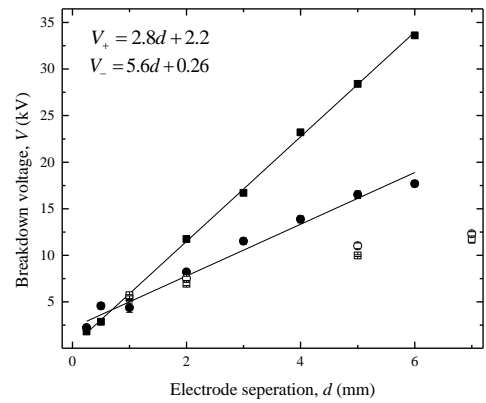
(c) 0.2 MPa



(d) 0.25 MPa



(e) 0.3 MPa



(f) 0.35 MPa

- Positive energisation breakdown voltage, V_+
- Negative energisation breakdown voltage, V_-
- Positive energisation corona inception voltage
- Negative energisation corona inception voltage

Point electrode radius – 0.068 mm.

Gas – bottled air (~20°C, 12.5%rh).

Figure 5.7 Breakdown voltage as a function of gap separation for a point-plane topology in air.

The range of electrode separations was increased or decreased sufficiently to provide critical gap and show clear positive negative energisation separation. The critical gap was calculated from trend lines fitted to linear data on the breakdown voltages as a function of electrode separation. The empirical fittings are only valid for the parameter range they are fitted across starting with 0.25 mm electrode gap, if the electrode separation was reduced to 0 mm, the actual breakdown voltage would tend to 0 V.

The critical gap is dependent on the applied pressure, at ~1.4 mm at 0.1 MPa reducing to ~1.2 mm as the pressure is increased to 0.15 MPa. As the pressure keeps being increased, the critical gap reduces further until at 0.35 MPa the critical gap is ~0.75 mm. Past the critical gap, the breakdown voltage increases linearly with electrode separation for all air pressures tested in Figure 5.7. Below the critical gap, breakdown due to negative energisation remains linear but positive energised breakdown is not always linear. This is more obvious with large radii point electrodes and will be discussed in the last section of this chapter. Figure 5.8 shows the breakdown voltage as a function of electrode separation for each pressure tested in 60%/40% nitrogen/oxygen mixture.

The breakdown voltage in 60%/40% nitrogen/oxygen mixture as a function of electrode separation is similar to that in air. The breakdown voltage increases linearly and positive and negative energised breakdown voltages converge. The critical gap for this gas mixture is larger than for air, at ~2.5 mm compared to ~1.4 mm at 0.1 MPa. The critical gap reduces as the pressure is increased and at 0.15 MPa the critical gap for the mixture and air are the same, ~1.2 mm. The critical gap keep reducing when pressure is increased and is lower than air, ~0.39 mm compared to ~0.75 mm at 0.35 MPa. The 60%/40% nitrogen/oxygen gas mixture is more electronegative than air due to ~20% more oxygen. Next the breakdown performance of nitrogen was investigated as a potential electropositive alternative to gases which contain the electronegative component, oxygen.

As was discussed (Section 5.2.1), when considering the breakdown voltage as a function of pressure, the breakdown voltage in nitrogen (Figure 5.9) is not as stable as in air and nitrogen/oxygen mixture.

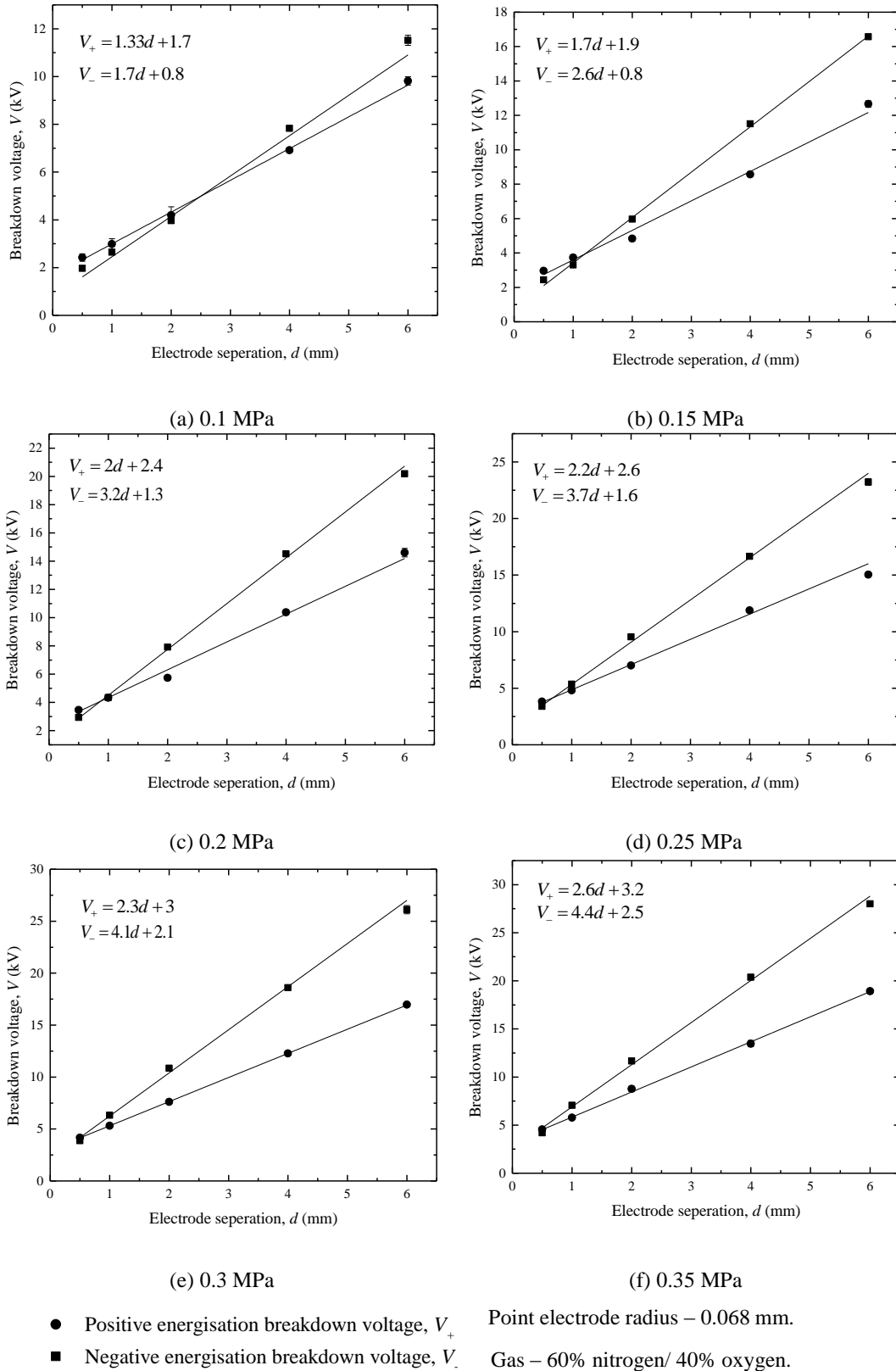


Figure 5.8 Breakdown voltage as a function of gap separation of a point-plane topology in 60%/40% nitrogen/oxygen mixture.

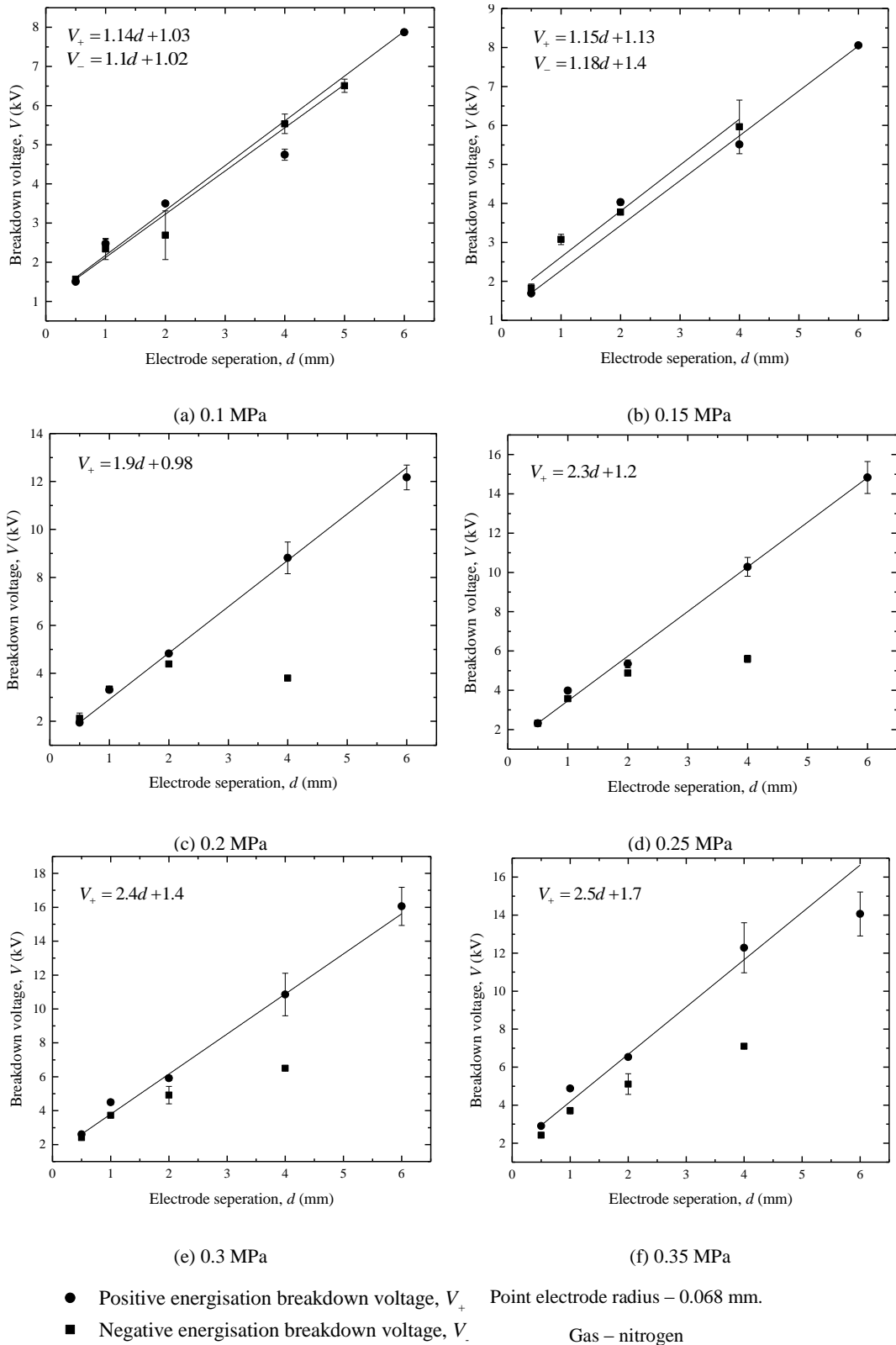


Figure 5.9 Breakdown voltage as a function of gap separation of a point-plane topology in nitrogen.

Breakdown under positive DC energisation behaves in a similar way to in electronegative gases (air and nitrogen/oxygen mixture), increasing linearly as the gap is increased. But under negative polarity, breakdown voltage is much less predictable, increasing linearly and with similar voltage to positive energisation at first, up to a 2 mm gap, and then reducing rapidly as the gap is increased. Breakdown transitioned from corona to arc without causing a spark and rapid reduction of voltage at larger gaps; therefore, it was not possible to collect breakdown data for 6 mm gaps. Due to the nature of breakdown in nitrogen, it was not possible to fit the negative breakdown voltages (Figure 5.9) with a linear function. It was discussed that the critical gap for each gas reduces as the pressure is increased. Figure 5.10 shows the critical gap, d_{crit} , as a function of gas pressure for air and the gas mixture.

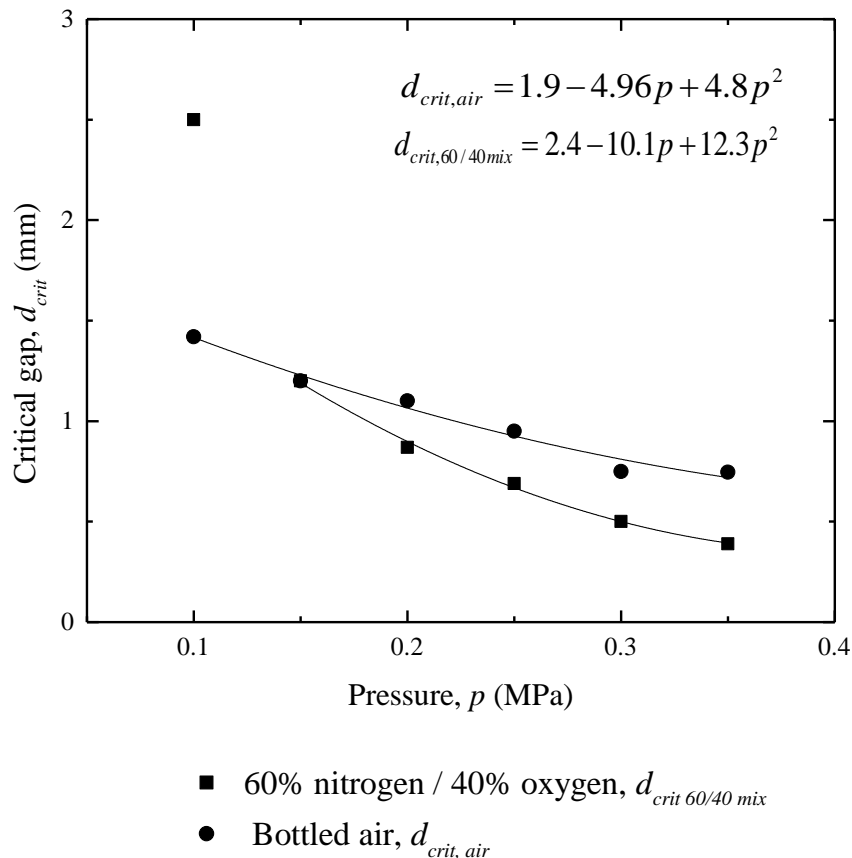


Figure 5.10 Critical gap, d_{crit} , as a function of pressure.

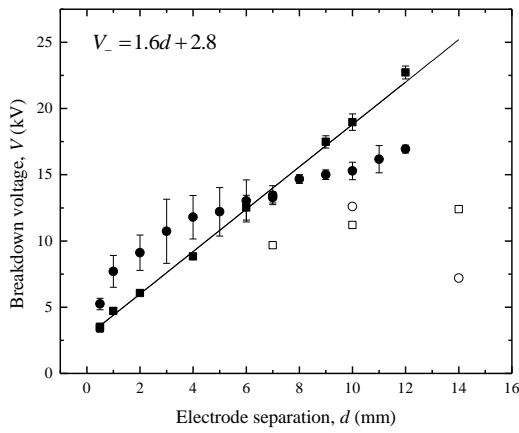
In this figure, solid lines are empirical fit lines which have been obtained using OriginPro 9.0 graphing software. These empirical fit equations (which are included in Figure 5.10) allow prediction of critical length to be made in the gas pressure range from 0.1 MPa to 0.35 MPa. The critical gap for both air and the mixture reduce as the gas pressure is increased. The

critical gap for air is 44% smaller at 1.4 mm compared to 2.5 mm at 0.2 MPa and 0.1 MPa respectively. However, the critical gap for the mixture rapidly reduces and, at 0.15 MPa, the gaps for air and the mixture are the same, ~1.2 mm. The critical gap for air reduces at a lower rate of ~0.1 - 0.2 mm per 0.05 MPa compared to the mixture which, after 0.15 MPa reduces ~0.1 - 0.33 mm per MPa. Ultimately, i.e. at 0.35 MPa, the mixture has ~48% lower critical gap, but this is only 0.36 mm shorter than air. Therefore, for practical use with this electrode, they both produce similar results and there is no clear advantage to using the increased electronegativity of the mixture.

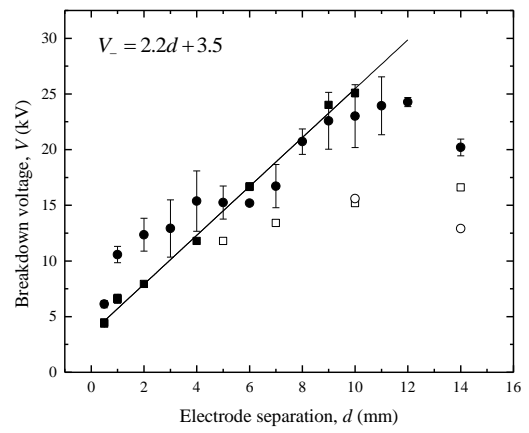
The next section will consider the breakdown voltage and the critical gaps with varying point electrodes. The aim of the next section is to determine a relationship between the critical gap and the radius of the point electrode.

5.2.3 Ramped Self-Breakdown Voltage as a Function of Point Electrode Tip Radius

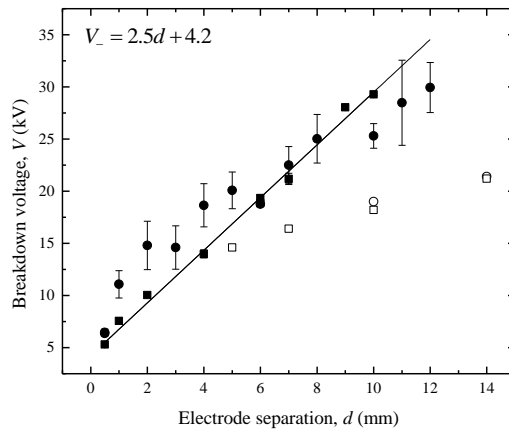
Based on the results obtained in the previous sections, it was found that nitrogen does not produce stable results in order to consider this gas for practical applications in spark switches with point-plane topologies and, since there is no significant difference between breakdown voltages in air and in the 60%/40% nitrogen/oxygen mixture, bottled air will be used to investigate breakdown voltage as a function of point electrode radius. Three electrodes were considered, Section 5.1.2, with point radii of: 0.038 mm, 0.068 mm and 0.8 mm. The 0.068 mm radius point electrode has already been presented in Section 5.2.3. In this section, first the 0.8 mm radius point electrode is presented and discussed, and then the 0.038 mm electrode will be discussed. These two new electrodes show the effect of a blunter electrode and a sharper electrode compared to the 0.068 mm that has so far been used. The electrodes have been described in Section 5.1.1. Figure 5.11 presents the breakdown voltage as a function of electrode gap for the 0.8 mm radius point electrode.



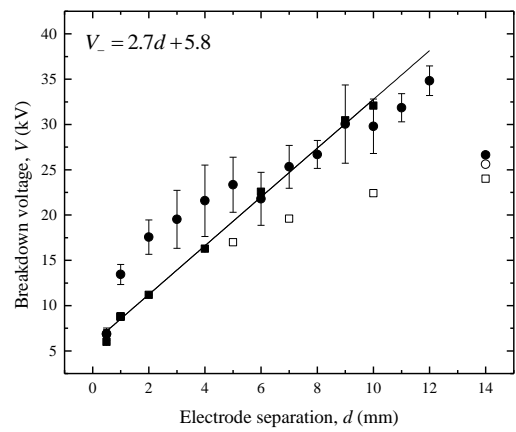
(a) 0.1 MPa



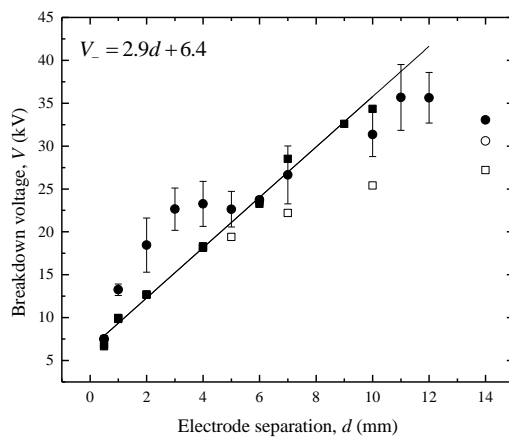
(b) 0.15 MPa



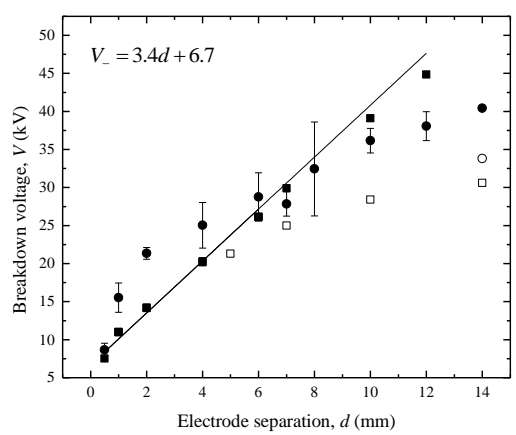
(c) 0.2 MPa



(d) 0.25 MPa



(e) 0.3 MPa



(f) 0.35 MPa

- Positive energisation breakdown voltage, V_+
- Negative energisation breakdown voltage, V_-
- Positive energisation corona inception voltage
- Negative energisation corona inception voltage

Point electrode radius – 0.8 mm.
Gas – bottled air (~20°C, 12.5%rh).

Figure 5.11 Breakdown voltage of a point-plane topology as a function of electrode separation.

As shown in Figure 5.11, the 0.8 mm radius of the tungsten rod doesn't create an intensive electric field at its tip compared to the sharper electrodes; the breakdown voltage is higher and the effects of space charge are reduced. The negative breakdown voltage of the 0.067 mm and the 0.038 mm electrode systems are ~30% lower at 0.1 MPa and ~60% lower at 0.35 MPa. Negative breakdown voltage increases linearly with increasing electrode separation with low standard deviations of below 0.03 kV. In contrast, the positive breakdown voltage increases non-linearly as the breakdown voltage is increased. This is different to what was observed with the sharper electrodes, Figure 5.7. With the sharper electrodes, positive breakdown voltage mostly increased linearly with electrode separation. However, in these graphs the positive-negative energisation breakdown voltage convergence was short, and the linear sections occurring far above the critical gap. With the 0.8 mm point electrode, the critical gap is much larger and as such the breakdowns are often occurring before the intersection point.

Below the critical gap, it can be seen that the breakdown voltage is not linear with pressure; clearly starting with breakdown voltage close to negative energisation, positive breakdown voltage increases before reducing back to be similar with negative energisation around the critical gap. As the gap is increased further the positive and negative breakdown voltage, at low pressure ~0.1 MPa, remain at similar levels for a small range of pressures before separating at the critical gap. After the critical gap, it is expected that positive breakdown voltage will increase linearly as in the case of the 0.067 mm radius point electrode, Figure 5.7, and the 0.038 mm radius gramophone needle, Figure 5.12. However, it can be seen in some of the sharper electrodes breakdown results that there is a slight increase in positive breakdown voltage.

The critical gap of the 0.8 mm electrode is much larger than the sharper electrodes and, as such, it was required to increase the range of electrode gaps. However, the test cell design can only increase the gap to 10 mm while remaining within the rule that the diameter of the plane is 4 times the gap. This helps to reduce the fringing effects of the plane edges. To achieve separation between positive and negative energisation for 0.8 mm, it was required to increase the gap beyond the 10 mm limit.

It was not possible to fit the positive breakdown voltage data with a straight line and, so to find the critical gap, the data had to be manually measured. Figure 5.11 shows the breakdown voltage for positive and negative energisation in air for a 0.8 mm radius tungsten rod as a less sharp alternative to the already discussed 0.067 mm radius sharpened tungsten

rod. Next, breakdown voltages in the case of a sharper 0.038 mm radius soft-tone gramophone needle were investigated, Figure 5.12.

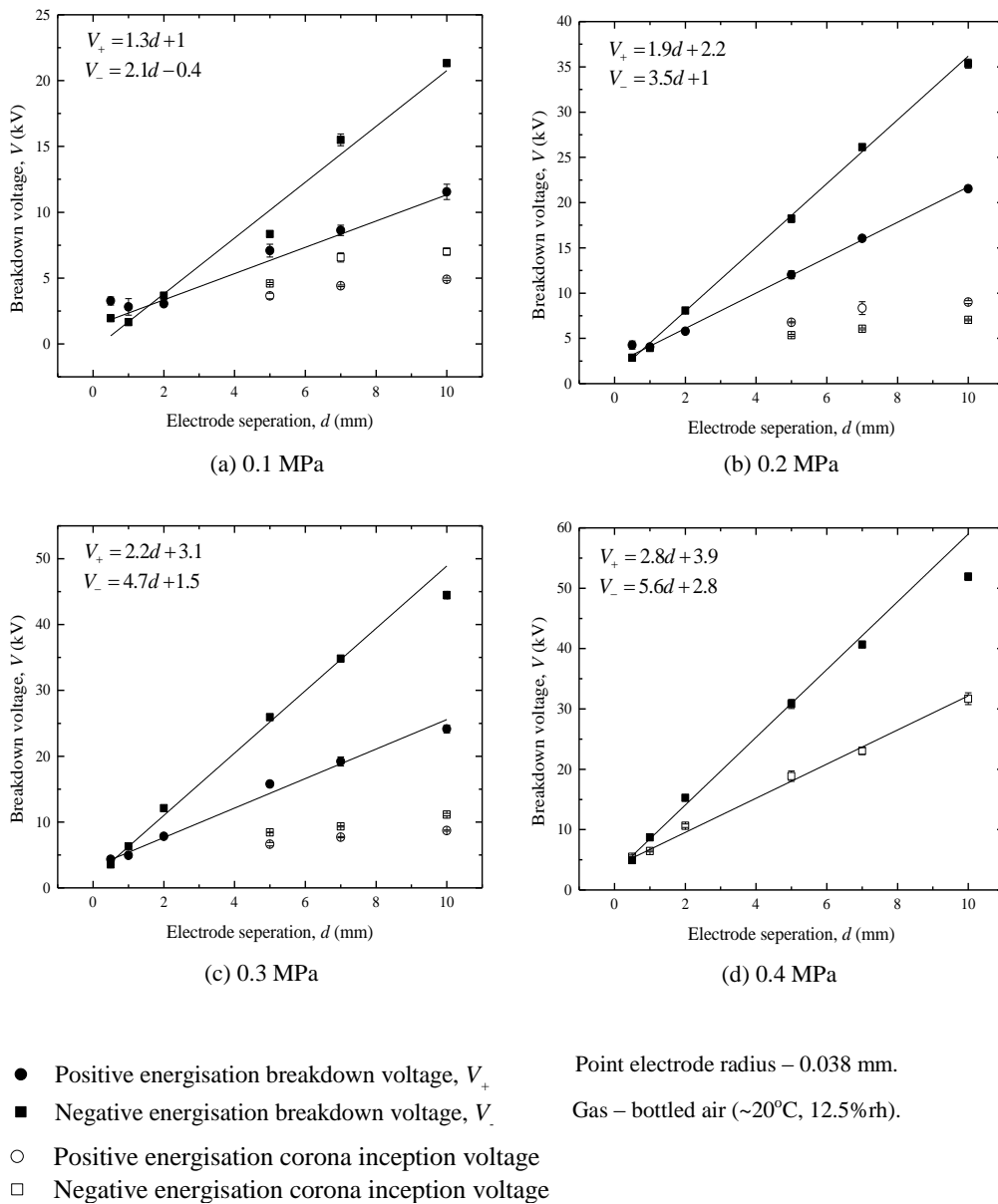


Figure 5.12 Breakdown voltage of a point-plane topology as a function of electrode separation for a 0.038 mm radius point electrode.

It was decided that it would be interesting to consider the effects of a sharper electrode than already used; the soft-tone gramophone needle was the perfect option. Gramophone needles have many advantages for use in spark switches because they have a very consistent and smooth tip with sharp radius of 0.038 mm. The investigation of the gramophone needle was done at increments of 0.1 MPa as it was decided that the 0.05 MPa increments were

superfluous to the requirement. It was found that the breakdown voltage could be again separated into two sections around the critical gap. At the shortest gaps, the breakdown voltage was higher or similar to the negative breakdown voltage. For electrode separations greater than the critical gap, positive breakdown voltage was lower than negative.

Both positive and negative breakdown voltage increases linearly with respect to increasing the electrode separation at gaps larger than the critical gap. Using a line of best fit, the intersection point between positive and negative energisation was found and the critical gap calculated. Figure 5.13 shows the critical electrode gaps as a function of the applied pressure for all three point electrodes in bottled air.

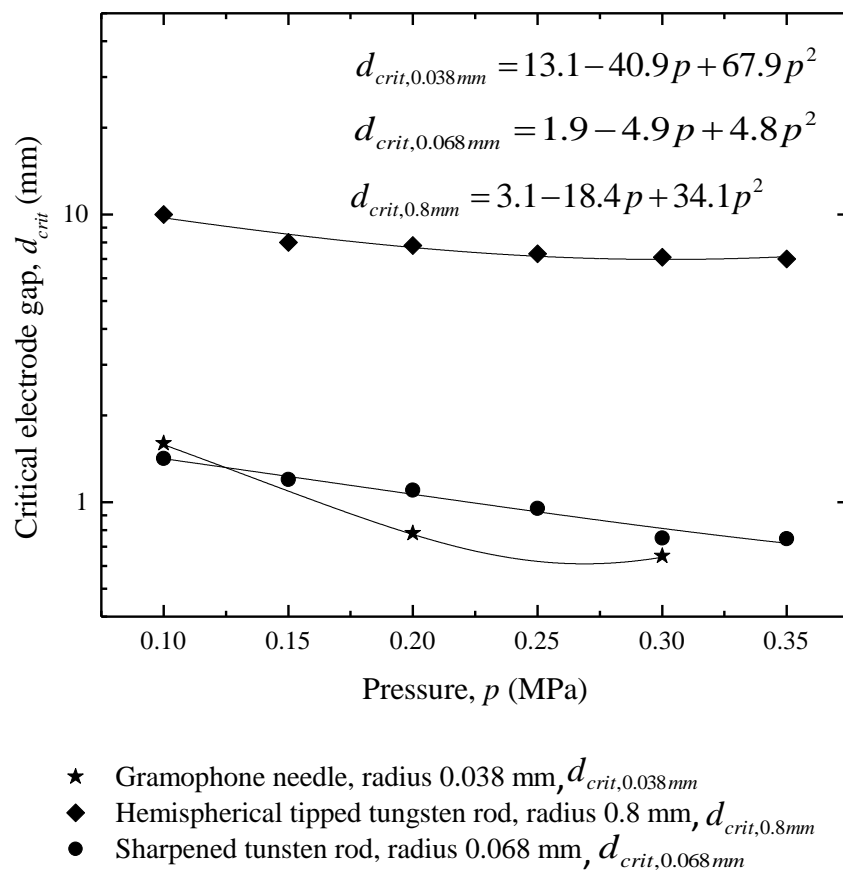


Figure 5.13 Critical gap as a function of pressure and point radius.

The observed values of the critical gap, d_{crit} , depend on the pressure of the gas in the gap and the radius of the electrode tip; the critical gaps were plotted as functions of air pressure for all 3 electrodes (Figure 5.13). Empirical fit lines were obtained using OriginPro 9.0 graphing software. These empirical fit equations are included in Figure 5.13 and they allow prediction of critical length to be made in the gas pressure range from 0.1 MPa to 0.35 MPa. As the pressure is increased, d_{crit} becomes smaller. The critical gap for the 0.8 mm radius point

electrode reduces from ~10 mm at atmospheric pressure down to ~8 mm at 0.15 MPa, a 20% reduction in critical gap with an increase of pressure of 0.05 MPa. However, with further increase in pressure, up to 0.2 MPa, the reduction in d_{crit} is smaller ~2.5%. This trend continues and d_{crit} appears to reach a constant value for higher pressures around 0.35 MPa. The critical gaps for the gramophone needle and sharp point tungsten electrode (radius 0.068 mm) were similar to each other and significantly smaller than the critical gap for the 0.8 mm radius point electrode. However, the same trend in reduction of the critical gap for both of these sharp electrodes was observed: for gramophone needles, the gap reduces by 51% from 1.6 mm to 0.78 mm, with an increase from 0.1 MPa to 0.2 MPa. Table 5.1 shows the critical gaps of 0.1 MPa bottled air with critical gaps extrapolated from literature data.

Table 5.1 Comparison of critical distance results and literature data.

Authors	Electrode radius	Critical distance
	0.036 mm	1.6 mm
	0.067 mm	1.4 mm
	0.8 mm	10 mm
[Kara 2010]	1 mm	7 mm
[Meek1953]	2 mm	~25 mm
[Isa 1991]	2 mm	~24.4 mm

The results achieved in this investigation are in line with data available from literature, Table 5.1. Using data taken from literature, the critical gap has been calculated for comparison. At atmospheric pressure, the critical electrode gaps were found for point radii of 0.8 mm, 0.067 mm and 0.038 mm to be 10 mm, 1.4 mm and 1.6 mm respectively. It was calculated that data from Strigel and Uhlmann found critical gap of ~8 mm but there is no explanation of the exact radius of the points [Strigel 1939][Uhlmann 1929]. Meek and Craggs present data for a hemispherical tipped rod with radius of 2 mm and the measured critical electrode gap is ~25 mm [Meek 1953]. Given that, for a 0.8 mm radius point, the critical gap was 10 mm, a ~25 mm critical gap for a 2 mm gap is consistent with the results found in this investigation. Isa *et. al* also published positive and negative breakdown voltage for a 2 mm radius point electrode where the critical gap has been measured as ~24.4 mm

[Isa 1991]. A 1 mm radius point was used by Kara *et. al* which, when re-plotted, gives a critical gaps of ~ 7 mm [Kara 2010]. The results obtained in this research confirm the extrapolated critical gap taken from literature data.

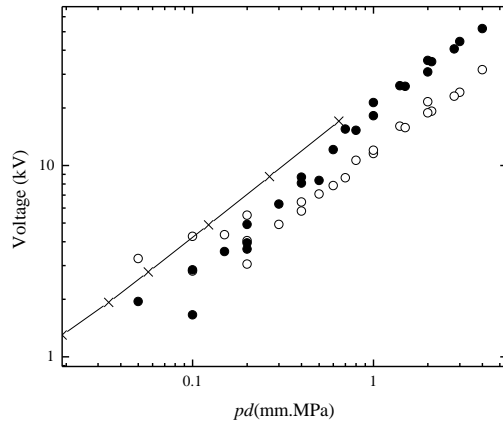
For the range of point electrodes discussed here, it is suggested that there is a critical gap at which a spark switch could be designed to have equal breakdown voltages for positive and negative energisation. However, there are limitations to how this could be scaled to larger radii points. For instance, using data published by Arora and Mosch in which long air gaps up to 2.5 m were evaluated and the extrapolated critical gap would be -14.3 cm which suggests that a critical electrode separation cannot be extrapolated to all electrode gaps and point electrodes, no information on the point radius was given [Arora 2012].

5.2.4 Analysis of Paschen Characteristics of Spark Switches Filled with Air

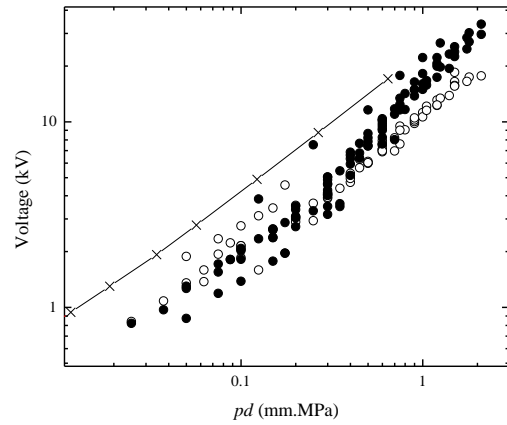
It is common, in gas discharge switches, to display the breakdown voltage as a function of the product of gas pressure and inter-electrode separation, pd . The breakdown voltage of uniform field topologies can be predicted given the inter-electrode gap and gas pressure using Paschen's Law.

While Paschen's Law cannot be used to determine the breakdown voltage of non-uniform topologies, it can be used for a comparison. Figure 5.14 shows the breakdown voltage of the non-uniform point-plane topologies alongside a known Paschen curve from literature.

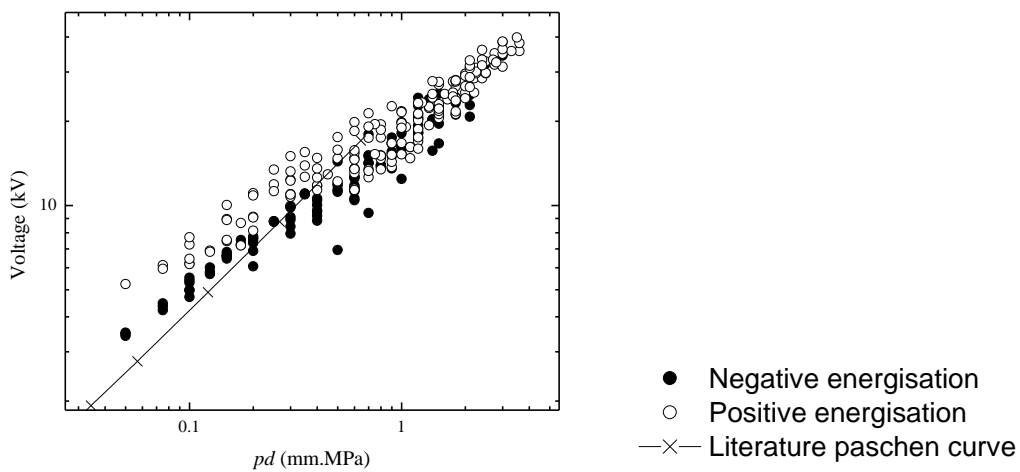
The breakdown voltages in non-uniform topologies obtained in the present study were also plotted as $V_{br}(pd)$ functions for all pressures and electrode radii. Figure 5.14 shows the obtained breakdown voltages of each of the three electrodes as a function of the product of pressure and distance (pd) alongside the right branch of conventional Paschen breakdown curve (at values of pd above the Paschen minimum). Conventional Paschen data for air were taken from the literature, [Brown 1966] in order to compare the results obtained in the present paper with already published $V_{br}(pd)$ data.



(a) 0.036 mm radius gramophone needle



(b) 0.068 mm radius gramophone needle



(c) 0.8 mm radius hemispherical tipped rod

Figure 5.14 Breakdown voltage with Paschen curve from literature [Brown 1966]. Individual breakdown voltages were plotted.

Figure 5.14 shows that, the data obtained in the present work closely follows the conventional Paschen's law, and there is a strong scaling tendency for breakdown voltages in highly divergent electric fields which can be utilised in the design of plasma closing switches and other component parts of compact high-voltage systems.

5.2.5 Conclusions

This chapter presents the results into investigation of the breakdown voltages in the point-plane topology filled with air, nitrogen and a 60%/40% nitrogen/oxygen mixture using a single point HV electrode. Breakdown voltages for the three different point electrodes: a 0.036 mm sharpened tungsten rod; a 0.068 mm soft-tone gramophone needle; and a 0.8 mm hemispherical tipped tungsten rod were then compared. It was found that the breakdown

voltage for positive and negative energisation converged to be similar in magnitude as pressure and distance between the electrodes change. The electrode separation, at which the convergence occurred, the critical electrode gap, was identified. It was found that the critical gap was directly impacted by the gas type, pressure and point electrode radius.

The different gases were compared using a 0.068 mm radius point electrode; it was found that air and nitrogen/oxygen mixture provided similar, predictable, relationships with respect to electrode separation. The critical electrode gap for these two gases was similar, starting with a larger critical gap, but with higher pressures having a lower critical gap. The critical gap for air and the mixture at 0.1 MPa is ~1.4 mm and ~2.5 mm respectively. At 0.35 MPa, the mixture has a lower critical gap of ~0.39 mm compared to ~0.74 mm in air. It was found that, in nitrogen, the negative breakdown was unstable and was deemed not suitable for use in non-uniform spark switches. Having compared the 3 insulating gases: air, nitrogen, and the 60%/40% nitrogen/oxygen mixture it was established that for further experiments, nitrogen was not a usable gas with non-uniform field topologies and the nitrogen/oxygen mixture showed no improvement over air. Therefore, air was chosen to the insulating gas for all further investigations. In this research, normal atmospheric air (12.5%rh), was used because it is readily available and a cheap alternative to some of the gases currently used in the pulse power industry. Dry air is often used to improve performance and would give improved performance with more repeatable results due to the lower moisture content.

Using air as the insulating gas, three point electrodes with different point-radii were tested. The two sharpest points: 0.067 mm and 0.038 mm have similar critical gaps with the sharper being just shorter at the higher pressures. The critical gap for the 0.038 mm radius point at 0.1 MPa is ~1.6 mm compared to ~1.42 mm for 0.068 mm radius point. However, at 0.3 MPa the critical gap for the sharper point is ~0.65 mm compared to ~0.95 mm for the 0.067 mm point. The largest point, 0.8 mm radius, had a much larger critical gap of ~10 mm at 0.1 MPa which reduced to ~7 mm at 0.35 MPa.

For atmospheric pressure air (0.1 MPa), the results have been confirmed with data taken from literature. Re-plotting data from literature gives critical gap for a range of point electrode radii, which are congruent with the measured results given here.

This section has looked at the breakdown voltage of point-plane gaps. To understand why there is a critical gap and why it is different for a range of pressures and point electrodes, it is necessary to investigate the pre-breakdown discharge activity (corona discharge) in the plasma closing switches.

6. CHARACTERISATION OF CORONA DISCHARGES IN SPARK SWITCHES

Corona discharge is used in the switch topologies developed in this research project in order to improve operational characteristics of plasma closing switches. Therefore, it is vital to understand the development of corona discharges and to characterise their influence on operation of gas-filled switches, in which this discharge takes place, before complete closure (breakdown) of the switch. In this sense, corona discharge is a pre-breakdown discharge occurring in localised intensive fields in the vicinity of sharp electrodes produced, for example, by point-plane and co-axial topologies [Kuffel 2000]. Ionisations and discharge processes are initiated in the high field regions where the electric field exceeds the critical ionisation threshold. However, as the electric field reduces rapidly away from the HV sharp electrode, corona discharge does not develop into sparks because the electric field reduces below the level capable of sustaining the ionisation in the whole inter-electrode gap [Kuffel 2000]. Corona discharge can be characterised by a localised ionisation zone which can be present as a faint to bright glow radiating from a focal, initiation point [Loeb 1939] and a transport zone, the zone through which ions travel to the opposite electrode. Corona discharge is of particular interest to the power and pulsed power industry and environmental/biological applications.

In the power industry, corona discharge is usually avoided because it can have many negative effects on transmission of power. Power transmission cables have localised intensive fields which can initiate corona discharge resulting in losses and degradation of cable insulation and corrosion of electrodes.

Corona discharge is also utilised in the environmental applications such as sterilisation and water purification [Wang 2012][Li 2013]. By-products of corona discharge such as ozone and oxygen radicals can kill some bacteria, especially when used in conjunction with surfaces impregnated with oxidising agents such as titanium dioxide. Corona discharge can

also be used in water purification where oxygen radicals and ozone are passed through and over the water.

Corona discharges are usually avoided in HV systems such as transmission lines, HV terminals of pulse generators etc.. However, corona discharges are utilised in corona stabilised spark switches used in high repetition rate pulse power systems. Corona discharges were used to increase the performance of high repetition rate plasma closing switches: to delay breakdown allowing voltage to recover which resulted in reduced pre-fire rate (probability) and ultimately leads to higher repetition rates [Tuema 1999][Beveridge 2008]. It is hypothesised, that the corona discharge could be used to improve the performance of spark switches, in terms of standard deviation of self-breakdown voltage, time delay to breakdown and jitter [Frey 2009]. Usually, point electrodes are introduced into switch topologies in order to promote the development of corona discharge before switch closure.

As shown in Chapter 2 of this thesis, breakdown voltages in the point-plane topology are significantly impacted by pre-breakdown corona discharge. Therefore, in order to optimise the operational performance of the switch equipped with the point-plane topology, it is necessary to investigate corona discharge characteristics in this topology filled with gases used in the present study. Results from this investigation were published in the IEEE Transaction on Dielectric and Electrical Insulation [Hogg 2015].

This section reports on the results of investigation of the pre-breakdown corona activity in the point-plane topologies. Point-plane topologies create very intensive electric fields, ideal for developing corona discharge [Coelho and Debeau 1971]. Corona discharges in air filled point-plane gaps, energised by positive and negative voltages, were investigated and their volt-current characteristic obtained. Corona discharges were investigated at a range of inter-electrode gaps, using 3 point electrodes and filled with air between 0.1 MPa and 0.35 MPa. A 100 k Ω shunt resistor was placed between the switch and ground connection to measure corona discharge current. The corona discharge analysis circuit is shown in Section 3.3.

To measure DC breakdown voltage and $V-I$ corona characteristics, high voltage DC stresses of both polarities were used to energise the point electrode with steadily increasing voltage until breakdown occurred. Figure 3.7 shows the experimental design where a Glassman HVDC power supply (EH series 0-60 kV) provided up to 60 kV to the point electrode via a 1 M Ω charging resistor. The output voltage of the HVDC supply increased at a stepped rate of 370 V/150 ms until breakdown occurred. The voltage increase was controlled via a LabVIEW program interfacing with a National Instruments DAQ (USB6008). Figure 6.1 and

Figure 6.2 show example waveforms of positive and negative breakdowns, indicating breakdown and corona inception. The corona inception voltage was measured by plotting the voltage and current waveforms and visually identifying the initial rise of current due to corona discharge and measuring the voltage. This was decided to be the best method as the signal to noise ratio meant an analytical approach wouldn't give accurate results. This approach was validated by optical emission measurements using photomultipliers.

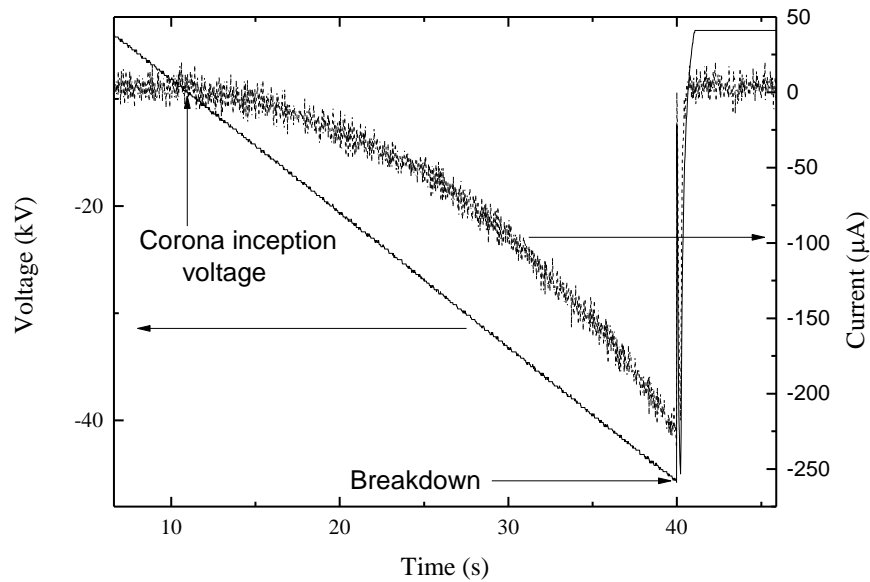


Figure 6.1 Example waveforms of DC self-breakdown voltage and current signals, showing breakdown and corona initiation. Point radius, - 0.036 mm; gap - 10 mm; 0.3 MPa air.

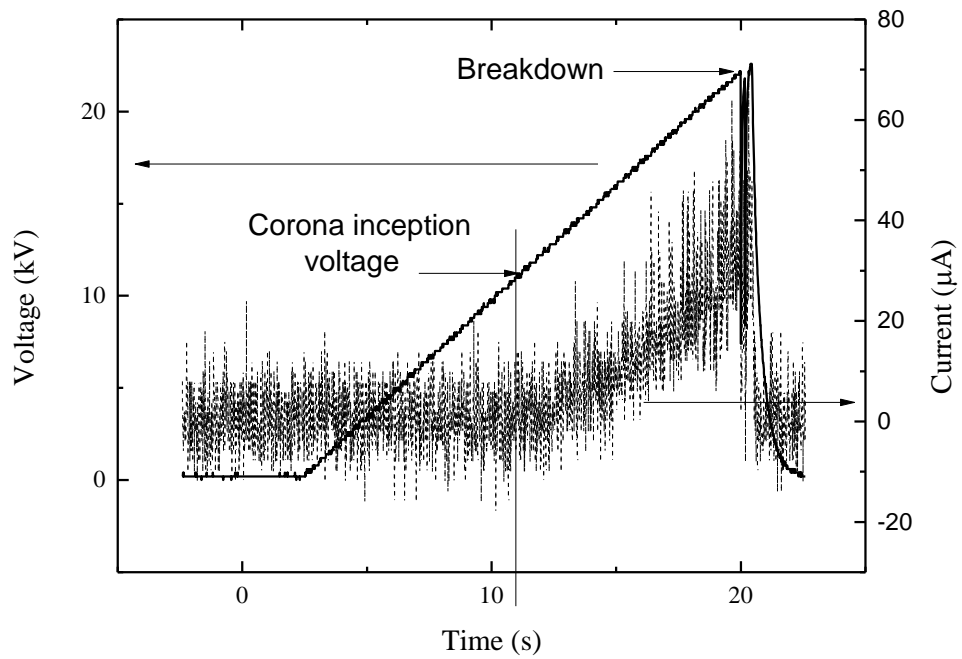


Figure 6.2 Example waveforms of positively energised DC self-breakdown voltage and current signals, showing breakdown and corona initiation of a point-plane topology. Point radius, - 0.036 mm; gap - 10 mm; 0.3 MPa air.

A specially designed corona measurement test cell with inter-changeable point and plane electrodes with variable gaps was developed to measure corona inception voltage. The test cell is a hollow cylindrical black PVC with one open end and a quartz window on the side. A PVC end piece was secured by 6 bolts. Using specially designed brass blocks, the point and plane electrodes could be secured to the top and bottom of the test cell and allow connection to HV and ground. The plane electrode was raised and lowered using spacers to set the inter-electrode gap.

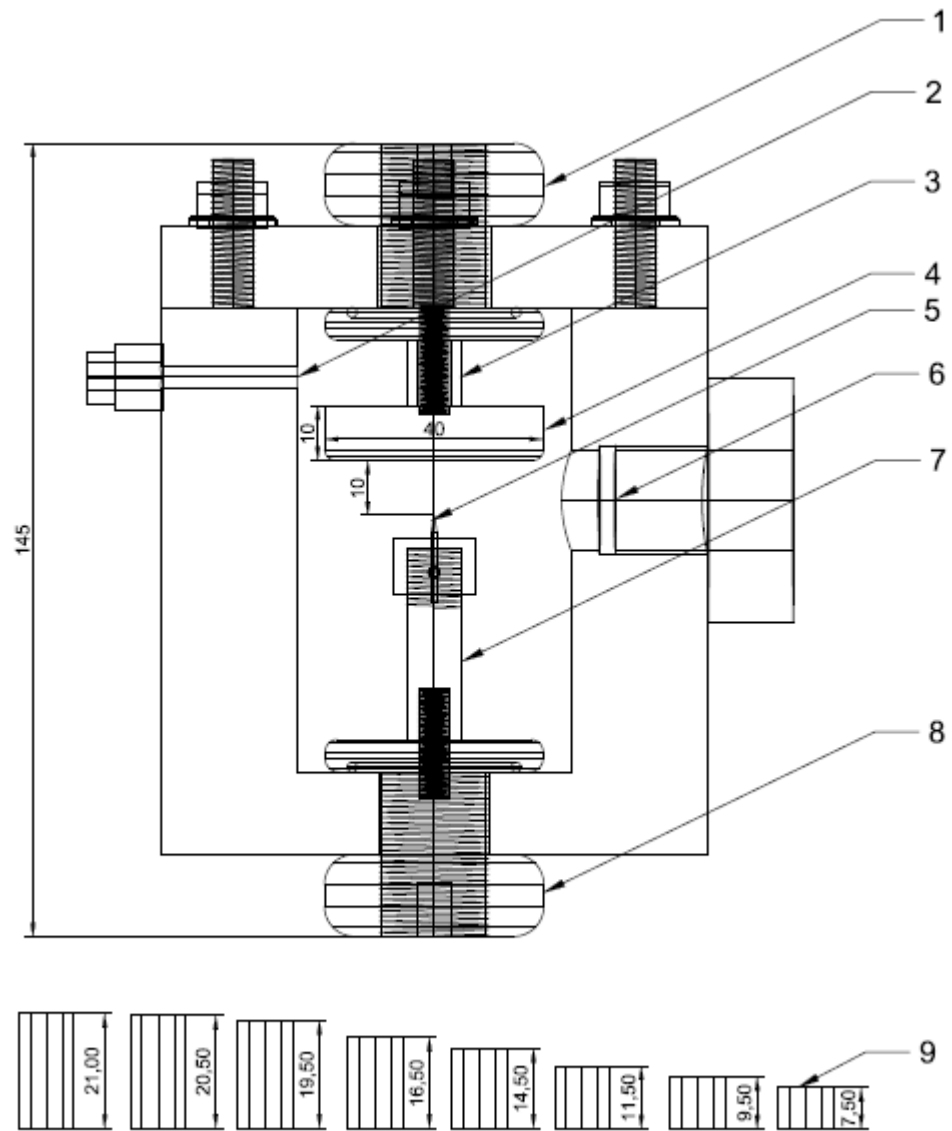


Figure 6.3 Corona observation, point-plane test cell with quartz window and inter-changeable electrodes
 1 - Ground connection, 2 - Gas inlet, 3 - Gap setting spacer (10 mm gap), 4 - Plane electrode, 5 - Point-electrode, 6 - Quartz window, 7 - Point electrode holder, 8 - HV connection, 9 - Gap setting spacer set.



Figure 6.4 Corona observation test cell.

The point electrodes each had a specifically designed holder such that when complete they each were the same length from tip of point to the base of the electrode holder. The electrode and holder could then be secured to one end of the test cell. The 3 electrodes used were:

1. Soft-tone gramophone needle, radius 0.036 mm;
2. Sharpened tungsten rod, radius 0.068 mm;
3. Hemispherical tipped tungsten rod, radius 0.8 mm.

The plane electrode was machined brass with a diameter of 50 mm and flat polished top and rounded edges. The plane electrode was designed to have a radius twice as large as the largest gap.

The quartz window in the body of the test cell was used to monitor corona discharges optically, a fibre optic was attached to the quartz window and a photomultiplier unit (Hamamatsu H10721 PMT, rise time of 0.5 ns) was used to monitor optical signals generated by corona discharges. Simultaneously, the current and voltage waveforms were measured and the current waveforms obtained using the current viewing resistor. Optical and current signals proved to have strong correlation, showing a light intensity increase as corona current is increased.

In Section 6.1, the corona discharge inception voltage with respect to air pressure and then by inter-electrode gap will be discussed. Then the voltage-current relationships are analysed and mobility of charge carriers in corona discharge obtained from $V-I$ characteristics.

6.1 CORONA DISCHARGE INCEPTION VOLTAGE

In this section, corona discharge inception voltages were determined in order to correlate corona-induced space charge effects with the breakdown voltage. Figure 6.5 shows the corona discharge inception voltage as a function of gas (air) pressure. Each data point in this chapter is an average of 10 measurements; the test cell was filled with fresh air before each series of measurements which were performed without changing the gas in the test system. The error bars in Figure 6.5 show the standard deviation of corona inception voltages. In the following sections, the results are fitted with empirical fittings. These fittings are only valid for the experimental conditions used in this research.

A large amount of work has been completed on corona inception voltage in the literature [Peek 1915][Loeb 1939]. However, most of the analytical formulas, such as proposed by Peek [Peek 1915], are not directly applicable to point-plane topologies. It was therefore important that a standalone study was conducted. The results here do not follow the simplified models that are used by Peek and as such an empirical fitting procedure was used to fit the experimental points with linear empirical functions using OriginPro 9.0 software package (Figure 6.5). The empirical equations with corresponding coefficients describe these linear fit lines with breakdown voltage, V_{br} (kV) as a function of pressure, p (MPa):

$$V_{br} = Ap + B \quad (6.1)$$

where A (kV/MPa) and B (kV) are fitting coefficients, given in these figures for each combination of polarity of the applied voltage and the presence and absence of the corona electrodes. These coefficients are given in Figure 6.5.

From the corona inception voltage graphs (Figure 6.5) the following conclusions can be drawn:

- the relationship of corona to pressure for different point radii,
- the effect of changing the electrode gap on the relationship of corona inception voltage with pressure,
- the difference between positive and negative energisation on the corona inception voltage,
- if corona is present before breakdown depending on electrode gap and pressure.

As can be seen in Figure 6.5, the voltage at which corona initiates for both positive and negative energisation is linearly proportional to the air pressure. The gradient coefficient for the linearity is dependent on: the radius of the point electrode; the inter-electrode gap; and the polarity of applied voltage. The rate of rise of the corona discharge inception voltage (the gradient of the linear empirical fit lines) is lower for the sharper points, ~ 23 kV/Pa and ~ 19 kV/Pa for 0.068 mm and 0.036 mm radius respectively in a 10 mm negatively energised gap. With the larger radius of the HV needle, the rate of rise (the slope of the empirical fit lines) has ~ 4 -fold increase at ~ 72 kV/Pa with a 10 mm gap. Therefore, the dependence of corona inception voltage on pressure is much stronger in the case of larger radius points, and there is a strong chance of the development of complete spark breakdown in the switch without appearance of pre-breakdown corona discharge at higher pressures for the inter-electrode gaps investigated in this thesis.

It is more useful to investigate the dependence of corona inception voltage on the inter-electrode distance by re-plotting the corona inception voltage as a function of electrode separation. Figure 6.6 to Figure 6.8 display the corona inception voltage as a function of inter-electrode spacing and will be discussed collectively. As in Figure 6.5, the analytical formulae proposed in literature are not directly applicable to point-plane topologies and results here do not follow the simplified models that are used by Peek and as such an empirical fitting procedure was used to fit the experimental points.

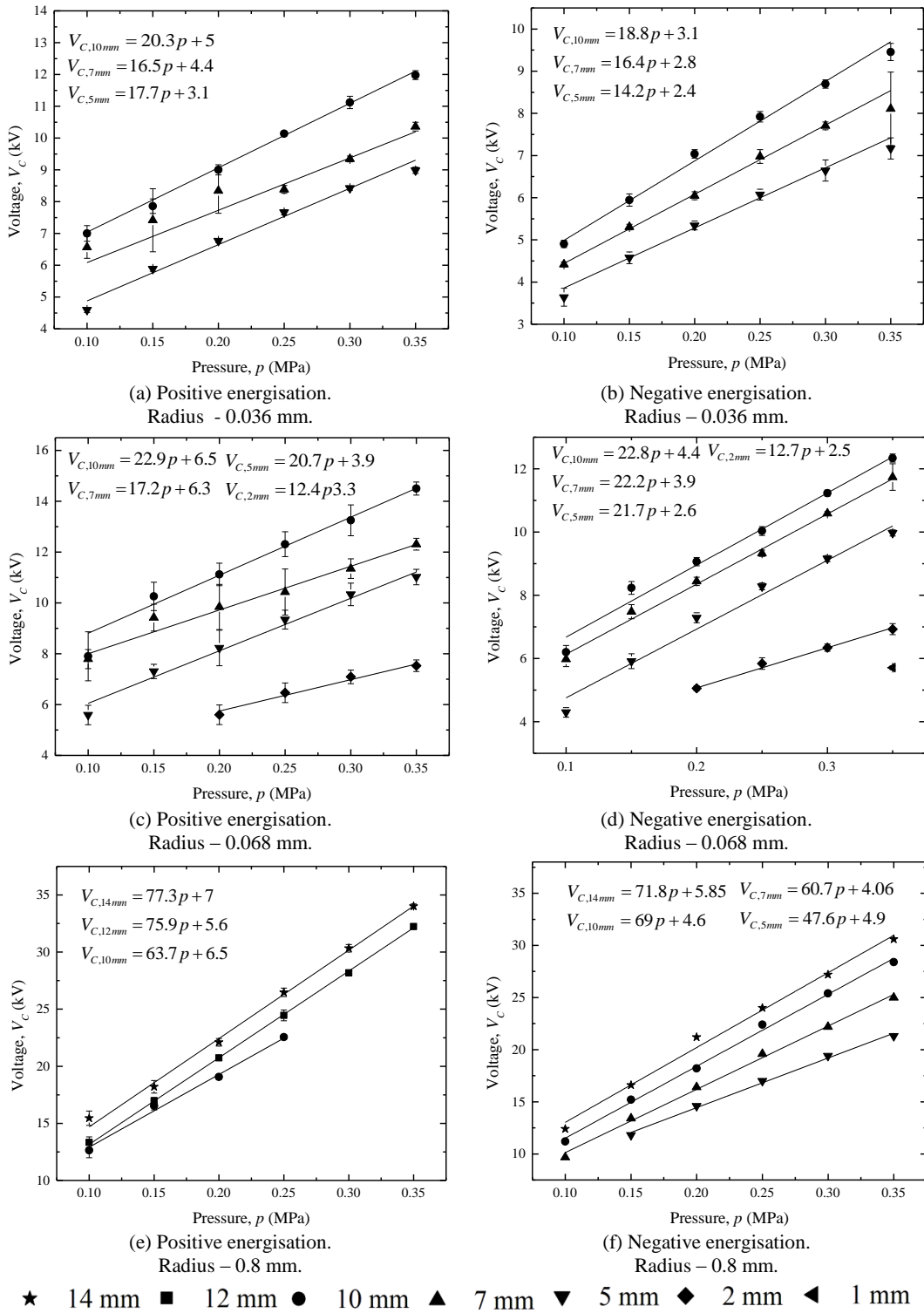


Figure 6.5 Corona inception voltage in point-plane topologies as a function of air pressure.

Each graph displays the data for pressure range 0.1 - 0.35 MPa and has been fitted with empirical allometric lines of best fit because it provided a simplistic, reasonable fit to the majority of the data (which was conducted using OriginPro 9.0 software package):

$$V_C = Ad^B \quad (6.2)$$

where A and B are coefficients of fitting, V_C (kV) is the corona inception voltage, and d (mm) is the inter-electrode gap. Table 6.1 - Table 6.3 display the coefficients A and B for 0.036 mm, 0.068 mm and 0.8 mm radius points respectively.

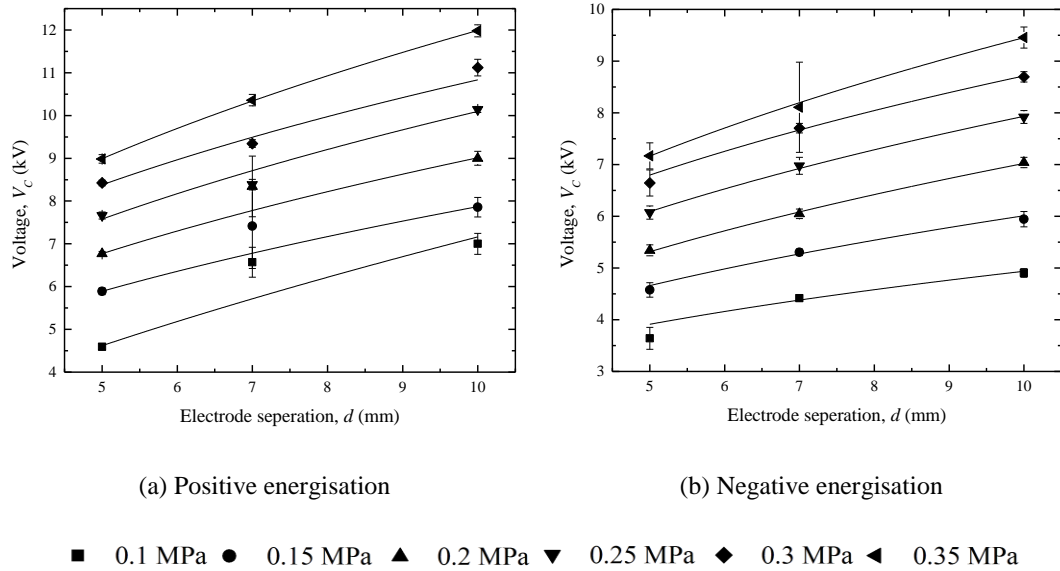


Figure 6.6 Corona inception voltage in a point-plane topology as a function of electrode separation. Point electrode - 0.036 mm soft-tone gramophone needle.

Table 6.1 Allometric fitting coefficients for corona inception voltage with a 0.036 mm radius point, Figure 6.6.

Pressure MPa	Negative energisation		Positive energisation	
	A	B	A	B
0.1	1.7	0.63	2.3	0.34
0.15	3	0.42	2.6	0.37
0.2	3.5	0.41	2.8	0.4
0.25	3.9	0.41	3.2	0.38
0.3	4.6	0.37	3.8	0.36
0.35	4.6	0.41	3.8	0.4

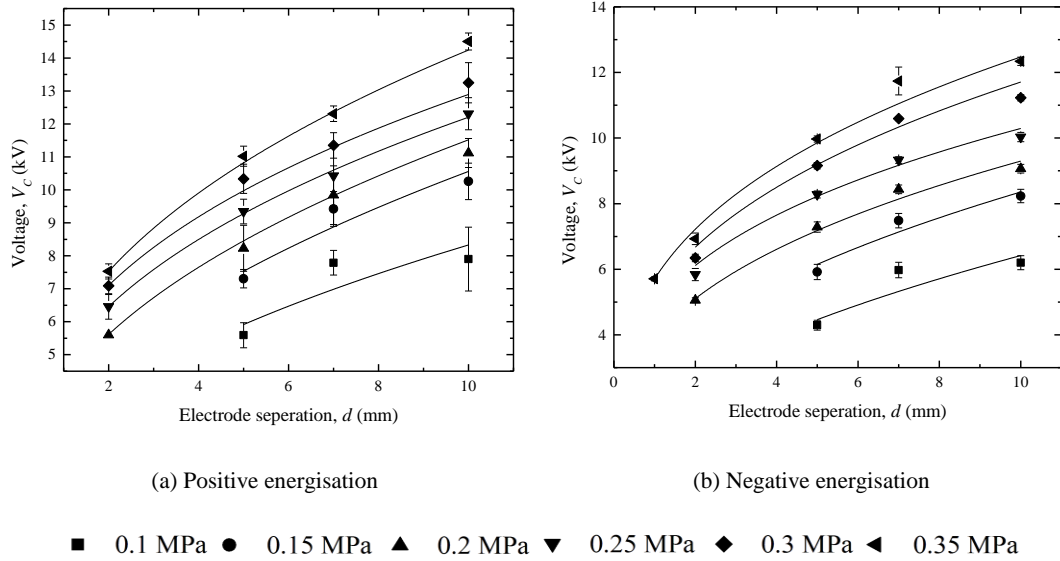
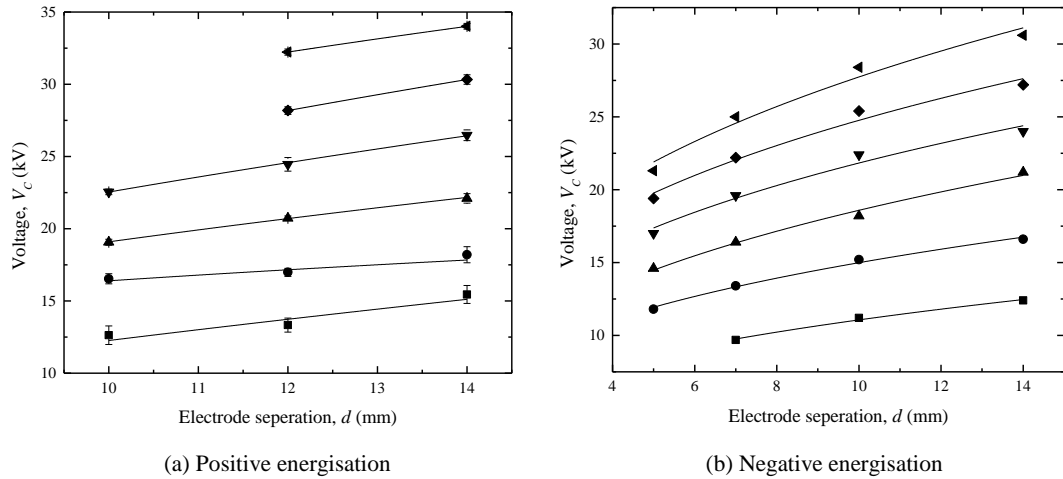


Figure 6.7 Corona inception voltage in a point-plane topology as a function of electrode separation. Point electrode - 0.068 mm sharpened tungsten rod.

Table 6.2 Allometric fitting coefficients for corona discharge inception voltage for a 0.068 mm radius point, Figure 6.7.

Pressure MPa	Positive energisation		Negative energisation	
	A	B	A	B
0.1	2.7	0.49	1.9	0.52
0.15	3.4	0.49	3	0.44
0.2	4.1	0.45	3.9	0.37
0.25	4.9	0.39	4.9	0.32
0.3	5.5	0.37	5.2	0.35
0.35	5.7	0.4	5.7	0.34



■ 0.1 MPa ● 0.15 MPa ▲ 0.2 MPa ▼ 0.25 MPa ◆ 0.3 MPa ◀ 0.35 MPa
 Figure 6.8 Corona inception voltage in a point-plane topology as a function of electrode separation. Point electrode - 0.8 mm sharpened tungsten rod.

Table 6.3 Allometric fitting coefficients for corona discharge inception voltage for a 0.8 mm radius point, Figure 6.8.

Pressure MPa	Positive energisation		Negative energisation	
	A	B	A	B
0.1	2.9	0.6	4.9	0.35
0.15	9.2	0.24	7	0.3
0.2	6.9	0.44	8.1	0.36
0.25	7.6	0.47	10.2	0.33
0.3	8.6	0.48	11.7	0.32
0.35	13.5	0.35	12.7	0.34

The empirical fit applied to the corona inception voltage, Figure 6.6 to Figure 6.8, provided a reasonable fit. Due to the stochastic nature of gas discharge, there are data points that do not match up with the best fit empirical line and some data points have large standard deviations. However, the fitting coefficients give reasonable likeness to the trend of the majority of the data. Figure 6.6 to Figure 6.8, show that the corona inception voltage can be reasonably

Table 6.4 Linear fitting of the allometric coefficient ‘A’ with regards to pressure.

Point radius	Gradient, m		Y Intercept, c	
	Positive energisation	Negative energisation	Positive energisation	Negative energisation
0.036 mm	11.3	6.6	1	1.6
0.068 mm	12.6	15.2	1.5	0.68
0.8 mm	19.7	31.5	1.4	2

The effect of increasing the electrode gap on the corona inception voltage depends on the polarity of energisation. Using an allometric fitting function, it can be seen in Table 6.1 – Table 6.3, the power fittings, B , are virtually constant as the electrode gap is increased for each point radius. Figure 6.9 shows a plot of the fitting coefficients as a function of pressure where it can be seen that the B coefficient is mostly unaffected by pressure. From 0.1 MPa to 0.15 MPa, there is a slight reduction of ~ 0.2 for the B coefficient for both positive and negative energisation. Thereafter, the B coefficient remains quasi-constant at ~ 0.37 for negative energisation. The B coefficient is slightly higher for positive energisation in most cases at ~ 0.45 across all pressures.

The A fitting coefficient increased linearly as the pressure was increased, Figure 6.9. Fitting the A coefficient with a linear line of best fit, the A coefficient largely defines the magnitude of the corona inception voltage and it can be seen in Figure 6.9, with the increasing point radii, the gradient of A coefficient increases proportionally. Table 6.4 gives the linear fitting coefficients for A and B with respect to pressure where, as the point radius is increased from 0.036 mm to 0.068 mm, the gradient increases from 11.3 to 12.6 which increases further to 19.7 for positive energisation. For negative energisation, the gradient increases similarly from 6.6 to 15.2 and up to 31.5 as the radius is increased from 0.036 mm to 0.068 mm and 0.8 mm. The higher gradients describe the higher corona discharge inception voltages of the less sharp electrodes.

An important factor of pre-breakdown corona is the corona inception voltage (voltage at which it occurs) with respect to the energisation polarity. Corona discharge initiating at lower voltages results in more corona activity before complete (spark) breakdown in the switch. By plotting the corona inception voltage for both positive and negative energisation

together with the spark breakdown voltage, the difference between positive and negative energisation can be established with reference to breakdown voltage, Figure 6.6 - Figure 6.8. Negative corona initiates at consistently lower voltages than positive corona in the same electrode configuration and at the same gas pressure. At shorter gap intervals, 2 mm, positive corona inception voltage is 18-30% higher than negative corona inception for the point electrode with 0.068 mm radius. In the case of the 0.8 mm radius point HV electrode, positive corona inception voltage is ~42% lower than the negative corona inception voltage at 0.1 MPa, positive inception voltage becomes ~22% lower than the negative inception voltage at 0.15 MPa. However, at higher pressures, 0.3 - 0.35 MPa, positive corona inception voltage is ~10-12% higher than the negative corona inception voltage. In most cases, positive corona discharges initiates at higher voltages than negative corona discharges.

6.1.1.1 Conclusions on investigation of corona inception voltages

Comparing the positive and negative corona inception voltages is required to explain the discrepancy between the complete (spark) breakdown voltages in air in the point-plane topology. However, there is not such a significant difference in positive and negative corona inception voltages as in the case of the positive and negative spark breakdown voltages. In the case of shorter gaps, spark breakdown can occur without appearance of corona discharge. Moreover, in the range of combination of pressure and distances where the breakdown voltage between positive and negative energisation becomes different (for distances above the critical gap d_{crit} , Section 5), corona discharge is not always present before breakdown.

The appearance of corona discharge is dependent on the radius of the point electrode, the air pressure and the electrode separation. Figure 6.5 displays the corona inception voltage as a function of pressure, distance, and polarity where it can be seen there is no corona at some low pressure or short gaps. The conditions where corona discharge occurs prior to complete breakdown depend on applied voltage polarity, gas pressure, and the radius of the point electrode.

In the present experiments, it was found that at shorter gaps (depending on pressure and electrode radius), there was no detectable pre-breakdown current that would be indicative of intensive corona discharge for either positive or negative energisation. For example, in the case of the 0.036 mm radius HV electrode (Figure 6.6), there was no corona discharge at 0.5 mm inter-electrode spacing for pressures equal to and below 0.2 MPa.

In the cases where corona discharges appeared prior to complete breakdown, it was observed that negative energisation would produce detectable corona discharge at smaller gap spacing, whereas positive energisation lead directly to spark breakdown under similar conditions. Figure 6.6 shows corona ignition voltages (open symbols) for negative energisation starting from 1 mm, but positive energisation corona not starting until an inter-electrode spacing of 2 mm.

The probability of corona discharge appearing before complete breakdown in the switch was dependent on the air pressure in the switch. As pressure is increased, the probability that corona will precede spark breakdown increases for the sharp point electrodes. For example, at 0.1 MPa using a 0.036 mm radius HV electrode, no corona was detected for 0.5 mm, 1 mm, or 2 mm electrode gaps. At 0.35 MPa, negative energisation corona discharges precede complete breakdown in all inter-electrode gaps; corona activity starts at 2 mm for positive energisation.

The appearance of corona discharge before breakdown is also highly dependent on the radius of the point electrode. The sharper electrodes produced corona discharges prior to breakdown under both polarities of energisation for similar gap distances (1 - 4 mm). In the case of the 0.8 mm radius electrode, corona discharge before breakdown was observed for smaller gap distances (~5 mm) and for negative energisation as compared with positive energisation (~10 mm). This can clearly be seen in Figure 6.8, negative energisation corona discharge is observed before breakdown for gaps greater than 5 mm while positive energisation corona discharge is only observed for a gap of 14 mm.

6.2 VOLTAGE-CURRENT RELATIONSHIP IN POINT-PLANE TOPOLOGY

The relationship between applied voltage and the current on the plane electrode informs on the amount of charge being injected into the inter-electrode gap, and as such, the effects of corona discharge. In a parallel-plane topology, before Townsend discharge is initiated, there is a small current due to the ionisation naturally occurring in the earth's atmosphere. The ions drift to the electrodes creating a small current in order of pA. The current saturates when the charge being removed equals that created by the atmospheric ionisations. In non-uniform topologies, the intense local electric field can cause ionisations leading to ignition of corona discharge and larger current levels. The corona current provides information on the amount

of charge being injected into a switch at any given applied voltage. Therefore, the space charge effects can be inferred, which is the main factor affecting the breakdown voltage.

Using the steady rate of rise of voltage and current signal from the current viewing resistor, the relationship between the applied voltage and corona current were recorded from the inception voltage until complete breakdown. All of the $V-I$ curves can be found in Appendix 3. Example $V-I$ relationships for negative and positive energisation are shown in Figure 6.10 and Figure 6.11 respectively. The $V-I$ curves were created by taking the current waveform and plotting it as a function of the voltage waveform such as shown in Figure 6.1 and Figure 6.2. Apparent current on the $V-I$ curve when there is no voltage ($V=0$), and apparent negative current, is a result of noise on the voltage and current waveforms.

Table 6.5 and Table 6.6 show the coefficients for fitting using Equation (6.4) [Meng 2008]. The fitting procedure was conducted on the corona current (pre-breakdown current above 0 A) using OriginPro 9.0 software package:

$$I = V(V - V_0)C^* \quad (6.4)$$

where I is the corona current (μA), V_0 is a fitting constant (kV), V is the applied voltage (kV), and C is fitting coefficient ($\mu\text{A}/(\text{kV})^2$).

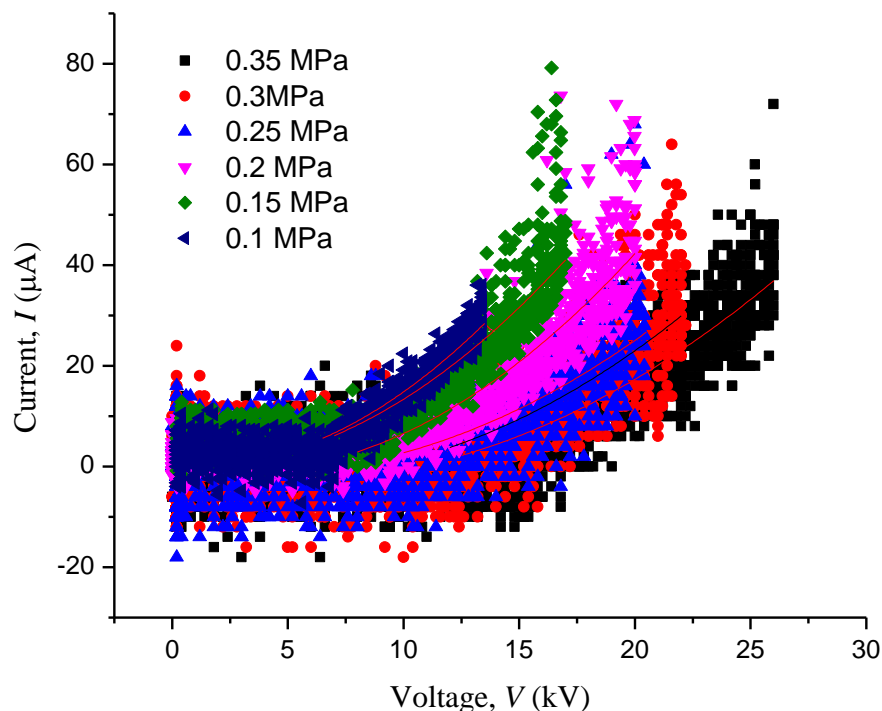


Figure 6.10 Positive energised voltage-current relationship for 10 mm gap gramophone needle, radius 0.036 mm, in air.

Table 6.5 Fitting for positive energisation corona V - I curves in Figure 6.10 using Equation (6.4).

Air pressure (MPa)	V_0 (kV)	C^* ($\mu\text{A}/(\text{kV})^2$)
0.1	1.7	0.18
0.15	1.3	0.15
0.2	5.5	0.15
0.25	7.2	0.1
0.3	9	0.1
0.35	10.6	0.09

From the V - I curves collected in the corona discharge investigation, some key differences were observed:

1. the pre-breakdown corona current was an order of magnitude higher for negative than positive energisation,
2. positive energisation corona discharge had a clear initiation, with a rapid rise in current to a few μA ,
3. negative energisation corona current increased very gradually with increasing voltage.

Much larger corona current resulted from negative energisation which is initiated at lower voltages and appears in shorter gaps and lower pressures creating a volumetric space charge that significantly screens the electric field at the point cathode. Figure 6.10 and Figure 6.11 show typical V - I curves for a 10 mm gramophone needle-plane gap in positive and negative energisation respectively.

Using the V - I curves for the point-plane topology, a greater understanding of the increased breakdown strength of the topology can be understood given the significantly increased current of the negative energisation compared to positive energisation.

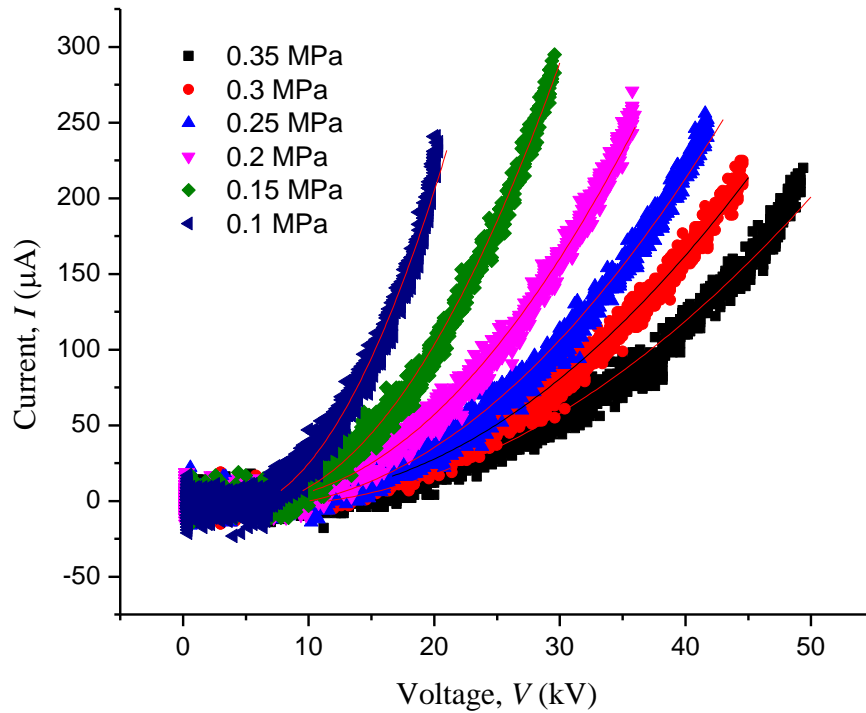


Figure 6.11 Negative energised voltage-current relationship for 10 mm gap gramophone needle, radius 0.036 mm, in air.

Table 6.6 Fitting for negative energisation corona V - I curves in Figure 6.11 using Equation (6.4).

Air pressure (MPa)	V_0 (kV)	C^* ($\mu\text{A}/(\text{kV})^2$)
0.1	7.8	0.8
0.15	9.5	0.45
0.2	10.3	0.26
0.25	10.1	1.8
0.3	12.6	0.14
0.35	11.5	0.1

These V - I curves show much larger charge injected into the point-plane gap which results in a larger space charge. To further analyse the space charge effects, finding the mobility of the charge carriers in corona discharge aids the understanding of the amount of space charge. By fitting the experimental V - I curves with empirical lines obtained using Equation (6.4), the charge carrier mobility could be extracted. The next section presents the results of investigation into the mobility of the charge carriers in corona discharges.

6.3 MOBILITY OF CHARGE CARRIERS IN CORONA DISCHARGES

Using the coefficient C^* (C when using S.I. units) from Equation (6.4), in Table 6.5 and Table 6.6 the mobility of electrons, can be approximated by:

$$\mu = \frac{Cd}{2\varepsilon_0\varepsilon_r} \quad (6.5)$$

Where μ ($\text{m}^2/\text{V}\cdot\text{s}$) is mobility, d (m) is the inter-electrode gap, ε_0 is the permittivity of free space ($\varepsilon_0 = 8.854 \times 10^{-12}$ F/m), and ε_r is the relative permittivity ($\varepsilon_r = 1$ for air).

Figure 6.12 shows the mobility of charge carriers as a function of air pressure and energisation polarity. Each point represents a mobility value extracted by fitting empirical lines (Equation (6.4)) to the experimental V - I curves. Polynomial fitting was conducted using OriginPro 9.0 software package in order to find empirical fitting equations for mobility as a function of gas pressure for different energisation polarities and inter-electrode distances. These empirical equations are provided in Figure 6.12.

The mobility of charge carriers in corona discharges, in the point-plane topology, is dependent on the pressure of the air, the electrode separation, and the polarity of energisation voltage. For both positive and negative energisations, the mobility reduces as the pressure is increased. This is expected because with increased pressure, the mean free path reduces and so should the mobility of charge carriers. Negative corona, in a point-plane gap, has higher mobility electrons than positive energisation. At 0.1 MPa (atmospheric pressure), the mobility of charge carriers in the case of negative energisation is $48.2 \mu\text{m}^2/\text{V}\cdot\text{s}$, ~5-fold higher than in the case of positive energisation for 5 mm gap. Mobility of charge carriers for negative energisation is always higher than mobility of charge carriers in the case of positive energisation; this difference depends on the inter-electrode spacing. The mobility of charge carriers in the case of negatively energised point-plane corona decreases as the inter-electrode gap is increased, from $48.2 \mu\text{m}^2/\text{V}\cdot\text{s}$ with a 5 mm gap to $22.6 \mu\text{m}^2/\text{V}\cdot\text{s}$ with a 10 mm gap, a 2.1-fold reduction in 0.1 MPa air.

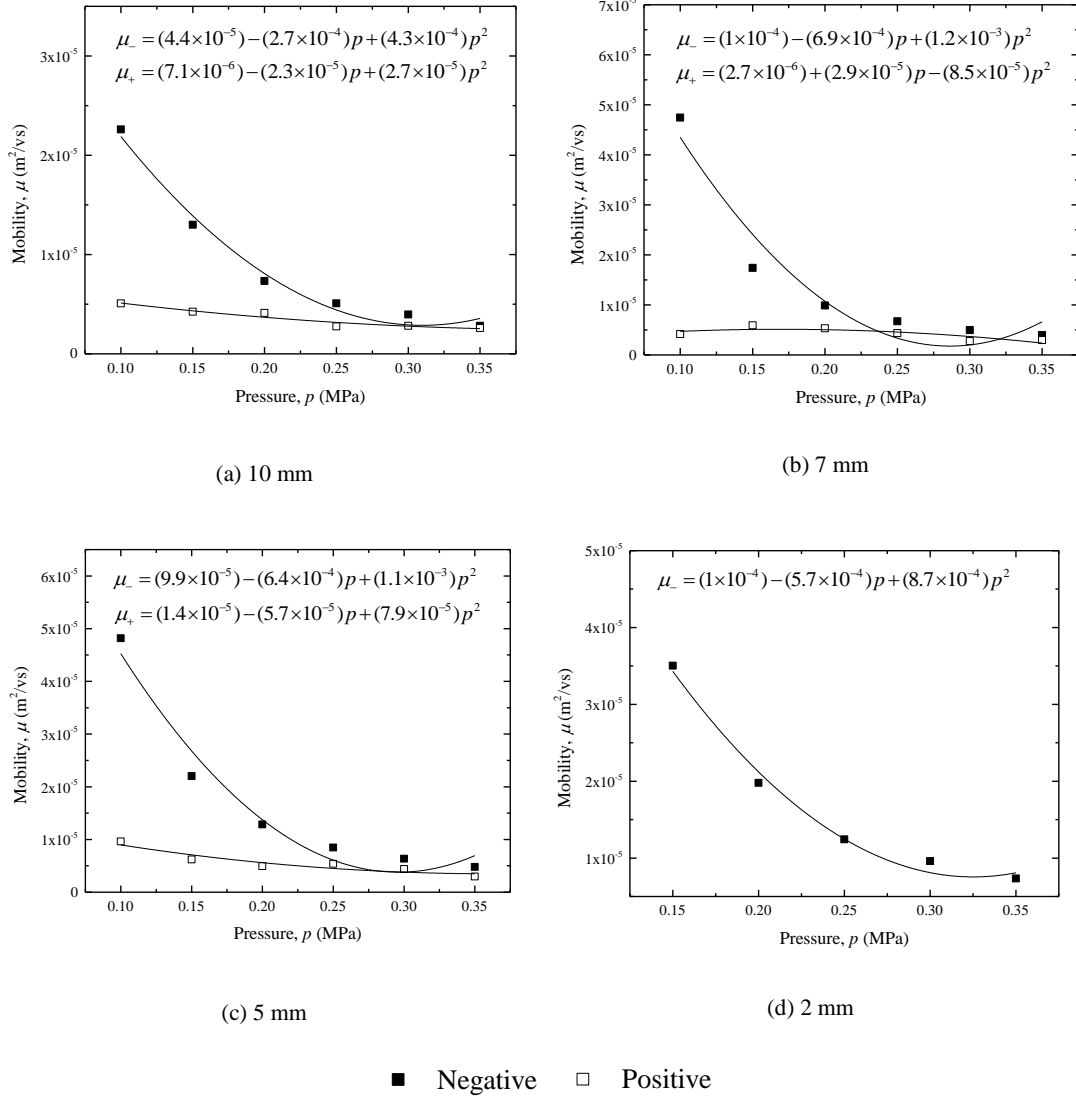


Figure 6.12 Mobility of electrons as a function of air pressure and energisation polarity for gramophone needle, radius 0.036 mm. Calculated using Equation (6.5).

The mobility of charge carriers in air for positive energisation is not strongly influenced by electrode gap: mobility of charge carriers in the case of positive energisation is $\sim 1 \text{ m}^2/\text{V}\cdot\text{s}$ with a 5 mm gap and reduces at most to $\sim 0.67 \text{ m}^2/\text{V}\cdot\text{s}$ with a 10 mm gap. The trend of mobility reducing with increasing inter-electrode gap is present, but compared to the level of reduction with negative energisation, it is insignificant.

Using the mobility values found in this section, the electric field accounting for space charge effects could be estimated using empirical equations. Section 6.4 discusses the space charge effected electric field, to aid the analysis of breakdown characteristics in the point-plane topology.

6.4 ELECTRIC FIELD IN THE SWITCH INFLUENCED BY SPACE CHARGE

The field distribution between a point-plane topology influenced by space charge can be approximated using analytically found formulae given by Coelho and Debeau [Coelho and Debeau 1971]. Coelho and Debeau's equation for space charge affected field distribution is given in Appendix 4.

The space charge influenced electric field along the inter-electrode axis for both positive and negative energisation is given in Figure 6.13, for the gramophone needle, and compared with the Laplacian (electrostatic, no space charge effects) field; the normalised gap is 0 at the tip of the electrode and 1 at the plane electrode.

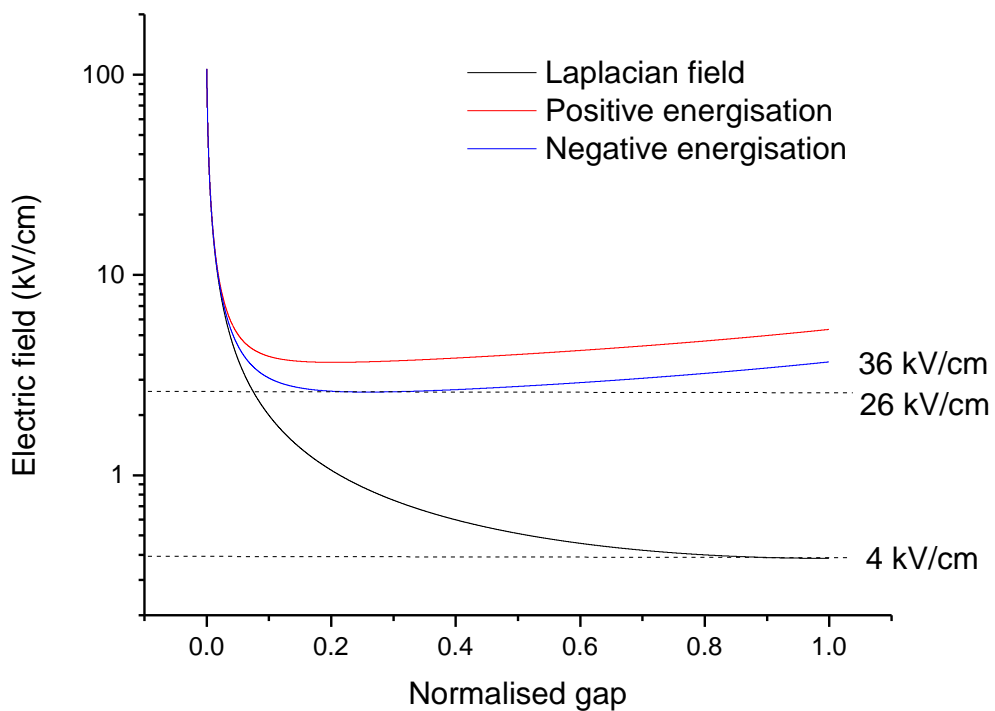


Figure 6.13 Electric field along point-plane inter-electrode axis accounting for space charge for a 10 mm gap and gramophone needle point electrode.

The influence of space charge on the positive and negative energisation on the electric field along the inter-electrode axis is clear in Figure 6.13, where the field remains much larger to the plane electrode with space charge. In Figure 6.13, the field along the inter-electrode axis

was calculated using the current taken from the $V-I$ curves at the breakdown voltage of the positive energisation. It shows that the field in the gap at the same voltage is lower for negative compared to positive energisation with a minimum of 2.6 MV/m compared to 3.6 MV/m with positive energisation. The average field in the drift region of the gap remains below the breakdown threshold of air ~ 30 kV/cm (3 MV/m) when energised with negative voltage whereas, positive is above 30 kV/cm.

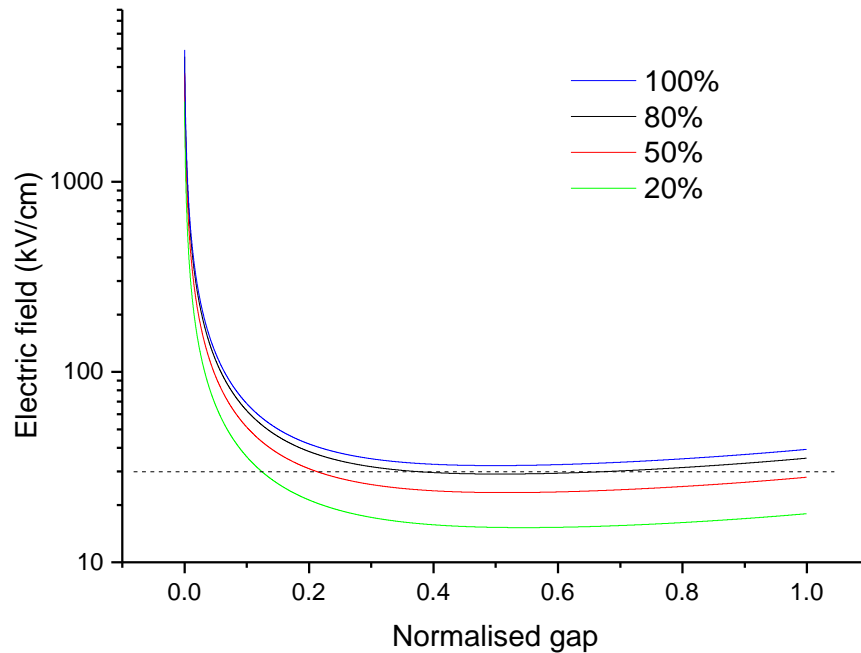


Figure 6.14 Electric field along point-plane inter-electrode axis accounting for space charge at different stages of along the $V-I$ curve. 100% - the voltage before breakdown. Dashed line – 30 kV/cm.

Figure 6.14 shows the electric field along the inter-electrode gap influenced by space charge effects at different levels of corona discharge. 0% means the initiation of corona discharge, and 100% corresponds to complete spark breakdown in the switch. Figure 6.14 shows the electric field distribution between the point and plane electrodes at different levels of corona discharge based on the voltage from 20% of the breakdown voltage, up to 100% of the breakdown voltage where the pre-breakdown voltage and current are highest. As the voltage is increased, the electric field minimum is higher until the electric field minimum is above ~ 30 kV/cm.

Using the analytically calculated electric field distribution due to space charge (Coelho and Debeau approach Equation (17.12)), it was possible to analyse the effects of space charge. This approach can indicate some of the effects of space charge and gives an understanding as to why breakdown voltage is higher for negative than positive energisation. However, this

approach cannot predict complete breakdown voltage on its own because it does not account for localised field enhancements at the tips of discharges such as streamers. It can reasonably be assumed that when the minimum of the electric field is higher than ~ 30 kV/cm, it is likely that breakdown will occur soon as there is sufficient energy to cause ionisation throughout the inter-electrode gap. When streamers are formed, local field enhancements and photo-ionisation effects reduce the required field for streamer propagation to 18 kV/cm for negative streamers and 5 kV/cm for positive streamers [Haddad and Warne 2007]. The results of this section are focused on the analysis of the field in the main section of the inter-electrode gap, and this analysis demonstrates that the average field in the gap increases as the corona discharge intensifies. However, at the same time, this intensive corona discharge results in significant increase in space charge in the vicinity of the corona electrode, thus the local field around the HV corona electrode will be screened and reduced. This is the main reason for an increase in the breakdown voltage in the case of negative polarity as compared with positive polarity of the applied voltage. The analytical method for analysing the space charge affected fields used in the present study does not identify the reduction of the electric field at the tip of the point electrode due to space charge screening processes.

6.5 CONCLUSIONS

Investigation into the positive and negative breakdown voltages in the presence of corona discharges has been conducted. It has been established that the corona discharge activity significantly influences the breakdown voltage and it is believed to be due to the development of volumetric space charge. It has been found that the breakdown voltage is higher for negative energisation, compared to positive energisation in gaps larger than d_{crit} , and this difference increases with an increase in the inter-electrode spacing, Figure 5.13. For distances shorter than d_{crit} , the difference in the behaviour of the positive and negative breakdown voltages is not well pronounced. With an increase in the gap, the effects produced by the volumetric negative space charge continue to govern the breakdown voltage behaviour (almost linear increase in V_{br} with an increase in the gap spacing). However, in the case of positive energisation, the field screening effect produced by a weaker positive space charge is not so effective (positive energisation corona current for this range of distances and electrode radii is $\sim 90\%$ lower than the negative energisation one at the same level of the applied voltage). Thus, the rate of rise of the positive breakdown voltage with inter-electrode

distance decreases. In the case of 0.8 mm gap, no positive energisation corona current was observed for gaps shorter than 14 mm which results in deviation of the positive breakdown voltages from the negative energisation ones at larger inter-electrode gaps (larger critical gap).

7. SUPERIMPOSED TRIGGERING OF SPARK SWITCH FILLED WITH AIR

In this chapter, a new approach to triggering spark switches which can be used to operate compact spark switches with high degree of controllability is introduced as discussed in Chapter 2. Spark switches can be each be categorised by the means they are triggered. There are many variations of triggered spark switches, and each can fall into one of these general categories:

1. Self-breakdown switches (no triggering);
2. Pneumatically triggered switches;
3. Field distortion triggered switches;
4. Trigatron switches;
5. Radiation triggered switches.

Spark switch triggering methods are discussed in Section 2.1.3, however, a brief overview of the merits of each method is given in this chapter. As well as a summary of the triggering techniques from Section 2.1.3, particular focus is given to the operating parameters: DC energisation level, time delay to breakdown, and jitter which gives context to the investigation of the new triggering method.

Self-breakdown switches (no external triggering) are the simplest spark switches with just two electrodes and long life time [Mesyats 2005]. These switches close when the breakdown strength of the gap is exceeded by the field created between the electrodes. This can occur because either the voltage applied to the switch increases beyond the threshold breakdown voltage, or the breakdown strength of the gap is reduced through reducing the gap length or gas pressure. In applications such as over-voltage protection of power equipment where sensitive equipment must be protected from voltages above their operating voltages, self-closing switches automatically operate if the voltage increases, as in the case of a switching

fault or lightning impulse. In pulsed power generators, self-breakdown switches are often triggered by reducing the strength of the switch by reducing the pressure of gas. The breakdown strength could also be reduced by reducing the inter-electrode gap; however, this is much less convenient and consistent. Pulsed power generators such as Marx generators often use self-breakdown switches to fire the generator once it is fully charged by reducing the gas pressure (pneumatic triggering). Field distortion triggering requires an extra electrode, these switches are composed of at least three electrodes; two DC energised main electrodes and a trigger electrode. The main electrodes are usually energised to ~60-90% of the self-breakdown voltage and the trigger electrode remains at floating potential. A fast rise, opposite polarity, high voltage trigger impulse is applied to the trigger electrode which is situated between the main electrodes. The field between the trigger electrode and one of the main electrodes becomes highly distorted and switch closure is initiated.

Field distortion triggering is widely used in pulsed power technologies because it can have low miss fire and pre-fire rate with the charging voltage being as low 60% of the self-breakdown voltage. Much work was done on developing field distortion switches in the 60's and 70's working with a range of operating parameters. Mercer *et al.*, working with high pressure (1 MPa) SF₆ presented switches with closure time of ~20 ns and jitter of 1 ns and 2 ns [Mercer 1976]. Bernstein and Smith worked with a short gap, 1.8 mm, achieving jitter of 2-3 ns and Vorob'ev and Mesyats worked with voltages as low as 10-15 kV DC and achieved jitter of 1 ns by adding UV radiation [Bernstein and Smith 1973] [Vorob'ev and Mesyats 1963][Li 2015a].

Trigatron switches are considered with two mechanisms of triggering which both start by creating a mini discharge between trigger electrode and main electrode. Trigratrons have two main DC energised electrodes and a third trigger electrode positioned inside one of the main electrodes. An insulation sheath keeps the trigger electrode at floating potential until a triggering impulse is applied. A fast, high voltage impulse is applied to the trigger electrode creating a mini discharge. The mini discharge can initiate switch closure via UV radiation or the spark expanding between the main electrodes. Trigratrons are popular in pulsed power technologies because they are relatively simple compared to field-distortion and radiation trigger switches and they are very reliable. The time delay to breakdown and jitter decrease as the DC energisation is increased and as the rise time of triggering impulses decreases [Mesyats 2005]. With UV radiation alone, jitter of ~10 ns can be achieved [Mesyats 2005]. When the spark is expanded across between the main electrodes jitter can be as low as ~1 ns [Theophanis 1960]. Lavoie, Markis, Martin, and Couperstein presented trigratrons with short

time delay to breakdown, 10-20 ns, and jitters of below 3 ns (90% V_{BD}), 1.5 ns and ~2 ns [Lavoie 1964] [Markis 1971] [Martin 1973] [Couperstein 1973].

Radiation triggering can be sub-categorised depending on the type of radiation. Intensive UV pulses, lasers and electron beams are used to trigger spark switches. UV pulses, 1100 Å, are intensively applied to the spark gap to initiate switch closure [Godlove 1961]. A pulse of ~1 ns can trigger switch closure if the switch is energised to 90-95% of the self-breakdown voltage and time delay to breakdown of ~10 ns can be achieved with jitter <<10 ns [Larsson 2014][Stolen 1969] [Godlove 1961]. UV radiation is an effective method of triggering spark switches. However, for low jitter and short time delays, it is required that the switch be energised to 95-98% of the self-breakdown voltage [Mesyats 2005].

Laser triggering was first proposed and used by Pendelton and Guenther in 1965 as a means of triggering spark switches [Pendelton and Guenther 1965]. High power lasers beams focused on the electrons in the gas can develop electron avalanches through multiple photon ionisation processes leading to the development of a spark and initiation of switch closure [Raizer 1991]. Using a ruby laser, 164 GW/cm², Moriarty achieved breakdown times of ~10 ns and jitter of ~1 ns when the switch was energised to 94% of the self-breakdown voltage. Comprehensive reviews of laser triggering switches were conducted by Williams and Guenther and by Raizer [Williams and Guenther 1990] [Raizer 1974].

Electron-beam triggering is similar to laser and UV triggering where DC energised switches are triggered by injecting external ionisation in the spark switch [Mesyats 1982]. Electron beam triggering is useful for triggering high voltage, MV, switches where it can be expected that time delay will reduce [El'chaninov 1975]. Koval'chuk achieved time delays of ~30 ns with jitter ~1 ns and Bortnik achieved 15 ns delay with jitter 0.8 ns using 85% self-breakdown voltage energisation [Koval'chuk 1970a, b]. The issue with electron beam triggering is that it is hard to get short, stable delay times using low current beams [Mesyats 2005].

This chapter introduces a new approach to triggering plasma closing switches based on superposition of the DC stress and triggering impulse. Using a simple two electrode switch, it is possible to pre-energise the switch with DC energisation and to trigger the switch by applying a superimposed triggering impulse. The triggering impulse raises the voltage to cause an overvoltage breakdown in the switch. Results from this investigation were presented and published in the conference proceedings of the XX International Conference on Gas Discharges and their Applications in 2014 [Hogg 2014a].

The experimental design of the switch used in the present study is given in Section 3.4. Two 19 mm diameter spheres formed a sphere-sphere topology with a 2 mm gap. The switch design given in Figure 7.1 was the same as used in Chapter 4 used with additional spacers to set the gap to 2 mm from 5 mm.

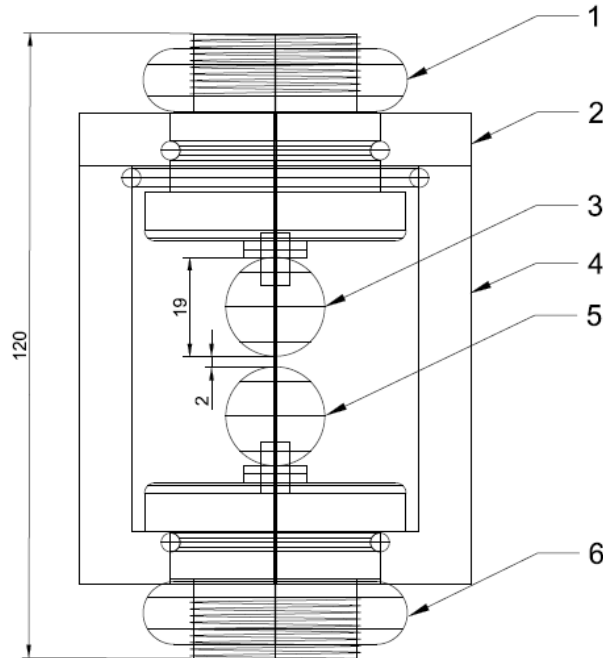


Figure 7.1 Sphere-sphere topology switches. 1 – HV connection, 2 – Clear acrylic switch top, 3 – HV sphere electrode, 4 – Clear acrylic switch body, 5 – Ground sphere electrode, 6 – Ground connection. Dimensions in mm.

Section 7.1 discusses the results of investigation of operational performance of the switch triggered by superimposed impulse with respect to the time delay to breakdown.

7.1 SUPERIMPOSED TRIGGERING: TIME DELAY TO BREAKDOWN

The time delay to breakdown was measured from the moment of application of the triggering impulse to the moment of collapse of voltage. The switch was filled with bottled air. Fast closing times are critical in the pulsed power industry and, therefore, it is important to identify operating parameters that can reduce the time delay to breakdown. It was found that with superimposed triggering, the time delay to breakdown reduced as the DC pre-energisation level approaches the self-breakdown voltage, Figure 7.2.

30 breakdown measurements were observed, and each data point in Figure 7.2 is an average of the 30 shots. The time to breakdown was measured between the application of trigger voltage above the DC energisation level until the collapse of voltage. The time measurements were also confirmed by Pearson coil current probe (250 MHz). Arguably, the most important aspect of switch closure in pulse power applications time is its jitter. Therefore, to achieve reliable results, the measurement process was kept consistent and using oscilloscope cursors this method was the most repeatable. The switch was filled with a fresh portion of gas before each series of 30 measurements; gas remained in the switch without change during 30 breakdown measurements. The fitting procedure was implemented using OriginPro 9.0 software. The empirical function which describes fit lines obtained using this fitting procedure is a linear function of the percentage of the self-breakdown voltage (y represents time to breakdown and x represents percentage of self-breakdown voltage):

$$y = Ax + B \quad (7.1)$$

where A (ns/%) and B (ns) are fitting coefficients. The trend line fittings are only fitted to the linear section of the data and are only valid for the energisation above 15% of the self-breakdown voltage.

Shown in Figure 7.2, the time delay to breakdown with 0 V DC (impulse stress only) energisation is an order of magnitude larger than when energised to 90% of the self-breakdown voltage. Non-breakdown events occurred when the switch failed to close on application of the triggering impulse. In this case it was assumed that breakdown would occur if the trigger impulse was lengthened because the voltage is much higher than the breakdown voltage. Therefore, for analysis in this work, non-breakdown events were given a time equal to the trigger pulse duration (284 ns) as minimum time assuming breakdown would have occurred at some point after if the trigger pulse was infinitely longer. Non-breakdown events increase the perceived breakdown time showing the switch is unstable if charging voltage is below 10% of self-breakdown DC voltage. In the case when DC pre-energisation is ~10% of the self-breakdown voltage, the time delay to breakdown is no longer being influenced by non-breakdown events because breakdown is consistently occurring within the rise of the triggering impulse.

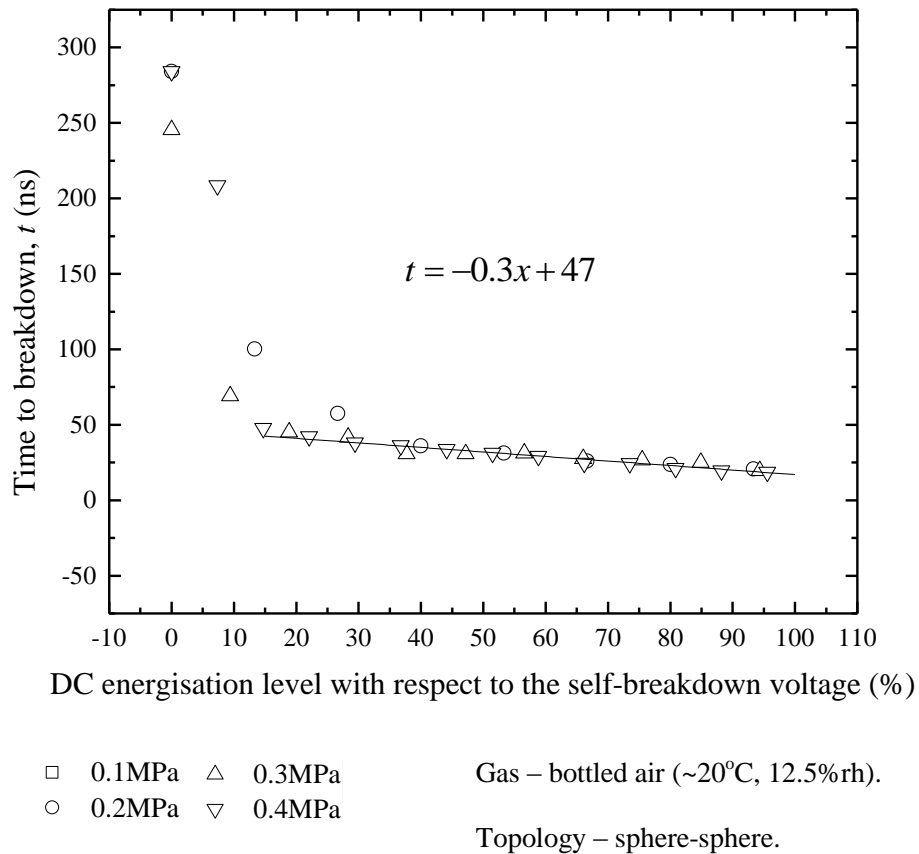


Figure 7.2 Time delay to breakdown of a sphere-sphere, superimposed impulse triggered switch as a function of DC pre-energisation level (x%), Solid line – empirical fitting.

Time delay to breakdown is strongly influenced by the DC pre-energisation voltage applied to the switch prior to breakdown. Figure 7.2 shows, irrespective of air pressure (in the range between 0.1 MPa and 0.4 MPa), the time delay to breakdown is only dependent on the DC pre-energisation voltage level (expressed as a percentage of DC self-breakdown voltage at corresponding gas pressure). Increasing the DC energisation from 20% to 90% of the self-breakdown voltage reduced the time delay to breakdown from ~40 ns to ~20 ns for each pressure.

Short time delay is critical in the pulsed power industry and, therefore, the results shown in Figure 7.2 are important for design and optimisation of the switches to reduce the time delay. By increasing DC energisation level from ~10% of self-breakdown voltage (which is minimum level for stable operation of the switch) to the level close to self-breakdown level (almost 100% of self-breakdown voltage) has led to a 4-fold decrease in time delay in switch operation. Time delays achieved using superimposed triggering are comparable with values in time delay achieved in very high voltage linear transformer driver switches. These switches operate at ± 100 kV in which advanced triggering mechanisms (such as laser

triggering) are used in order to reduce time delay to breakdown, which in turn allow 10's of ns time delay to be achieved.

Time delay to breakdown is an important parameter in switch operation and ideally should be minimised, but critically it is required that this time remains consistent. The degree of consistency in time to breakdown is obtained by calculating the standard deviation of this time which is called jitter. Section 7.2 presents the results on jitter of the switch is operated in DC superimposed triggering mode.

7.2 SUPERIMPOSED TRIGGERING: SWITCH JITTER

The variation in the time delay to breakdown is expressed as a standard deviation of the mean delay time. Jitter is a very important parameter for pulsed power applications as it provides information of the stability of operation of the plasma closing switches. Minimum values of jitter of the plasma switches allow synchronisation of operation of a multiple pulsed power system to be achieved in order to deliver significant power into a single load.

Figure 7.3 shows the jitter for all three pressures and all DC energisation levels. Non-breakdown events are not included in the discussion of jitter and are considered separately in reliability tests in Section 6.5.

The empirical equations were obtained by using linear fitting procedure in OriginPro 9.0 software package. Equation (7.2) states that the jitter, σ (expressed in ns), is linearly dependent on the self-breakdown voltage percentage, x (%). The fitting coefficients, A and B , have been obtained using OriginPro 9.0 graphing software package. These linear fit lines are shown in Figure 7.3 and Figure 7.5 and corresponding coefficients A and B are also given in these figures:

$$\sigma = Ax + B \quad (7.2)$$

where A (ns/%) and B (ns) are fitting coefficients, $x\%$ is energisation level percentage of self-breakdown voltage where 0% has no DC pre-energisation and 100% the switch is energised to the self-breakdown voltage.

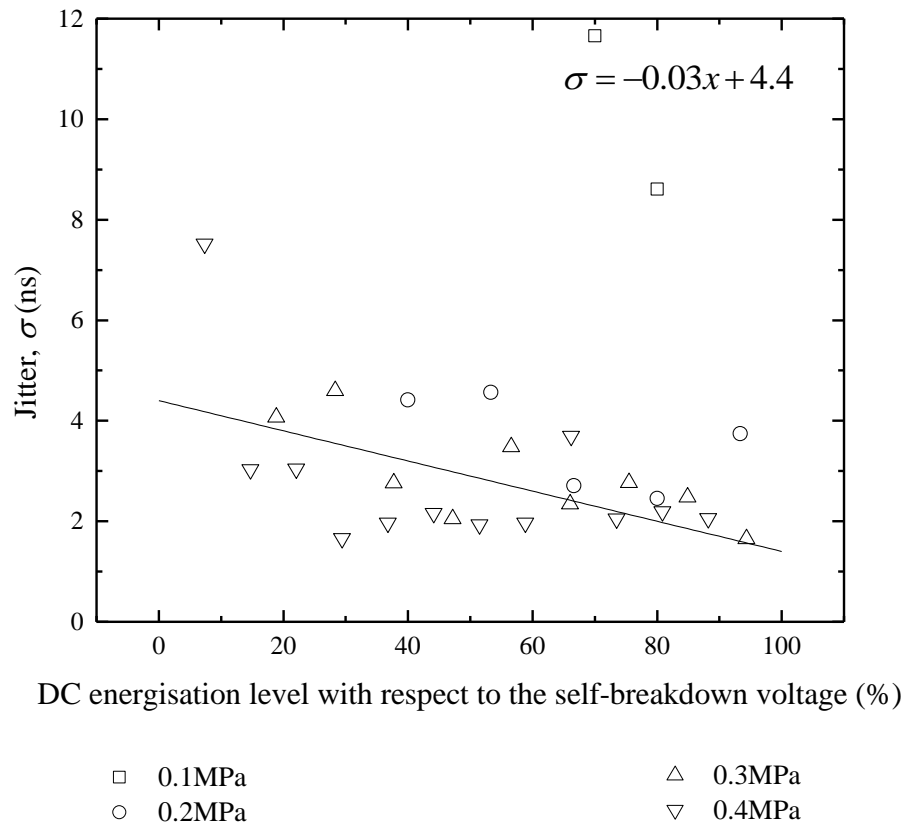


Figure 7.3 Jitter of the time delay to breakdown of a sphere-sphere, superimposed impulse triggered switch in compressed bottled air as a function of DC pre-energisation level. Solid line – empirical fitting.

Switch jitter was calculated for each DC pre-energisation level, and it was found that the jitter reduced as the stress voltage level was increased. For stress voltages in the region between 20% and 100% of DC self-breakdown voltage level, breakdowns occurred on the rising slope of the triggering impulse, this is discussed further in Section 6.4. It was found that, in this region of the pre-breakdown stress, jitter is as low as 1.6 ns and consistently lies between ~1.6 ns and ~5 ns. Jitter values between ~2 ns and ~4 ns are considered good performance for any plasma closing switch including advanced triggering mechanisms such as laser and UV triggering, specifically used to reduce jitter, achieving jitter of ~2 ns at ~90% self-breakdown voltage pre-energisation.

7.3 PRE-BREAKDOWN IONISATION EFFECT ON TIME DELAY TO BREAKDOWN

Coronating electrodes, at potential with HV electrode, causing pre-breakdown ionisations within the switch were investigated. Soft-tone gramophone needles were used in the vicinity

of the high voltage electrode, Figure 4.3b. The gramophone needles were located the same as Figure 4.3b, 5 mm shorter than level with the tip of the spheres and 17 mm from the centre of the switch. Localised high field in the vicinity of the point electrodes creates ionisations prior to the formation of a spark between the sphere electrodes. Corona discharge may be initiated if the applied field exceed the ionisation threshold (the applied voltage exceeds the corona ignition voltage). Time delay to breakdown and jitter were investigated with pre-breakdown ionisation electrodes, Figure 7.4 and Figure 7.5 where the sub-script *C* signifies results obtained with coronating electrodes. Section 7.3 presents the results of investigation into the effects of the coronating electrodes on the time delay and jitter.

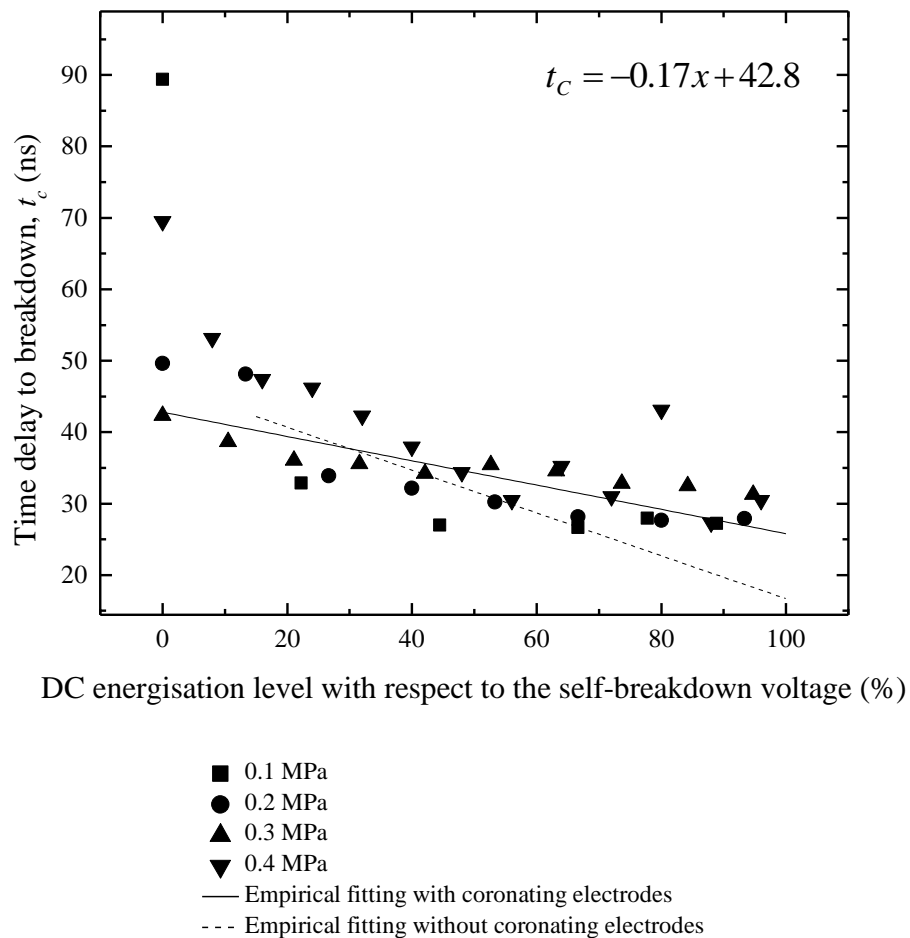


Figure 7.4 Time delay to breakdown of a sphere-sphere, superimposed impulse triggered switch in compressed bottled air as a function of DC energisation level with pre-breakdown ionisation electrodes. The dashed line represents the best fitting of the data collected in Figure 7.2, the time delay to breakdown without the coronating electrodes. The term, t_c , in the fitting equation represents the time delay to breakdown with the coronating electrodes.

It was shown that time delay to breakdown is impacted by the inclusion of pre-breakdown ionisation electrodes into the switch. The trend line fittings are only fitted to the linear section of the data and are only valid for the applied range. Time to breakdown in the topology with the corona electrodes becomes shorter than the delay time in the switch without corona electrodes for DC energisation levels below 40% of the self-breakdown level. The delay times become longer for DC energisation levels above 40% of the self-breakdown level as shown in Figure 7.4. The relationship between the time delays to breakdown is independent of pressure and can be predicted given the percentage of self-breakdown voltage the switch is energised to. As the DC pre-energisation is increased above 40% of the self-breakdown level, the time delay to breakdown does not reduce as much as without corona discharge electrodes. It is clear that coronating pre-ionisation electrodes in the switch reduce the impact of increasing the DC energisation level on the time delay to breakdown.

The jitter of the superimposed triggered switch with coronating electrodes is given in Figure 7.5 where the empirical fitting procedure was implemented in OriginPro 9.0 software package. Linear functions were used to fit experimental data on jitter as a function of percentage of the DC self-breakdown voltage.

Superimposed triggered switch performance has been evaluated by measuring the time delay to breakdown and jitter, and it was found that, with coronating electrodes, lower jitter was achieved when the switch was energised below ~70% DC energisation. At low levels of DC energisation (including 0 V, no energisation voltage at all), coronating electrodes improve the stability of the switching time delay (reduce jitter). With further increase in the DC energisation level, jitter no longer decreases.

To achieve reliable operation of the switch, the switch should ideally close on the rising edge of the trigger impulse. Short time delay and low jitter are vital for the uses of spark switches. However, if they do not consistently close on the rising edge of the trigger pulse, the time delays can be much longer and jitter significantly increases.

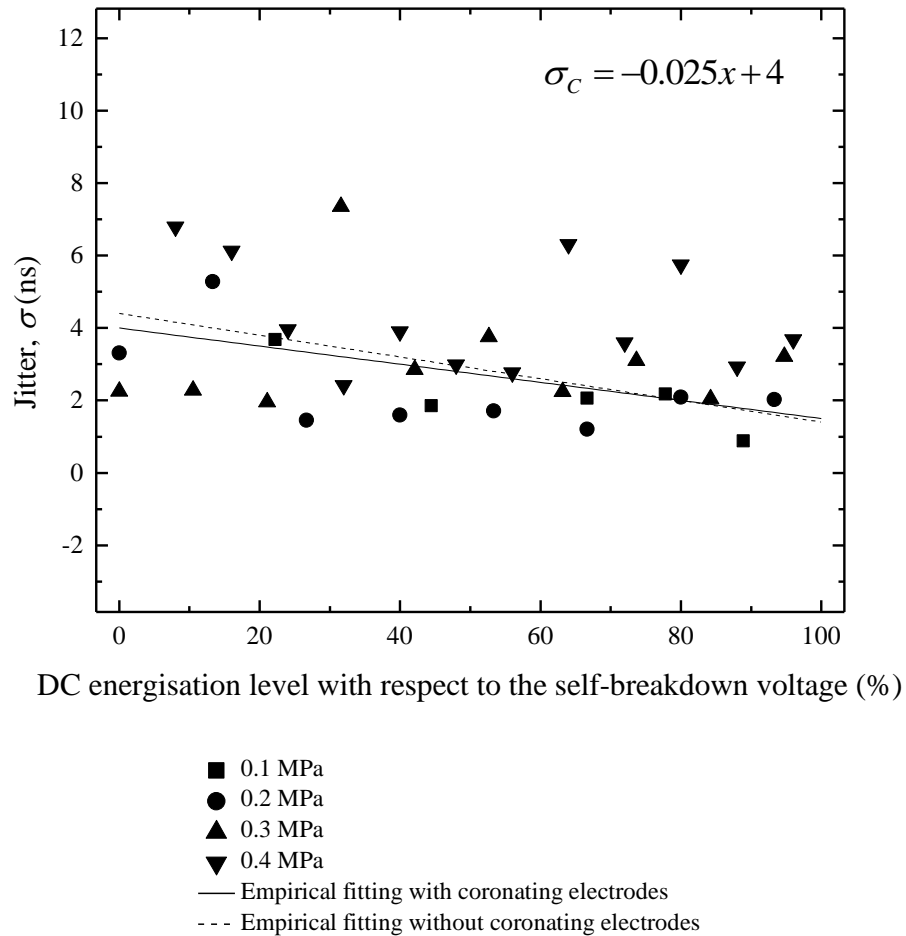


Figure 7.5 Jitter of the time delay to breakdown of a sphere-sphere, superimposed impulse triggered switch in compressed bottled air as a function of DC energisation level with coronating electrodes. The dashed line represents the best fitting of the data collected in Figure 7.3, the jitter without the coronating electrodes. The term, σ_c , in the fitting equation represents the time delay to breakdown with the coronating electrodes.

The time delay increases significantly because after the peak of the impulse, the voltage oscillates at voltages lower than the peak voltage for the duration of the impulse, Figure 3.9. The next section discusses the number of breakdowns occurring on the rise of the impulse.

7.4 PRE-BREAKDOWN IONISATION EFFECT ON SWITCH MISS-FIRE RATE (PROBABILITY)

The switch operational stability is strongly dependent on the air pressure, Figure 7.5. It was shown in the present work that pre-breakdown corona discharges (produced by ionisation electrodes) can reduce jitter at low pressures but increases switch jitter at 0.2 MPa.

Therefore, the switch is less stable by including pre-breakdown ionisation electrodes. For highest performance, it was advantageous to achieve breakdown of the switch on the rising edge of the triggering impulse. Adding pre-breakdown ionisation electrodes reduces the number of impulses not occurring on the rising slope of the trigger impulse (occurring after the peak voltage), Figure 7.6.

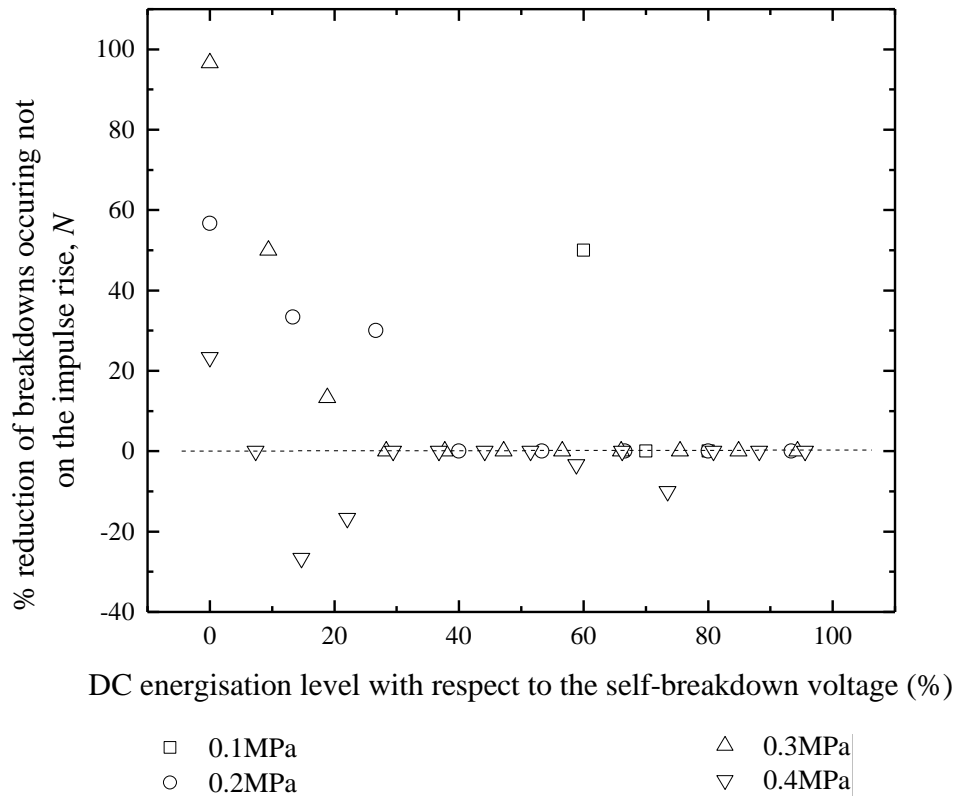


Figure 7.6 Percentage reduction of breakdowns not occurring on the rise of the trigger impulse (i.e. before the peak voltage) as a function of the DC pre-energisation level with reference to self-breakdown voltage of the switch by the inclusion of pre-breakdown ionisation electrodes. Above 0 line (dashed) shows improvement of switch performance.

At 0.1-0.3 MPa, the number of breakdowns occurring before the peak of the trigger impulse increased. With no pre-energisation (0 V), there was an improvement in all pressures with the largest improvement at 0.3 MPa. As the DC energisation is increased, the influence of the pre-breakdown ionisation electrodes is reduced. Eventually, the pre-breakdown ionisation electrodes have no positive impact on the number of breakdowns occurring on the rising edge of the trigger impulse. The level at which the pre-breakdown ionisation electrodes have no effect is dependent on the pressure, for 0.1 MPa air: ~60% self-breakdown voltage; for 0.2 MPa, it is ~40%; for 0.3 MPa is about 30% and for 0.4 MPa only 0 V of pre-energisation level showed an improvement.

Ultimately, it can be concluded that the effect of adding pre-breakdown ionisation electrodes is useful within a range of lower pressures and pre-energisation levels. Up to 100% more breakdowns occur on the trigger impulse rising edge when pre-breakdown ionisation electrodes were included. Breakdown times, below ~40% of DC breakdown energisation level, were reduced and the jitter was reduced. Improvement in switch performance was observed at low pressures and DC pre-energisation levels, but at high DC pre-energisation and high pressures the coronating electrodes had a detrimental effect on performance.

Section 7.5 continues to evaluate the effect of the coronating electrodes by analysing the time delays using Laue statistical analysis.

7.5 STATISTICAL AND FORMATIVE TIMES OF ANALYSIS SUPERIMPOSED TRIGGERED SWITCH: LAUE ANALYSIS

Using the Laue analysis method, the time delay to breakdown data can be statistically analysed to separate the statistical time and formative time delays. This can then help to analyse the results by indicating if the time delay to breakdown reduction with DC energisation is a reduction in statistical time or formative time. In breakdown in gas, it is typically assumed that the time delay to breakdown is made up of two different time delays: statistical time and formative time. Statistical time is defined as the time from application of voltage capable of causing breakdown to the appearance of an electron capable of initiating discharge. The formative time is the time which is required for the discharge to cross the inter-electrode space, the time from the end of the statistical time to switch closure.

Developed by Max von Laue, this statistical method assumes that the formative time lag is distributed normally and is much longer than the statistical time lag which is distributed exponentially. Using external ionising techniques, such as UV light, the statistical time can be reduced to negligible durations, and it has been shown that formative times follow a normal distribution.

Assuming the formative time, t_f , has a distribution related to the normal distribution and statistical time is almost constant, $\overline{t_{st}}$, Laue showed that by plotting the logarithm of the ratio of the number of breakdown events with the total time lag longer than a given time, N_t , to the

total number of breakdowns, N_0 , can reveal the statistical and formative time lags, Figure 7.7:

$$-\ln\left(\frac{N_t}{N_0}\right) = \frac{t - t_f}{\bar{t}_{st}} \quad (7.3)$$

where t is the total breakdown time, t_f is the formative time and t_{st} is the average statistical time.

By isolating a linear section as shown in Figure 7.7, and plotting a straight line that intersects 0, the formative time can be found. The point at which linear section crosses 1, this is the average time delay to breakdown and by removing the formative time the average statistical time can be found.

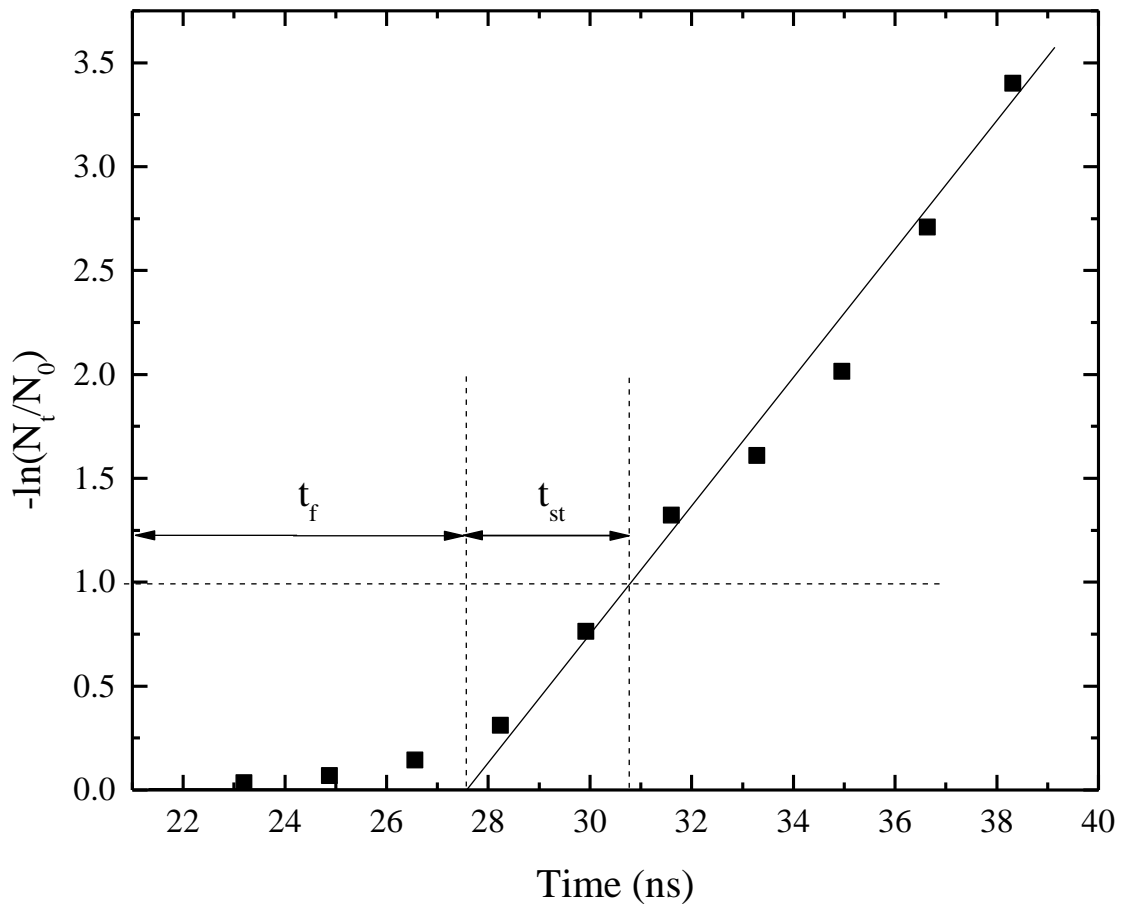
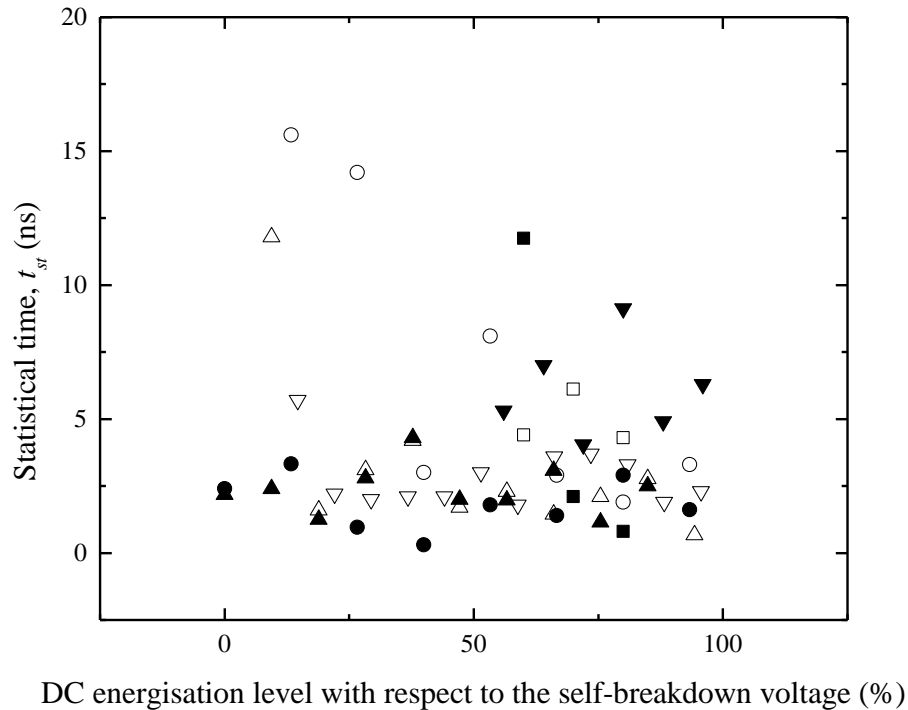


Figure 7.7 Laue plot for 1 bar air with a DC energisation of 14 kV with formative and statistical time indicated.

Using Laue analysis, the time delay to breakdown data was analysed, and the statistical and formative time delays were found for each air pressure and DC pre-energisation level. Figure 7.8 shows the statistical time from the Laue analysis reducing as the DC pre-energisation is increased.

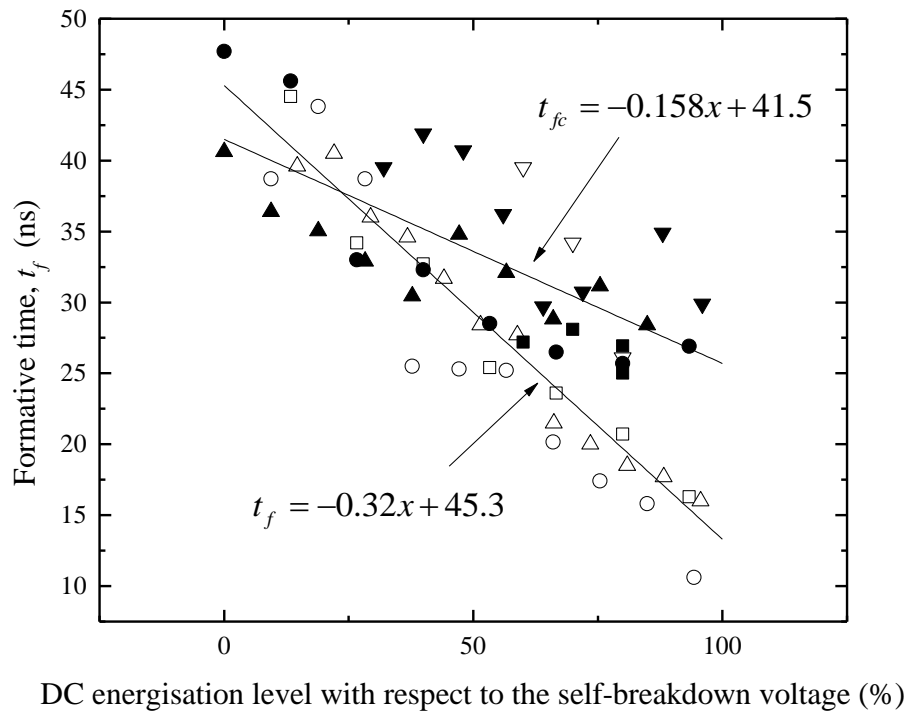


- | | |
|---|--------------------------------------|
| □ 0.1 MPa without coronating electrodes | ■ 0.1 MPa with coronating electrodes |
| ○ 0.2 MPa without coronating electrodes | ● 0.2 MPa with coronating electrodes |
| △ 0.3 MPa without coronating electrodes | ▲ 0.3 MPa with coronating electrodes |
| ▽ 0.4 MPa without coronating electrodes | ▼ 0.4 MPa with coronating electrodes |

Figure 7.8 Statistical time lag from Laue statistical analysis on the time delay to breakdown data for a sphere-sphere superimposed triggered switch with compressed bottled air as a function of DC energisation.

Without coronating electrodes, the statistical time-lag is reduced when the DC energisation is increased for all air pressures, Figure 7.8. Between 0 kV and ~20%, the statistical time reduces quickly from ~14 ns to ~2-4 ns where further increase in DC level has less of an impact on the statistical time. Between 20% and 100%, the statistical time varies for each pressure, but, on average, it is ~1 ns suggesting the high levels of DC energisation effectively removes the statistical time. However, it does not sufficiently provide explanation of the 20-30 ns reducing in time delay to breakdown in some cases shown in Figure 7.2. With coronating electrodes, the statistical time was much lower than without coronating electrodes at lower DC energisation levels. At 0-30% DC level, the statistical times were ~2 ns, ~7-fold shorter than without coronating electrodes. At 0.1 MPa and 0.2 MPa, the

statistical time remained between ~1 ns and ~3 ns. Above 0.2 MPa, the statistical time increased as the DC level was increased above 30% of the self-breakdown voltage. Figure 7.2 shows a reduction in time delay to breakdown by including coronating electrodes at low DC levels and pressures and an increase in time at higher DC energisation and pressures. Figure 7.8 suggests the differences in time are at least partly influenced by the statistical times. To account for the 20-30 ns reduction in time delay seen in Figure 7.2, the formative time should also be considered. Figure 7.9 shows the formative time lags found using Laue analysis reducing as a function of DC pre-energisation level for each air pressure.



- | | |
|---|--------------------------------------|
| □ 0.1 MPa without coronating electrodes | ■ 0.1 MPa with coronating electrodes |
| ○ 0.2 MPa without coronating electrodes | ● 0.2 MPa with coronating electrodes |
| △ 0.3 MPa without coronating electrodes | ▲ 0.3 MPa with coronating electrodes |
| ▽ 0.4 MPa without coronating electrodes | ▼ 0.4 MPa with coronating electrodes |

Figure 7.9 Formative time lag from Laue statistical analysis on the time delay to breakdown data for a sphere-sphere superimposed triggered switch with compressed bottled air as a function of DC energisation. Solid line – empirical fitting.

Seen in Figure 7.9 as the DC energisation is increased, the formative time reduces linearly. For all air pressures, it can be seen that formative time is high, at low DC levels, ~40-45 ns and reduces as the DC level is increased. The formative time reaches ~10-15 ns for all pressures, and is only dependent on the magnitude of the DC level as a percentage of the breakdown strength.

Coronating electrodes decrease time to breakdown at low DC levels, Figure 7.2. The shorter time delays at low (<30%) DC energisation are produced by a reduction in statistical time, Figure 7.8. The formative time at low (<30%) DC level is similar with and without coronating electrodes. At higher DC levels, the time to breakdown increases, Figure 7.2, which can be attributed to both an increase in statistical time and formative time, Figure 7.8 and Figure 7.9. Increasing the DC level with the coronating electrodes creates significant space charge effects. The space charge screens the electric field between the electrodes, delaying the initiation and development of the discharge. This increases the time delays to initiate a discharge leading to longer statistical time and prevents the advancement of discharge leading to longer formative times.

7.6 CONCLUSIONS

A new approach to triggering of DC energised compact switches has been developed in this chapter. An experimental system was designed and tested to apply a triggering impulse superimposed on a DC energisation level. It was shown that this approach could trigger simple 2 electrode switches with performance equalling the most effective switches already in use. Switching times of ~20 ns was achieved with jitter of ~1-2 ns which is comparable with laser triggered switches. It was also shown that the time delay to breakdown and the jitter are primarily dependent on the DC energisation level as a percentage of the self-breakdown voltage and not significantly dependent on the pressure of the switch.

In an attempt to investigate methods of improving performance, coronating electrodes were added to the high voltage electrode. It was found that including the coronating electrodes would slightly reduce the time delay at low DC levels (<30%). Above ~30% of the breakdown voltage, it was found that the time delay increased. This is likely due to space charge screening effects. At the lower DC levels, the coronating electrodes increased the number of breakdowns occurring on the rising slope of the trigger impulse. This increases the performance.

Laue analysis has shown that the improvement of performance of the switch with the coronating electrodes when the switch is used at low DC energisation (<30%) can be attributed to aiding the initiation of a discharge. The high fields created by the coronating electrodes have reduced the statistical time by aiding the initiation of the discharge. It is not possible to specifically say how it reduces the initiation time. However, it is possible that the high fields inject free electrons into the gas. At low DC levels, the injected electrons would

not cause significant ionisation and the amount of electrons will not create significant space charge. However, the free electrons could provide the initiation of avalanche without having to inject seed electrons from the much lower field topology. Making it easier to initiate a discharge has also improved upon the stability of the switch closing on the rising edge of the impulse, Figure 7.6. Using the coronating electrodes a 100% improvement was achieved getting the switch to close on the rise of the impulse for a 0 V energisation at 0.3 MPa. It can be concluded that including coronating electrodes is useful for low (<30%) DC energisation applications. However, it is not suitable for higher DC levels where significant corona discharge could be initiated and space charge effects are prominent.

8. MULTI-STAGE SPARK SWITCHES

So far, this research project has focused on spark switches which have just one spark gap. Three different topologies have been investigated with respect to breakdown voltage and its standard deviation and a further in depth analysis of point-plane topology completed. For switching higher voltages, multi-stage spark switches are used in pulsed power systems. Therefore, in order to expand potential practical applications of the switches and triggering method developed in the present work, a multi-stage switch has been designed and developed based on the results obtained for single stage topologies. The results obtained using the point-plane topology were used in the design of the multi-stage spark switch, and this chapter presents an investigation into operational characteristics of this switch. For the first time, a multi-gap switch was investigated with gaps specifically set to close to the critical gap (identified in Chapter 5). The main aim of this part of the research programme is to develop a high-performance multi-stage spark switch topology, with improved performance characteristics such as an increased breakdown voltage and lower spread in breakdown voltage values. This chapter presents the results of investigation of an operational performance of the multi-stage topology filled with environmentally-friendly gases. The main parameters which have been investigated included: the breakdown voltage and its standard deviation; the time delay to breakdown and its jitter; and pre-breakdown current-voltage characteristics. Section 8.1 presents the switch design and topology used in Chapter 8.

8.1 MULTI-STAGE SPARK SWITCH TOPOLOGY

From the work completed on the self-breakdown voltage in different topologies, Chapter 4 and Chapter 5, it was determined that the point-plane topology can provide stable operational characteristics and can be used as a basis in the design of the multi-stage spark switches to increase operational voltage of these switches. Originally, a cone-plane topology suggested that it was worth investigating sharper point-plane configurations, and then, further analysis

showed the soft-tone gramophone needle point electrode produced the most interesting results. For the gramophone needle, it was found that, at ~2 mm, the breakdown voltage for negative and positive energisations were similar. The gramophone needle was the sharpest point electrode investigated in Chapter 4 and Chapter 5. While it is possible to sharpen needles, it is not easy to get consistency in the apex diameter of sharpened needles. Gramophone needles, as received from supplier, have a good consistency in terms of their topology (apex diameter).

Each gap is a separate switching stage (unit) which consists of a point-plate topology. When stacked with another unit, they complete a multi-stage switch. Each unit has a point electrode held in a flat topped brass block and an outer container. The flat top brass block acts as the plane electrode for the unit above when they are stacked. Figure 8.1 to Figure 8.3 show the design and finish of the multi-stage spark switches.

Each 30 mm thick brass plane is 36 mm in effective diameter with 9 mm extra to act as support on the container and for an 'o' ring so the switch can be pressurised. The brass plane electrodes have a 4 mm hole for a push fitting (banana plug) in the side for measurements, grounding, HV or triggering.

The 25 mm thick walls of the container were made of black PVC, machined to provide a 2 mm gap when stacked with another unit. Six 12 mm threaded rods pass through the walls of each of the units to hold each stage together.

The end units are similar to the middle units except the brass blocks are 30 mm thick and each has a 4 mm push fitting hole in the middle of the top of the brass. The bottom piece does not have a point electrode. Instead, it has a push fitting hole for connecting to ground. The walls of the end units are also extended to 60 mm instead of 5 mm to increase the path between the electrodes on the outside of the switch. Blocks of black PVC are used to push down on the brass electrodes to compress the switch together. With a top and bottom piece any number of gaps can be created by just adding another middle unit.

Quartz windows have been put into the walls of each stage of the switch for visual confirmation that all the stages of the switch are breaking down. The switch can be pressurised to 0.4 MPa.

For monitoring of optical and electrical characteristics, two experimental systems were designed and developed: one for measuring of self-breakdown voltages and corona/ $V-I$ characteristics; and another one for analysis of triggered operation of the multi-stage switch. Both of these investigations observe the effect of increasing the number of spark gaps

including 1 stage, 2 stages and 3 stages, on operational characteristics of the multi-stage switch.

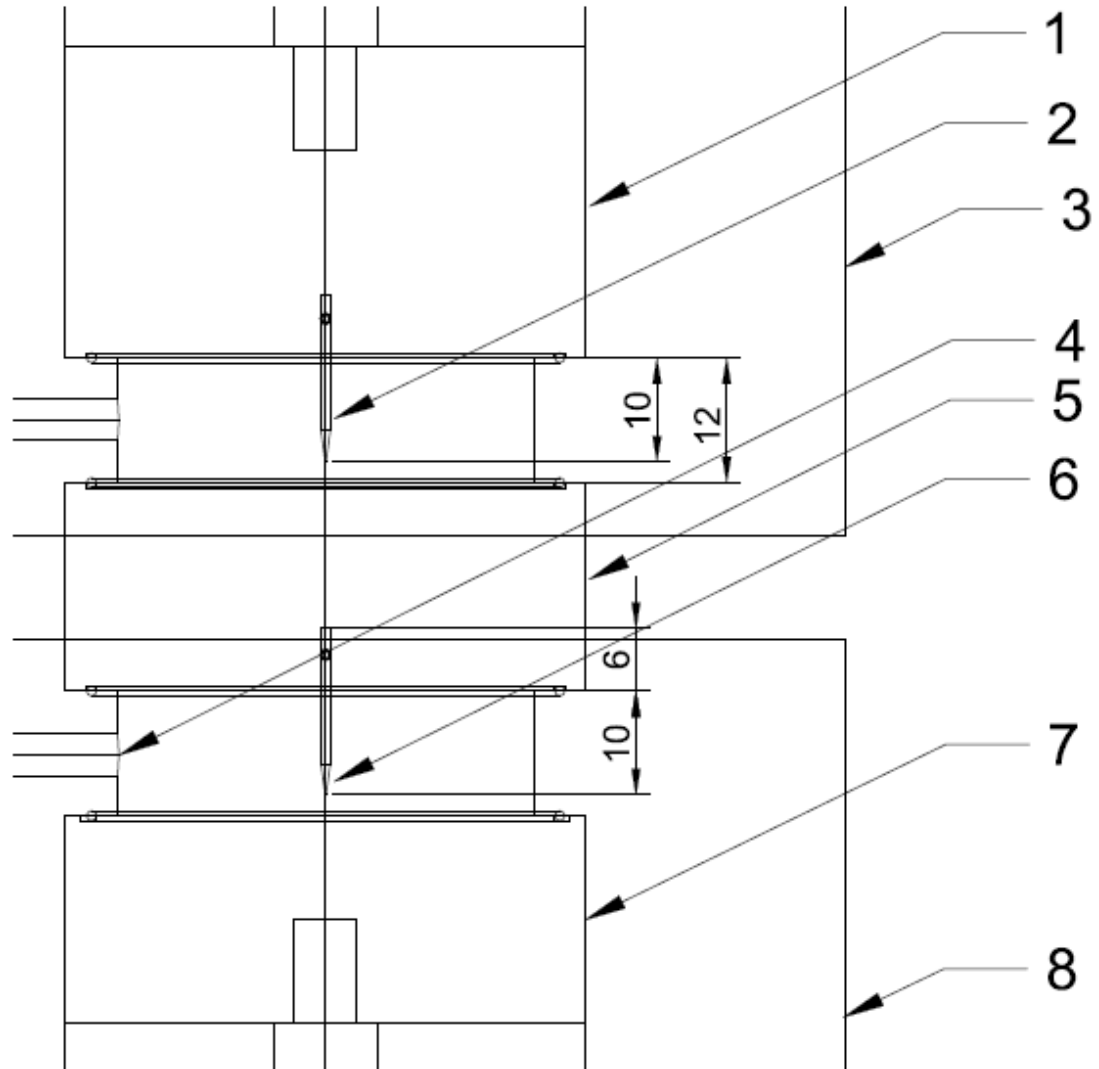


Figure 8.1 Stacked point-plane electrode topology's in multi-gap switch. 1 – Brass HV point electrode holder and HV connection, 2 – Point electrode, 3 – Black nylon upper body, 4 – Gas inlet, 5 – Brass middle electrode plane and point holder, 6 – Point electrode 2, 7 – Brass Ground plane electrode and ground connection, 8 – Black nylon lower body.

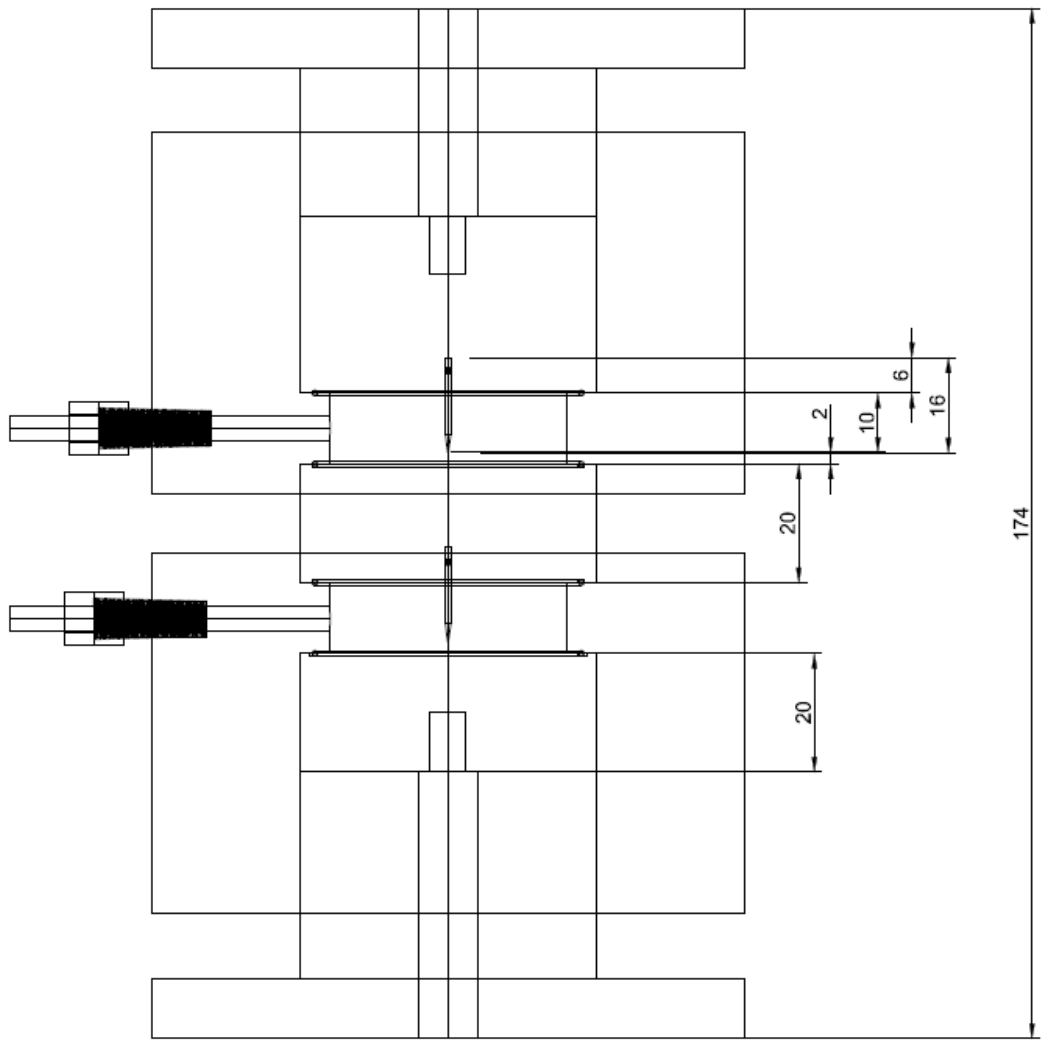
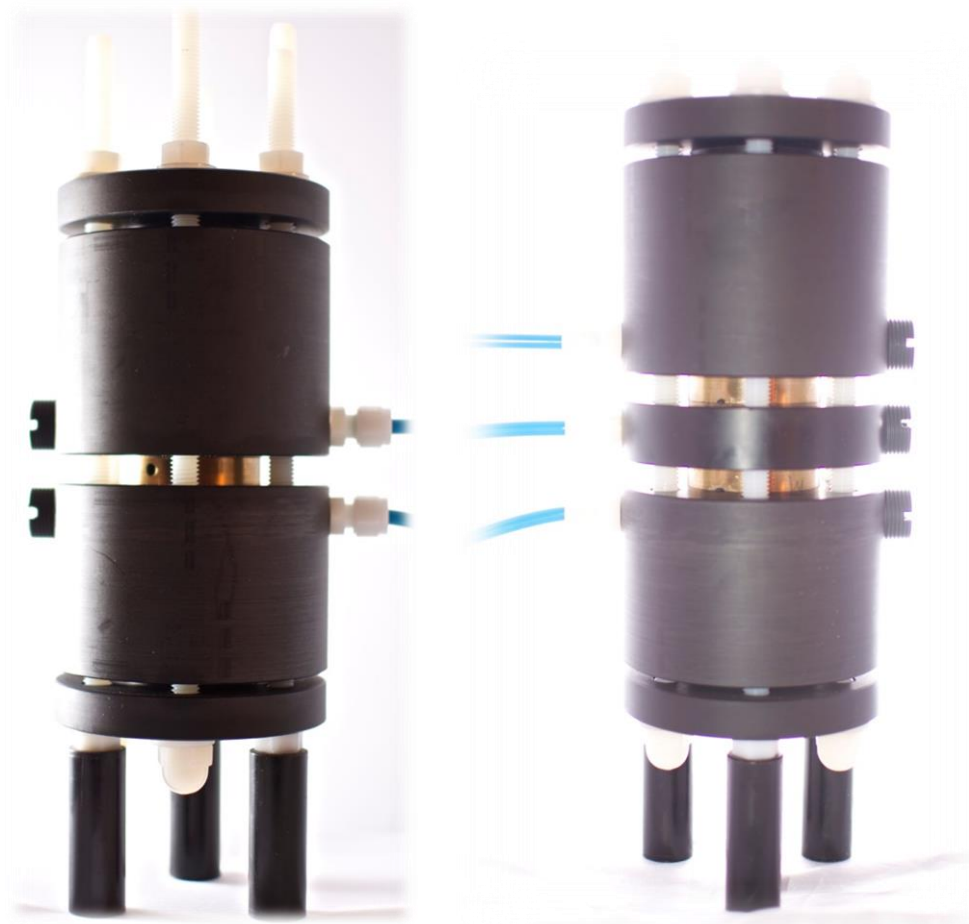


Figure 8.2 Schematic of 2 stage multi-gap spark switch.



(a) 2 stage spark switch.

(b) 3 stage spark switch.

Figure 8.3 Photographs of multi-stage switches.

It was required that a test system be created to measure: the self-breakdown voltage; the corona discharge inception voltage; and the voltage-current pre-breakdown relationship. Bottled air was used as gas medium in the switch, the switch was pressurised up to 0.4 MPa, positive and negative energisation was used. Details of the experimental set up and procedure can be found in Section 3.2 and Section 3.3 for the breakdown and corona observation experiments respectively.

8.2 SELF-BREAKDOWN VOLTAGE OF MULTI-STAGE SWITCH FILLED WITH AIR

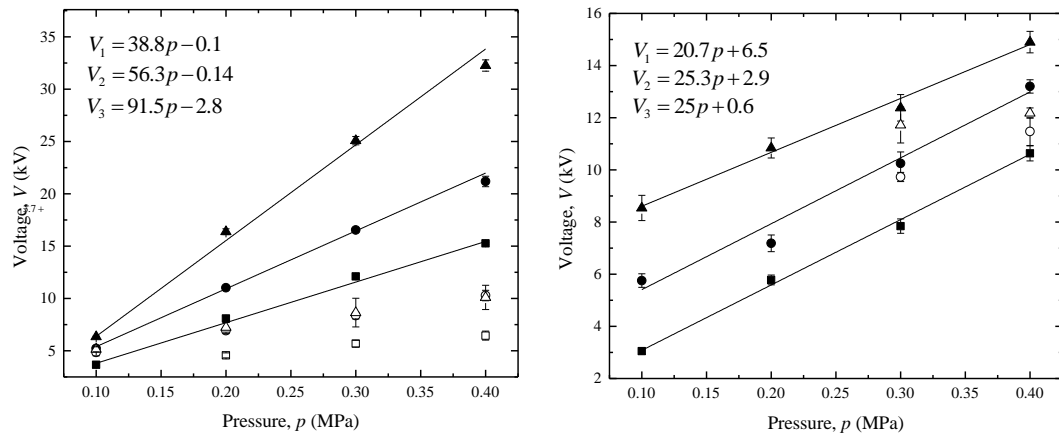
The aim of this chapter was to determine the performance of point-plane multi-stage topology based on the topology which was developed and investigated in Chapter 5, with

additional stages. For a spark switch, there are many aspects that are of vital importance, and breakdown voltage is one of the most important factors. In this section, the breakdown voltage is investigated with respect to the number of spark gaps, energisation polarity, gas type, and pressure. Figure 8.4 shows the breakdown voltage for the negative polarity with 1, 2, and 3 spark-gaps. Each data point in this chapter is an average of 30 measurements; error bars show the standard deviation. The switch was filled with a fresh portion of gas before the tests and the gas was changed after each run of 30 measurements.

As before, and in this chapter, an empirical fitting procedure was used to fit the experimental points with linear empirical functions using OriginPro 9.0 software package. The empirical equations with corresponding coefficients which describe these linear fit lines with breakdown voltage, V_{br} (kV) as a function of pressure, p (MPa):

$$V_{br} = Ap + B \quad (8.1)$$

where A (kV/MPa) and B (kV) are fitting coefficients, given in these figures for each combination of polarity of the applied voltage and the presence and absence of the corona electrodes.



(a) Negative energisation

(b) Positive energisation

- 1 spark gap breakdown voltage
- 2 spark gaps breakdown voltage
- ▲ 3 spark gaps breakdown voltage
- 1 spark gap corona inception voltage
- 2 spark gaps corona inception voltage
- △ 3 spark gaps corona inception voltage

Figure 8.4 Breakdown and corona initiation voltage of air filled multi-stage switches.

The breakdown voltage of multi-stage switches is shown in Figure 8.4 for both (a) negative energisation and (b) positive energisation in 1, 2, and 3 stage switches.

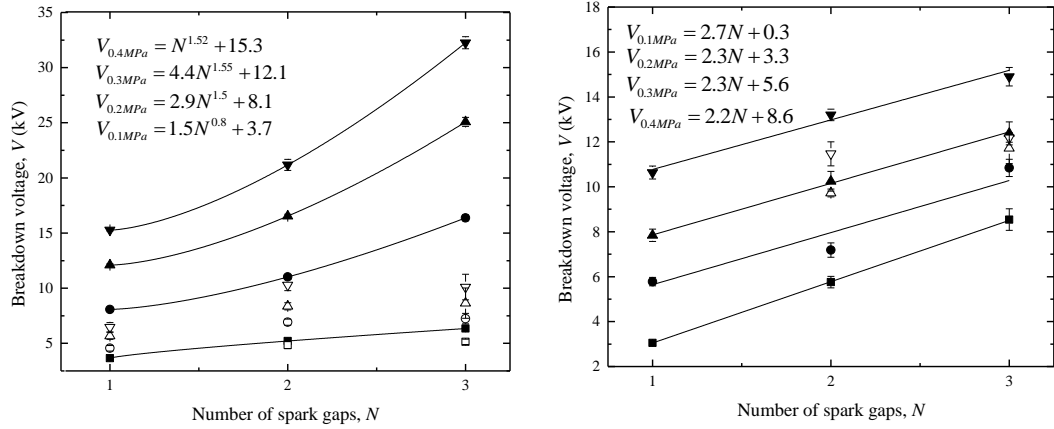
It was found that positive and negative energisation have slightly different effects on the breakdown voltage with regards to pressure for the range of 0.1 - 0.4 MPa air. For all tested switches, the rate that the breakdown voltage increases with regards to pressure increase is higher for negative energisation than positive energisation. For a single gap switch, negative breakdown voltage increases at a rate of ~39 kV/MPa whereas positive energisation increases at a rate of ~21 kV/MPa. This is due to the fact that negative breakdown voltage is strongly dependent on the corona discharge. Corona discharge was initiated in most of the single and multi-gap switch configurations at much lower voltages than positive energisation corona discharge. The pre-breakdown discharge initiation and current will be discussed in its own right.

To compare breakdown voltages with an increasing number of spark gaps, it is convenient to consider the results as a function of the number of gaps, Figure 8.5. In Figure 8.5(b), positive energisation is fitted with the line of best fit using the linear function given in Equation (8.1). However, it is not suitable to fit negative breakdown voltage in Figure 8.5(a) with a linear function and so a line of best fit with power function:

$$V = DN^A + B \quad (8.2)$$

was used, where V (kV) is the breakdown voltage, N is the number of gaps, and A , B (kV), and D (kV) are fitting coefficients.

Breakdown voltage is a key parameter for spark switches, and this investigation looks to see how using additional spark gaps can increase the breakdown voltages of the multi-stage switches equipped with the point-plane topology. Figure 8.5 presents the breakdown voltage of 2 mm spark gaps as a number of switch stages using (a) negative energisation and (b) positive energisation. Adding additional spark gaps stages increases the breakdown voltage significantly, it's also expected that the voltage across all the spark gaps is graded due to corona discharge in each individual gap. Corona discharge spreads the charge amongst the different stages of the spark switch, resulting in reduced voltage across a single spark gap stage. Additional stages and corona grading result in more uniformly distributed stress across each gap and in an overall higher breakdown voltage for the whole switch. The relationship between the number of spark gaps and the breakdown voltage is not the same for positive and negative energisation.



(a) Negative energisation

(b) Positive energisation

- | | |
|-----------------------------|------------------------------------|
| ■ 0.1 MPa breakdown voltage | □ 0.1 MPa corona inception voltage |
| ● 0.2 MPa breakdown voltage | ○ 0.2 MPa corona inception voltage |
| ▲ 0.3 MPa breakdown voltage | △ 0.3 MPa corona inception voltage |
| ▼ 0.4 MPa breakdown voltage | ▽ 0.4 MPa corona inception voltage |

Figure 8.5 Breakdown voltage as a function of the number of spark-gaps in air.

Non-uniform field topologies used in multi-stage high-repetition switches, grade voltage between the stages of the switch with charge transferred by the corona discharge current, to increase the breakdown strength and the improve voltage recovery [Harrower 2001]. Therefore, it is expected to similarly increase breakdown strength in single shot regime implemented in this research. Voltage grading achieved in repetitive regimes (>1 kHz) distributed the voltage between shots in <1 ms. Consequently, it is expected there will be ample time for voltage grading in the single shot regime used in this research [Harrower 2001].

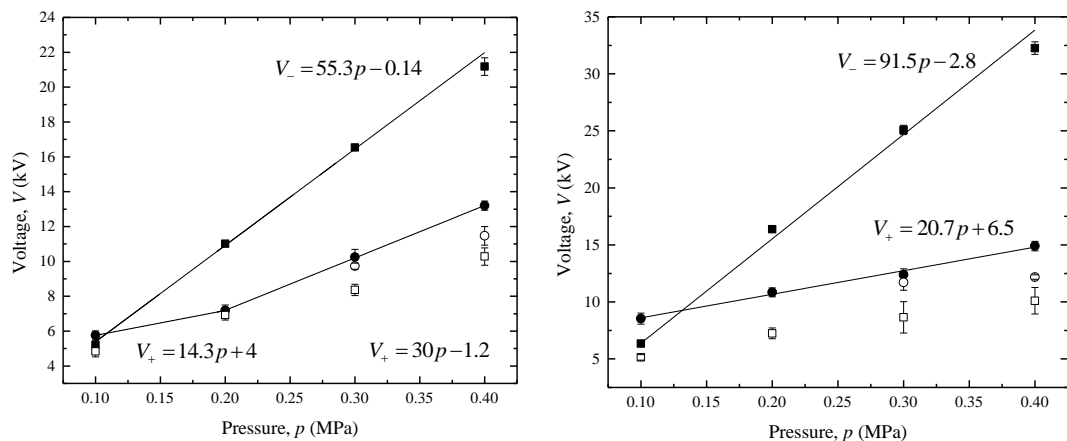
For positively energised multi-gap switches, in the pressure range 0.1-0.4 MPa, the breakdown voltage increases linearly at rate of ~2.2 - 2.7 kV/spark-gap for all pressures. The rate at which the breakdown voltage increases is similar with 1, 2 and 3 stages with a mostly consistent difference across the pressure ranges which is likely due to the fact that there is little corona discharge for positive energisation to have significant impact on the breakdown voltage.

In the case of negative energisation, the breakdown voltage of the multi-gap switch does not increase linearly with pressure in the pressure range used in this research. It was shown that the best empirical fit to the experimental data is provided by an allometric fitting for the negative breakdown voltage as a function of the number of spark stages. At 0.1 MPa, it was

found that the breakdown voltage was close to linear with a power fitting of ~ 0.8 . This is likely due to the fact that there is very little pre-breakdown corona discharge. Above 0.1 MPa, the breakdown voltage increases non-linearly with respect to the number of spark gaps with a power of ~ 1.5 for 0.2 MPa up to 0.4 MPa. By increasing the number of spark gaps from 1 to 3, the breakdown voltage has increased by ~ 26 kV at 0.4 MPa. To achieve the same increase in negative breakdown voltage by increasing pressure alone, an increase of 0.47 MPa is required for a 2 mm gap.

Negative energisation of multi-gap switches can have much higher breakdown voltages than positive energisation. This is observed and discussed for single gap spark switches too due to negative space charge, Chapter 6. Volumetric space charge significantly screens the electric field around the tip of the point electrode resulting in higher breakdown voltages. This is amplified in multi-gap switches because there are multiple points and multiple space charges amplifying the breakdown voltage increase with each additional spark gap.

To compare breakdown voltages for positive and negative energisation, it is convenient to consider the 2-stage and 3-stage switches, Figure 8.6.



(a) 2 spark gaps

(b) 3 spark gaps

- Negative energisation breakdown voltage
- Positive energisation breakdown voltage
- Negative energisation corona inception voltage
- Positive energisation corona inception voltage

Figure 8.6 Breakdown and corona initiation voltage of a 2 and 3 gap multi-gap switch with positive and negative energisation.

Single gap switches with highly non-uniform topology point-plane electrodes were investigated in detail in Chapter 5 and Chapter 6. It was found that there is a critical

electrode separation, d_{crit} for a given point electrode and pressure where positive and negative breakdown voltages are equal. Using this data, the multi-stage switch was designed with multiple spark gaps in the region of the critical gap for a soft-tone gramophone needle. The distance is fixed at 2 mm in this case, so it is not possible to find critical gaps for multi-gap switches in this investigation. However, the critical gap is a function of pressure and since pressure is the controlling factor in this investigation of multi-spark-gap switches, a critical pressure can be found instead of a critical gap. A critical pressure, p_{crit} , of ~0.11 MPa and ~0.13 MPa was extrapolated for the 2 and 3 stage spark switches respectively. The positive and negative breakdown voltages in the single gap switch did not intersect in the pressure ranges discussed. However, from the observed trend between breakdown voltage and pressure, it was extrapolated that the critical pressure would be ~0.05 MPa.

The critical pressure increases as the number of spark-gaps is increased. As has been discussed in Chapter 5, the critical gap and pressure is dependent on the pre-breakdown corona activity. The increase in the number of stages, where corona discharge is present, grades the voltage between the different stages resulting in reduced magnitude at each point electrode. Therefore, higher voltages are required to initiate corona and as such the critical pressure increases.

The breakdown voltage at which the critical separation occurs is also an important operating parameter. The critical voltage, V_{crit} , for a single 2 mm gap was extrapolated to be 1.8 kV at a pressure of ~0.05 MPa. The critical voltage increases as the number of stages is increased and the critical pressure increases to ~5.9 kV for 2 spark gaps and ~9.2 kV for 3 spark gaps at 0.11 MPa and 0.13 MPa respectively. Using multi-gap switches significantly increases the critical voltage by ~4 kV with each additional spark gap. This is useful for practical operations that might require higher breakdown voltages.

This investigation has shown that the critical parameters for attaining similar breakdown voltages for positive and negative energisations obtained in Chapter 6 can be achieved in multi-gap switches. Furthermore, using multiple gaps increases the critical breakdown voltage significantly.

To aid in the further understanding of the difference between positive and negative breakdown voltages and for optimisation of the performance of triggered multi-stage switches, the corona characteristics were investigated. The breakdown voltage graphs have displayed the corona initiation voltage. However, it is also important to consider them carefully in their own right as well as the pre-breakdown current-voltage relationships.

8.3 CORONA INCEPTION VOLTAGE OF MULTI-STAGE SWITCH FILLED WITH AIR

Initially, it is important to establish, would corona discharge be initiated in the switch at a specific gas pressure or not. An initiation of corona discharge at low voltages relative to the breakdown voltage will allow extensive space charge to develop and can lead to the increase in breakdown voltage. Figure 8.7 shows the corona discharge inception voltage as a function of (a) pressure, and (b) number of spark gaps. In Figure 8.7(a), empirical fitting procedure was used to fit the experimental points with linear empirical functions using OriginPro 9.0 software package. The empirical equations with corresponding coefficients which describe these linear fit lines with breakdown voltage, V_c (kV) as a function of pressure, p (MPa):

$$V_c = Ap + B \quad (8.3)$$

where A (kV/MPa) and B (kV) are fitting coefficients. Figure 8.7(b), was plotted with interconnected data points and not a best fit function.

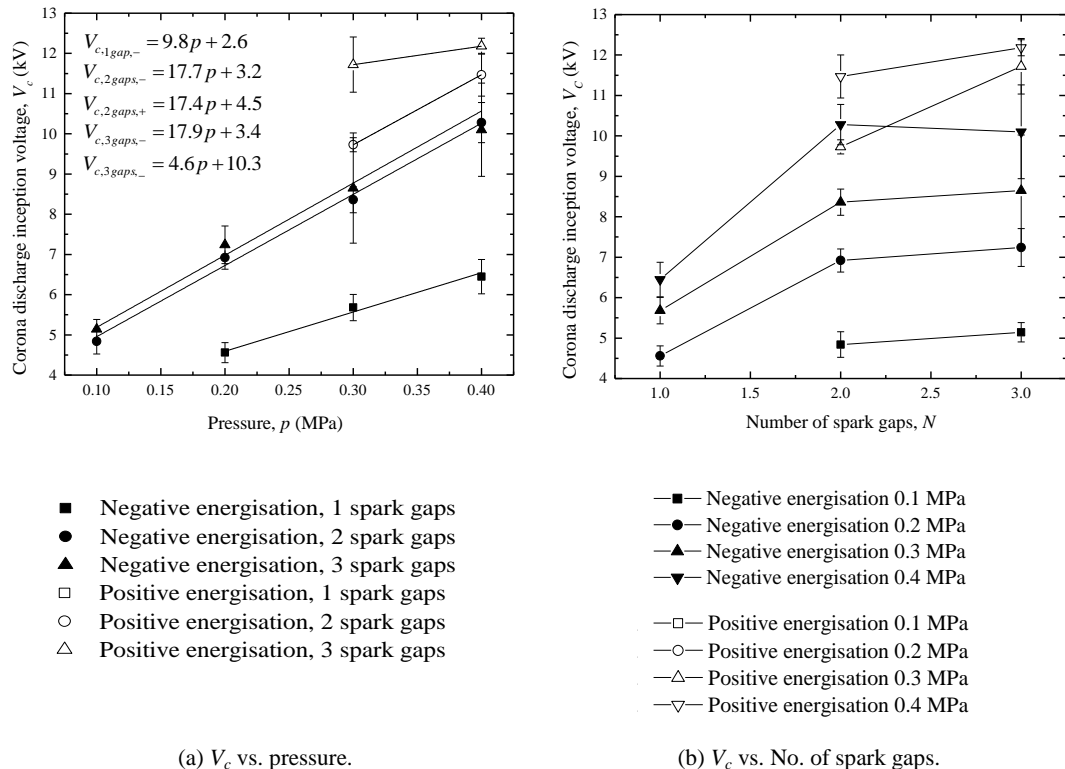


Figure 8.7 Corona inception voltage of multi-stage switches with respect to (a) Pressure, and (b) number of spark gaps.

Figure 8.7 shows that for negative energisation, corona inception voltage for multi-stage switches is larger than for a single stage 2 mm gap. The corona inception voltage for switches of 1, 2 and 3 stages with negative energisation increases linearly and at the same rate with increasing pressure. The corona inception voltage for the 2 and 3 stage switches are similar with 3 stages being only ~0.5 kV larger than 2 stages. However, the multi-stage switches have a 2-fold higher corona inception voltage than a single spark gap.

While negative corona discharge is present across most of the pressure range for switches with 1, 2, and 3 stages, positive energisation corona discharge was only detectable at higher pressures, above 0.3 MPa for multi-gap switches and 0.35 MPa for a single spark gap. Positive corona discharges, if present, have a higher inception voltage than negative energisation.

The initiation voltage of corona discharge has been discussed. However, to get a more comprehensive understanding of the pre-breakdown corona discharge activity, it is important to obtain the relationship between the applied voltage and the corona current.

8.4 PRE-BREAKDOWN CORONA DISCHARGE VOLTAGE-CURRENT RELATIONSHIP FOR MULTI-STAGE SWITCH FILLED WITH AIR

The relationship between the applied voltage and current ($V-I$ characteristic) is a fundamental characteristic of corona discharge which provides information regarding the space charge in the electrode gap. It was shown in Chapter 7 that the relationship between voltage and current can be used to extrapolate the mobility of the charge carriers and this, in turn, can be used to evaluate the space charge effects on the electric field in the inter-electrode gap. Therefore, the $V-I$ curves for the multi-stage switches have been investigated and the results of this study are given in Figure 8.8. Due to the nature of the waveform capture equipment and process, there were quantisation and sampling limitations. The discrete sampling intervals are a by-product of these limitations.

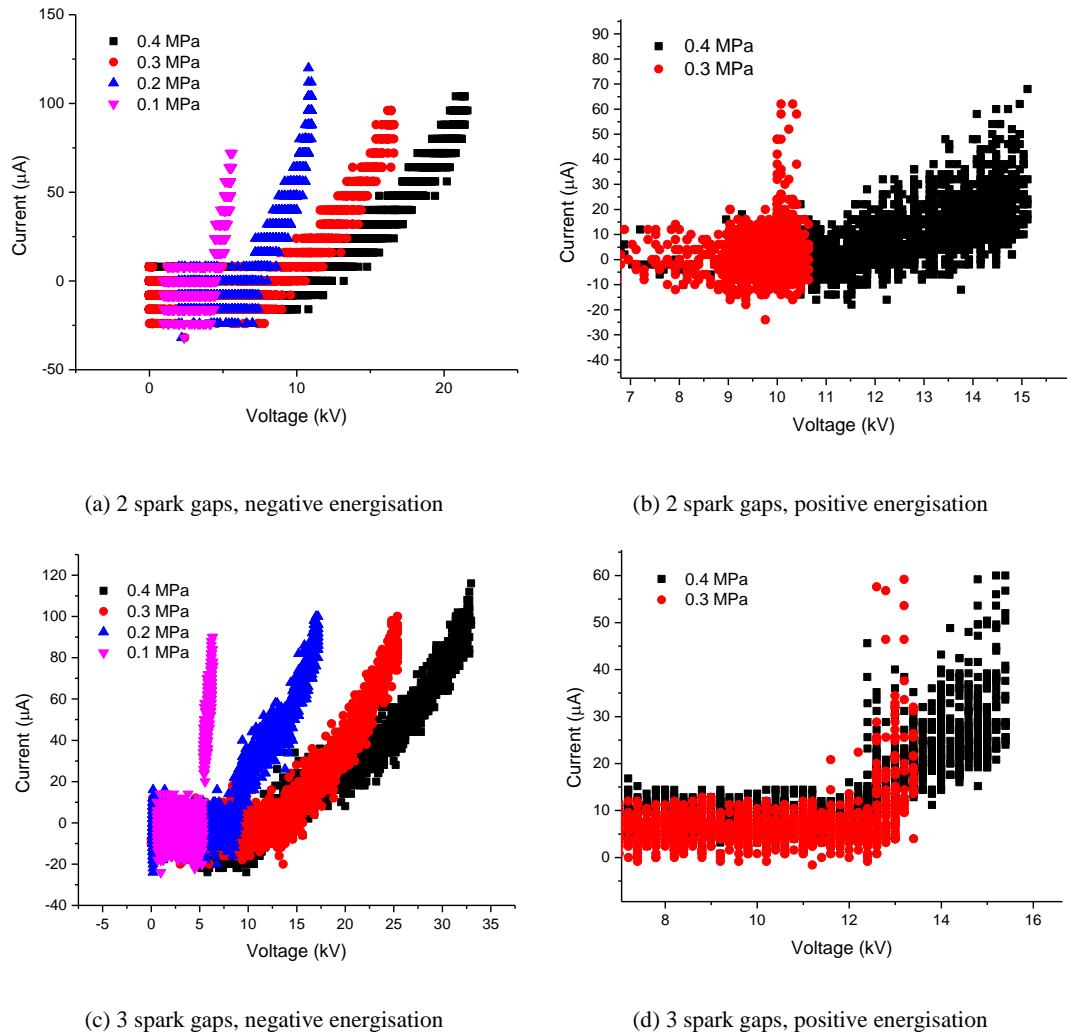


Figure 8.8 Pre-breakdown V-I relationship of multi-gap switches.

As previously discussed, positive corona discharge initiates at higher voltages, and it is not present for pressures 0.2 MPa and below. If there is no corona discharge, the switch will transition directly to a spark discharge. Negative energisation, for both 2 and 3 spark-gap switches provides an appearance of corona discharge preceding spark breakdown.

At low pressures, negative corona discharge initiates close to the breakdown voltage and the current rises rapidly to $\sim 70\text{-}90\ \mu\text{A}$. As the voltage is increased, there is a more gradual increase of current, increasing with respect to V^2 up to $\sim 100\ \mu\text{A}$. The peak current before breakdown is not dependent on the number of spark gaps, and there is little difference in the increasing pressure for the multi-gap switches.

Positive corona discharge has a less gradual increase of current with voltage. In the multi-gap switches, the current rises rapidly from the point of initiation. However, compared to negative energisation, there is far less corona discharge current. The magnitude of the current

is dependent on the gas pressure, at low pressures a spark develops quickly after the initiation of corona and the current only reaches $\sim 20 \mu\text{A}$. When the pressure is increased from 0.3 MPa to 0.4 MPa, there is a longer period before spark breakdown and corona can develop up to $\sim 35 \mu\text{A}$. The number of spark gaps has little effect on the positive energisation corona discharge voltage-current relationship. The only significant effect of increasing the number of spark gaps on the voltage-current relationship is the initiation voltage and maximum voltage before spark breakdown.

The significantly higher current in the pre-spark breakdown corona discharge observed with negative energisation explains why there is higher breakdown voltage compared with positive energisation. The corona discharge current of the multi-stage switches is ~ 5 -fold higher before spark breakdown occurs for negative energisation compared to positive energisation. The significantly higher current means much more charged particles are present in the discharge gap which results in much more significant space charge screening, discussed in Chapter 6. The next section discusses the operation of the multi-spark switches in a triggered regime.

8.5 TIME DELAY TO BREAKDOWN IN MULTI-STAGE SWITCH FILLED WITH AIR

This thesis has considered the multi-gap switches operating in self-closing regimes, triggering by increasing the DC voltage. In many practical applications, it is required that the switches can be DC energised to a desired pressure where it will remain open until triggered. The DC energised switch should trigger consistently and with low time delay jitter. This section discusses the time delay to breakdown and its jitter of the multi-gap switches.

The experimental system designed to complete this work is discussed in Section 3.5. DC energised switches are triggered by energising one of the middle electrodes with a triggering pulse generated by the Blumlein circuit. The switches were energised with DC high voltage and a triggering pulse of opposite polarity was applied to the middle (or second from top) electrode. The switch was energised from 1 kV to V_{BD} with 1 kV increments and the time from the application of trigger voltage capable of causing breakdown until the collapse of voltage was recorded as the breakdown time. The time to breakdown was also measured using the current signal from the Pearson current monitor (model 6585, 250 MHz

bandwidth) on the ground electrode. For this investigation, 10 measurements were taken to ensure accurate results.

The time delay to breakdown of the multi-stage switches was measured using positive and negative DC energisation with air pressure between 0.1 MPa and 0.4 MPa. Positive and negative energisations have slightly different responses to increasing pressure and DC energisation and so will first be considered separately. Figure 8.9 and Figure 8.10 show the time delay to breakdown of the positively energised multi-stage switches for 2 stage and 3 stage switch respectively.

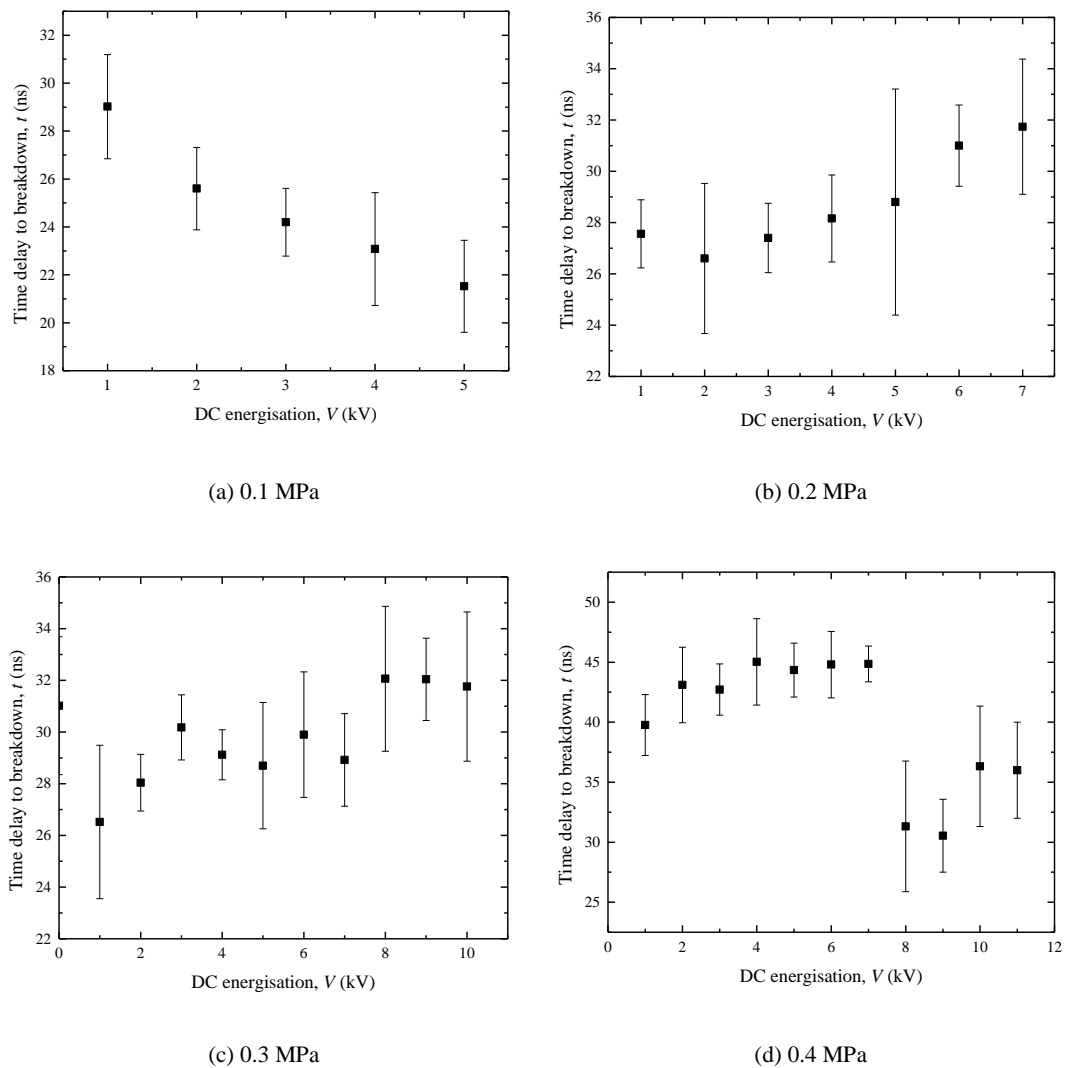


Figure 8.9 Time delay to breakdown of a 2 stage spark switch. Positive DC energisation.

As the DC voltage is increased, the time delay to breakdown is affected. At 0.1 MPa, the time delay to breakdown reduces as the DC voltage is increased, Figure 8.9(a). As the DC

energisation level is increased by 1 kV, the time delay to breakdown reduces by ~1 ns. Maintaining experimental conditions and diagnostic set up allows for resolution of 1 ns jitter. Jitter measurement is a comparative shift in relation to previous measurements and if the rise time of the measurement equipment is larger than the jitter, it is consistent for all measurements and therefore the relative shift in time can still be resolved. The time decreases at a rate of ~1 ns/kV, equal to the rate of rise of the triggering voltage impulse. This is explained by the fact that raising the starting potential by 1 kV means the triggering pulse only needs to reach 1 kV lower level to cause breakdown. Therefore, reducing the impulse breakdown level by 1 kV results in a 1 ns shorter delay. There is no detectable corona discharge in the 0.1 MPa pressure with 2-stage switch, and so the time delay is easily explained.

When the pressure is increased to 0.2 MPa and above, Figure 8.9(b-d), the time delay increases when the DC energisation is increased. The rate of rise in time is ~1 ns/kV for 0.2 MPa and ~0.7 ns/kV at 0.3 MPa and 0.4 MPa. There is no corona discharge at 0.2 MPa but, at 0.3 MPa and 0.4 MPa, there is detectable steady corona discharge just prior to breakdown. It is assumed that even though there is not steady corona current, a dark pre-spark partial discharge is present creating space charge screening. Space charge screening effects could reasonably account for the increase in time delay as it prevents the formation and propagation of discharges.

At 0.4 MPa, the time delay increases as DC voltage is increased until 8 kV. From 7 kV increasing to 8 kV, the time delay decreases from ~45 ns to ~30 ns. This is the shortest time delay for the 0.4 MPa pressure as when the DC voltage is increased further the time delay increases again. The sudden reduction is likely due to more intensive pre-spark partial discharge activity such as current pulses and flashing corona discharge. Steady state corona discharge activates at just a couple of kV higher, ~11.4 kV and so it is likely that the sudden drop is related to corona discharges initiation. Figure 8.10 shows the time delay to breakdown of the 3 stage switch with positive DC energisation.

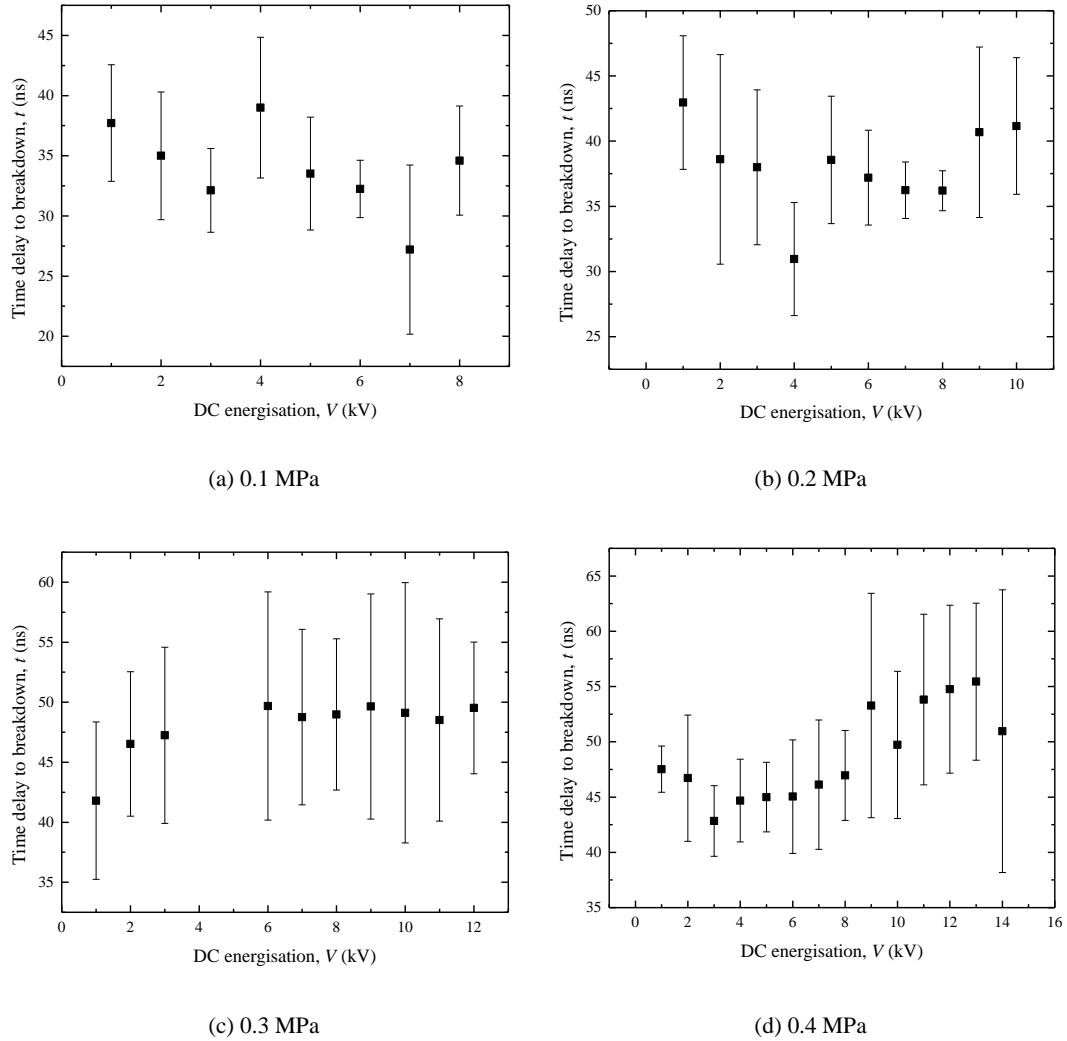


Figure 8.10 Time delay to breakdown of an air filled 3 stage spark switch. Positive DC energisation.

The 3-stage spark switch results for positive energisation, Figure 8.10, follow a similar pattern as described for the 2 spark gap switch. The time delay for 0.1 MPa and 0.2 MPa pressures, reduced on average ~ 1 kV/ns, Figure 8.10(a) and (b) respectively. At 0.1 MPa at 7-8 kV the time begins to increase and at 0.2 MPa the time starts to increase at ~ 8 kV.

It was observed at ~ 4 kV for all pressures, the breakdowns occurred unpredictably compared to all other tests. At 0.1 MPa, the time delay increased out of trend with surrounding results. At 0.2 MPa it reduced significantly, and at 0.3 MPa, there were no breakdowns at all. No reasonable explanation can be given at this point as to why there was trouble at this particular DC energisation. It can be hypothesised that 4 kV was the voltage at which the field was sufficiently high to inject electrons from the tip of the needle into the gas.

For pressures above 0.2 MPa, the time delay to breakdown starts to increase as the DC energisation level is increased. The time delay increases on average at ~ 0.9 ns/kV, similar to the rate at which it increases in the 2 spark gap switch. However, at 0.4 MPa, there was no point at which the time rapidly reduced similar to Figure 8.9(d). To try to explain why there is not a sudden reduction in time delay, the pre-breakdown activity was considered. The steady state corona discharge is only present at 0.3 MPa and 0.4 MPa where it initiates at 11.8 kV and 12 kV respectively, closer to the self-breakdown voltages compared to the 2 stage switch. There is just 1-2 kV between the corona inception voltage and the self-breakdown voltage. Therefore, corona discharge has less impact on the time delay to breakdown, and there is no sudden reduction.

Having identified the phases that the time delay to breakdown results go through as the DC energisation is increased for 2 and 3 gap switches positively energised, they can be discussed and compared relatively. As expected, when the air pressure is increased, the time delay to breakdown increases also. This is due to two contributing factors: the increased pressure increases the breakdown strength and as such the breakdown occurs further into the triggering impulse; and the increased density of the gas can reduce the mobility of charge carriers and slow down the discharge progress. In 0.4 MPa air, the 3 stage switch time delay increases from ~ 38 ns to ~ 47.5 ns at 1 kV energisation, Figure 8.10(a) and (d) respectively.

Increasing the number of spark gaps from 2 to 3 results in an increased time delay. With an extra spark gap to close, there are a few reasons why the time delay to breakdown could be increased, the extra gap means there is a time delay for initiation of discharge and extra delay for propagation of discharge. Also, the extra spark gap means the charge is distributed further over an extra stage, and there is less voltage forming the discharge. It is hard to compare the different pressures and stages because there are such significant increases and decreases due to the space charges. However, using 1 kV energisation, it is obvious that there is an increase in time delay of $\sim 8 - 16$ ns. The shortest time delay of all positive energisation pressure tests was observed at ~ 21.5 ns with 5 kV energisation using the 2 gap spark switch. It is shown that negative energisation can produce even shorter time delays of 18.8 ns and ~ 18 ns, Figure 8.11(a), and Figure 8.11(d) respectively. Figure 8.11 shows the time delay of the negatively charged 2 spark gap switch.

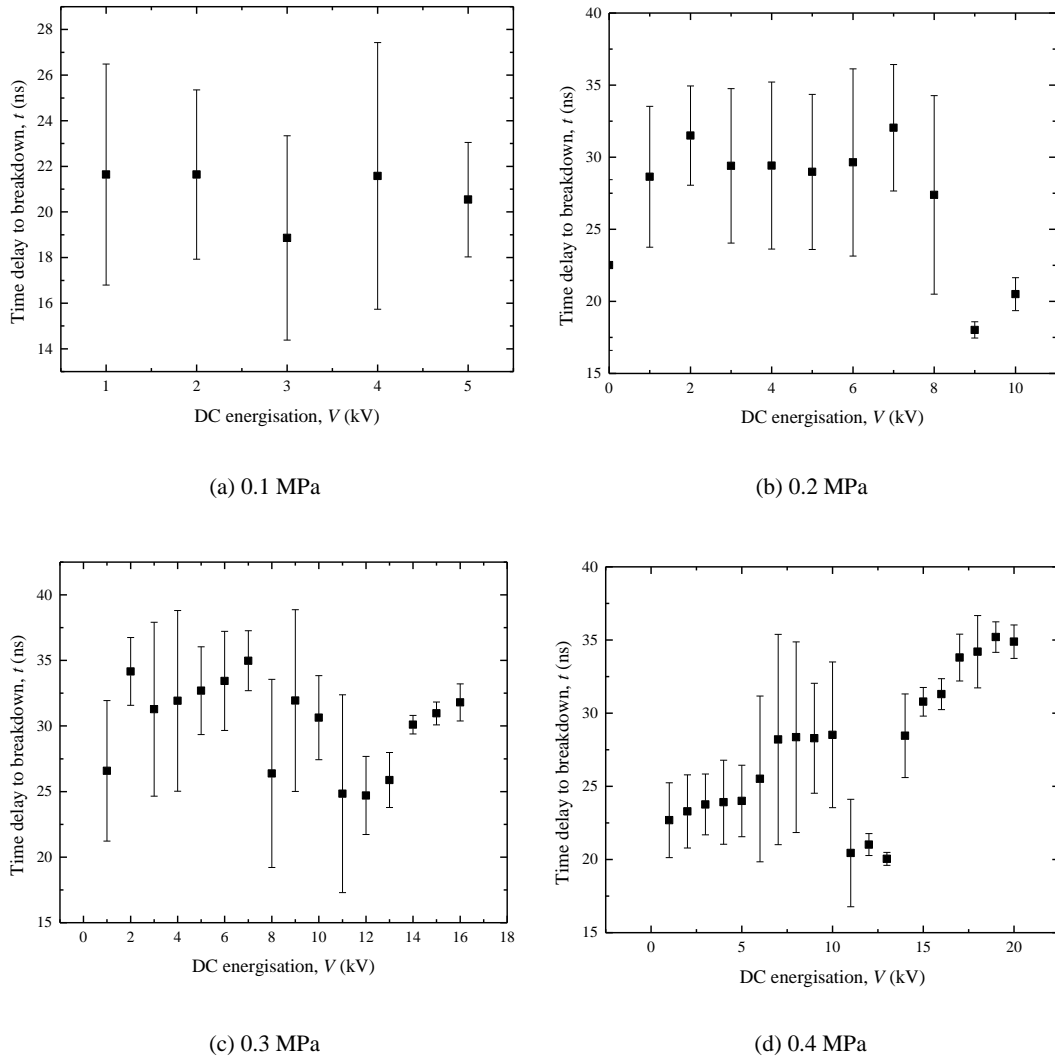


Figure 8.11 Time delay to breakdown of an air filled 2 stage spark switch. Negative DC energisation.

With the negatively energised 2 stage switch pressurised at 0.1 MPa, the time delay to breakdown reduces as the DC voltage is increased with an average rate of ~ 0.25 ns/kV. This is much slower than the ~ 1 ns/kV occurring in positive energisation and above 0.1 MPa there is no reduction. Above 0.1 MPa, the time delay to breakdown increases as the DC energisation level is increased. At 0.2 MPa, the time delay increases by ~ 0.8 ns/kV and at 0.3 MPa and 0.4 MPa it increases by ~ 1 ns/kV similar to positively energised 2 gap switch. Similarly to positive energisation, it is suggested that the time delay increase is a product of space charge screening effects delaying initiation and propagation of discharges.

The time delay to breakdown of the 2 stage negatively energised switch reaches a maximum, where the time delay begins to reduce quickly until just a few kV higher the time delay is the shortest. With 0.2 MPa, the time reduces from ~ 34 ns to ~ 26 ns when the DC energisation is

increased from 7 kV to 9 kV, a 24% reduction. At 0.3 MPa, there is a 29% reduction from ~35 ns to ~25 ns and at 0.4 MPa a 30% reduction was observed from ~26 ns to ~18 ns. The sudden drop in time delay can be loosely correlated to the corona inception voltage occurring a few (0.8 – 2.5 kV) before the drop in time delay. A steady state corona discharge was initiated at ~7.2 kV for 0.2 MPa and the time delay reduced to a minimum at 9 kV. Similarly, corona discharge initiated at 8.5 kV and 10.2 kV for 0.3 MPa and 0.4 MPa respectively and the time delay reached a minimum at 11 kV DC energisation for both pressures.

After the time delay has reached its minimum, it starts to increase again as the DC level is increased. The delay rapidly jumps back up 25-30% with a 1 kV increase and then continues to rise at a rate of ~1 ns/kV.

Both positive and negative energised 2-stage switches display complex relationship with the DC energisation level, pressure, and time delay. However, negative energisation shows a significant improvement in the jitter of the switch, within a defined DC energisation range, that is not observed with positive energisation. Jitter is a key parameter for spark switches in most applications and identifying a switch and operating parameters that can reduce the jitter from up to 10's ns to just ~1-2 ns is an important result. The time delay suddenly shortens by ~10 ns and the jitter significantly reduces from 5 ns to 1 ns.

With negative energisation, there is a clear region of increased stability in the 2 stage switch. Using the multi-gap switch, it would be required that the switch be operated in the DC energisations resulting in ~1-2 ns rather than >5 ns. Figure 8.12 shows the time delay to breakdown of the 3 spark gap switch with negative energisation.

With 3 spark gaps, similar changes in time delay to breakdown occur as in the 2-stage switch. However, the breakdown voltage is ~12 kV larger at ~32 kV while the corona inception voltage is only ~1 kV larger than the 2-stage switch. Therefore, the switch can operate with DC energisation level well exceeding the corona initiation voltage of ~12 kV. This creates a much larger operating range of DC energisation that can provide low jitter performance. The largest range of DC energisation achieving corona discharge jitter stabilisation occurs in 0.4 MPa and 0.3 MPa where the jitter is ~1 - 2 ns. At 0.4 MPa, jitter is low from 20 kV DC energisation up to the breakdown voltage of ~32 kV. Low jitter is achieved between 15 kV and 24 kV for 0.3 MPa, whereas, low jitter is only achieved from 13 kV to 16 kV for 0.2 MPa.

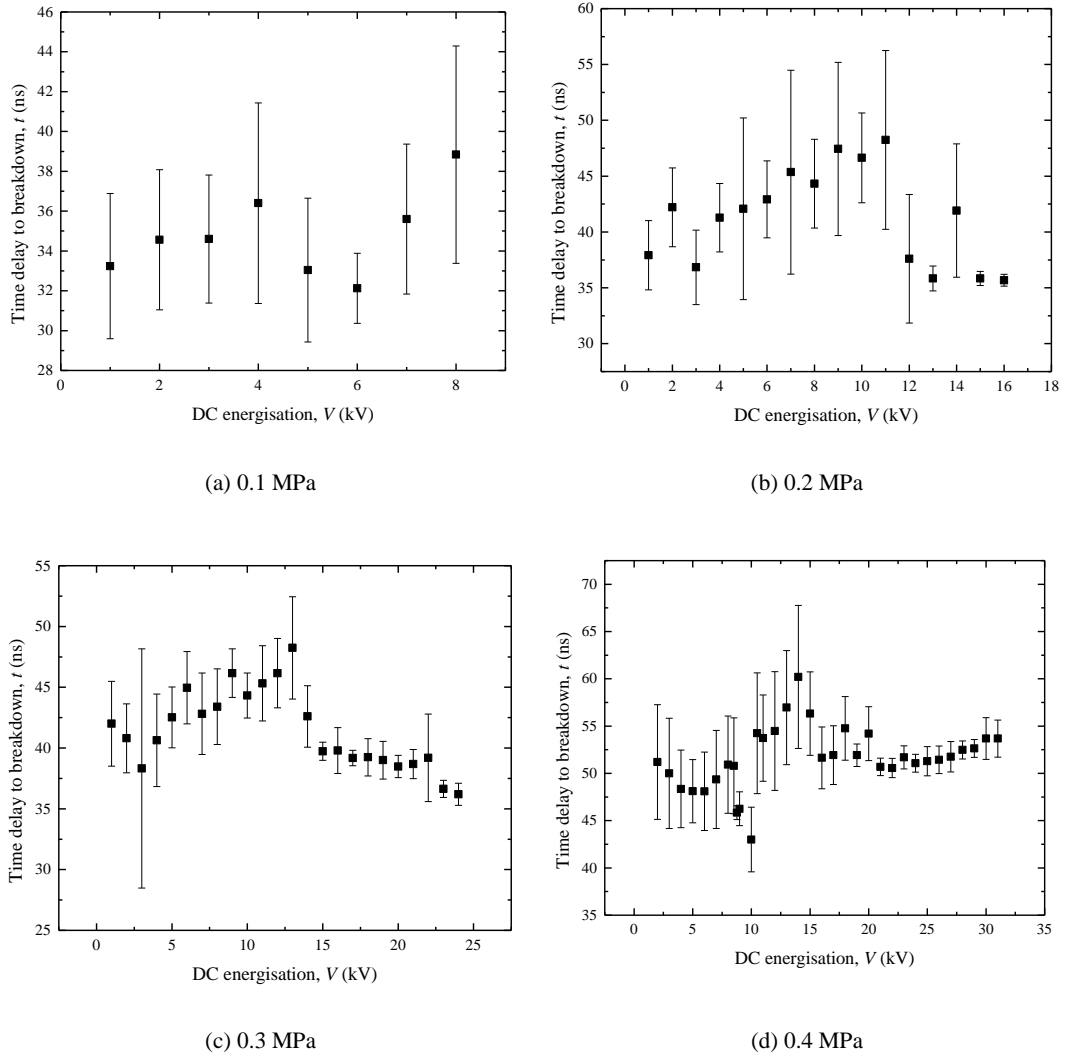


Figure 8.12 Time delay to breakdown of an air filled 3 stage spark switch. Negative DC energisation.

Achieving low jitter is very important for spark switches and should be as low as 4 ns to be considered for some applications. Jitter of 1 - 2 ns has been achieved using spark switches with varying methods but many of them require the energisation level to be close to the self-breakdown strength. To achieve 2 ns jitter laser triggering can require switches to be energised up to 90% of the self-breakdown voltage. The results here show that a multi-gap switch can achieve 1 - 2 ns jitter with just 60% DC energisation. Achieving consistent triggering at lower energisation levels ensures there is no unwanted closer of the switch when there is no trigger impulse.

High performance switches used in pulsed power require low jitter of a few ns to be competitive with currently used switches. This research has looked at developing new switches using bottled air and the multi-gap switch. 1 - 2 ns jitter was achieved with stable

operation of a negatively energised 3 stage switch. The results here are comparable with linear transformer driver multi-gap switches achieving jitter of ~2-4 ns.

8.6 CONCLUSIONS

Concluding the multi-gap switch investigation, there are a number of important results which have been obtained and that are of interest to the pulsed power industry. Building on from the investigation into point-plane topology, a new expandable switch was designed that could increase or decrease the number of gaps easily. Investigating the use of multi-stage switches with the point-plane topology has shown that the breakdown voltage can be increased by adding additional gaps. The rate that the voltage increases is linear with respect to the number of gaps. The breakdown voltage could be predicted reasonably and switches could be reliably designed to have higher breakdown voltage by increasing the number of gaps.

An investigation into corona discharge has shown that corona activity is nearly always present prior to breakdown with negative energisation in the multi-gap switches. However, positive corona discharge only occurs prior to breakdown at 0.3 MPa and 0.4 MPa, and it occurs within 1 - 2 kV of the breakdown voltage. Corona *V-I* curves were obtained for both polarities and all gas pressures in the switch; it was found that the positive energisation pre-breakdown current-voltage relationship is short with a rapid increase in current up to ~20 μA . Negative energisation, on the other hand, increases more gradually up to ~200 μA , which is an order of magnitude higher. Therefore, there are significantly reduced corona discharge effects in the case of positive energisation of the switch. This is the reason why the breakdown voltage is so much lower in single gap switches as well as multi-gap switches and has been discussed in Chapter 5 and Chapter 6.

The final section of this chapter investigated the multi-gap switches in triggered regime. With DC positive and negative energisation ranging from 1 kV up to the self-breakdown voltage in 1 kV increments, the time delay to breakdown was observed for 2-stage and 3-stage switches. It was found that the time delay decreased and increased, as the DC energisation level was increased depending on the magnitude. It is hypothesised that space charge screening effects was the reasoning for the increasing time delay. The jitter with positive energisation averaged ~10 ns and remained high at all DC energisation levels. Negative energisation had similarly high jitter which reduced down to 1 - 2 ns at higher DC energisations.

The compact design of the multi-stage switches makes them useful for the implementation of small foot print pulse power machines. The inter-changeable switches have a diameter of 100 mm and a maximum length, with 3 stages, of 206 mm. Other multi-stage switches in literature can be as small as ~100 mm in length however most of these switches have close to uniform fields, no coronating electrodes and have a fixed number of stages [Woodworth 2010].

This thesis has so far focused on the pre-breakdown processes and the breakdown voltage. However, in multiple pulsed power applications, spark resistance and inductance is arguably the most important aspect of a spark switch. The next chapter discusses the spark resistance and inductance of post breakdown spark plasma.

9. ANALYTICAL MODELLING OF SPARK RESISTANCE

Chapter 9 of this thesis is the natural progression of the direction the work was taking, moving into analysis of the post-breakdown plasma processes. As was discussed in Section 2, there is a need for spark switches with minimal plasma resistance and inductance because many of the applications of spark switches require high current, and fast rising current pulses. Therefore, the next step in this thesis would be to investigate the transient plasma characteristics (resistance of spark and its inductance) after switch closure (after breakdown). This chapter introduces a new approach to simulating the transient plasma resistance based on the models available in literature. Using PSpice software package, models of dynamic plasma resistance have been developed, in order to verify these models transient plasma resistance and inductance was obtained for experimental conditions taken from papers [Braginskii 1958] [Toepler 1906] [Rompe 1944] [Barannik 1975] [Popovic 1974] [Demenik 1968] [Kushner 1985]. Based on the results presented in this chapter, the model which provides the best fit to the experimental results will be identified and recommended for future studies of post-breakdown processes in the plasma closing switches.

Plasma resistance and inductance simulation is of particular interest to researchers developing systems that require ultra-fast rising (ns) high peak current (kA). The plasma resistance and inductance of the spark switches reduce the current magnitude and the rise time and so they look to minimise the effects. These systems could use 1000's of switches and as such modelling such a system requires advanced modelling software such as PSpice. For the first time, this new approach allows for complex systems to be modelled with plasma dynamic resistance. Also, within these complex systems, there are many sparks switches and this is the first approach that would realistically allow for multiple time varying spark resistances to be modelled. This new approach was presented and published in the proceeding of the IEEE International Power Modulator and High Voltage Conference in 2014 [Hogg 2014b].

To simulate dynamic plasma resistance, a basic model for breakdown was developed using PSpice software to represent plasma channel as an electric circuit with lumped elements. A basic HVDC circuit was used with a closing switch (found in the 'eval' library of PSpice software) to simulate a breakdown in the switch. Figure 9.1 shows the basic circuit simulating breakdown with plasma parameters.

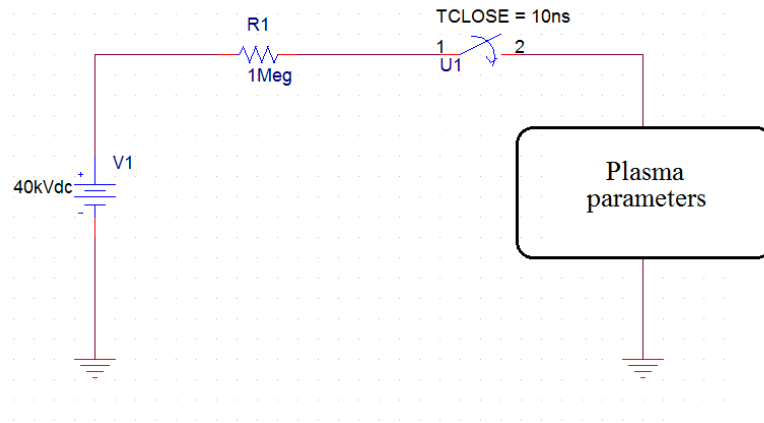


Figure 9.1 Plasma simulation circuit.

A 1 MΩ charging resistor acts as a current limiter and also effectively decouples the circuit from the plasma upon breakdown. The open circuit impedance of the switch was selected as 1000 MΩ. The switch closing with a very fast close time (1 ns), and closed circuit impedance of the switch was selected 0.01 Ω which reasonably simulates a breakdown event in the practical switch. The plasma parameters were initially modelled as fixed parameters, Figure 9.2.

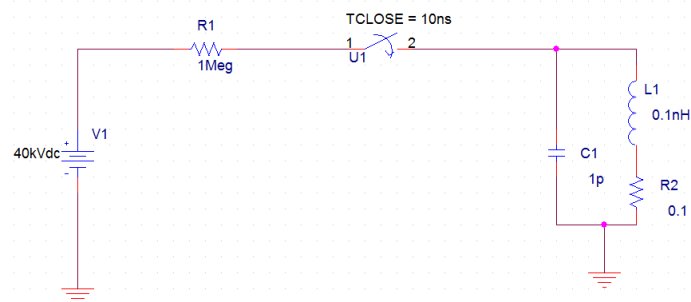


Figure 9.2 Plasma RLC circuit

The next step toward the complete model of transient plasma resistance was to find a way to introduce the time varying plasma resistance. Since PSpice software does not have a resistor component that can be dependent on a function, a voltage controlled current source was used

with a function for plasma resistance. The voltage dependent current source is a component in the ‘analogue behavioural model (ABM)’ library called ‘*Gvalue*’ which is shown in Figure 9.3.

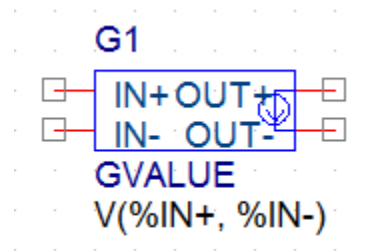


Figure 9.3 ABM model *Gvalue* component

The *Gvalue* component takes a voltage input and outputs a current equal to it with a proportionality given by the expression given to the ‘*value*’. By configuring the *Gvalue* component, as shown in Figure 9.4, it can now represent a dynamic resistance controlled by the function, $r(t)$ given to the *value*.

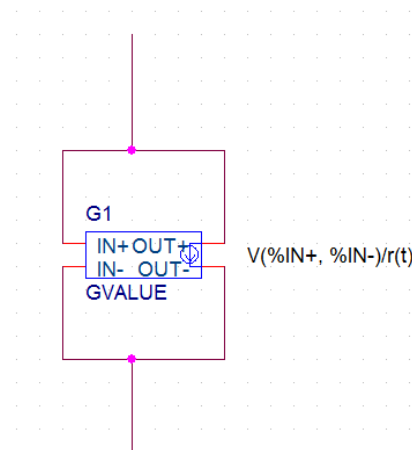


Figure 9.4 Voltage controlled current source. *Gvalue* as a dynamic resistor.

In Figure 9.4, the *value* was the controlling variable function, $r(t)$ which represented the resistance. The *Gvalue* now represents a time varying resistance which is proportional to $r(t)$. By taking data from literature, [Engel 1989], for plasma resistance and re-plotting it in OriginPro 9.0 graphing software, plasma resistance could be represented as a function best fitting the data.

The plasma resistance was fitted with the function:

$$r(t) = at^{-n} \quad (9.1)$$

where:

- $r(t)$ is the plasma resistance,
- a and n are constants,
- and t is time.

Therefore, the dynamic resistance using *Gvalue* component in PSpice software can be simulated as shown in Figure 9.4, where the value includes Equation (9.1) for plasma resistance. To simulate the equation above, there are syntax that must be used in PSpice: time, t is given in PSpice as a variable called 'TIME' and the mathematical operators are: power - ^ and multiply - *. Figure 9.5 shows the voltage controlled current source configured to act as a resistor with resistance equal to Equation (9.1).

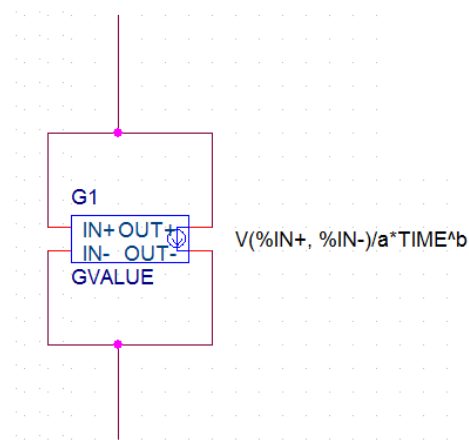


Figure 9.5 Dynamic resistance represented by a fitting curve.

The circuit can be completed using Figure 9.5 configuration for plasma resistance with lumped elements for inductance and capacitance with the DC breakdown simulation experiment. Figure 9.6 shows the basic DC breakdown circuit with time varying plasma resistance from Equation (9.1).

This circuit shows that it is possible to solve PSpice simulations with time varying resistance. However, it does not calculate real time resistance from the current. It is purely based on the time and data from literature.

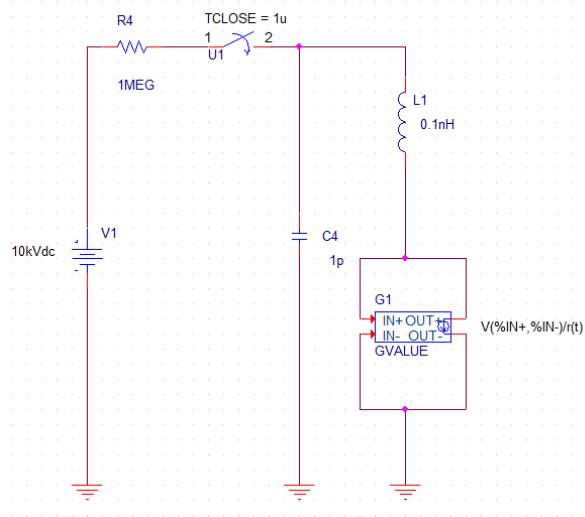


Figure 9.6 Plasma simulation circuit with $r(t)$ Gvalue resistance.

To get realistic dynamic resistance, the transient models from literature (Section 2.2) should be used in place of Equation (9.1). PSpice has the ability to do some basic manipulation of voltage signals using analogue behavioural modelling, and there is enough capability to calculate integrals, powers, sums and multiplications necessary to solve the plasma resistance equations given in literature by Braginiskii, Toeple, Rompe and Weizel, Barannik *et al*, Popovic *et al*, Demenik *et al* and Kushner *et al* which have been discussed in Section 2.2 [Braginskii 1958] [Toeple 1906] [Rompe and Weizel 1944] [Barranik 1975] [Popovic 1974] [Demanik 1968] [Kushner 1985].

To solve these equations using PSpice, the dependent current needs to be represented by a voltage signal to be inputted into the mathematical operators provided in the ABM library. This is achieved by using another ABM component, the current controlled voltage source, which outputs a voltage signal equal to that of the current signal. The current controlled voltage source is the *H* component in the ABM library and is represented with the icon shown in Figure 9.7.

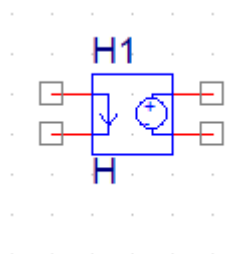


Figure 9.7 PSpice ABM current controlled voltage source.

Placing the current controlled voltage source in-line with the plasma components as shown in Figure 9.8, it takes the current and represents it as a voltage signal without causing negative effects on the current waveform. Figure 9.8 shows the current controlled voltage source in the circuit which simulates breakdown; basic components for plasma resistance have been used for clarity at this stage.

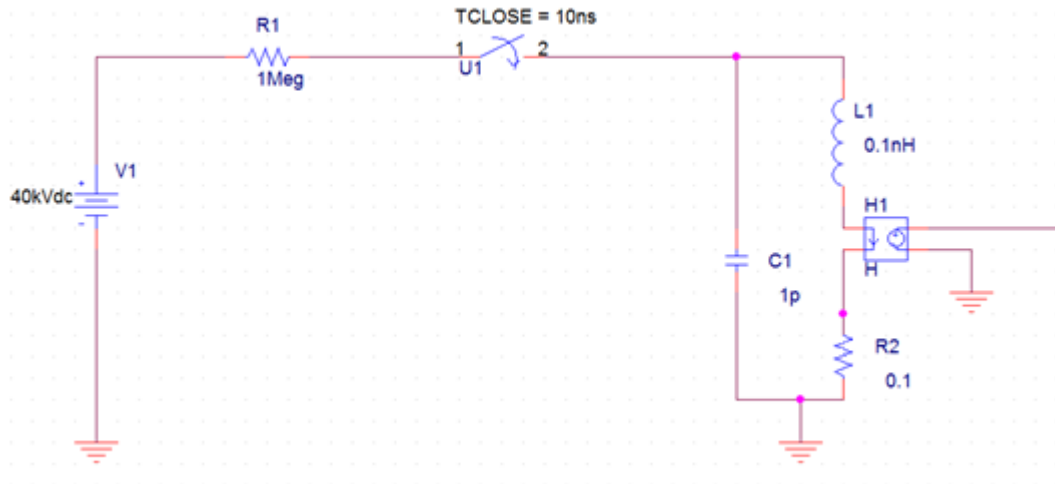


Figure 9.8 Voltage representing current using ABM H component.

Using the configuration in Figure 9.8, the current is now represented as a voltage signal and can now be used with mathematical components to solve the plasma resistance equations from literature. The mathematical components from the ABM library for integration, differentiation, power, addition and multiplication can be seen in Figure 9.9 with their component names in PSpice.

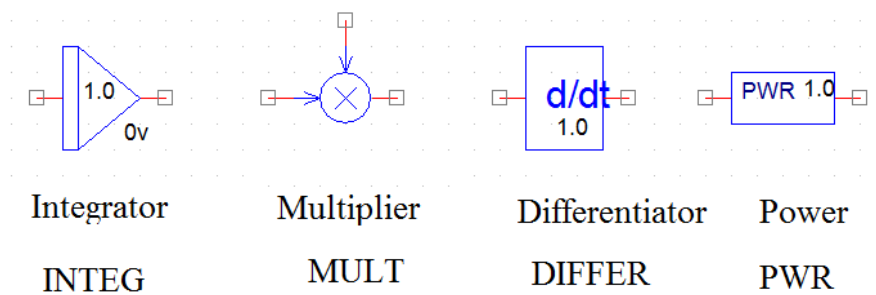


Figure 9.9 ABM mathematical components.

The voltage signal representing current is manipulated using the components above to solve the plasma resistance equations; an example equation from Toepler (Equation (2.12)) [Toepler 1906] has been solved in Figure 9.10.

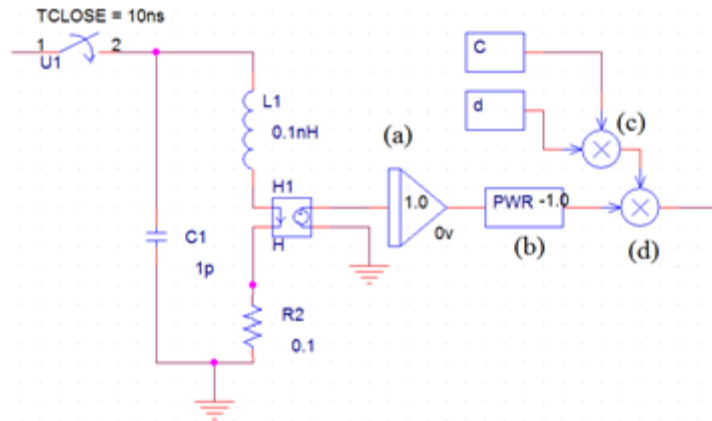


Figure 9.10 Solving Toepler's equation in PSpice (Equation (2.12)).

In Figure 9.10, the plasma resistance equation is solved using the current in the plasma elements. The steps by which the equation is built are listed:

- The voltage signal representing current is first integrated using component (a), as per the stipulation of Toepler's equation. The equation after component (a) is: $\int i dt$.
- Since there is no division component, the power function is used to put the integral of current to the denominator of the equation by raising it to the power of -1 in component (b). The equation after component (b) is: $\frac{1}{\int i dt}$.
- Components (c) and (d) are multipliers which multiply the constants C and d and then multiply them with the output of component (b) to complete the equation: $\frac{cd}{\int i dt}$.

The output of the mathematical manipulation of the current controlled voltage now represents the resistance of the plasma channel as given by Toepler if the current were unaffected by the resistance of the plasma. However, this is not the case and, as such, there needs to be a feed back to change the resistance so that the current can be adjusted appropriately. The value for resistance must now be fed into the dynamic resistance component *Gvalue* shown in Figure 9.5. This will complete a fully self-consistent model where the current depends on the plasma resistance and the plasma resistance depends on the current (via literature equations discussed in Section 2.2). To put the equation into the

Gvalue component, the best method is to create a variable which represents the voltage out of the resistance equation shown in Figure 9.10.

A variable that represents a voltage in a wire at any point in a circuit can be created in PSpice by placing a ‘new alias’. A net alias is a marker placed on the wire with a name which is the name of variable and, in this case, is placed on the output of the mathematical equation for plasma resistance. Figure 9.11 shows how a net alias looks and where it is placed.

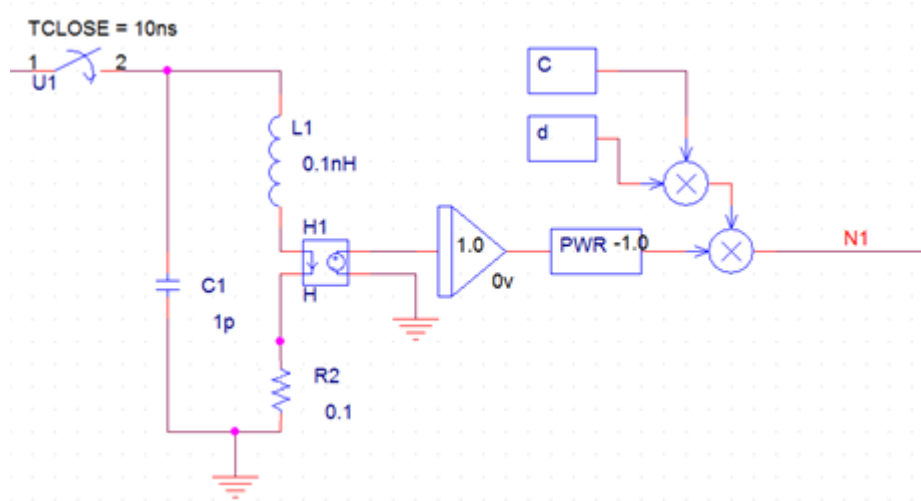


Figure 9.11 Using net alias to set plasma resistance as a variable *N1*.

Using the net alias on the output of the plasma resistance equation, the dynamic plasma resistance is stored in the variable *N1*. Figure 9.12 shows the circuit for calculating the plasma resistance using the ABM components that has been discussed and includes the placement and naming of the net alias which is used to create the dynamic resistance when inputted into the *Gvalue* component *value* in place of the $r(t)$ function.

The circuit shown in Figure 9.12 simulates a self-consistent model for dynamic plasma resistance which is dependent on current which is in turn dependent on plasma resistance (using Toepler’s equation [Toepler 1906]).

This technique has been used to simulate all of the dynamic plasma resistance equations that were discussed in Section 2.2 and the plasma resistance results can be seen with respect to current and voltage.

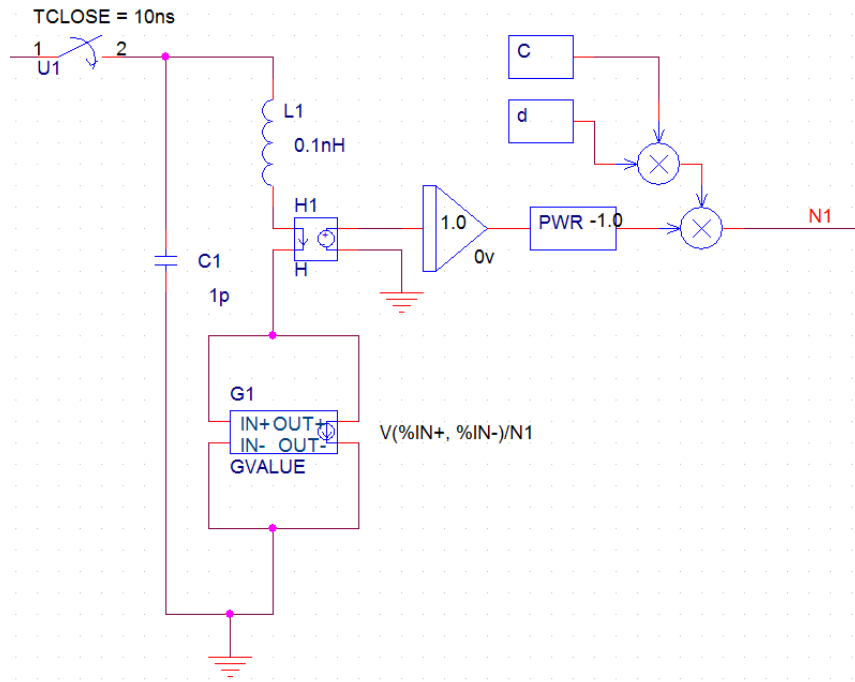
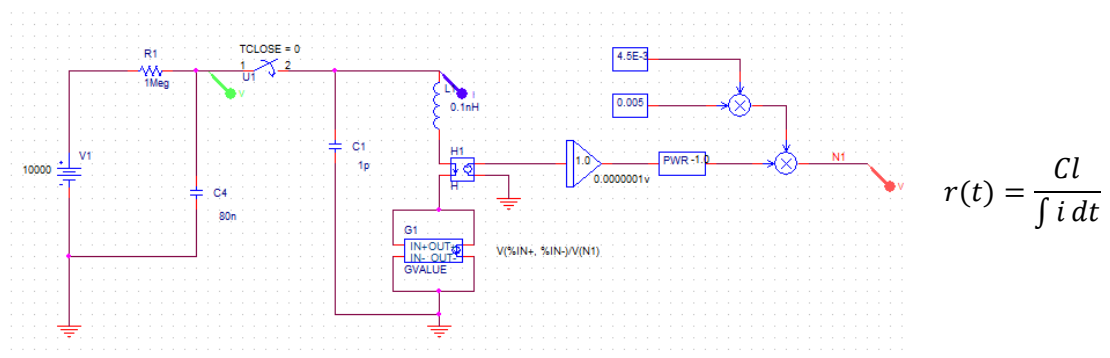


Figure 9.12 Self-consistent plasma resistance model.

Figure 9.13 to Figure 9.17 show the plasma resistance equations, the PSpice simulated models and results for equations suggest by Braginiskii, Toepler, Rompe and Weizel, Barannik *et al*, and Popovic *et al*.



$$r(t) = \frac{Cl}{\int i dt}$$

Figure 9.13 Toepler's equation - plasma model [Toepler 1906].

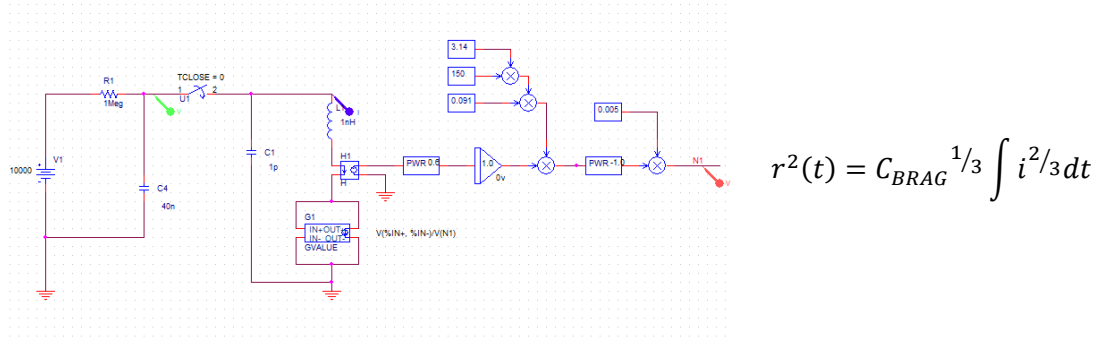


Figure 9.14 Braginskii's equation – plasma model [Braginskii 1958].

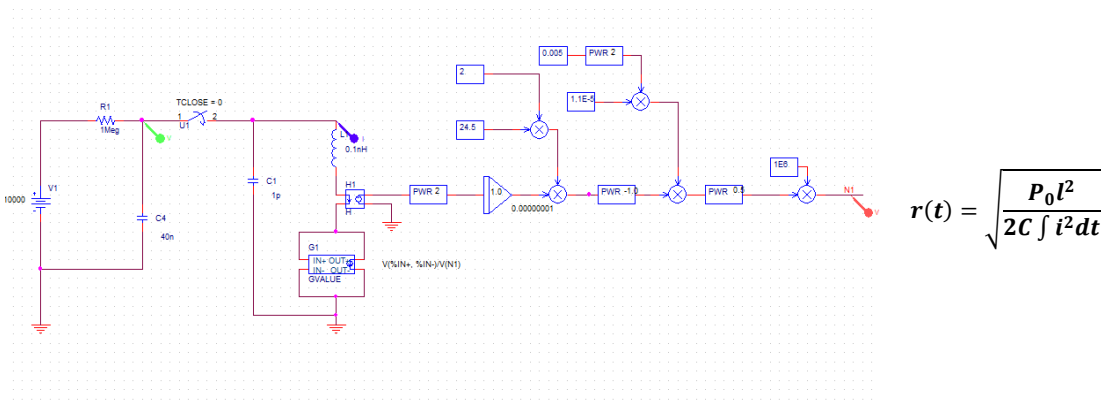


Figure 9.15 Rompe and Weizel equation-plasma model [Rompe 1944].

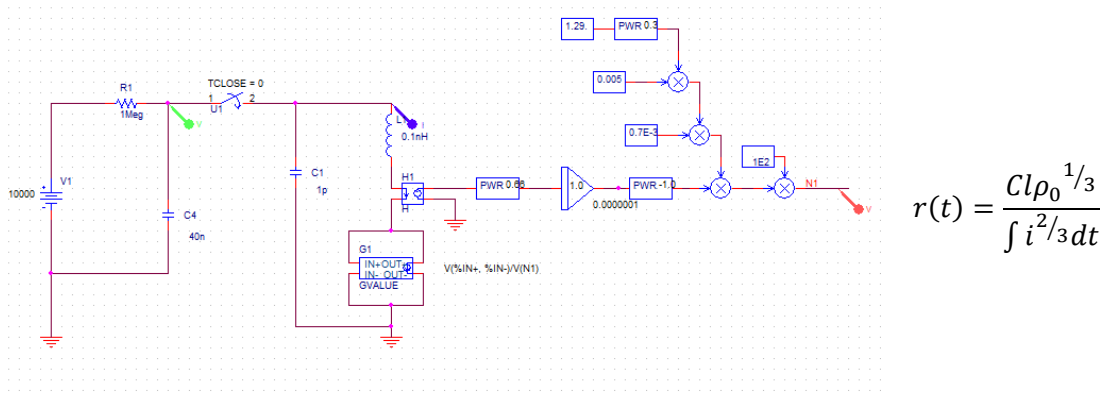


Figure 9.16 Barannik equation-plasma model [Barannik 1975].

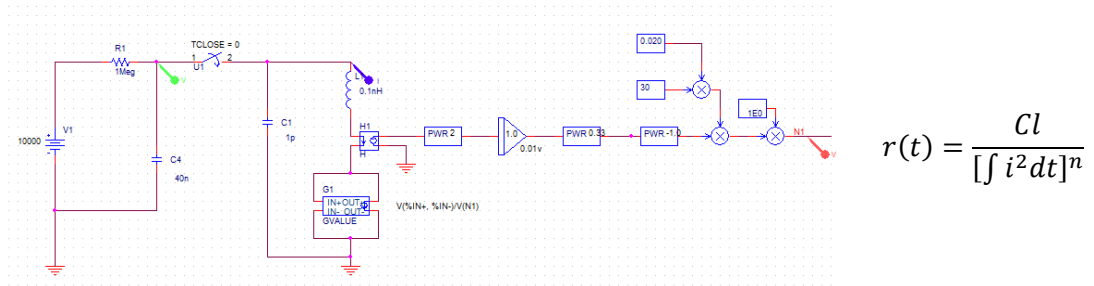


Figure 9.17 Popovic equation – Plasma model [Popovic 1974].

The plasma resistance results from each equation have been plotted on the same graph for comparison and can be seen in Figure 9.18. Figure 9.18 shows the plasma resistances in the regions close to peak current which is where the resistance is at a minimum. This is the region of most importance when considering plasma resistance for pulse power systems.

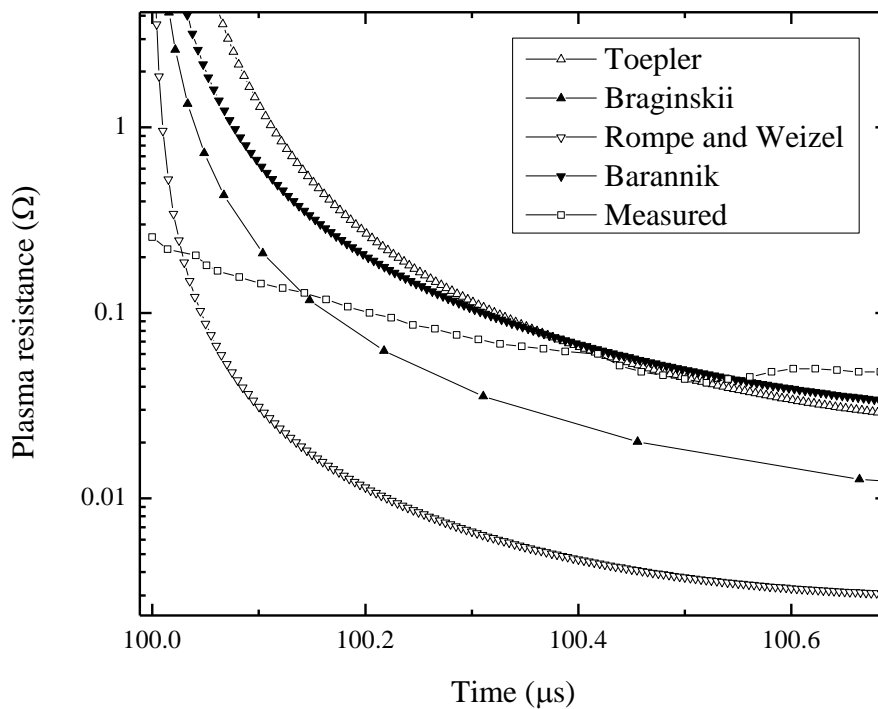


Figure 9.18 Plasma resistance from literature equations (Section 2.2) simulated using PSpice. [Braginskii 1958] [Toepler 1906] [Rompe 1944] [Barannik 1975] [Popovic 1974].

The measured experimental plasma resistance curve taken from literature [Akiyama 1988] reaches a minimum at $\sim 0.5 \mu\text{s}$. The models simulated in this work investigated the first and most basic model from Toepler with the inverse integral of current and the more complex variations by Rompe and Weizel and Barannik as well as the hydrodynamic based model by Braginskii. It was found that Rompe and Weizel's model produced resistances that were an order of magnitude lower at the minimum $\sim 0.0035 \Omega$ compared to the measured resistance

of $\sim 0.04 \Omega$. Braginskii's model was closer with a minimum resistance of $\sim 0.02 \Omega$ but the models by Barannik, and Toepler's models gave by far the most accurate minimum resistance of $\sim 0.04 \Omega$ and $\sim 0.05 \Omega$.

It has been shown that, PSpice simulation package is able to accurately simulate dynamic plasma resistance models provided in literature. The results are consistent with analytical based numerical simulations of similar circuits, however this approach allows the plasma resistance to be incorporated into much more complex circuits. While models proposed by Barannik and Toepler provided the closest fit at the minimum resistance, it was decided that Braginskii's model is the preferred model of the author because it is phenomenologically derived from hydrodynamic equations with fewest restricting parameters (arc length, gas type, etc) meaning it can be adapted for the widest range of applications.

In the models from literature, the assumption has been made that plasma inductance can be assumed to be constant for the sake of developing a plasma resistance model. However, in reality the plasma inductance will depend on the arc radius. The next section discusses the more advanced PSpice model that accounts for plasma inductance.

9.1 DYNAMIC INDUCTANCE AND RESISTANCE OF SPARK SWITCH

In the models proposed in the literature above, the plasma resistance is linked to the current in the circuit. Dynamically solving Kirchhoff's equations for these lumped element circuits means the dynamic resistance of plasma channel can be found. Fitting the analytical results to the experimental data meant that a value of inductance of plasma switch could be obtained interactively to provide analytical current pulses comparable with the experimentally observed current wave-forms. This is the approach commonly used to solve plasma resistance models because it is impractical to derive full circuit equations accounting for more advanced models. However, using PSpice software, it is possible to create more advanced circuits and as such the dynamic inductance of a spark can be simulated along with resistance. The model based around Braginskii's hydrodynamic model for plasma resistance was chosen to further advance the simulation to include dynamic inductance [Braginskii 1958]. For the purposes of this simulation, plasma inductance has been simulated by representing its inductance as that of a single straight wire.

The inductance of a straight wire can be calculated if the length and radius of the wire is known. The inductance of a straight wire can be expressed by [Grover 1962]:

$$L = 2d \left[\ln \left(\frac{2d}{a} \right) - 0.75 \right] nH \quad (9.2)$$

where:

- L is the inductance,
- d is the length of the wire,
- and a is the radius of the wire.

The inductance of a wire with a fixed length will only depend on the radius of the wire. In the case of plasma arc this equation can be used with d as the arc length and a as the radius of the arc. The plasma arc, radius can be calculated from hydrodynamic equations discussed in Section 2.4 which were derived by Braginskii and experimentally confirmed to be reasonable by Mesyats [Braginskii 1958] [Mesyats 1971]. Engel used Braginskii's approach and some improvements to come up with a new equation for plasma arc resistance that proved to reasonably approximate plasma arc radius [Engel 1989]. Engel's equation or plasma arc radius was used in this model to find arc radius for inductance calculations and is expressed as [Engel 1989]:

$$a(t) = \left[3 \int_0^t \left[\int_0^t \frac{i^2}{\pi^2 K p_0 \sigma} dt + v^2(0) \right]^{1/2} dt + a(0) \right]^{1/3} \quad (9.3)$$

where:

- $a(t)$ is the time varying plasma arc radius,
- $a(0)$ is the initial arc radius,
- $v(0)$ is the initial plasma expansion velocity,
- p_0 is the initial gas density,
- σ is the conductivity,
- K is a constant,
- and i is the current.

Values for the parameters required to solve Equation (9.3) were provided by Engel which were taken from experimental data $K = 0.09$, $a(0) = 6 \times 10^{-4}$ m, $v(0) = 2500 \text{ ms}^{-1}$, $\sigma = 2.2 \times 10^4 \Omega \text{m}^{-1}$, $p_0 = 1.29 \text{ kg/m}^3$) and used in this simulation [Engel 1989] [Gruber 1969].

By first solving the plasma radius equation using current signals from the current controlled voltage source (H) in the ABM modelling, a dynamic plasma arc radius is represented by a voltage signal shown in Figure 9.19. Figure 9.19 shows the circuit used to solve Equation (9.3) for plasma arc radius from the voltage representing current. This section of the circuit is separate from the main circuit but takes the voltage signal from an alias, 'vi' placed on the output of the current controlled voltage source. Using the ABM component 'ABM', a source can be created using the variable set by the alias which is used in Figure 9.19.

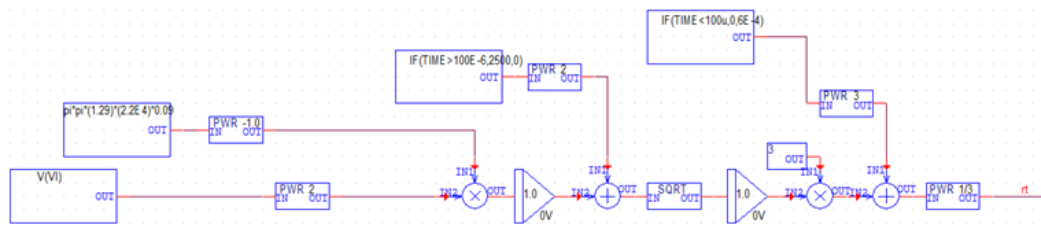


Figure 9.19 Solving plasma arc radius using PSpice ABM circuit equation.

A net alias is placed on the output of the plasma radius equation circuit to create a variable representing the channel radius. This now creates a variable, 'ar' that stores a value for plasma channel radius which can be used to solve the inductance equation given in Equation (9.2). The inductance equation is solved using the ABM model mathematical components and the arc radius calculated in circuit shown in Figure 9.19. Figure 9.20 shows the plasma inductance equation circuit used in the advanced simulation model.

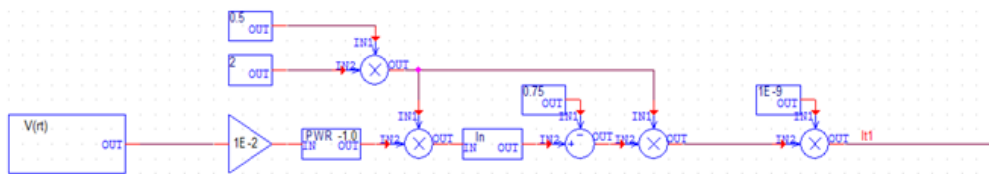


Figure 9.20 Solving plasma inductance using dynamic plasma arc radius in an ABM circuit equation in PSpice.

Using another net alias the value of inductance is stored in the variable 'l1' which changes with respect to the current in the channel as it expands. With the value for inductance, as

with resistance, there is no inductor component that takes a variable. However, an inductance can be resolved by representing its inductive voltage drop which is expressed as:

$$V = L \frac{di}{dt} \quad (9.4)$$

where:

- V is the voltage across the inductor,
- L is the inductance,
- i is the current,
- and t is time.

Therefore, the role of inductance in the circuit can be simulated through a voltage that represents Equation (9.4). Equation (9.4) is solved by taking the voltage signal representing current and differentiating it and then multiplying it by the inductance calculated in the equation circuit shown in Figure 9.20. The equation circuit for Equation (9.4) is shown in Figure 9.21 where the input is the variable from the inductance equation circuit and the output has a net alias $lt2$, creating a variable storing the voltage from the inductor.

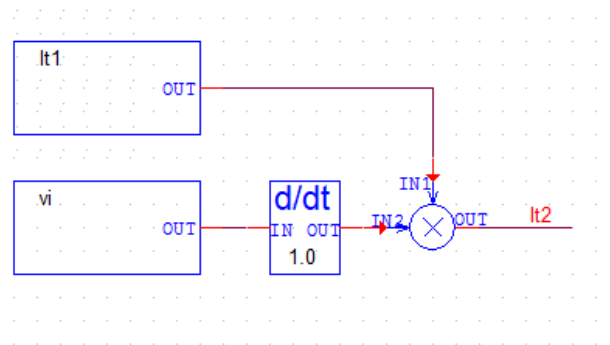


Figure 9.21 PSpice equation circuit solving inductor voltage for advance simulation.

There is now a variable, $lt2$, which represents the voltage that is across the inductance which can be used to simulate an inductor. This can be done in PSpice using the ABM component voltage controlled voltage source which is the 'E' component in the Analogue library and the controlling voltage represents the equation circuit solving Equation (9.4), $lt2$. Figure 9.22 shows the E component and how it can represent inductance.

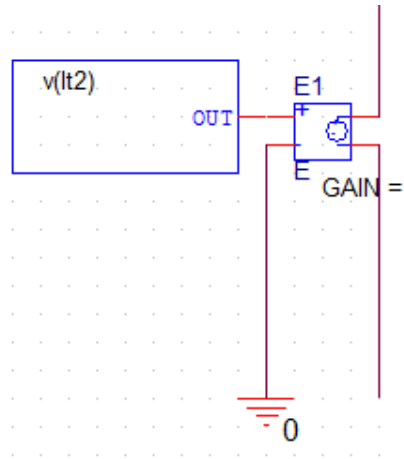


Figure 9.22 PSpice dynamic inductor controlled by voltage signal.

The simulated inductance shown in Figure 9.22 can be incorporated into the plasma simulation model derived which includes dynamic resistance. Figure 9.23 shows how the dynamic inductance is fitted into the plasma simulation model to complete the advanced simulation model.

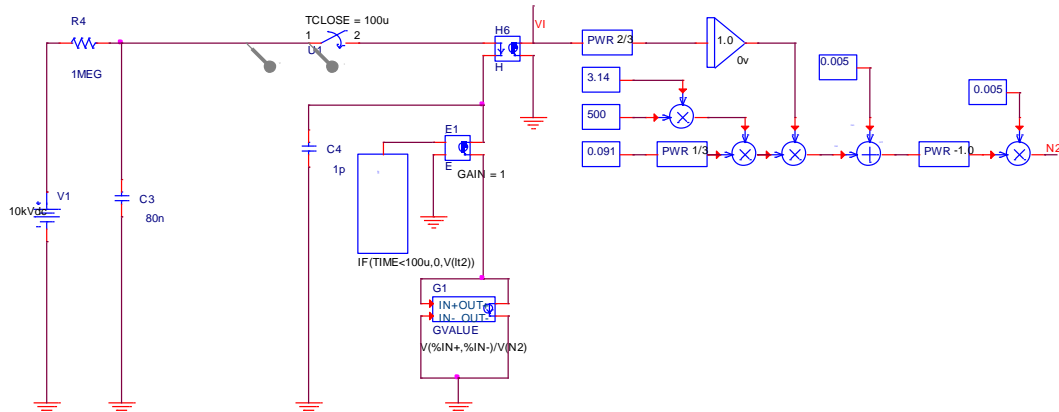


Figure 9.23 Advanced plasma simulation model using PSpice with dynamic resistance and inductance.

This model is the most complete model for simulating plasma properties as it takes into account both dynamic resistance and inductance of the spark channel. The results of the simulation of the switch circuit shown in Figure 9.23 are displayed in Figure 9.24 with the resistance, voltage and current. The plasma inductance calculation had to have an initial condition to start only after breakdown (switch closure) to solve an issue with initial conditions for differentiation. Figure 9.24 presents the simulated plasma resistance with a measured plasma resistance from literature for a 10 mm gap and initial pressure of 0.086 MPa [Engel 1989].

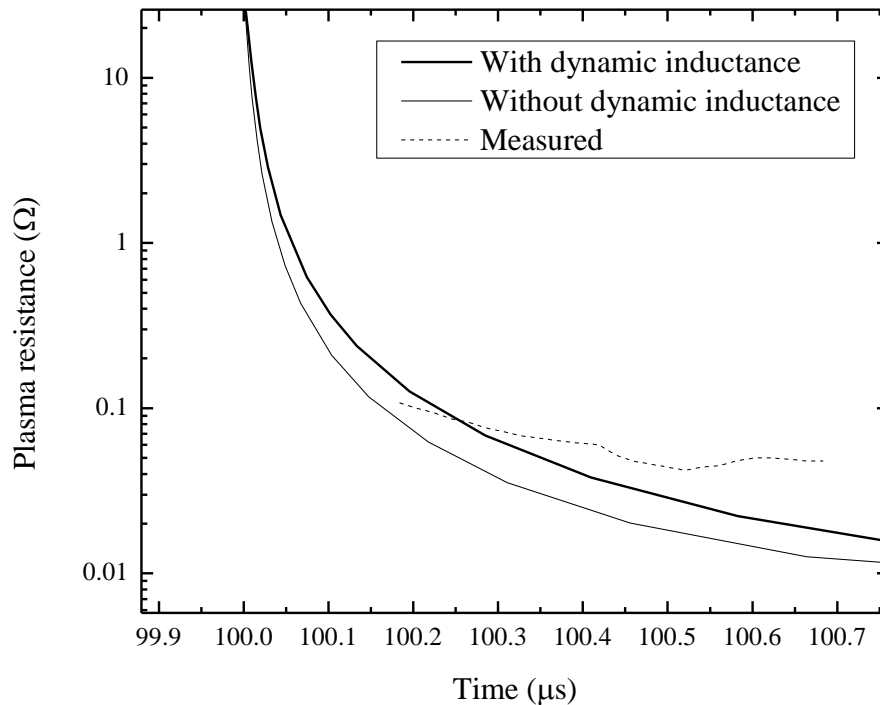


Figure 9.24 Results of advanced plasma simulation model using PSpice. Measured resistance taken from Engel [Engel 1989].

Solving dynamic plasma resistance with inductance creates more accurate models than the usual approach of just solving resistance. Adding dynamic inductance impacts on the current which has a knock on effect to the resistance which feeds back to the current and as such inductance again. The dynamic resistance simulation using the dynamic resistance and inductance is closer to the measured plasma resistance than without the dynamic inductance, Figure 9.24.

9.2 CONCLUSIONS

This chapter was focused on the development of an advanced dynamic self-consistent model of spark channel in plasma switch after its closure using PSpice software. It has been shown that this model can be successfully used to simulate dynamic plasma resistance and inductance and the results of these simulations are close to the experimentally measured values of transient plasma resistance. This model has an advantage over deriving circuit equations manually because it allows for complex circuits into which the plasma can be simulated such as Marx generators or circuits with many stray capacitances and parasitic inductances. Using traditional methods, solving circuit equations by hand derivations would be impractical for complex circuits and, as such, usually only basic circuits are used. They

also may only use simplistic forms of the differential equations required to solve circuit currents. PSpice software can not only simulate complex circuits with plasma, but it also uses complex equations to accurately represent current and voltage in circuits.

10. GENERAL CONCLUSIONS

The main aim of this thesis was to develop and investigate compact spark switches and to develop a triggering strategy that could be used in pulsed power. The focus of this research was on the development and characterisation of a switch topology that would be compact, and filled with environmentally friendly gases and operate with relatively low pressure gas. During the course of this research project, the operational characteristics of gas filled spark switches were examined at up to 0.4 MPa with air, nitrogen and a nitrogen/oxygen mixture. Previously, sulphur hexafluoride gas was the most commonly used gas for spark switches due to its high breakdown strength and electronegative properties. The overall aim of this research is to investigate the operational performance of switches filled with environmentally friendly gases and to develop an advanced electrode topology with the aim of designing high performance switches. Specifically, the novelty of using pre-breakdown corona discharge in switches was investigated for improvement of switching performance in environmentally friendly gases.

A comprehensive review of literature was conducted on many aspects of pulsed power including: spark switch topology designs and switch operation, pulsed power generators and diagnostics, theory of gas discharge breakdown and corona discharges. Reviewing literature outlined the areas in which this research would focus and provided a starting point for testing topologies. In Chapter 2, the work from each of the reviewed investigations is summarised and concluded showing the progression of the thesis and how it has evolved. The literature review provided a firm understanding of the important characteristics of spark switches which highlighted the aspects that formed the outline of the direction of the research.

An advanced experimental test bed was designed and constructed to investigate operational characteristics of plasma closing switches: breakdown voltage, time to breakdown (in the case of triggered switches) and pre-breakdown discharge activity. A program in LabVIEW software environment, interfacing with high-voltage equipment and measurement systems using a digital acquisition device and an RS232 connection, was developed for this experimental test bed; this programme provided consistent repeatable charging of the tested spark switches. Ramping the voltage up at a consistent rate until breakdown meant that if there were pre-breakdown discharges such as in the case of non-uniform fields, the

experimental conditions were similar each time. The breakdown events were identified through real time analysis of the voltage wave-forms obtained from a digitising oscilloscope using LabVIEW program. This experimental system proved to be a key tool in the progression of the experimental work presented in this thesis, being used to measure breakdown voltages and pre-breakdown $V-I$ curves of corona discharges with a current viewing resistor. The experimental systems discussed in Section 3 provided the capability to examine the important aspects of sparks switches to analyse test the hypothesis of each investigation.

For the first time, a comprehensive investigation into the operational performance of spark switch topologies utilising corona discharge, filled with environmentally friendly gases: air, nitrogen and a 60%/40% nitrogen/oxygen mixture has been conducted. Based on the analysis of the literature results, three different electrode topologies: plane-plane, sphere-sphere, and cone-plane were chosen for experimental study in the framework of this project. Sharp coronating electrodes to generate pre-breakdown discharge activity were added to the switch topologies and their performance has been investigated. Positive and negative energisation was used with all the 3 switch topologies filled with gas from 0.1 MPa to 0.35 MPa. It was found that including the coronating electrodes reduced the standard deviation of breakdown voltage for some topologies. However, improvement was not noticed in all configurations and it was not possible to conclusively identify when the coronating electrodes would improve stability of the breakdown voltage in the case of the single shot operation. Investigating all three insulating gases produced no marked improvement using nitrogen or the mixture over compressed air. It was found that the negative breakdown voltage in the case of the cone-plane topology, the most non-uniform field, was higher than positive breakdown voltage and negative breakdown voltage was increased faster than the positive with increasing gas pressure in the switch. At low pressure, 0.1 MPa, the positive and negative breakdown voltages were similar, and it was thought that, given the right conditions, they would be equal. This formed the basis of the next stage of the thesis: investigation of operational characteristics of switches with point-plane topologies. This investigation into the breakdown voltage of a range of topologies and gases was vital in determining the fundamentals of which gases, pressures, and topologies were best for spark switches. Leading to more focused investigations into time delay to breakdown, its jitter, and breakdown voltage analysis of more refined topologies.

Following on from the results gathered in the comparison of topologies, it was decided that a full investigation into the point-plane topology should be conducted. Three point-electrodes

were used: a sharpened tungsten rod with radius 0.068 mm; a hemispherical tipped tungsten rod with tip radius 0.8 mm; and a soft-tone gramophone needle with a tip radius of 0.036 mm. A new test cell was designed to precisely control the gap between the point and plane electrodes using a digital micrometre depth gauge. It was found that, by measuring the breakdown voltage from sub-mm gaps up to over 10 mm, it was possible to identify electrode configurations where positive and negative breakdown voltages were equal (critical gap). Having re-plotted data from literature it was confirmed with all three point electrodes that spark switches could be designed to produce similar breakdown voltages for positive and negative energisation. A critical gap was identified for each point electrode using 0.1MPa - 0.35 MPa bottled air, where positive and negative energisation breakdown voltages are equal. For sharp point (0.036 mm and 0.068 mm radii) the critical gap was ~1 - 2 mm when the air pressure was 0.1 MPa. When the pressure was increased to 0.35 MPa, the critical gap reduced to ~0.76 mm. Increasing the air pressure reduced the critical gap of all of the point electrodes. With the 0.8 mm radius point, the critical gap reduced from ~10 mm to ~7.4 mm when increasing pressure from 0.1 MPa to 0.35 MPa; increasing the radius of the point increases the critical gap. The critical gap at 0.1 MPa is 8 - 9 mm larger for the 0.8 mm radius point compared to the sharper electrodes. This was also confirmed by extrapolating re-plotted literature data to find critical gaps. This is the first comprehensive investigation into the critical gaps of point-plane topologies with different electrode radii, and environmentally friendly gases, at a range of gas pressures. The critical gap which was introduced in this research is an important parameter for designing spark switches and compact high-voltage systems. To understand the processes involved in the point-plane topology, an investigation into corona discharge pre-breakdown currents was conducted.

Corona discharge is utilised in the switch topologies developed in this research project in order to investigate its impact on switching performance; therefore, it was deemed important to investigate corona discharge in its own right. Using the LabVIEW controlled experimental system and a current viewing shunt resistor, pre-breakdown currents ($V-I$ characteristics) were measured. Literature review showed that corona discharges generated by positive and negative energisation of sharp electrodes are different in their nature. This investigation has shown that positive energisation corona discharge initiates at a higher voltage than negative energisation. It has also shown that the pre-breakdown currents are ~7-fold lower for positive than negative energisation. This leads to far less space charge screening effects and explains why negative energisation has higher breakdown voltages. The corona discharge

investigation provided theoretical clarifications to the space charge effects utilised in the non-uniform topologies used in this research and has led to a greater understanding of corona discharge for use in spark switches.

In the next phase of this research project, the operational performance of triggered spark switches filled with environmentally friendly gases was investigated. In the pulsed power industry, it is important to be able to control the operation of spark switches precisely. Therefore, it was decided that following on from the self-breakdown results already collected, an investigation into the time delays to breakdown should be investigated. A novel method of triggering of spark switches using superposition of the DC stress and impulsive trigger signals has been proposed in the current research project. Operational performance of the spark switches stressed and triggered using this novel method and filled with environmentally friendly gases has been investigated. It was established that fast closing times of ~ 20 ns and jitter of ~ 1 ns were achievable by superimposing a triggering impulse onto the top of the DC energised switch. This new method of triggering spark switches can be used in purpose built systems or applied retrospectively to pre-existing switches because it does not require additional triggering electrodes. Simple, 2 electrode switch designs can reduce electrode erosion which can increase the lifetime of the switch. This research could lead to a new approach in the development of high performance triggered switches.

Multi-stage spark switches were investigated, focusing on switching performance such as: breakdown voltage; time delay to breakdown; and its jitter. Building on the investigation of point-plane topologies, a 2 mm gap was chosen as it is close to the critical gap found in previous chapters and a switch was designed to cascade 2, and 3 gaps with 2 mm spacing. It was found that the positive breakdown voltage increased by ~ 3 kV with each new stage from 0.1 MPa up to 0.4 MPa. However, negative breakdown voltage increase with each additional stage was not equal for all pressures. As the pressure was increased, the increase in breakdown voltage due to more stages increased. This investigation has shown that increasing the number of cascaded spark gaps in a switch can increase the breakdown voltage in a predictable manner. The time delay to breakdown of the multi-gap switches showed that it was not possible to accurately characterise the delay time with respect to the DC charging level. However, it was possible to identify DC charging levels at which the time delay jitter reduced to $\sim 1 - 2$ ns. Therefore, this research has identified multi-gap switch configurations that can operate at high DC energisation levels with low jitter and with DC energisation at just $\sim 60\%$ of the self-breakdown voltage. However, the critical gap of ~ 2 mm of the single gap spark switch does not remain when more than one are cascaded. Non-

uniform topologies breakdown at voltages lower than uniform field topologies and as such higher pressures or larger gaps are required than uniform topologies. Increasing the breakdown strength of the non-uniform topologies was investigated by adding additional stages. The time delay to breakdown and its jitter has also been investigated which is vital for the pulse power industry for realistic applications. These investigations have completed a rounded investigation into gas filled spark switches topology's.

The final stage of this research project moves the focus from the pre-breakdown processes to analysis of the post breakdown plasma characteristics. Post-breakdown plasma properties are vitally important for the design and operation of pulse power generators, this investigation into the plasma resistance and inductance simulation improves the understanding gas filled spark switches for use in pulse power generators. The literature review discussed hydrodynamic models for dynamic plasma resistance, highlighting the differences between the models. A novel approach to the modelling of the post-breakdown processes in plasma closing switches has been proposed in the present research project and an advanced model for analysis of the transient plasma resistance and inductance has been developed. This model has been used to obtain the transient post-breakdown parameters (spark channel resistance and inductance), and it was shown that this model provided good agreement with the experimental values available in the literature. A new approach to solving the hydrodynamic plasma resistance models was developed using PSpice software. It was shown that the dynamic plasma resistance equations could be solved using the analogue behavioural modelling package in PSpice environment. A selection of the plasma resistance models from literature have been analysed and implemented using the PSpice approach. The obtained analytical results (dynamic plasma resistance) have been verified using simulation and experimental data available in the literature. It was shown that the approach developed in the present work has significant advantages over the usual approach of deriving and solving circuit equations because complex circuits can be built. This meant an advanced model for dynamic plasma properties could be created with a dynamic resistance and dynamic inductance. Using the hydrodynamic equation for plasma arc radius, which is used for solving Braginskii's model, the plasma inductance could be approximated. Including the dynamic plasma inductance into the model for plasma resistance is shown to improve upon Braginskii's model for plasma resistance on its own; the plasma resistance follows experimental results even closer. The new approach to solving the dynamic plasma resistance equations using PSpice has shown that it can be done, and both dynamic resistance and inductance can be solved simultaneously. Using this newly developed approach to

simulating plasma resistance, for the first time, complex pulse power systems could be solved including those with multiple spark switches.

Throughout this thesis, there has been one clear aim: to design and optimise gas-filled spark switches with improved operational characteristics and filled with environmentally friendly gases. This thesis has utilised the novelty of corona discharge in most of the experiments as a means hypothesised to improve switching performance. This thesis has found spark switch topologies that can operate with the environmentally friendly gases air, N_2 and N_2/O_2 mixtures; it has shown that high voltage breakdowns can be achieved and with low standard deviation. It was shown that adding coronating electrodes, creating pre-breakdown corona discharge, has improved the standard deviation of the breakdown voltage for some topologies; no specific trend could be highlighted to predict if an improvement would occur. Following on from basic topologies, the point-plane topology was developed and its operational characteristics were investigated thoroughly. Based on the results obtained for a single-stage point-plane topology, a multi-spark switch was developed. Multi-spark switches were investigated using the point-plane topology which created corona discharge in each gap, and it was shown how adding multiple stages could be used to find an optimal switching performance. Concluding, this thesis has achieved its desired outcome of showing how a high-performance switch can be achieved using environmentally friendly gases with the aid of corona discharge. This research has shown that, if single shot operation is required, non-uniform topologies can be used to produce high voltage, low jitter spark switches that can be tailored to requirements including equal breakdown voltage for positive and negative energisation.

11. FUTURE WORK

This research investigated spark switches from basic topologies up to advanced multi-spark switches capable of high hold-off voltages with low jitter. With the focus on developing high performance spark switches using environmentally friendly gases and investigating novel approaches of corona discharge, there are some aspects of the research that could be investigated further. This research has shown the future work that should be conducted next.

The investigation into point-plane topologies discovered critical electrode separations where positive and negative energisations have the same breakdown voltage. This research identified the critical gaps using different pressures and point electrode radius. Identifying critical gap aids the design of compact spark switches and pulsed power systems. The next step in this research is to investigate more electrode radii to extend the useful range of the results gathered here. This research investigated different insulating gases with varying electronegativity. However, many pulsed power systems use different insulating gases and higher pressures where critical gaps could provide useful aids. Extending the range of air pressures and gases would provide useful aids to the design of pulsed power switches and compact systems.

Building on from the investigation of point-plane spark switches, multi-gap switches were investigated with 2 and 3 spark gaps. It was found that increasing the number of gaps predictably increased the breakdown voltage. High breakdown voltages with low standard deviation were achieved. Investigating the time delay to breakdown showed that a DC switch energisation voltage range could be identified where the multi-gap switches operated with low jitter. Further work in this area should include increasing the number of gaps, some spark switches use 10's of spark gaps. It was found that the critical gap of the multi-gap switches is different than single gap switches but it appeared that a critical gap could be found for a given number of spark gaps. This would be useful for systems that require high voltages with similar breakdown voltage for positive and negative energisations. Increasing the pressure and trying different gases to expand the range of operation for the switches would be of particular use in the pulsed power industry.

In the progress of designing triggered switches, a new method of triggering spark switches with just two electrodes was developed. A system was developed to trigger a sphere-sphere

topology using a fast rising impulse superimposed on a DC energisation. The results obtained during this research project have shown that fast closing times (~ 20 ns) with low jitter (~ 1 ns) is achievable with negative energisation. This method of triggering a 2 electrode switch has many advantages over other triggering mechanisms and it could be used in a wider range of switches. Initially, this work was only conducted with negative energisation and a sphere-sphere gap with just 2 mm gap. Further work would include using positive energisation, larger gaps, different insulating gases and higher pressures to expand on what was started in this thesis. Also, using this triggering method on multi-gap switches, and other 2 electrode topology designs including point-plane topologies. It was shown that adding coronating electrodes with the sphere-sphere gaps reduced the breakdown time at lower DC energisation levels and improved performance. Expanding into the point-plane topology will help to see how the corona discharge affects the time delay and jitter for a full range of energisation voltages.

The last section of the thesis focuses on post breakdown plasma resistance and inductance modelling. The majority of the thesis focused on the pre-breakdown effects and breakdown voltages. However, many of the applications of plasma switches require low resistance and inductance to achieve fast rising high current outputs. Therefore, the logical progression of the investigation into spark switches should include post breakdown plasma analysis. This was introduced by investigation of the models of plasma resistance already presented in literature. A new approach to modelling dynamic plasma resistance and inductance was developed using PSpice modelling software. This approach allows dynamic plasma resistance and inductance to be simulated simultaneously with advanced software and can be inserted into complex circuits. Traditional approaches to simulating dynamic resistance used hand derived circuit equations to solve for plasma resistance iteratively. Using the PSpice approach plasma resistance could be used in complex pulse power systems such as Marx generators where many spark switches may need to be included. Further work in this area would include gathering new data for plasma resistance, developing a new model for plasma resistance, and finding new fitting coefficients for existing models using the advanced PSpice system.

12. REFERENCES

- (Arora 2012) R. Arora, and W. Mosch, *High Voltage and Electrical Insulation Engineering*, New Jersey (USA), Wiley-IEEE Press, 2012.
- (Akiyama 1988) H. Akiyama, M. Kristiansen, H. Krompholz, and B. Maas, "Current-Voltage Characteristics of High-Current Pulsed Discharge in Air," *IEEE Transactions on Plasma Science*, Vol. 16, No. 2, pp. 312-316, 1988.
- (Barannik 1957) S. I. Barannik, S. B. Vasserman, and A. N. Lukin, "Resistance and Inductance of a Gas Arc," *Soviet Physics Technical Physics*, Vol. 19, No. 11, pp. 1449-1453, 1975.
- (Bernstein and Smith 1973) B. Bernstein and I. Smith, "Aurora, an Electron Accelerator" *IEEE Transactions on Nuclear Science*, Vol. 20, No. 3, pp. 294-300, 1973.
- (Beveridge 2008) J. R. Beveridge, S. J. MacGregor, I. V. Timoshkin, and J. M. Lehr, "A Corona-Stabilised Plasma Closing Switch," 28th *IEEE International Power Modulators and High Voltage Conference*, pp. 487-490, 2008.
- (Bowles 2010) M. Bowles, "State Electricity Profiles 2008," *US Energy Information Administration*, 2010.
- (Bradbury 1934) N. E. Bradbury, and E. Norris, "Note: The Electronic Configuration of Molecules and Their Electron Affinity," *Journal of Chemical Physics*, Vol. 2, No. 12, pp. 840, 1934.

- (Bradbury 1936) N. E. Bradbury and R. A. Nielsen, "Absolute Values of the Electron Mobility in Hydrogen," *Physical Review*, Vol. 49, No. 5, pp. 388-393, 1936.
- (Bluhm 2006) H. Bluhm, *Pulsed Power Systems: Principles and Applications*, New York, Springer, 2006.
- (Blumlein 1941) A. D. Blumlein, *UK patent*, No. 589127, 1941.
- (Bohr 1913) N. Bohr, "On the Constitution of Atoms and Molecules," *Philosophical Magazine*, Vol. 26, No. 1, pp. 1-24, 1913.
- (Boulind 1934) H. F. Boulind, "Corona Discharges in Various Gases," *Philosophical Magazine*, Vol. 18, No. 122, pp. 909-921, 1934.
- (Boulind 1935) H. F. Boulind, "Velocities of Positive Ions in the Corona Discharge," *Philosophical Magazine*, Vol. 20, No. 131, pp. 68-75, 1935.
- (Bowls 1939) W.E. Bowls, "The Effect of Cathode Material on the Second Townsend Coefficient for Ionization by Collision in Pure and Contaminated N₂ Gas," *Physical Review*, Vol. 53, No. 4, pp. 293-301, 1938.
- (Braginskii 1958) S. I. Braginskii, "Theory of the Development of a Spark Channel," *Soviet Physics JETP*, Vol. 34, No. 7, pp. 1068-1074, 1958.
- (Brown 1959) S. C. Brown, *Basic Data of Plasma Physics*, London, Chapman and Hall ltd, 1959.
- (Bruce 1930) J. H. Bruce, "Corona Discharge in Hydrogen," *Philosophical Magazine*, Vol. 10, No. 64, pp. 476-480, 1930.

- (Coelho and Debeau 1971) R. Coelho and J. Debeau, "Properties of the tip-plane configuration," *Journal of Physics D*, Vol. 4, No. 9, pp. 1266-1280, 1971.
- (Colli 1952) L. Colli and U. Facchini, "Drift Velocity of Electrons in Argon," *Review of Scientific Instruments*, Vol. 23, No. 1, pp. 39-42, 1952.
- (Cooperstein 1973) G. Cooperstein, J. J. Condon, and J. R. Boller, "The Gamble 1 Pulsed Electron Beam generator," *Journal of Vacuum Science and Technology*, Vol. 10, No. 6, pp. 961-964, 1973.
- (Demenik 1968) I. V. Demenik, V. E. Mnuskin, B. V. Skortsov, and V. B. Fedorov, "Resistance of a Xenon Plasma in a Large Flash Lamp," *Soviet Physics Technical Physics*, Vol. 13, No. 6, pp. 829-832, 1968.
- (Engel 1956) A. von Engel, "Ionization in Gases by Electrons in Electric Fields," *Handbuch der Physik*, Berlin, Springer Verlag, Vol. 21, No. 4, pp. 504-573, 1956.
- (Engel 1965) A. von Engel, *Ionised Gases (2nd edn)*, Oxford, Clarendon Press, 1965.
- (Engel 1989) T. G. Engel, A. L. Donaldson and M. Kristiansen, "The Pulsed Discharge Arc Resistance and its Functional Behaviour," *IEEE Transactions on Plasma Science*, Vol. 17, No. 2, pp. 323-329, 1989.
- (Fowler 1928) R. H. Fowler and L. W. Nordheim, "Electron Emission in Intense Electric Fields," *Proceedings of the Royal Society of London A*, Vol. 119, No. 781, pp. 173-181, 1928.
- (Fox 1956) R. E. Fox, *Research Report 60-94439-4-R2*, Westing-house

Electric Corporation, Aug. 15th 1956.

- (Frey 2009) W. Frey, M. Sack, R. Wuestner, and G. Mueller, "Gas-Insulated Self-Breakdown Spark Gaps: Aspects on Low-Scattering and Long-Lifetime Switching," *2nd Euro-Asian Pulsed Power Conference*, Vol. 115, No. 6, pp. 1016-1018, 2009.
- (Gardner 1953) A. L. Gardner, *US Patent*, No. 2 659 839, 1953.
- (Given 2011) M. J. Given, I. V. Timoshkin, M. P. Wilson, M. J. MacGregor, and J. M. Lehr, "A Novel Design for a Multi-stage Corona Stabilized Closing Switch," *IEEE Transactions on Dielectric and Electrical Insulation*, Vol. 18, No. 4, pp. 983-989, 2011.
- (Godlove 1961) T. F. Godlove, "Nanosecond Triggering of Air Gaps with Intense Ultraviolet Light," *Journal of Applied Physics*, Vol. 32, No. 8, pp. 1589-1596, 1961.
- (Greason 1997) W. D. Greason, "Methodology of Study the Resistance of Spark Discharges," *32nd IEEE IAS Annual Meeting: Industry Applications Conference*, Vol. 3, No. 1, pp. 1907-1913, 1997.
- (Grover 1962) F. Grover, *Inductance calculations: Working Formulas and Tables*, Dover Publications, NY, 1962.
- (Gruber 1969) J. E. Gruber and R. Suess, "Investigation of the erosion phenomenon in high current, high pressure gas discharges," *Institut Fur Plasmaphysik, Garching bei Munchen*, Report No. IPP 4/72, 1969.
- (Haddad and Warne 2007) A. Haddad and D. Warne, *Advances in High Voltage Engineering*, Lightning Sources UK Ltd, UK, 2007.

- (Hall 1955) B. I. H. Hall, "The Diffusion of Slow Electrons in Deuterium," *Australian Journal of Physics*, Vol. 8, No. 3, pp. 468-473, 1955.
- (Harrower 2001) J. A. Harrower, "The Development and Characterisation of Corona-Stabilised Repetitive Closing Switches," Ph.D. Thesis, University of Strathclyde, Glasgow, 2001.
- (Healey 1941) R. H. Healey and J. W. Reed, *The Behaviour of Slow Electrons in Gases*, Sydney, Amalgamates Wireless, Ltd., 1941.
- (Hogg 2011) M. Hogg, I. V. Timoshkin, M. J. Given, M. P. Wilson, S. J. MacGregor, R. A. Fouracre, and J. M. Lehr, "Liquid Water Stressed with HV Impulses: Effect of Polarity on Transient Pre-breakdown Processes," *9th IEEE International Conference on Dielectric Insulation*, pp. 1-4, 2011.
- (Hogg 2012a) M. Hogg, "Liquid Water as a Dielectric Insulator," Masters by Research Thesis, University of Strathclyde, Glasgow, 2012.
- (Hogg 2012b) M. G. Hogg, I. V. Timoshkin, M. J. Given, M. P. Wilson, S. J. MacGregor, T. Wang, "Impulse Breakdown of Water with Difference Conductivities," *IEEE Transactions on Dielectric and Electrical Insulation*, Vol. 19, No. 5, pp. 1559-1568, 2012.
- (Hogg 2012c) M. Hogg, I. Timoshkin, S. MacGregor, M. Wilson, T. Wang, "Performance of Air Filled Plasma Closing Switch with Corona Pre-ionisation," *XIX International Conference on Gas Discharges and Their Applications*, pp. 504-507, 2012.

- (Hogg 2013) M. G. Hogg, I. V. Timoshkin, S. J. MacGregor, M. P. Wilson, M. J. Wilson, T. Wang, "Electrical breakdown of short non-uniform air gaps," *19th IEEE Pulsed Power Conference*, pp. 1-4, 2013.
- (Hogg 2014a) M. Hogg, I. Timoshkin, S. MacGregor, M. Given, M. Wilson, T. Wang, "Performance of Plasma Closing Switches Filled with Air, Nitrogen and a Nitrogen/Oxygen Mixture," *XX International Conference on Gas Discharges and their Applications*, Vol. 2, pp. 598-601, 2014.
- (Hogg 2014b) M. G. Hogg, I. V. Timoshkin, S. J. Macgregor, M. J. Given, M. P. Wilson, and T. Wang, "Simulation of Spark Dynamic Plasma Resistance and Inductance using PSpice," *2014 IEEE International Power Modulator and High Voltage Conference (2014 IPMHVC)*, 2014.
- (Hogg 2015) M. G. Hogg, I. V. Timoshkin, S. J. Macgregor, M. P. Wilson, and M. J. Given, "Polarity Effects on Breakdown of Short Gaps in a Point-plane Topology in Air," *IEEE Transaction on Dielectric and Electrical Insulation*, Vol. 22, No. 4, pp. 1815-1822, August 2015.
- (Holzer 1932) W. Holzer, "Optische Untersuchung der Funkenzündung in Luft von Atmosphärendruck mittels des unterdrückten Durchbruchs," *Zeitschrift für Physik*, Vol. 77, No. 9-10, pp. 676-694, 1932.
- (Hornbeck 1951) J. A. Hornbeck, "Microsecond Transient Currents in the Pulsed Townsend Discharge," *Physical Review*, Vol. 83, No. 2, pp. 374-379, 1951.
- (Howatson 1965) A. M Howatson, *An Introduction to Gas Discharges*, Oxford, Pergamon Press Ltd, 1965.
- (Humphreys 1985) D. R. Humphreys, K. J. Penn, J. S. Cap, R. G. Adams, J. F.

- Seamen, and B. N. Truman, "A Six Megavolt Laser-Triggered Gas-Filled Switch for PBFA II," *5th IEEE Pulsed Power Conference*, pp. 262-265, 1985.
- (Huxley 1928) L. G. H. Huxley, "The Corona Discharge in Helium and Neon," *Philosophical Magazine*, Vol. 5, No. 10, pp. 721-737, 1928.
- (Huxley 1930) L.G. H. Huxley, "The Corona Discharge in Nitrogen," *Philosophical Magazine*, Vol. 10, No. 62, pp. 185-191, 1930.
- (Isa 1991) H. Isa, Y. Sono, and M. Hayashi, "Breakdown Process of a Rod-to-Plane Gap in Atmospheric Air under DC Voltage Stress," *IEEE Transactions on Electrical Insulation*, Vol. 26, No. 2, pp. 291-299, 1991.
- (Istencic 2005) M. Istencic, I. R. Smith, and B. M. Novac, "Dynamic Resistance Calculation of Nanosecond Spark-Gaps," *15th IEEE International Conference on Pulsed Power*, pp. 608-611, 2005.
- (Kara 2010) A. Kara, O. Kalenderli, and K. Mardikyan, "DC Breakdown Voltage Characteristics of Small Air Gaps with Insulating Barriers in Non-Uniform Field," *2010 International Conference on High Voltage Engineering and Application*, pp. 425-428, 2010.
- (Kemp 2005) M. A. Kemp, "Simulation and Experimental Study of the Multichanneling Rimfire gas Switch," Masters of Science thesis, University of Missouri-Columbia, 2005.
- (Kemp 2006) M. A. Kemp, R. D. Curry, and S. D. Kovaleski, "Experimental Study of the Multichanneling Self-Breakdown Section of the Rimfire Switch," *IEEE*

Transaction on Plasma Science, Vol. 34, No. 4, 2006.

- (Kim 2006) A. A. Kim, V. G. Durakov, S. N. Volkov, A.N. Bastrikov, B.M. Kovalchuk, V.A. Sinebryukhov, S.V. Frolov, V.M. Alexeenko, L. Veron, M. Toury, C. Vermare, R. Nicolas, F. Bayol, C. Drouilly, "Gas switch performance depending on current in the circuit," *Symposium on High Current Electronics*, pp. 297-300, 2006.
- (Kim 2009) A. Kim, S. Frolov, V. Alexeenko, and V. Sinebryukhov, "Prefire Probability of the Switch Type Fast LTD," *17th IEEE Pulsed Power Conference*, pp. 565-570, 2009.
- (Kind 2001) D. Kind, and K. Freser, "Fundamental Principles of High-Voltage Test Techniques," *High Voltage Testing Techniques 2nd edition*, London, Nownes, 2001.
- (Kishner 1952) J. M. Kishner and D.S. Toffolo, "Drift Velocity of Electrons in Argon and Argon Mixtures," *Journal of Applied Physics*, Vol. 23, No. 5, pp. 594-598, 1952.
- (Koval'chuk 1970a) B. M. Koval'chuk, V. V. Kremnev, and G. A. Mesyats, "The Avalanche in Gas and Generation of Nano- and Subnanosecond High Current Pulses," *Proceedings of the USSR Academy of Sciences*, Vol. 191, No. 1, pp. 76-78, 1970.
- (Koval'chuk 1970b) B. M. Koval'chuk, V. V. Kremnev, and Y. F Potalitsyn, "Discharge in High Pressure Gas Initiated by Fast Electron Beam," *Proceeding of the X International Conference on Phenomena in Ionized Gases*, pp. 175-191, 1971.
- (Krasucki 1973) Z. Krasucki, *Breakdown of Commercial Liquid and Solid Dielectrics*, Oxford, Pergamon Press, 1973.

- (Kudelcik 2010) J. Kudelcik, "The Resistance of Plasma Channel in Transformer Oil," *The European Physical Journal Applied Physics*, Vol. 50, No. 1, pp. 11002-11007, 2010.
- (Kushner 1985) M. J. Kushner, W. D. Kimura, and S. R. Byron, "Arc Resistance of Laser Triggered Spark Gaps," *Journal of Applied Physics*, Vol. 58, No. 5, pp. 1744-1751, 1985.
- (Kuffel 2000) E. Kuffel, W. S. Zaengl and J. Kuffel, *High Voltage Engineering: Fundamentals*, Oxford, Butterworth Heinemann, 2000.
- (Larsson 2014) A. Larsson, D. Yap, J. Au, and T. E. Carlsson, "Laser Triggering of Spark Gap Switches," *IEEE Transactions on Dielectric and Electrical Insulation*, Vol. 42, No. 10, pp. 2943-2947, 2014.
- (Lavoie 1964) L. Lavoie, S. Parker, C. Rey, and D. M. Schwartz, "Spark Chamber Pulsing System," *Review of Scientific Instruments*, Vol. 35, No. 11, pp. 1567-1571, 1964.
- (LeChien 2010) K. R. LeChien, W. A. Stygar, M. E. Savage, P. E. Wakeland, V. Anaya, D. S. Artery, M. J. Baremore, D. E. Bliss, R. Chavez, G. D. Coombs, J. P. Corley, P. A. Jones, A. K. Kipp, B. A. Lewis, J. A. Lott, J. J. Lynch, G. R. McKee, S. D. Ploor, K. R. Prestwich, S. A. Roznowski, D. C. Spencer, S. D. White, and J. R. Woodworth, "6.1-MV, 0.79-MA laser-triggered gas switch for multimodule, multiterawatt pulsed-power accelerators," *Physical Review Special Topics – Accelerators and Beams*, Vol. 13, No. 3, 2010.
- (Lehr 2002) J. M. Lehr, J. P. Corley, J. E. Elizondo, P. Corcoran, D. L. Johnson, J. M. Maenchen, P. Wakefield, and K. Struve,

- “Multi-megavolt switching in water: Considerations for the Z-R machine,” *Annual Report: Conference on Electrical Insulation and Dielectric Phenomena*, pp. 554-557, 2002.
- (Li 2015a) J. Li, W. Chen, Z. Chen, J. Tang, W. Jia, F. Guo, T. Yang, A. Qiu, J. Zhao, and Q. Zhang, “Effects of Optical Pulse Parameters on a Pulsed UV-Illuminated Switch and Their Adjusting Methods,” *IEEE Transactions on Plasma Science*, Vol. PP. No. 99, 2015.
- (Li 2015b) J. Li, W. Chen, J. Li, W. Jiang, X. Zhong, and Y. Gou, “Robust Design for Linear Transformer Drivers,” *IEEE Transactions on Plasma Physics*, Vol. PP. No. 99, 2015.
- (Li 2013) S. Li, I. V. Timoshkin, M. MacLean, S. J. MacGregor, M. P. Wilson, M. J. Given, J. G. Anderson, and T. Wang, “Steady-State Corona Discharges in Atmospheric Air for Cleaning and Decontamination,” *IEEE Transactions on Plasma Science*, Vol. 41, No. 10, pp. 2871-2878, 2013.
- (Li 2014) X. Li, X. Liu, F. Zeng, H. Yang, and Q. Zang, “Study on Resistance and Energy Deposition of Spark Channel Under the Oscillatory Current Pulse,” *IEEE Transactions on Plasma Science*, Vol. 42, No. 9, pp. 2259-2265, 2014.
- (Llewellyn-Jones 1939) F. Llewellyn-Jones and J. P. Henderson, “The Influence of the Cathode on the Sparking Potential of Hydrogen,” *Philosophical Magazine*, Vol. 28, No. 188, pp. 328-337, 1939.
- (Llewellyn-Jones 1957) F. Llewellyn-Jones, *Ionization and Breakdown in Gases*, London, Methuen and co Ltd, 1957.
- (Loeb 1939) L. B. Loeb, *Fundamental Processes of Electrical Discharge in Gas*, New York, John Wiley and Sons Inc.,

1939.

- (MacDonald 2009) J. R. MacDonald, M. A. Schneider, J. B. Ennis, F. W. MacDougall, and X. H. Yang, "High Energy Density Capacitors," *29th IEEE Electrical Insulation Conference*, pp. 306-309, 2009.
- (Markins 1971) D. Markins, "Command triggering of Synchronized Megavolt Pulse Generators," *IEEE Transactions on Nuclear Science*, Vol. 18, No. 2, pp. 296-302, 1971.
- (Martin 1973) T. H. Martin, "Hydra, Electron Bean Generator," *IEEE Transactions on Nuclear Science*, Vol. 20, No. 3, pp. 283-293, 1973.
- (Martin 1993) T. H. Martin, J. F. Seamen, and D. O. Jobe, "Energy Losses in Switches," *9th IEEE Pulsed Power Conference*, pp. 463-470, 1993.
- (Marx 1923) E. Marx, *Deutsches Reichpatent*, No. 455 933, 1923.
- (Marx 1928) E. Marx, "Untersuchungen über den elektrischen Durchschlag und Überschlag im unhomogenen Felde," *Archiv für Elektrotechnik*, Vol. 20, No. 5-6, pp. 589-607, 1929.
- (Maas 1985) B. L. Maas, "Arc Current, Voltage, and Resistance in High Energy, Gas Filled Spark Gap," Masters thesis, Texas Tech University, 1985.
- (Mazarakis 2009) M. Mazarakis, W. Fowler, A. Kim, V. Sinebryukhov, S. Rogowski, R. Sharpe, D. McDaniel, C. Olson, J. Porter, K. Struve, W. Stygar, and J. Woodworth, "High current, 0.5-MA, fast, 100-ns, linear transformer driver experiments," *Physical Review ST Accelerator and Beams*, Vol. 12,

No. 5, pp. 050401-050411, 2009.

- (Meek 1953) J. M. Meek and J. D. Craggs, *Electrical breakdown of gases*, Oxford, Clarendon Press, 1953.
- (Meng 2008) X. Meng, H. Zhang, and J. Zhu, "A general empirical formula of current–voltage characteristics for point-to-plane geometry corona discharges," *Journal of Physics D: Applied Physics*, Vol. 41, No. 6, pp. 065209-06519, 2008.
- (Mercer 1976) S. Mercer, I. Smith, and T. Martin, "A Compact Multiple Channel 3 MV Gas Switch," 1st International Conference on Energy Storage Compression and Switching, *Energy Storage, Compression, and Switching*, Oxford, Plenum Press, pp. 459-462, 1976.
- (Mesyats 1960) G. A. Mesyats, "Delay of the Breakdown of a Spark Gap at High Overvoltages," *Izvestiya Vysshikh Uchebnykh Zavedenij*. Vol. 4, No. 1, pp. 229-231, 1960.
- (Mesyats 1971) G. A. Vorob'yev and G. A. Mesyats, *Technique of shaping high voltage nanosecond pulses*, Foreign Technology Division, Wright-Patterson Air Force Base, 1971.
- (Mesyats 1974) G. A. Mesyats, *Generation of High-Power Nanosecond Pulses*, Moscow, 1974.
- (Mesyats 1982) G. A. Mesyats, "High-Power Injection Switches," *Gas Electronics*, Novosibirsk, Nauka, 1982.
- (Mesyats 2005) G. A. Mesyats, *Pulsed Power*, New York, Springer, 2005.
- (Montano 2006) R. Montano, M. Becerra, V. Cooray, M. Rahman, and P. Liyanage, "Resistance of Spark Channels," *IEEE Transactions on Plasma Science*, Vol. 34, No. 5, pp. 1610-1619, 2006.

- (Nielsen 1936) R. A. Nielsen, "Absolute Values of the Electron Drift Velocity in Nitrogen, Helium, Neon and Argon," *Physical Review*, Vol. 50, No. 10, pp. 950-954, 1936.
- (Nielsen 1937) R. A. Nielsen, "Electron and Negative Ion Mobilities in Oxygen, Air, Nitrous Oxide and Ammonia," *Physical Review*, Vol. 51, No. 2, pp. 69, 1937.
- (Oreshkin and Lavrinovich 2014) V. I. Oreshkin and I. V. Lavrinovich, "Energy loss in spark gap switches," *Physics of Plasmas*, Vol. 21, No. 4, pp. 043513, 2014.
- (Peek 1915) F. W. Peek, *Dielectric Phenomena in High Voltage Engineering: First edition*, London, McGraw-Hill Book Company Inc., 1915.
- (Pendleton and Guenther 1965) W. K. Pendleton, and A. H. Guenther, "Investigation of a Laser-Triggered Spark Gap," *Review of Scientific Instruments*, Vol. 36, No. 11, pp. 1546-1550, 1965.
- (Popovic 1974) M. M. Popovic and S. S. Popovic, "Investigation of the Beginning of High Current Discharges in Pulsed Arcs," *4th International Conference on Gaseous Discharges and Their Applications*, pp.32-36, 1974.
- (Raizer 1974) Y. P. Raizer, *The Laser Spark and Propagation of Discharges*, Moscow, Nauka, 1974.
- (Raizer 1991) Y. P. Raizer, *Gas Discharge Physics*, Berlin, Springer, 1991.
- (Reg 2006) Regulation (EC) No. 842/2006 of the European Parliament and of the Council of 17th May 2006 on certain fluorinated greenhouse gases, *Official Journal of the European Union*, Vol. 49, pp. 11, 2006.

- (Rogowski 1923) W. Rogowski, "Die elektrische Festigkeit am Rande des Plattenkondensators," *Archiv für Elektrotechnik*, Vol. 12, No. 1, pp. 1-15, 1923.
- (Rompe 1944) R. Rompe and W. Weizel, "Über das Toeplersche Funkengesetz," *Zeitschrift für Physik*, Vol. 122, No. 9-12, pp. 636-639, 1944.
- (Rosenthal 2003) S.E. Rosenthal, J.M.Elizondo, J.E.Maenchen, K.W.Struve, D.H.McDaniel, J.P.Corley, D.L.Johnson, and B.V.Oliver, "Modeling 6-MV Gas Switches For the ZR Accelerator," *14th IEEE Pulsed Power Conference*, pp. 163-166, 2003.
- (Stolen 1969) S. Stølen, "Breakdown Induced by Transient U.V. Irradiation," *IX International Conference on Phenomena in Ionised Gases*, pp. 259, 1969.
- (Strigel 1939) R. Strigel, *Elektrische stossfestigkeit*, Berlin, Springer, 1939.
- Stygar (2007) W. Stygar, M. Cuneo, D. Headley, H. Ives, R. Leeper, M. Mazarakis, C. Olson, J. Porter, T. Wagoner, and J. Woodworth, "Architecture of Petawatt-Class Z-Pinch Accelerators," *Physical Review ST Accelerator Beams*, Vol. 10, No. 3, pp. 030401-030425, 2007
- (Somerville 1990) I. C. Somerville, S. J. MacGregor, and O. Farish, "An efficient stacked-Blumlein HV pulse generator," *Measurement Science and Technology*, Vol. 1, No. 9, pp. 865-868, 1990.
- (Theophanis 1960) G. A. Theophanis, "Millimicrosecond Triggering of High Voltage Spark Gaps," *Review of Scientific Instruments*, Vol. 31, No. 4, pp. 427-432, 1960.

- (Timoshkin 2006) I. V. Timoshkin, R. A. Fouracre, M. J. Given and S. J. MacGregor, "Hydrodynamic Modelling of Transient Cavities in Fluids Generated by High Voltage Spark Discharges," *Journal of Physics D: Applied Physics*, Vol. 39, No. 22, pp. 4808-4817, 2006.
- (Toepler 1906) M. Toepler, "Zur kenntnis der gesetz der gleitfunkenbildung," *Annalen der Physik*, Vol. 326 No. 12, pp. 193-222, 1906
- (Torres 1999) J.M. Torres, and R.S. Dhariwal, "Electric Field Breakdown at Micrometre Separations in Air and Vacuum," *Microsystem Technologies*, Vol. 6, No. 1, pp. 6-10, 1999.
- (Townsend 1914) J. Townsend, *Electricity in Gases*, Oxford, Clarendon Press, 1914.
- (Turman 1983) B. N. Turman, W. B. S. Moore, J. F. Seamen, F. Morgan, J. Penn, and D. R. Humphreys, "Development tests of a 6 mv, multistage gas switch for PBFA II," *4th IEEE Pulsed Power Conference*, pp. 617-619, 1983
- (Uhlmann 1929) E. Uhlmann, "Der elektrische Durchschlag von Luft zwischen konzentrischen Zylindern," *Arch Electrotech* Vol. 23, No. 3, pp. 323, 1929.
- (Volkov 1999) S.I. Volkov, A. A. Kim, B. M. Koval'chuk, V. V. Kremnev, and V. A. Sinebryukhov, "Multichannel Closing Spark Gap Switch for Water Energy Stores," *Russian Physics Journal*, Vol. 42, No. 12, pp. 1065-1072, 1999.
- (Vorob'ev 1959) G. A. Vorob'ev, "Device for Production of Short Rise Time Pulses," *USSR Inventor's Certificate*, No. 120 876, 1959.

- (Vorob'ev and Mesyats 1963) and G. A. Vorob'ev and G. A. Mesyats, *Techniques for the Formation of Nanosecond High Voltage Pulses*, Moscow, Gosatomizdat, 1963.
- (Williams and Guenther 1990) and P. F. Williams and A. H. Guenther, "Laser Triggering of Gas Filled Spark Gaps," *Gas Discharge Closing Switches*, New York, Plenum Press, pp. 145-187, 1990.
- (Wilson 2011) M. P. Wilson, "Impulse Breakdown of Liquid-Solid Interfaces," Ph.D. thesis, University of Strathclyde, Glasgow, 2011.
- (Woodworth 2009a) J. R. Woodworth, J. A. Alexander, W.A. Stygar, L. F. Bennett, H.D. Anderson, M.J. Harden, J.R. Blickem, F. R. Gruner, and R. White, "Low inductance switching studies for Linear Transformer Drivers," *18th IEEE Conference on Pulsed Power*, pp. 250-254, 2009.
- (Woodworth 2009b) J. Woodworth, J. Alexander, F. Gruner, W. Stygar, M. Harden, J. Blickem, G. Dension, F. White, L. Lucero, H. Anderson, L. Bennett, S. Glover, D. Van DeValde, and M. Mazarakis, "Low-inductance gas switches for linear transformer drivers," *Physical Review ST Accelerator Beams*, Vol. 12, No. 6, pp. 060401-060418, 2009.
- (Woodworth 2010) J. Woodworth, W. Stygar, L. Bennett, L. M. Mazarakis, H. Anderson, M. Harden, J. Blickem, F. Gruner, and R. White, "New low inductance gas switches for linear transformer drivers," *Physical Review ST Accelerator Beams*, Vol. 13, No. 8, pp. 080401-080410, 2010.
- (Woodworth 2011) J. Woodworth, W. Fowler, B. Stoltzfus, W. Stygar, M. Sceiford, M. Mazarakis, H. Anderson, M. Harden, J. Blickem, R. White, and A. Kim, "Compact 810 kA linear

transformer driver cavity,” *Physical Review ST Accelerator Beams*, Vol. 14, No. 4, pp. 040401-04048, 2011.

(Wu 2014) J. W. Wu, R. Y. Han, Y. F. Yiu, H. B. Zhou, Q. J. Liu, and W. D. Ding, “Research of high-power repetitive spark-gap switch under adverse conditions,” *IEEE 4th International Conference on High-Power Particle Beams*, pp. 1-6, 2014.

(Zou 2015) X. B. Zou, H. T. Shi, H. Xie, X. Wang, and G. Zhang, “Using fast moving electrode to achieve overvoltage breakdown of gas switch stressed with high direct voltages” *Review of Scientific Instruments*, Vol. 86, No. 3, pp. 034705, 2015.

13. LIST OF PUBLICATIONS

13.1 JOURNAL PUBLICATIONS

- M. G. Hogg, I. V. Timoshkin, S. J. Macgregor, M. P. Wilson, and M. J. Given, “Polarity Effects on Breakdown of Short Gaps in a Point-plane Topology in Air,” *IEEE Transaction on Dielectric and Electrical Insulation*, Vol. 22, No. 4, pp. 1815-1822, August 2015.

13.2 PRESENTATIONS AT INTERNATIONAL CONFERENCES AND WORKSHOPS

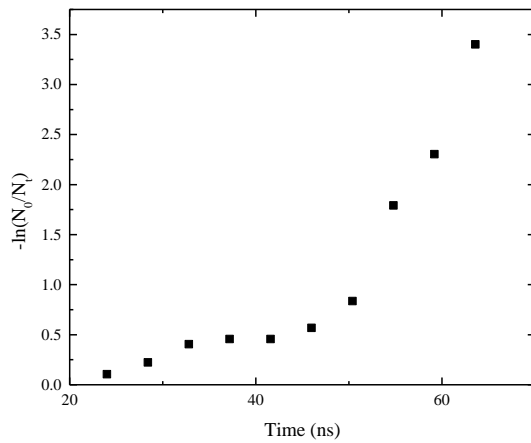
- M. G. Hogg, I. V. Timoshkin, S. MacGregor, M. Given, M. Wilson, and T. Wang, “Plasma Closing Switches Filled with Air: Effect of Corona Pre-ionisation of

Switching Performance,” 10th *Technological Plasma Workshop*, Manchester, UK, 5th-6th January 2012.

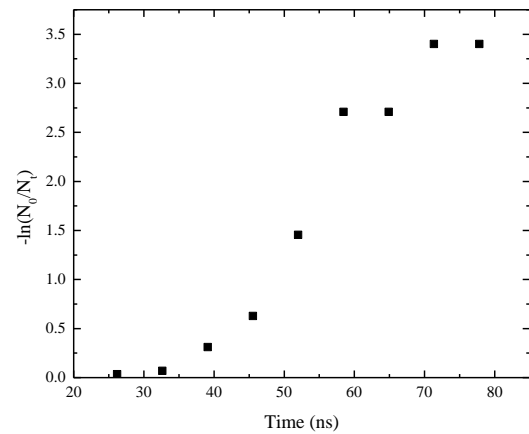
- M. G. Hogg, I. V. Timoshkin, S. J. MacGregor, M. J. Given, M. P. Wilson, and T. Wang, “Performance of Air-filled Plasma Closing Switch with Corona Pre-ionisation,” *XIX International Conference on Gas Discharge and Their Applications*, pp. 598-602, Beijing, UK, 2-7 September 2012.
- M. G. Hogg, I. V. Timoshkin, S. J. MacGregor, M. P. Wilson, M. J. Given, T. Wang, “Optimisation of gas-filled plasma closing switch by investigating dielectric medium and electrode topology with corona pre-ionisation,” *6th UHVnet colloquium*, Glasgow, UK, 16th-17th January 2013.
- M. G. Hogg, I. V. Timoshkin, S. J. MacGregor, M. P. Wilson, M. J. Given, and T. Wang, "Electrical Breakdown of Short Non-uniform Air Gaps," *19th IEEE Pulsed Power Conference (PPC)*, pp.1-4, San Francisco, California, USA, 16-21 June 2013.
- M. G. Hogg, I. V. Timoshkin, M. P. Wilson, T. Wang, S. J. MacGregor, “DC Breakdown of Non-uniform Topologies with Short Gas Filled Gaps,” *7th UHVnet colloquium*, Guildford, UK, 15th-16th January 2014.
- M. G. Hogg, I. V. Timoshkin, S. J. MacGregor, M. J. Given, and T. Wang, “Performance of Plasma Closing Switches Filled with Air, Nitrogen and a Nitrogen/Oxygen,” *20th International Conference on Gas Discharge and Their Applications*, pp. 598-602, Orléans, France, 6-11 June 2014.
- M. G. Hogg, I. V. Timoshkin, S. J. MacGregor, M. J. Given, M. P. Wilson, and T. Wang, “Simulation of Spark Dynamic Plasma Resistance and Inductance using PSpice,” *2014 IEEE International Power Modulator and High Voltage Conference (2014 IPMHVC)*, Santa Fe: New Mexico, USA, 1-6 June 2014.
- M. G. Hogg, I. V. Timoshkin, S. J. MacGregor, M. P. Wilson, M. J. Given, and T. Wang, “Operation of Gas Switch Stressed with Superimposed DC and Impulsive Voltage,” *8th UHVnet colloquium*, Stafford, UK, 14th-15th January 2015.

14. APPENDIX 1: LAUE GRAPHS

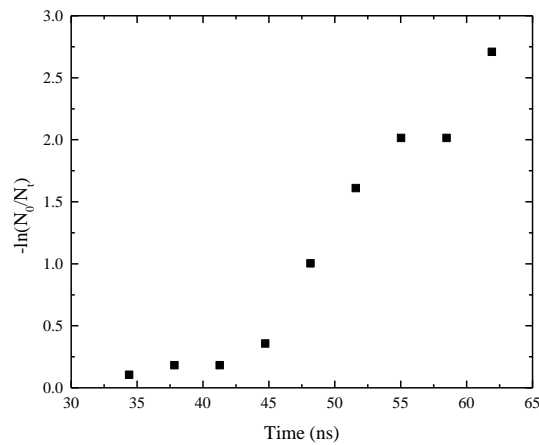
14.1 LAUE GRAPHS FOR DISCHARGES WITHOUT CORONATING ELECTRODES



(a) 6 kVDC energisation



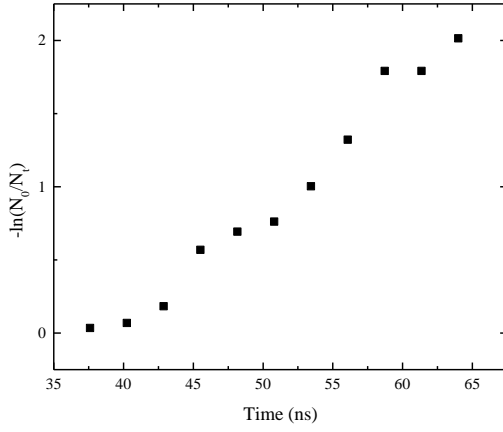
(b) 7 kV DC energisation



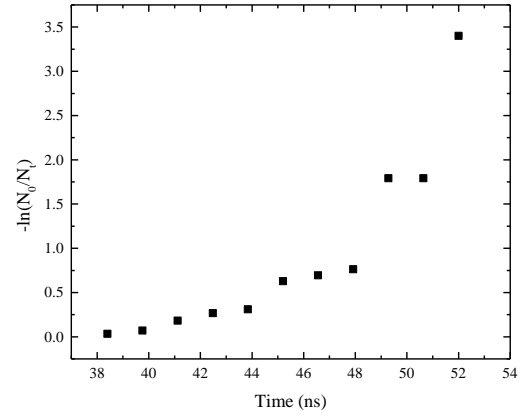
(c) 8 kV DC energisation

No coronating electrodes
Gas – Air
Pressure – 0.1MPa

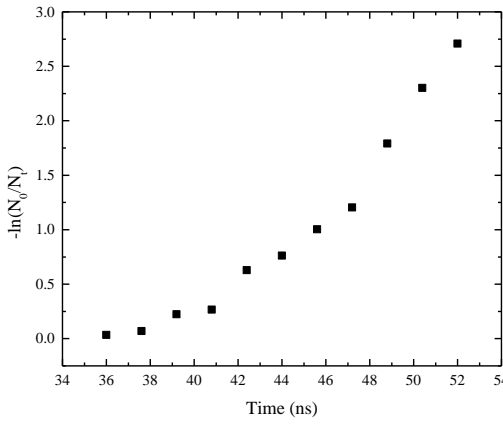
Figure 14.1 Laue graphs for 0.1 MPa air without corona discharge electrodes.



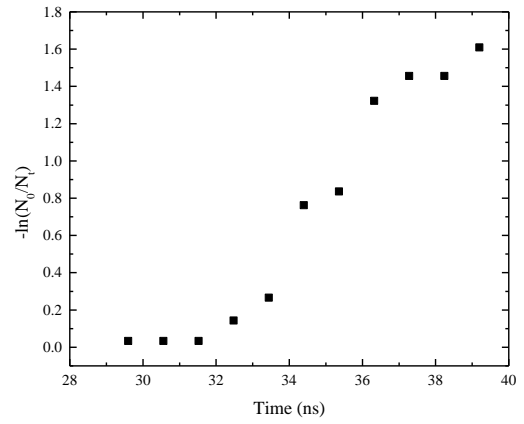
(a) 2 kV DC energisation



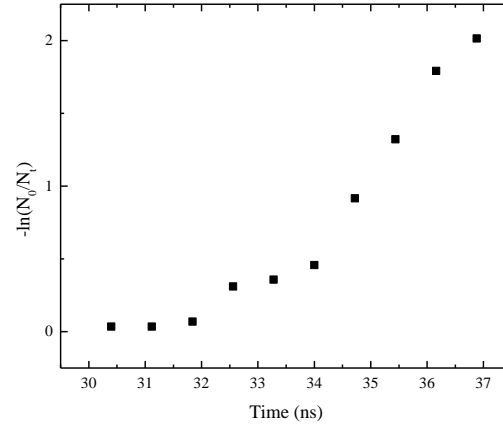
(b) 4 kV DC energisation



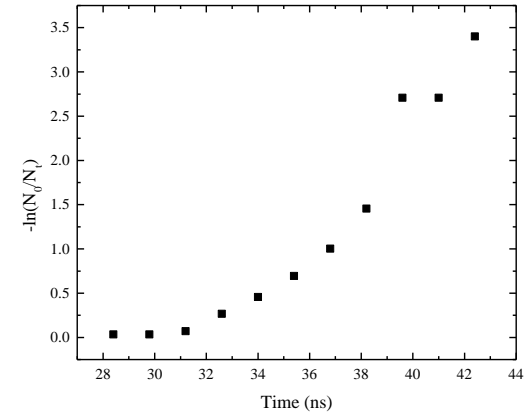
(c) 6 kV DC energisation



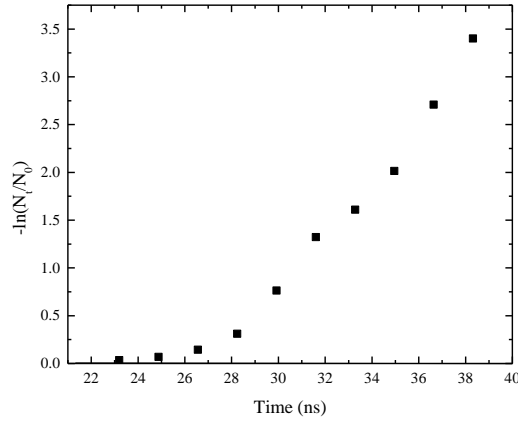
(d) 8 kV DC energisation



(e) 10 kV DC energisation



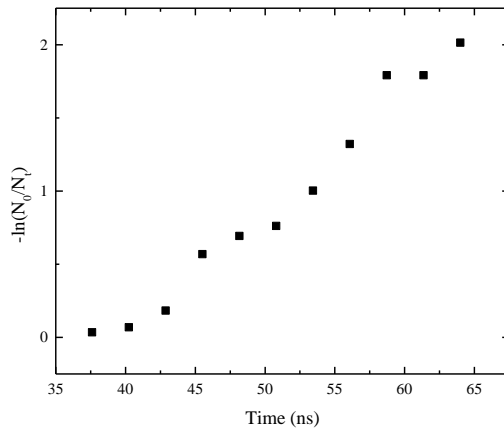
(f) 12 kV DC energisation



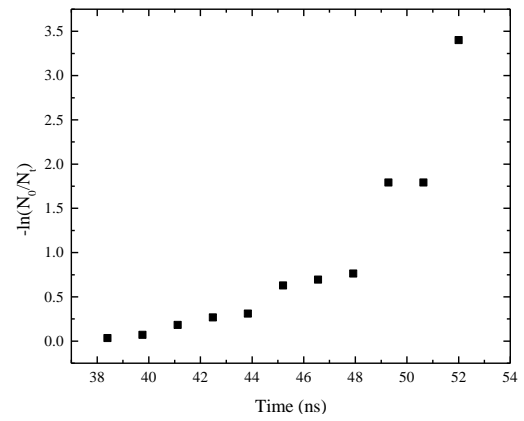
No coronating electrodes
 Gas – Air
 Pressure – 0.2 MPa

(g) 14 kV DC energisation

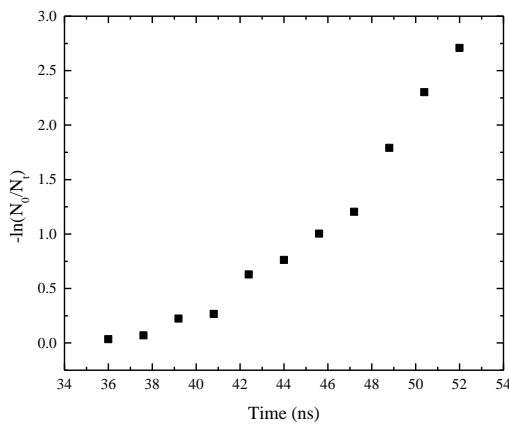
Figure 14.2 Laue graphs for 0.2 MPa air without corona discharge electrodes.



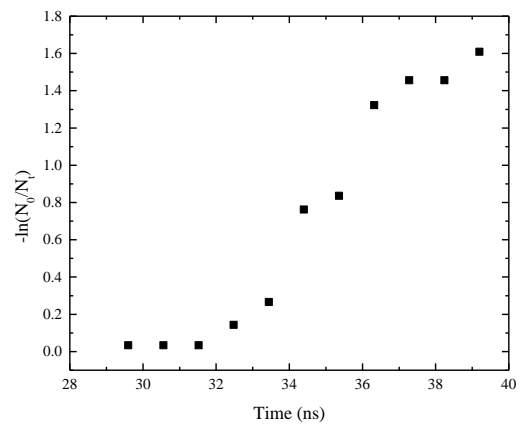
(a) 2 kV DC energisation



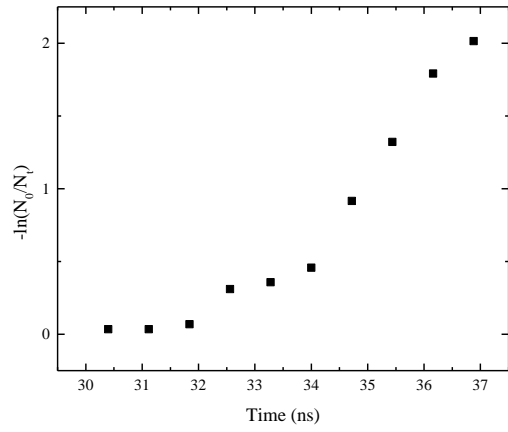
(b) 4 kV DC energisation



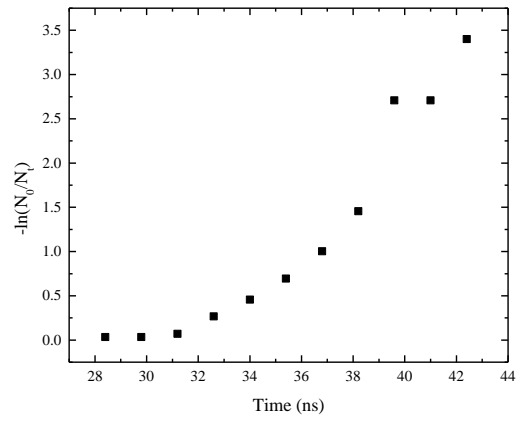
(c) 6 kV DC energisation



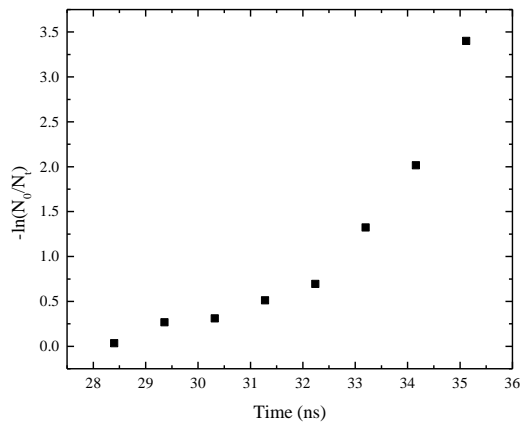
(d) 8 kV DC energisation



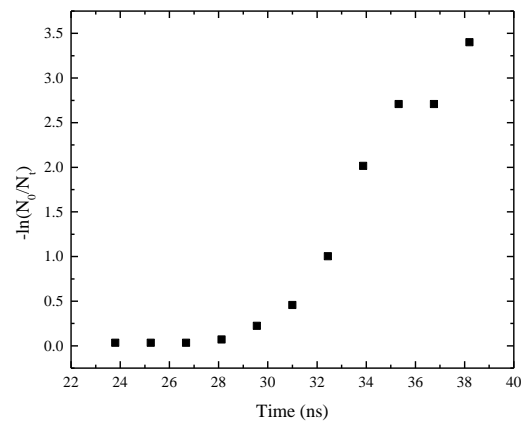
(e) 10 kV DC energisation



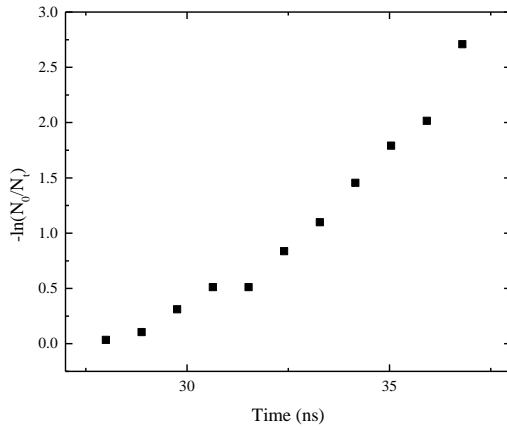
(f) 12 kV DC energisation



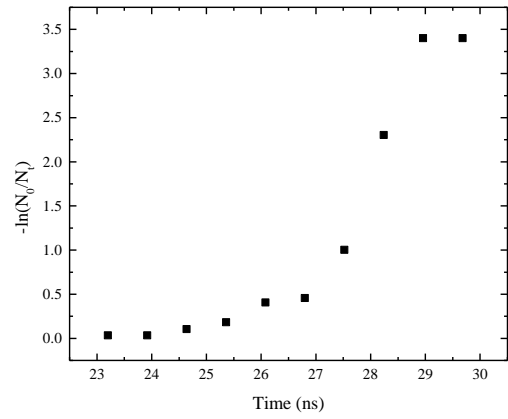
(g) 14 kV DC energisation



(h) 16 kV DC energisation



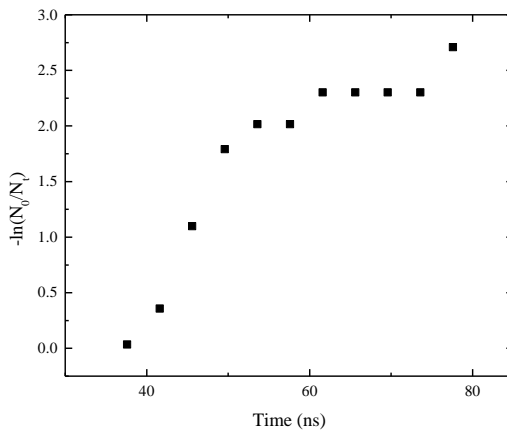
(i) 18 kV DC energisation



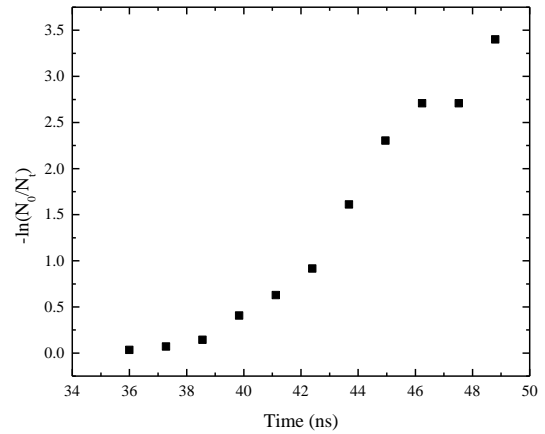
(j) 20 kV DC energisation

No coronating electrodes
 Gas – Air
 Pressure – 0.3 MPa

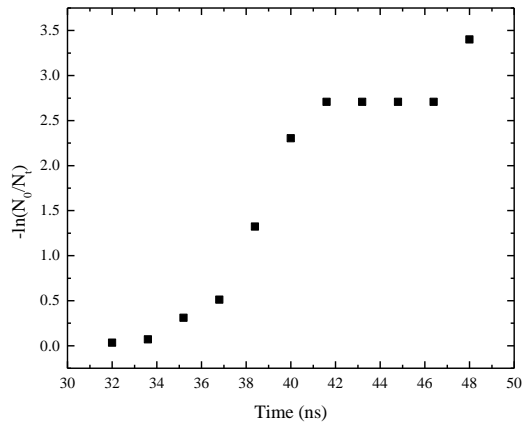
Figure 14.3 Laue graphs for 0.3 MPa air without corona discharge electrodes.



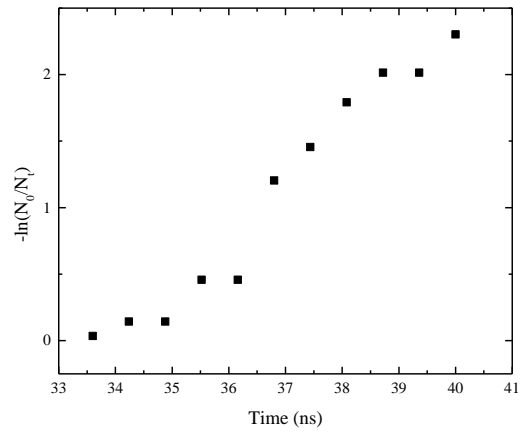
(a) 4 kV DC energisation



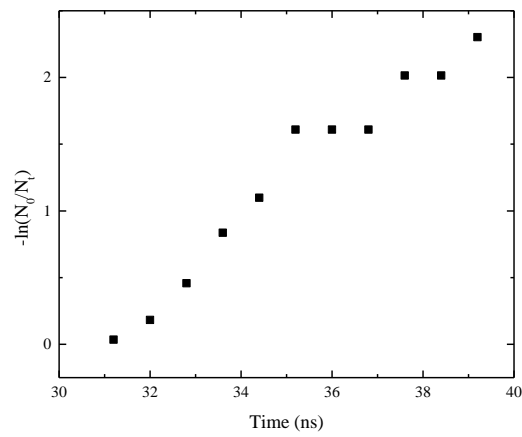
(b) 6 kV DC energisation



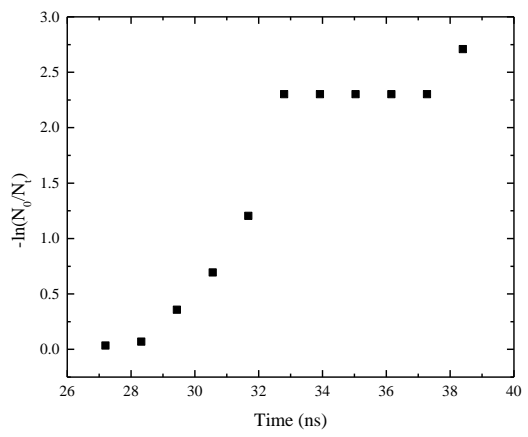
(c) 8 kV DC energisation



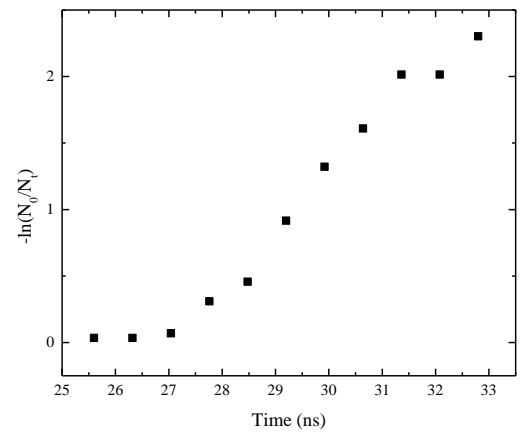
(d) 10 kV DC energisation



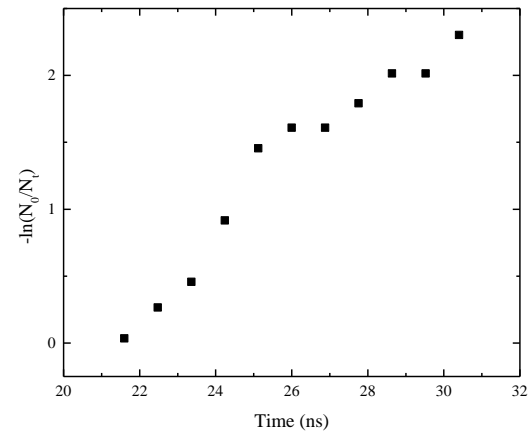
(e) 12 kV DC energisation



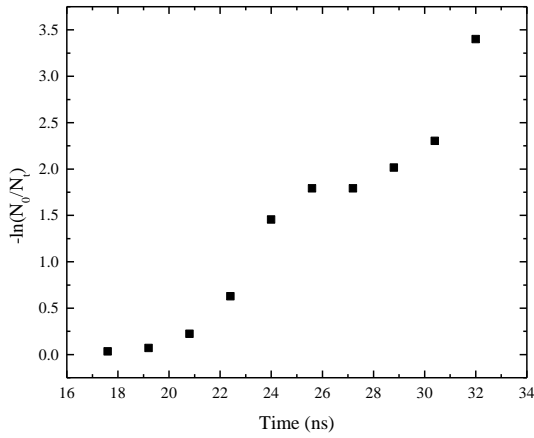
(f) 14 kV DC energisation



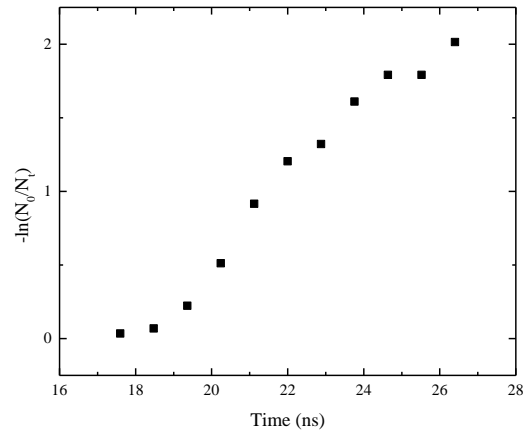
(g) 16 kV DC energisation



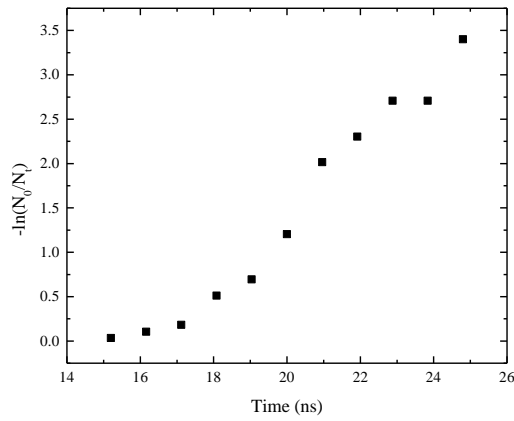
(h) 18 kV DC energisation



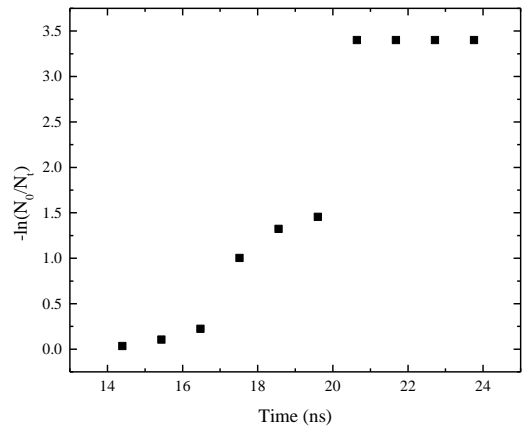
(i) 20 kV DC energisation



(j) 22 kV DC energisation



(k) 24 kV DC energisation

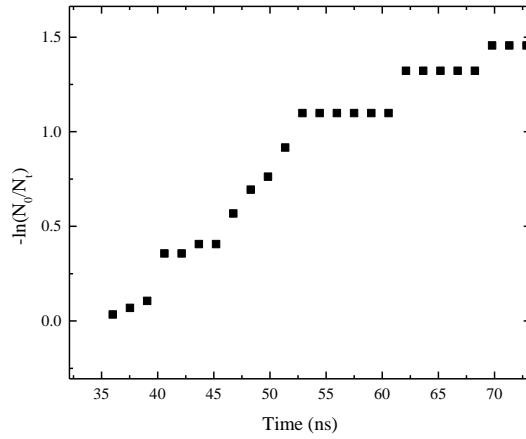


(l) 26 kV DC energisation

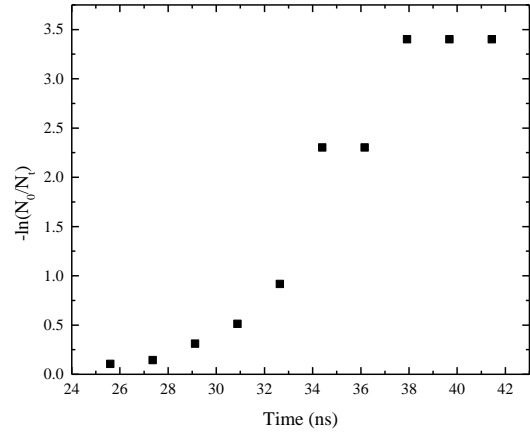
No coronating electrodes
 Gas – Air
 Pressure – 0.4 MPa

Figure 14.4 Laue graphs for 0.4 MPa air without corona discharge electrodes.

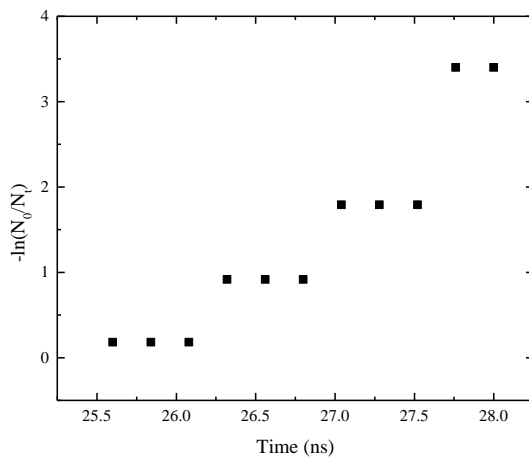
14.2 LAUE GRAPHS FOR DISCHARGES WITH CORONATING ELECTRODES



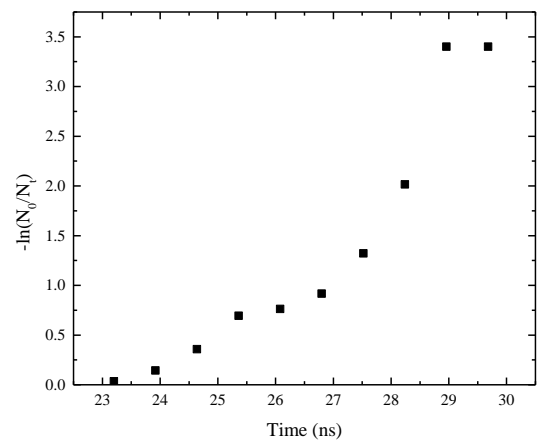
(a) 0 kV DC energisation



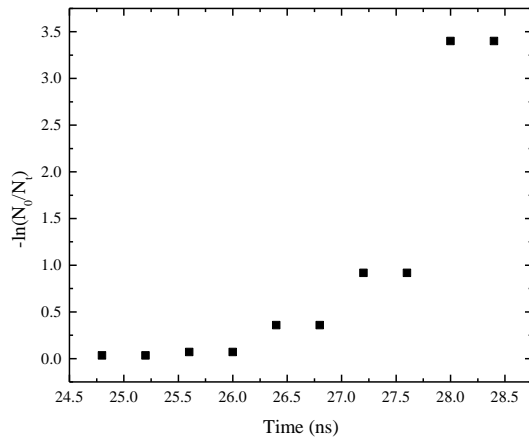
(b) 2 kV DC energisation



(c) 4 kV DC energisation



(d) 6 kV DC energisation



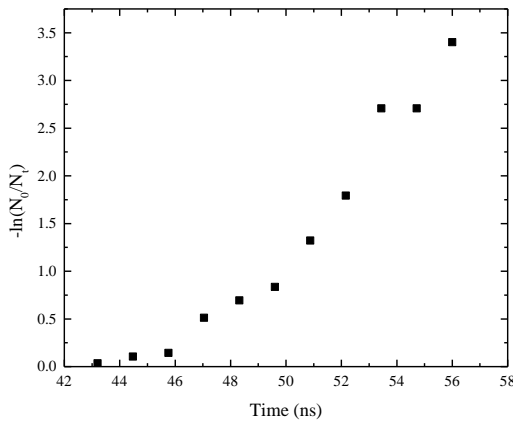
With high-tension corona electrodes

Gas – Air

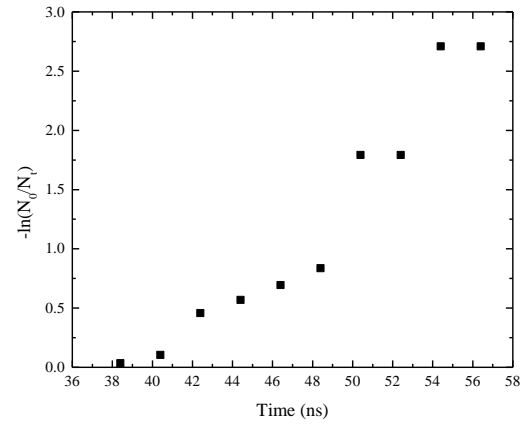
Pressure – 0.1 MPa

(e) 8 kV DC energisation

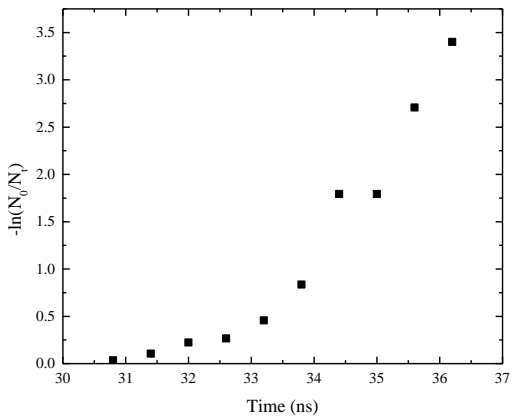
Figure 14.5 Laue graphs for 0.1 MPa air with corona discharge electrodes.



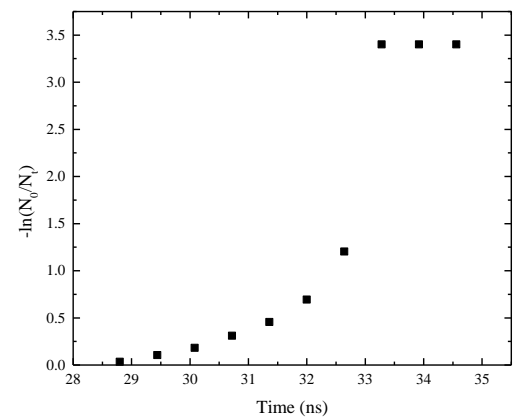
(a) 0 kV DC energisation



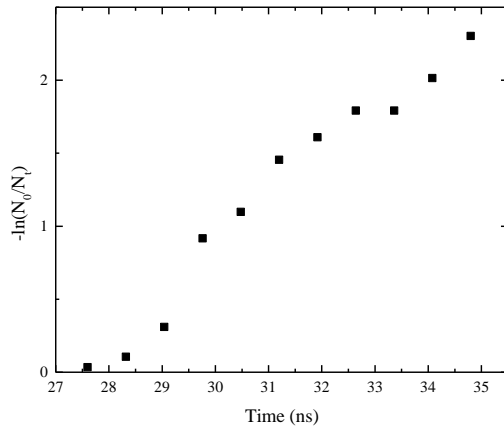
(b) 2 kV DC energisation



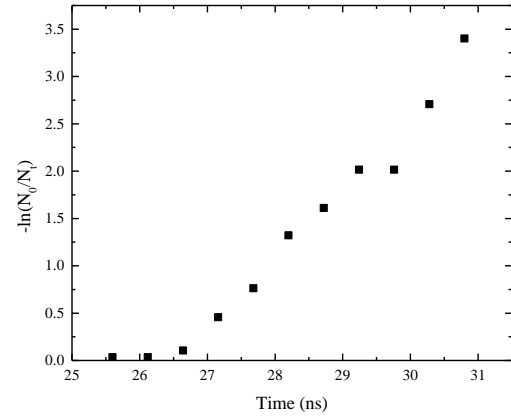
(c) 4 kV DC energisation



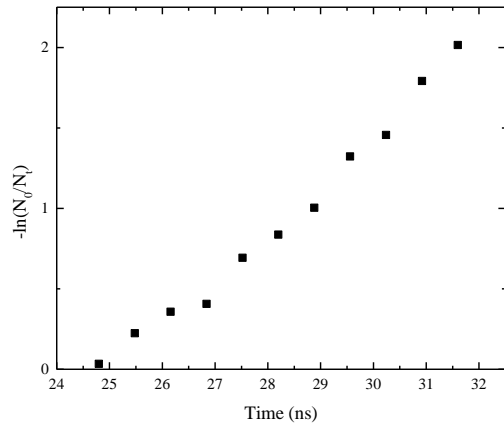
(d) 6 kV DC energisation



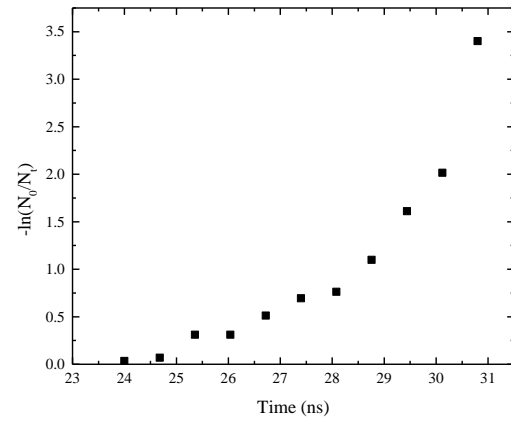
(e) 8 kV DC energisation



(f) 10 kV DC energisation



(g) 12 kV DC energisation



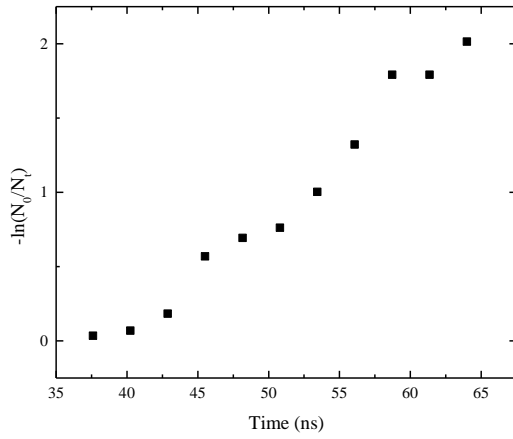
(h) 14 kV DC energisation

With high-tension corona electrodes

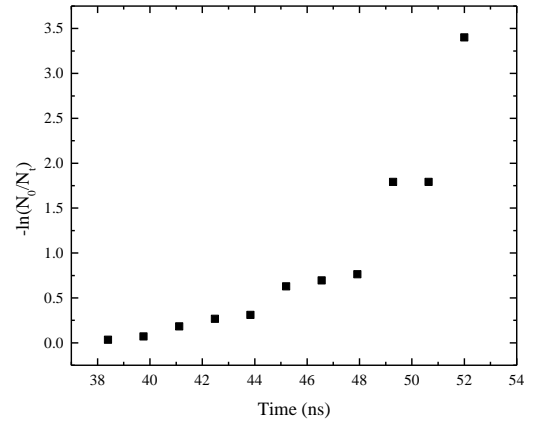
Gas – Air

Pressure – 0.2 MPa

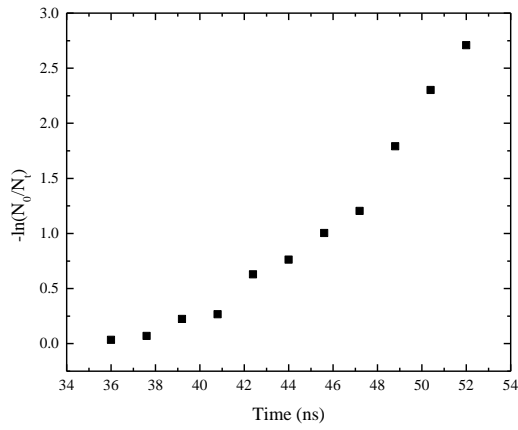
Figure 14.6 Laue graphs for 0.2 MPa air with corona discharge electrodes.



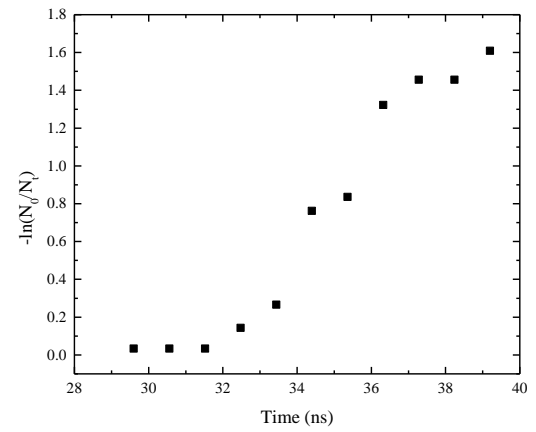
(a) 2 kV DC energisation



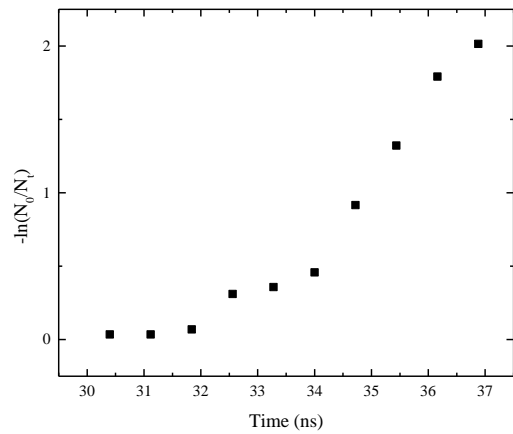
(b) 4 kV DC energisation



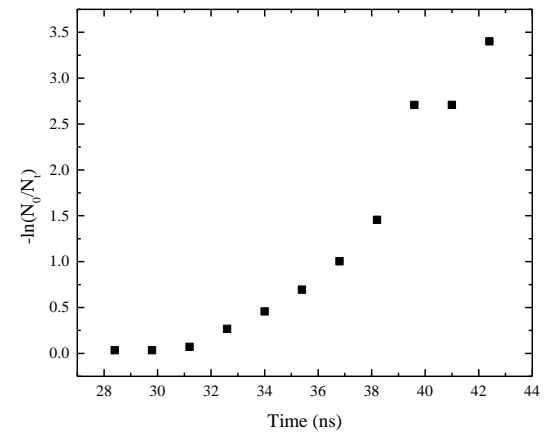
(c) 6 kV DC energisation



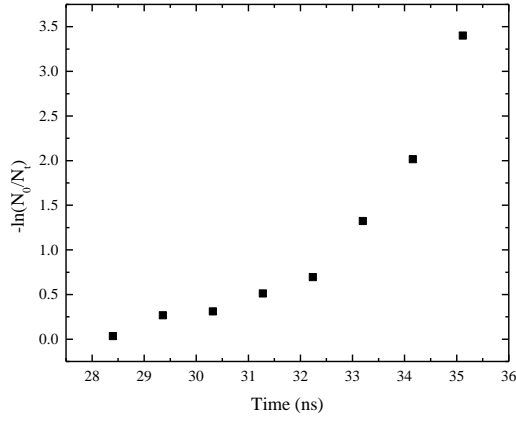
(d) 8 kV DC energisation



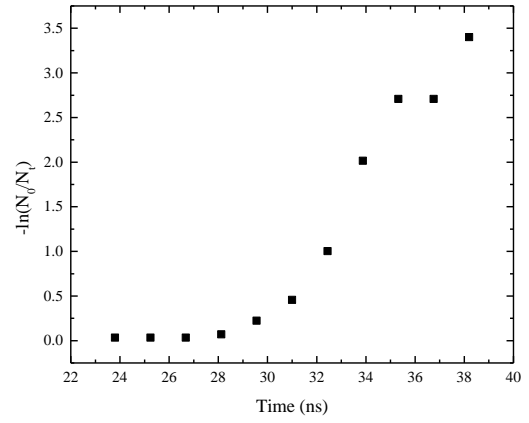
(e) 10 kV DC energisation



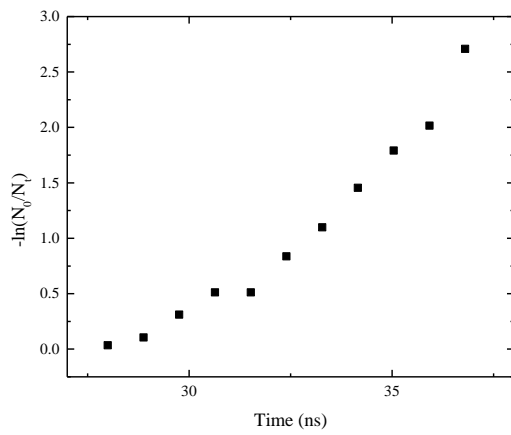
(f) 12 kV DC energisation



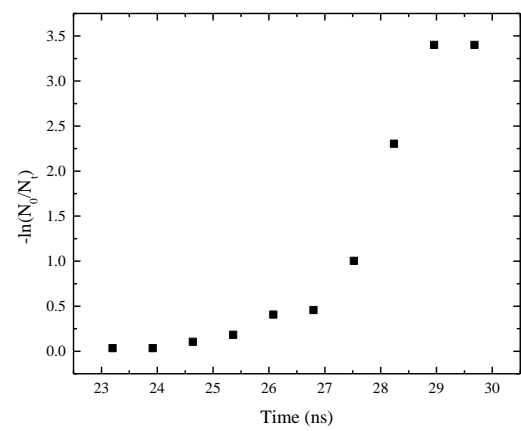
(g) 14 kV DC energisation



(h) 16 kV DC energisation



(i) 18 kV DC energisation



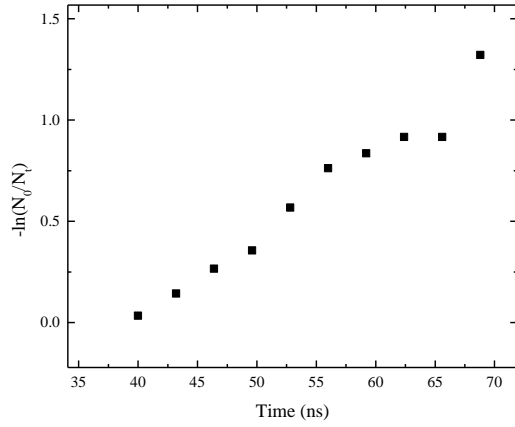
(j) 20 kV DC energisation

With high-tension corona electrodes

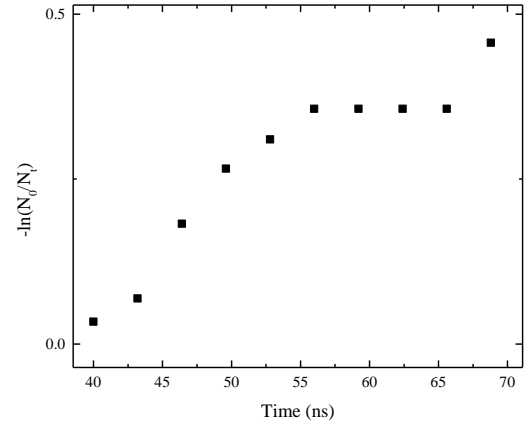
Gas – Air

Pressure – 0.3 MPa

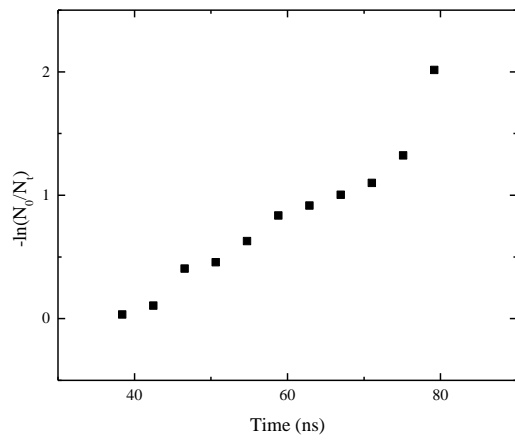
Figure 14.7 Laue graphs for 0.3 MPa air with corona discharge electrodes.



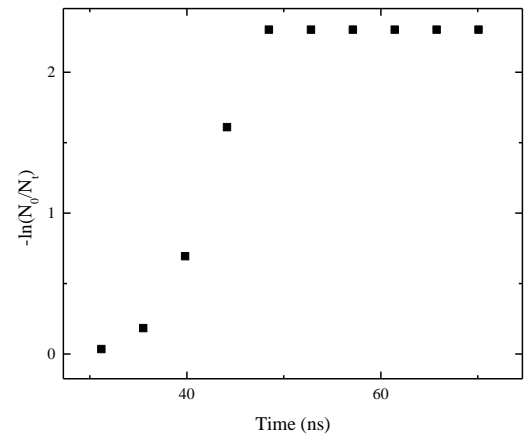
(a) 8 kV DC energisation



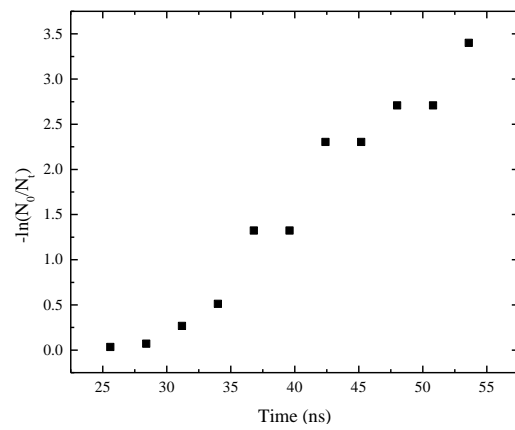
(b) 10 kV DC energisation



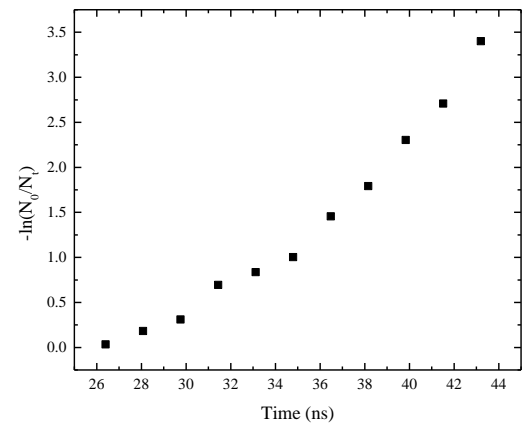
(c) 12 kV DC energisation



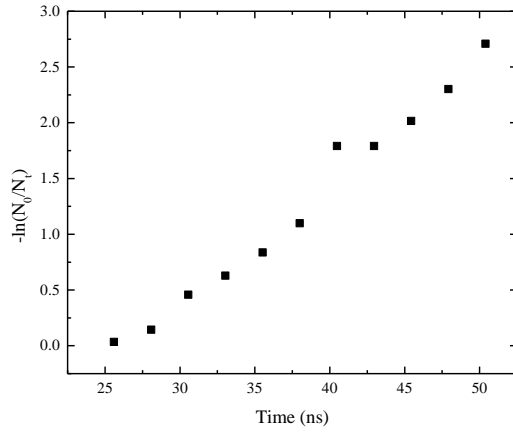
(d) 14 kV DC energisation



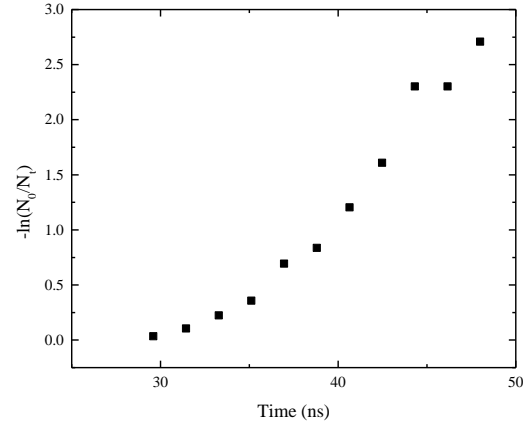
(e) 16 kV DC energisation



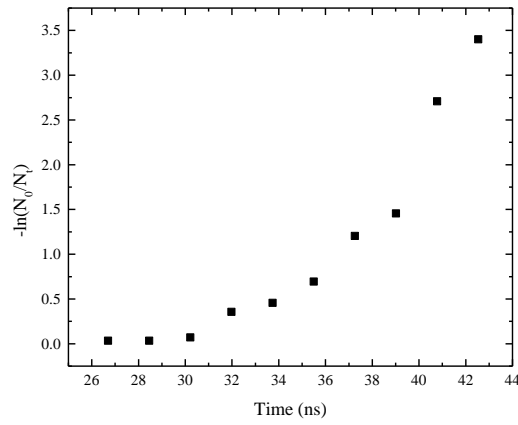
(f) 18 kV DC energisation



(g) 20 kV DC energisation



(h) 22 kV DC energisation



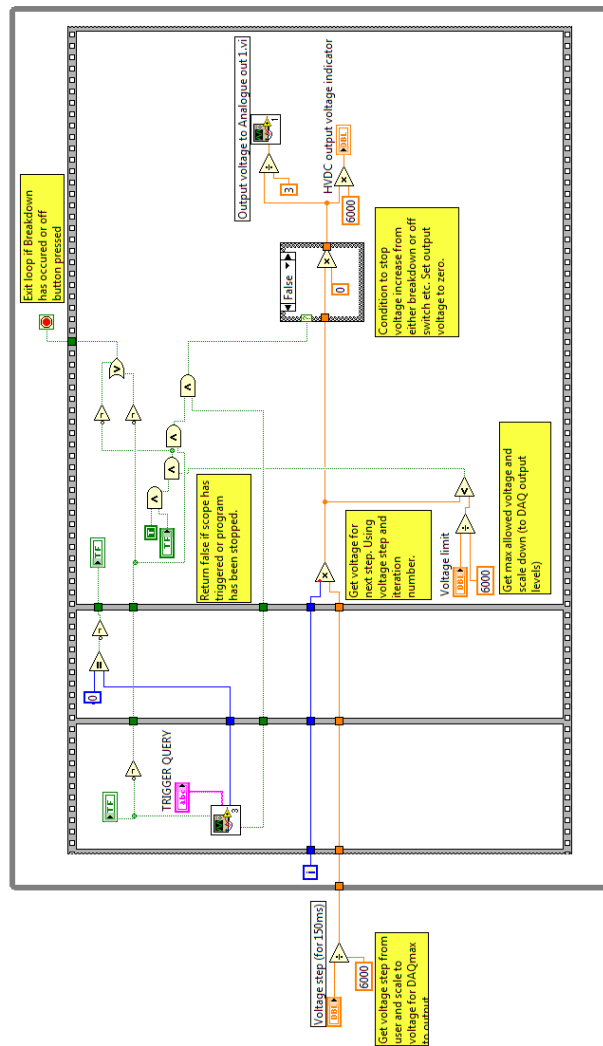
(i) 24 kV DC energisation

With high-tension corona electrodes
 Gas – Air
 Pressure – 0.4 MPa

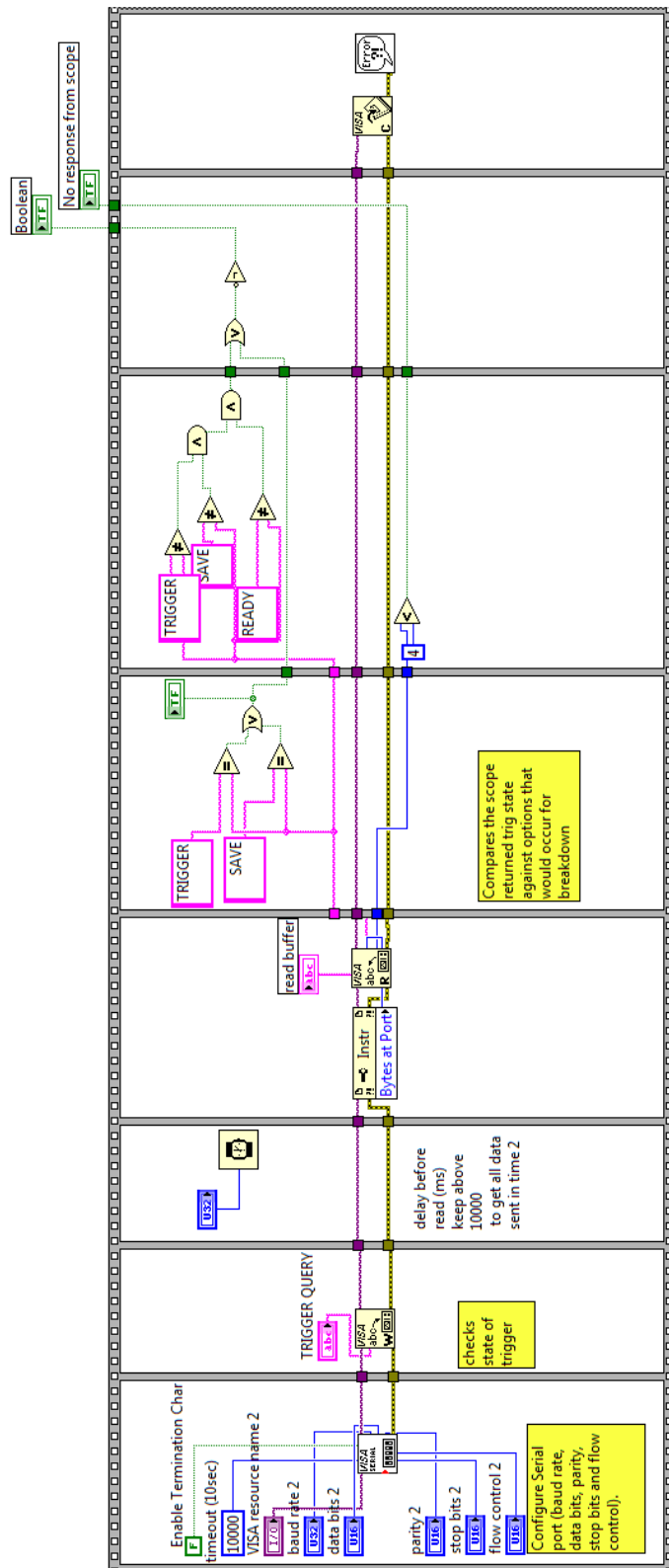
Figure 14.8 Laue graphs for 0.4 MPa air with corona discharge electrodes.

15. APPENDIX 2: LABVIEW CODE

15.1 MAIN BODY OF CODE

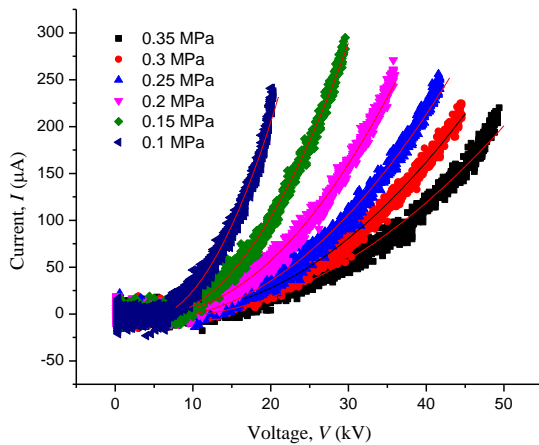


15.2 OSCILLOSCOPE TRIGGER CODE

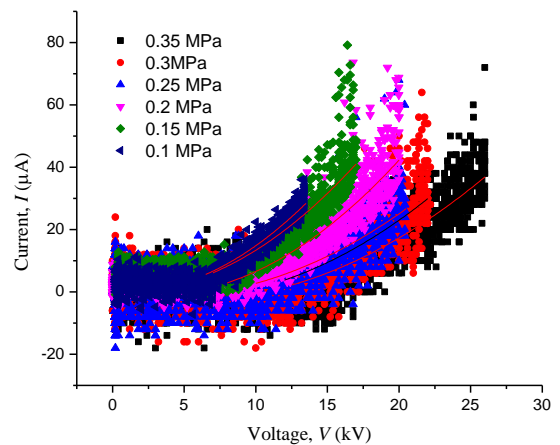


16. APPENDIX 3: CORONA DISCHARGE V - I CURVES

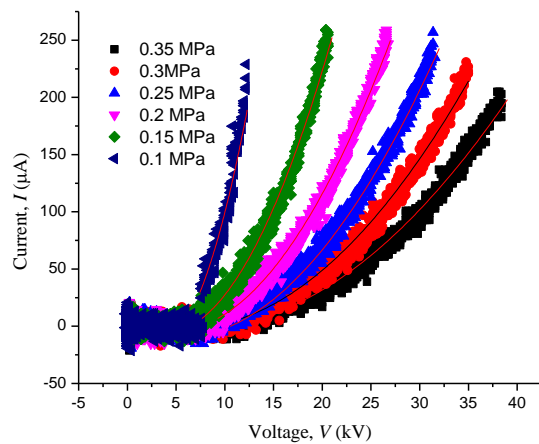
16.1 CORONA DISCHARGE V - I CURVES FOR GRAMOPHONE NEEDLE POINT ELECTRODE IN AIR



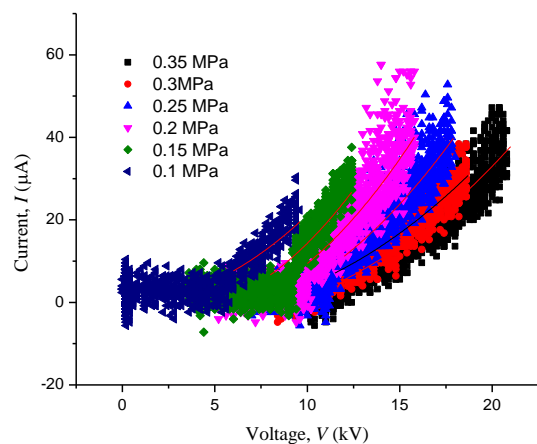
(a) 10 mm, Negative



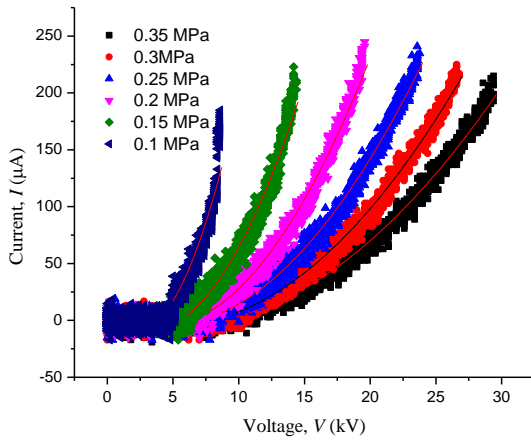
(b) 10 mm, Positive



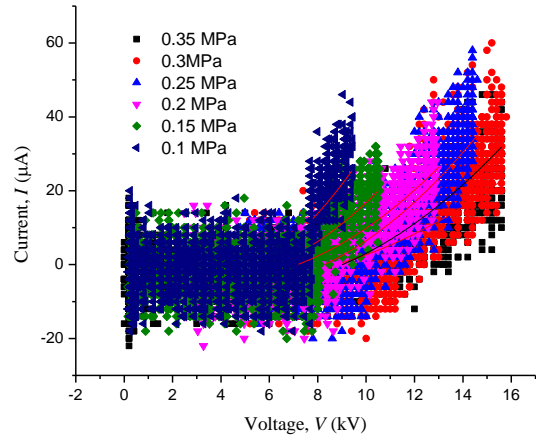
(c) 7 mm, Negative



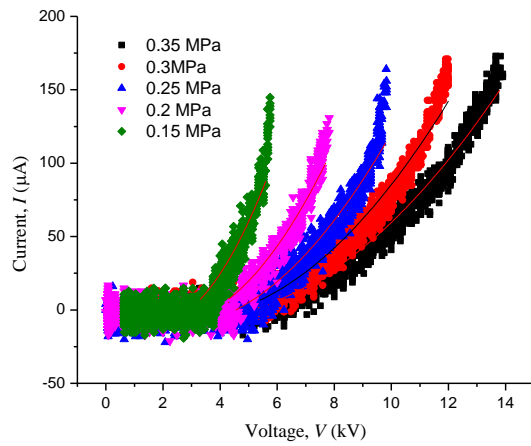
(d) 7 mm, Positive



(e) 5 mm, Negative



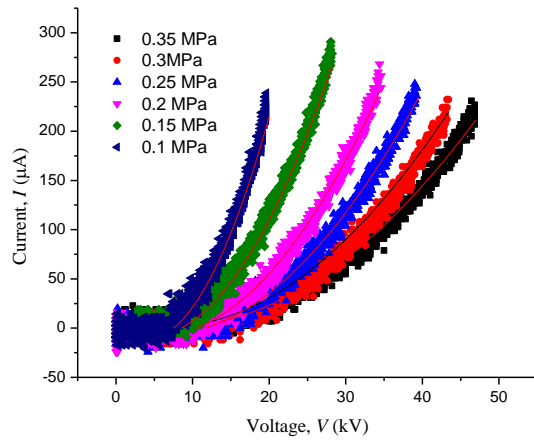
(f) 5 mm, Positive



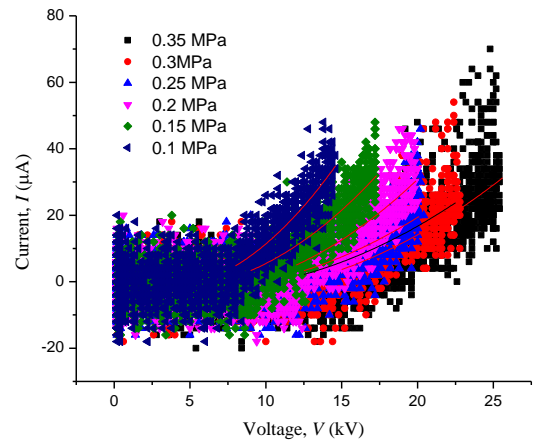
(g) 2 mm Negative

Figure 16.1: Corona discharge V-I curves for gramophone needle.

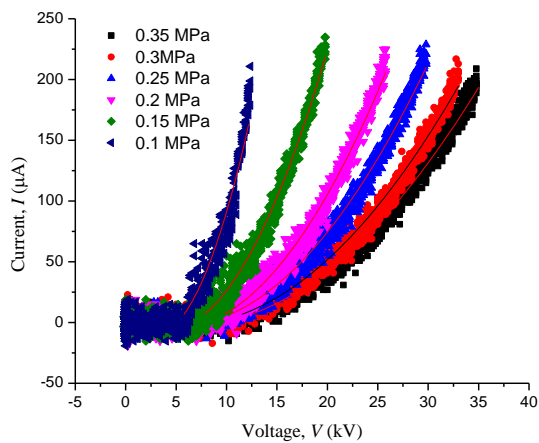
16.2 CORONA DISCHARGE V - I CURVES FOR 0.067 mm RADIUS POINT ELECTRODE IN AIR



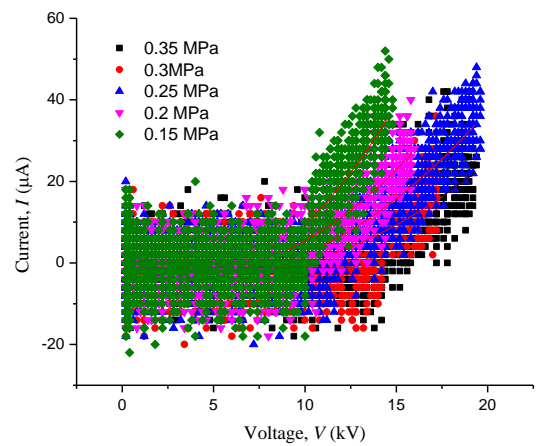
(a) 10 mm, Negative



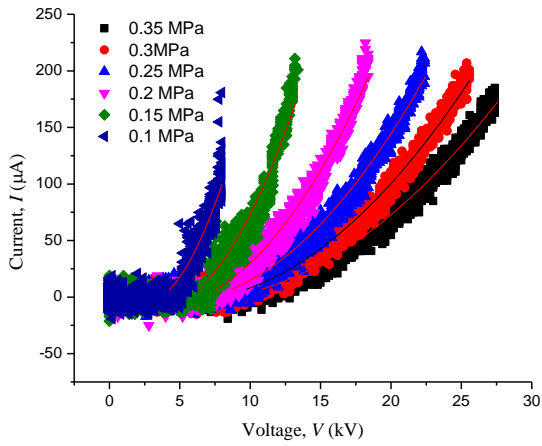
(b) 10 mm, Positive



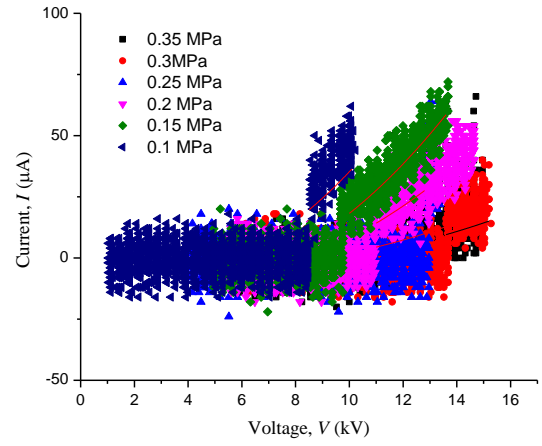
(c) 7 mm, Negative



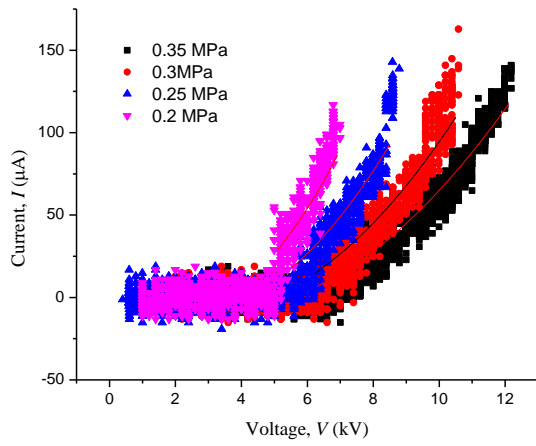
(d) 7 mm, Positive



(e) 5 mm, Negative



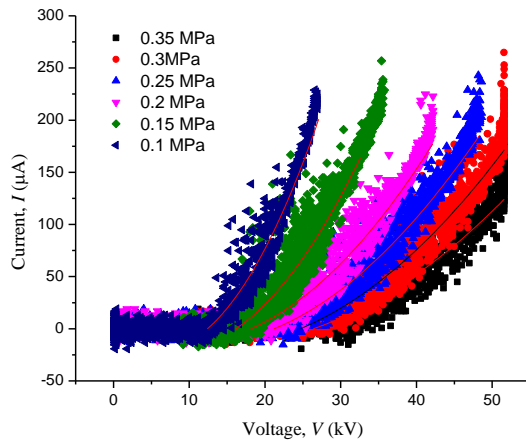
(f) 5 mm, Positive



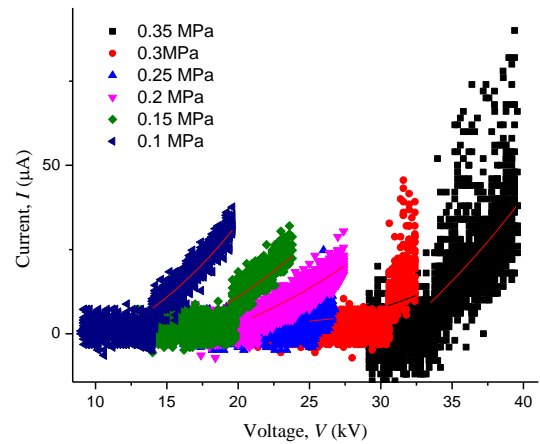
(g) 2 mm, Negative

Figure 16.2: Corona discharge V-I curves for 0.067 mm radius sharpened point tungsten rod point electrode.

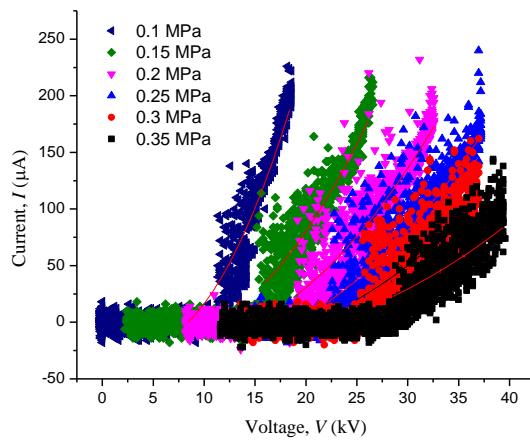
16.3 CORONA DISCHARGE V - I CURVES FOR 0.8 MM RADIUS POINT ELECTRODE IN AIR



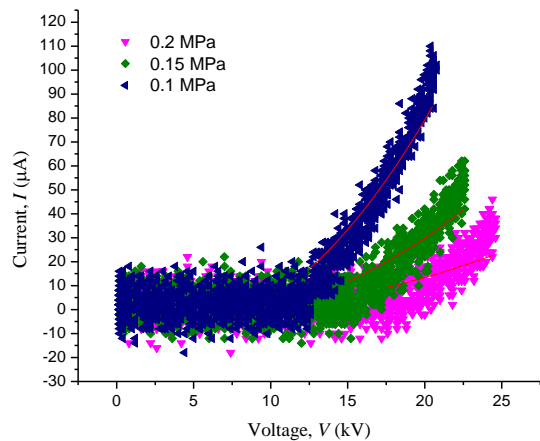
(a) 14 mm, Negative



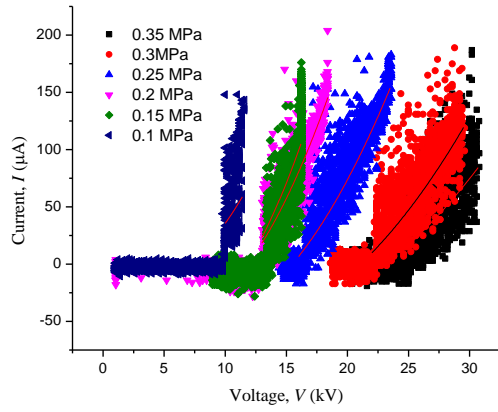
(b) 14 mm, Positive



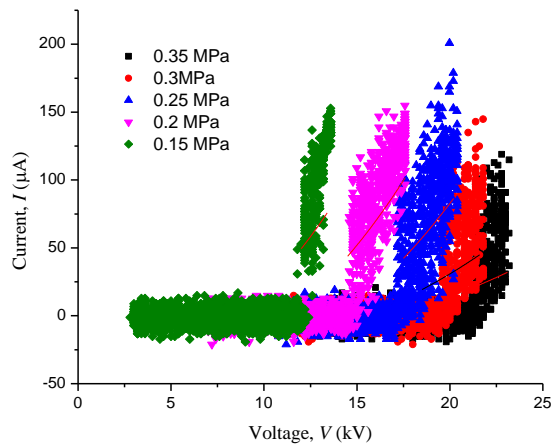
(c) 10 mm, Negative



(d) 10 mm, Positive



(e) 7 mm, Negative



(f) 5 mm, Negative

Figure 16.3: Corona discharge V-I curves for 0.8 mm radius hemispherical tipped tungsten rod point electrode.

17. APPENDIX 4

DISCHARGES AND ELECTRICAL BREAKDOWN OF GASES

This section will briefly describe gas discharges processes: Townsend avalanche, corona and spark breakdown, which are important in order to consider what breakdown is in terms of electrical conduction through gases. Electrical breakdown of gas is a process of a sudden increase in electrical conductivity of gaseous medium that was an insulator in its normal state. This section will discuss the mechanisms that turn a normal state insulating gas into a highly conductive plasma channel.

When an electric field is applied to a gas, charged particles which may naturally occur in the gas medium due to cosmic ray ionisation and/or other ionisation processes, drift towards the cathode (if positively charged) or anode (if negatively charged). The drift of charged particles results in a flow of current. The magnitude of current in this case is proportional to the applied field and is known as Ohmic conduction, identified in Figure 17.1. Ohmic conduction process is typically observed at relatively low fields in the case when the rate of creation of charged particles in gas is not much higher than the rate of their removal/disappearance. At 'ground level' there are ~ 1000 positive and negative charged particles per cm^3 and there are ionisation and recombinations occurring constantly [Howatson 1965]. The Ohmic region of current in an electric field will saturate when the current becomes limited by the number of supplied charges. i.e. the amount of ionisations per second in the gas which is between 2 and 10 ionisations per second per cm^3 . However, with an increase in the applied field the rate of production of charged particles in the gas can become significant leading to avalanche-type ionisation processes (Townsend avalanches) which will result in significant increase in conductivity of the gaseous medium. Figure 17.1 shows the current characteristics for a uniform electric field in a gas as field is increased identifying conduction current, current saturation and Townsend avalanche.

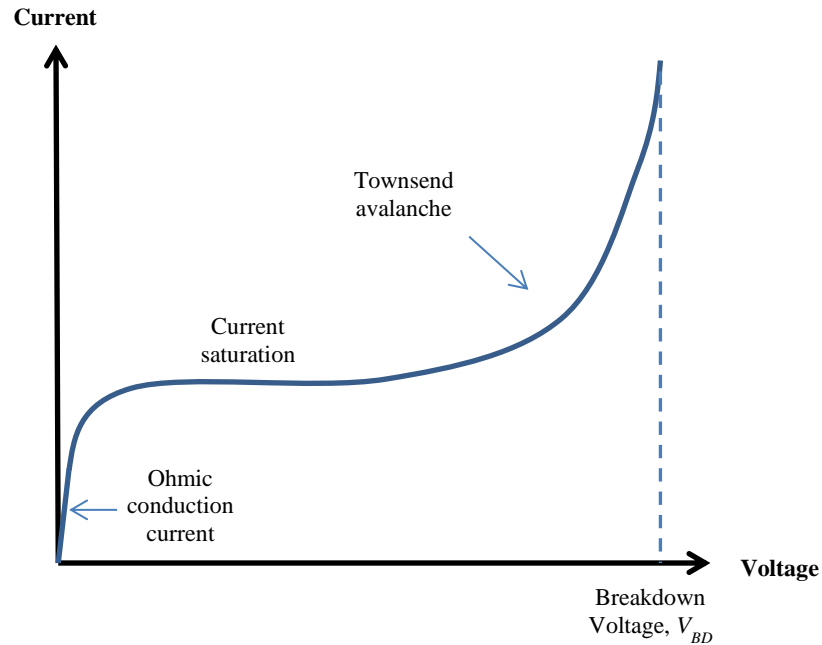


Figure 17.1 V-I curve showing current phases in a uniform electric field at low pressure.

Identified in Figure 17.1, after the Ohmic region the current has saturated and remains constant, defined by the ionisation rates of the gas. The current does not increase again until an electron avalanche (Townsend avalanche) develops. When the field (corresponding voltage) reaches an avalanche triggering level, electrons in the gas will have sufficient energy to cause ionisations resulting in extra free electrons. At this point successive ionisations can form an electron avalanche and the number of electrons increases exponentially. This is represented as an exponential increase in the current which is identified in Figure 17.1.

At specific pressure and inter-electrode distances a further phase of breakdown can be developed, this phase is called a streamer breakdown. An electron avalanche will transform into a plasma streamer when the charged particles at the head of the avalanche reach a critical concentration. The plasma streamer which is this channel filled with ionised gas propagates towards the opposite electrode through the gas filled gap and connects the electrodes. This is the moment of breakdown and the current will increase to a maximum as the plasma resistance reduces to a minimum.

Townsend Electron Avalanche

In the first instance, it is necessary to consider a scenario where there is a uniform electric field between two parallel plate electrodes where the gap much smaller than the width of the

electrodes. In this topology, the electric field can be assumed to be uniform across the inter-electrode gap and width of the electrode.

Electrons are produced (naturally occurring as well as induced by gas discharges) in the region of the cathode and are then accelerated in the electric field. The electrons collide with atoms or molecules of gas and if the electrons have gained sufficient energy the collisions can cause ionisations. After an ionisation by electron impact collision, there are two free electrons and a positive ion. The two electrons are accelerated in the electric field and may go on to cause their own ionisations. And their new electrons go on to ionise and so on and the number of free electrons grows exponentially [Townsend 1915]. Figure 17.2 shows the development of an electron avalanche in steps with one electron colliding with a particle and then both being free to collide again.

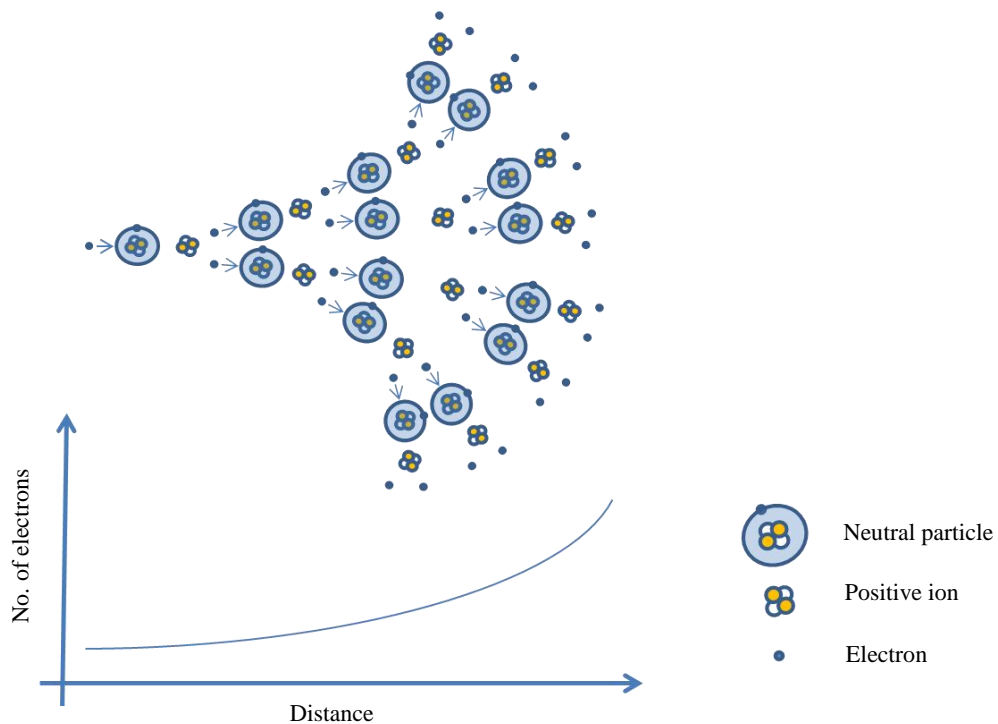


Figure 17.2 Electron avalanche stepped development.

As the number of electrons increases, it corresponds to an exponential increase in current, Figure 17.2, and can be seen in the Townsend region.

The increase in electrons can be described using Townsends first ionisation coefficient, α , defined as the number of ionisations events produced by an electron in a unit distance. In electronegative gases, electrons have an affinity to attach to neutral particles to form

negative ions. To account for attachment in Townsend avalanches, the effective Townsend avalanche coefficient, α_{eff} , should be used.

Townsend's first ionisation coefficient can be used to calculate an increase in electrons over a defined distance between the electrodes. The number of electrons increased can be expressed by [Townsend 1914]:

$$\frac{n}{n_0} = e^{(\alpha_{eff})x} \quad (17.1)$$

where:

- n is the number of electrons,
- n_0 is the initial density of particles,
- x is the distance of the electron avalanche,
- and α_{eff} is Townsends first ionisation coefficient.

Secondary initiating electrons can be produced at the cathode by positive ions colliding with gas particles, other ionisations due to particle collisions and photoionisation within the gas. However, the contribution of these processes is negligible compared to the electrons produced by positive ion bombardment. To account for secondary electrons, which will start their own Townsend avalanches, a second coefficient, γ , was proposed by Townsend.

Allowing for secondary electrons, the total current can be expressed as [Haddad and Warne 2007][Llewellyn-Jones 1957]:

$$i = i_0 \frac{\alpha e^{\alpha_{eff}d}}{1 - \gamma(e^{\alpha_{eff}d} - 1)} \quad (17.2)$$

where i is the current at the anode, i_0 is the current at the cathode, α_{eff} is the Townsends first effective ionisation coefficient and γ is Townsends second ionisation coefficient, and d is the electrode gap. The current will increase to a theoretical infinity when the denominator tends to zero:

$$1 - \gamma(e^{\alpha_{eff}d} - 1) = 0 \quad (17.3)$$

or

$$\sim \gamma e^{\alpha_{eff}d} = 1 \quad (17.4)$$

Townsend established that breakdown would occur when the condition in Equation (17.3) was true, and it is known as the Townsend sparking criterion. Townsend's sparking criterion in the form of Equation (17.3) allows the theoretical calculation of breakdown voltage for breakdown in uniform fields. The next section discusses the breakdown voltage of uniform topologies using Panchen's law.

Paschen's Law

It has been shown that the creation of secondary electrons is directly related to the electric field and gas pressure (Appendix 4). By taking α_{eff} and γ as a function of (E/p) as shown:

$$\gamma = f_1(E/p) \quad (17.5)$$

$$\alpha_{eff} = pf_2(E/p) \quad (17.6)$$

In a parallel plate topology the electric field can be calculated (Section 2.1.2) as the voltage difference between the electrodes and the distance between them ($E = V/d$). Therefore, E/p can be written as V/pd :

$$f_1\left(\frac{V_{BD}}{pd}\right) e^{pf_2\left(\frac{V_{BD}}{pd}\right)d} = 1 \quad (17.7)$$

where:

- E is the electric field strength,
- p is the gas pressure,
- d is the inter-electrode spacing,
- $pf_2(E/p)$ is Townsend's first ionisation coefficient as a function of electric field and pressure,
- $f_1\left(\frac{E}{p}\right)$ is Townsend's second ionisation coefficient as a function of electric field and pressure,
- V_{BD} is the breakdown voltage.

From Equation (17.7), for the sparking criterion, it can be seen that the voltage at which breakdown occurs is only dependent on the pressure and distance:

$$V_{BD} = f(pd) \quad (17.8)$$

which is known as Paschen's law. Paschen's law can be applied to a wide range of electric fields and pressures. Breakdown voltages can be predicted for a given gas by the pressure and electrode spacing (pd). For this reason, breakdown voltage data is often presented as a function of pressure and distance, $V(pd)$, as shown in Figure 17.3. Figure 17.3 depicts a Paschen curve with the Paschen minimum labelled.

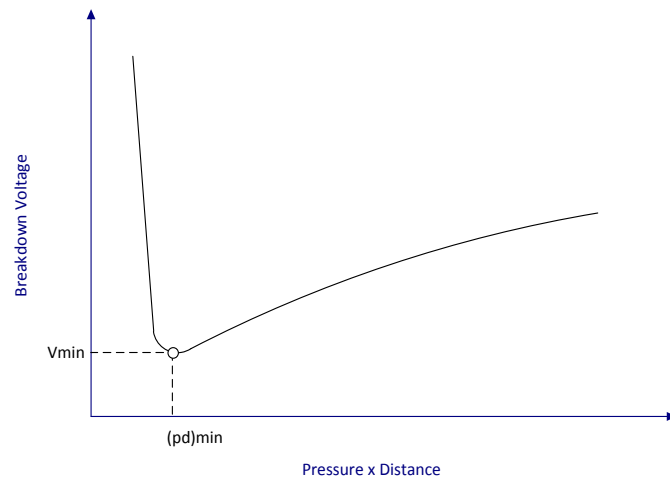


Figure 17.3 Paschen curve example.

Paschen curves can be split into two sections around the minimum. The left hand side (LHS) can be explained for very low pressure: there are few particles and it is difficult to form an electron avalanche and so the breakdown voltage is higher. On the right hand side of the Paschen minimum, the pd increases and there are plenty of atoms for an electron avalanche. However, at larger electrode gaps the electric field reduces and so a higher voltage is required to get the electric field up to breakdown level.

The minimum point of the curve in Figure 17.3 is known as the Paschen minimum, and is the optimal pressure to electrode spacing conditions for creating an electron avalanche and the least voltage to cause breakdown. The Paschen minimum for air is: $V_{min} = 352 V$ and $pd_{min} = 73 Pa.cm$ [Raizer 1991].

Paschen's law has been experimentally proven for low pressures, however, has limitations for its range of distances and at high pressures. At large gaps and high pressures, the mechanisms of breakdown are no longer purely based around the Townsend avalanche. At higher pressures close to the densities found in liquids, the breakdown mechanisms can change [Hogg 2012a]. A limitation of the Paschen curve that is particularly important in many current applications is very small inter-electrode gap (μm range) where the breakdown

voltage on the LHS of the Paschen minimum does not follow the Paschen theoretical curve and reduces even further below the Paschen minimum, Figure 17.4. Figure 17.4 shows a Paschen curve for a very small electrode gap (μm) where Paschen's law no longer holds.

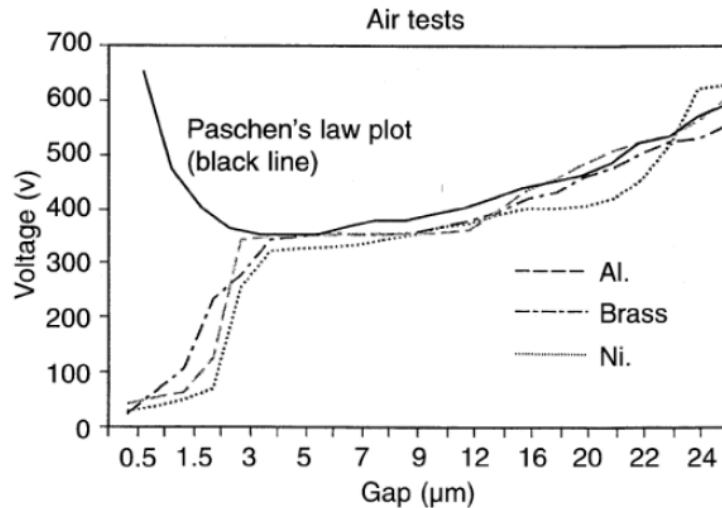


Figure 17.4 Paschen curve for micro-gaps [Torres 1999].

The process by which breakdown occurs in these very small gaps does not follow the theoretical Paschen's law instead of potential increase as the breakdown voltage as it would be expected from the classic Paschen curve for very low pd 's, the breakdown voltage reduces rapidly. This is of significance to micro and nano technological applications such as MEMS switches.

Townsend discharge does not sufficiently explain breakdown in all electrode topologies and gas pressures. At specific compositions of gas pressure, inter-electrode distance and applied voltage stress, Townsend avalanche can transition into a streamer discharge which is discussed in Appendix 4.

Anode Directed Streamer Discharge

The development of an electron avalanche will distort the local electric field in the region of the avalanche. The fast moving electrons leave behind positive ions after ionisations which have a negligible drift velocity compared to the electrons and can be assumed to be almost stationary. This results in a collection of positive charges mixed with some neutral particles, which gives a positive net charge in the region behind the electron advancement. The faster moving free electrons group to form a net negative charge region. These charged regions are

known as space charges. The space charges have their own field enhancements between the two regions of space charges and between the space charges and the electrodes, Figure 17.5.

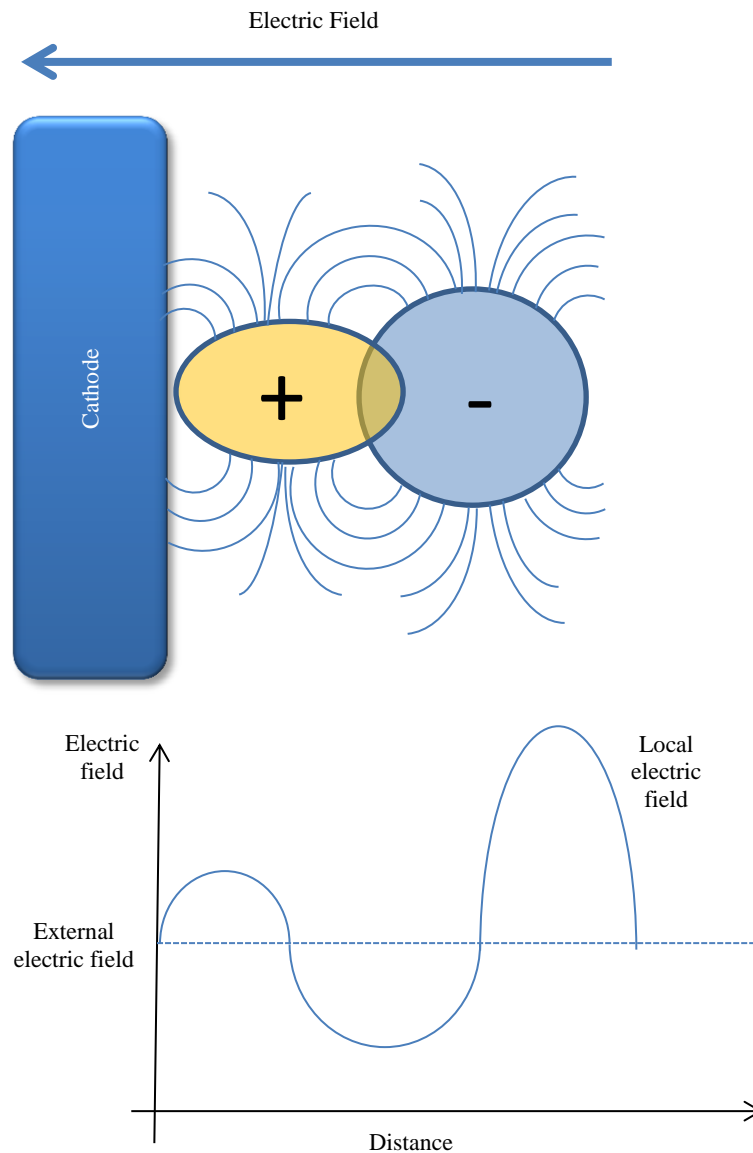


Figure 17.5 Avalanche space charge and local electric field enhancement.

The local fields created by space charge are superimposed with the external field to have a total field at the tip of the avalanche that is significantly higher than the externally applied field. The tip of the avalanche can be large enough to sustain ionisation even when the external field is reduced below that necessary to ionise. This is important when considering non-uniform field topologies where the electric field reduces exponentially from the high field to a much lower field across the electrode gap.

The Townsend discharge alone is not sufficient to explain the breakdown of all pressure ranges and electrode gaps. It was discovered that Townsend avalanches evolved into much narrower focused filamentary discharges known as streamers when the concentration of charges at the head of the streamer increased.

The transition criteria from avalanche to streamer for an anode directed discharge is based on a specific charge concentration at the head of the avalanche expressed as: [Bluhm 2006][Meek 1953][Kuffel 2000]:

$$n = \exp(\alpha X_c) \sim 10^9 \quad (17.9)$$

where:

- n is the number of electrons at the head of the avalanche,
- α is Townsend's first ionisation co-efficient,
- and X_c is the length of avalanche.

The avalanche to streamer transition criteria can be also expressed as a critical length of the electron avalanche based on Equation (17.9)

$$\alpha_{eff} X_c \approx 18 - 20 \quad (17.10)$$

The field at the head of the streamer is greatly increased due to high concentration of the electrons, the streamer starts to grow from the avalanche head, the velocity of streamer exceeds that of the Townsend avalanche (typically the velocity of the streamer can be approximated by the drift velocity of electrons in gas).

Thus far, the breakdowns considered have been for uniform fields. Paschen curves are theoretically not applicable to non-uniform fields because in non-uniform fields, electron energies and as such Townsend's ionisation coefficients are not constant across the inter-electrode gap. However, breakdown data is sometimes still represented as a function of pressure and distance and compared against actual Paschen curves.

Discharges in Highly Divergent Electric Fields

Non-uniform fields have localised regions of increased electric field strength, consequently, breakdown mechanisms are not exactly the same as in uniform fields. The distribution of electron energies in non-uniform fields isn't constant due to the varying electric field

intensity. Therefore Townsend's first ionisation coefficient, α , varies depending on electric field intensity [Loeb 1939]. Figure 17.6 shows Townsend's first ionisation coefficient with distance from a point electrode.

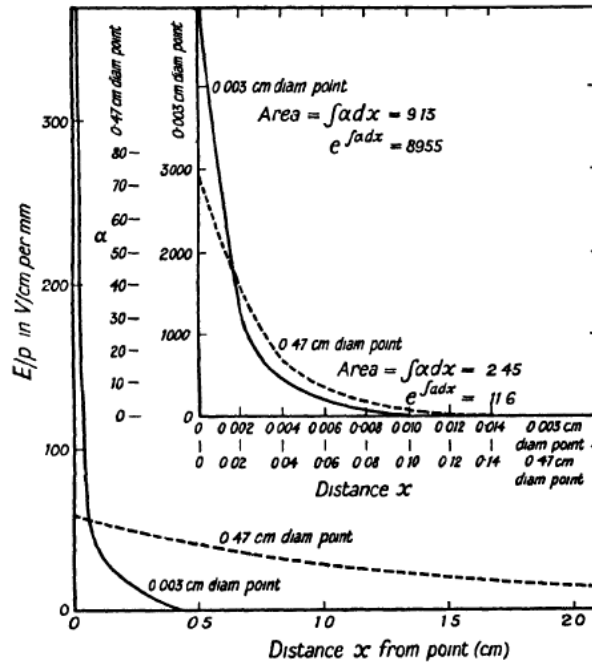


Figure 17.6 Townsend's first ionisation coefficient in non-uniform field [Loeb 1939].

Therefore, in considering Townsend avalanches the ionisation coefficient is now distance-dependant and the term $\alpha_{eff}d$ now becomes:

$$\int_0^d \alpha_{eff}(x) dx \quad (17.11)$$

where:

- α_{eff} is the effective Townsend's first ionisation coefficient,
- and d is the distance between the electrodes.

In localised high field regions, ionisation events are initiated and electron avalanches can occur. As the electron avalanche spreads to lower field regions, ionisations stop and the result is a partial-discharge known as 'corona discharge'. The next section discusses corona discharge from positive and negative energisation perspectives.

Corona Discharge

Corona discharge is a type of partial-discharge which does not cover the whole inter-electrode gap with a highly conductive plasma as it does in case of a spark discharge. In corona discharge, its ionisation zone expanding only into a small part of the inter-electrode gap. Occurring in non-uniform topologies with intense localised electric fields and low average field intensity, corona discharge presents with a luminous focal point in the high field regions, radiating into the lower field regions where it becomes less visible. The brightness and morphology of corona discharges depend on, amongst other parameters, the polarity of energisation voltage. Negative corona discharge radiates from sharp cathode and gradually decreases in light intensity. Positive energisation corona discharge presents with a focal point, branching off in bursts of focused bright filaments. In both, negative and positive energisation coronas, the size and volume of corona discharges depends on the applied voltage, gas type and pressure. The process behind the development of positive and negative energisation corona discharges is different. Therefore, they are discussed separately.

- *Negatively energised corona discharge*

Negative corona discharge occurs in high field regions where the field exceed the critical ionisation value, initiating electron avalanches and Townsend avalanches. When the discharge expands into lower field regions the ionisation processes rapidly reduces and recombination and attachment become the dominating processes. The electron avalanche stops advancing and results a concentration of charges forming localised regions of space charge, Figure 17.7.

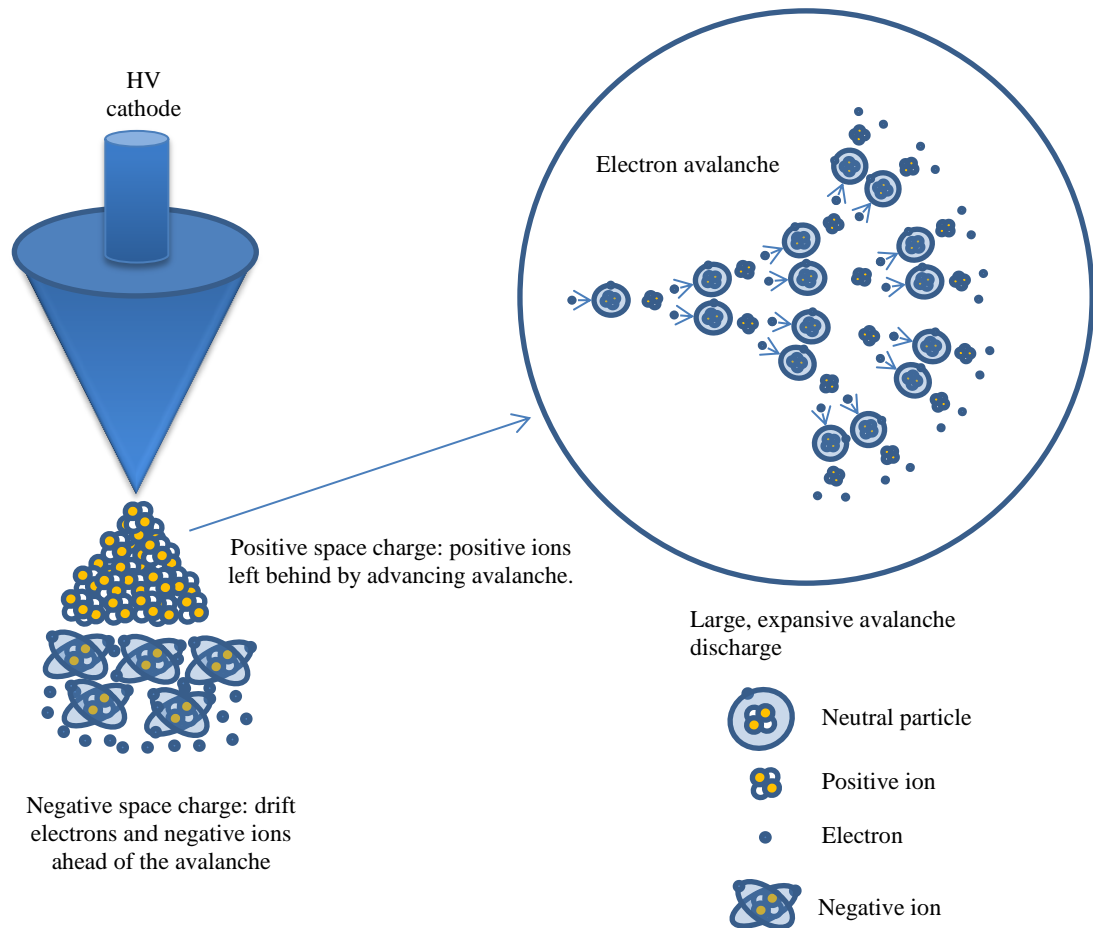


Figure 17.7 Negative space charge from a HV cathode point electrode.

Negative space charge regions created by negatively energised corona discharge in electronegative (attaching) gases has this space charge a significant impact on the eventual breakdown characteristics. Positively energised corona discharge mechanisms are different to negative corona and does not result in significant regions of space charge as in the case of negative corona. The next section discusses the development of positive corona discharge.

- *Positive corona discharge*

Initiation and development of the positively energised corona discharge also stems from the fundamental theory of ionisation, however, the discharge mechanisms are different from the negative corona. A high voltage sharp anode does not develop an expansive electron avalanche, instead it draws in miniature electron avalanches towards the high field region at the tip of the electrode. These avalanches are developed due to emission of photons from the ionization zone, thus photoionisation plays a significant role in developing positive corona discharges. The electrons accelerate towards the high field region and are absorbed by the

anode while the positive ions are left behind. Relatively slow moving positive ions form a net space charge in the close proximity to the sharp HV anode. Figure 17.8 depicts positive space charge forming in the region in front of a high-voltage anode point by mini electron avalanches leaving behind positive ions.

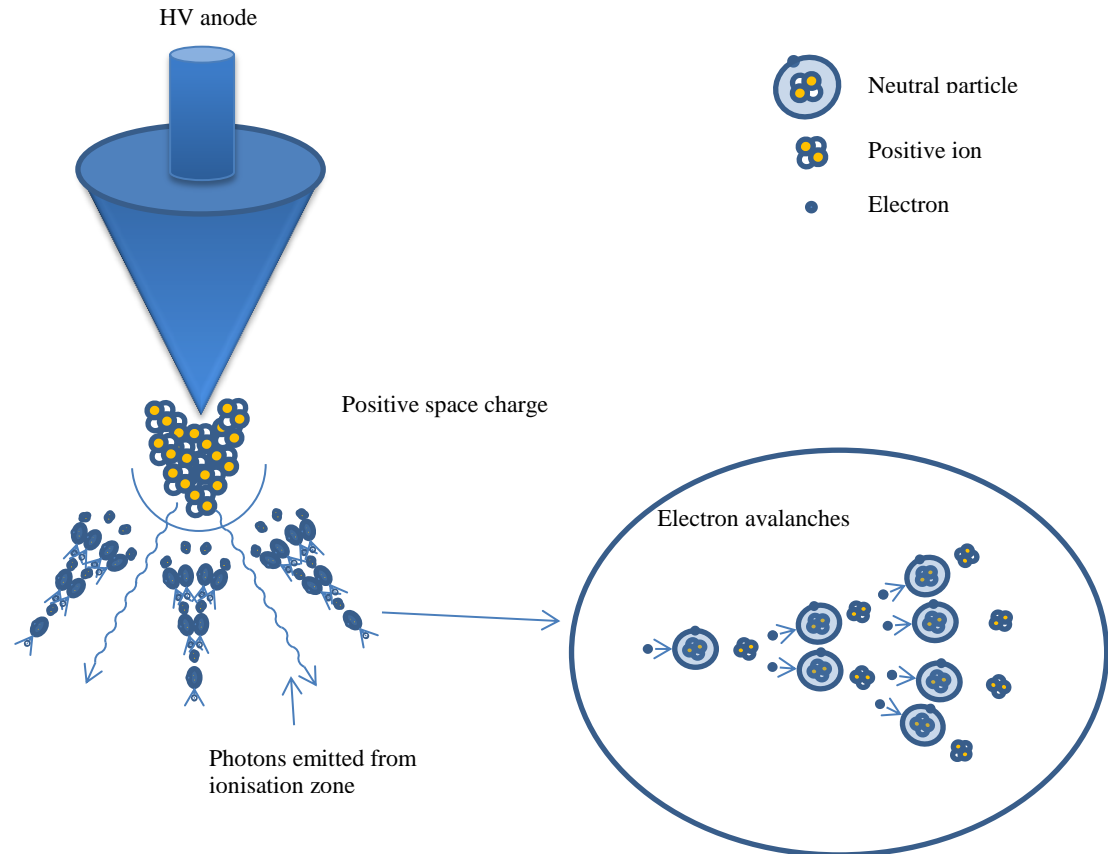


Figure 17.8 Positive space charge from a high-voltage anode point electrode.

Positive space charge plays a significant role in the development of the breakdown discharge known as a ‘cathode directed streamer’. However, there is comparatively little volumetric space charge compared with negative space charge.

Positive and negative corona discharges stop advancing when the electric field reduces below critical value (in atmospheric air this threshold is defined by equality of the effective ionisation coefficient to zero at 28-30 kV/cm/atm) and electrons recombine and attach to other particles.

In the case on negative corona in electro-negative gas, the electric field magnitude at the vicinity the tip of a point-plane topology is reduced due to development of volumetric space charge. The space charge region in front of the point electrode can ‘screen’ the electric field causing the peak field to be reduced, Figure 17.9.

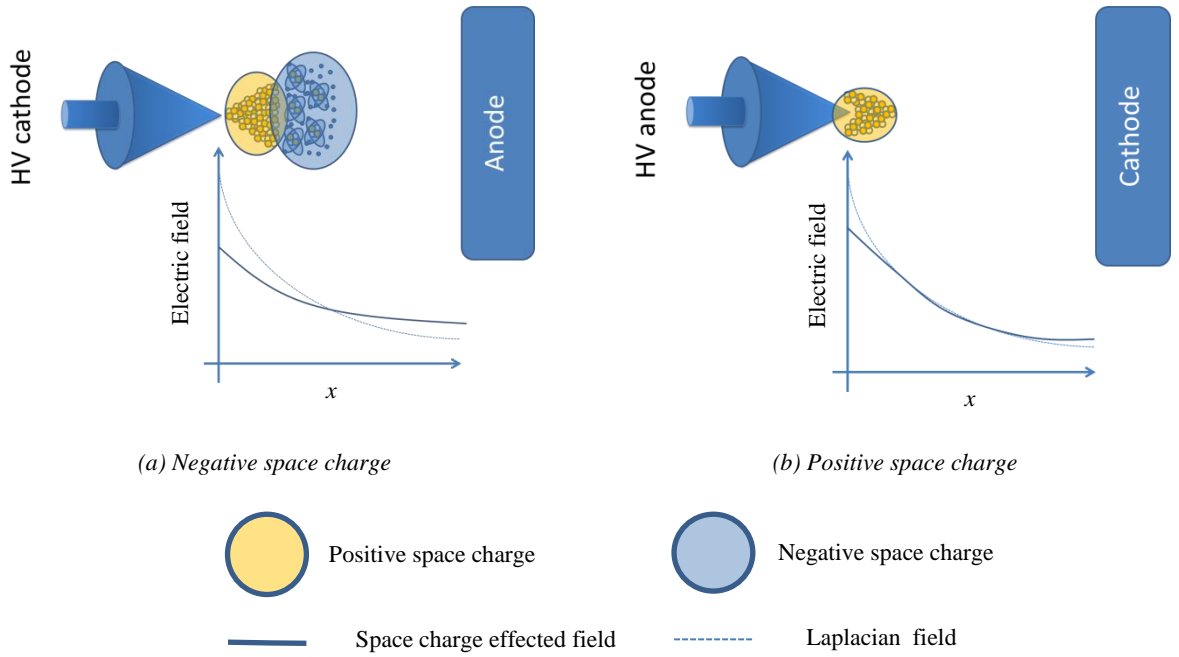


Figure 17.9 Illustration of space charge screening effects due to space charge.

Depicted in Figure 17.9, negative space charge from a point cathode (a) reduces the field at the tip of the electrode considerably more than positive space charge from a point anode (b). Space charge created by a high-voltage cathode can be significant in electronegative gases and result in higher breakdown voltages compared to a high-voltage anode. The next section gives a method for approximating the resulting electric field.

Space charge effected electric field

Using the mobility of the electrons, the space charge governed electric field can be obtained. Coelho and Debeau presents a method for calculation of the space charge governed field along the inter-electrode axis as [Coelho and Debeau 1971]:

$$E(v) = \frac{\sqrt{[\rho^2(2 - \rho)^2 E_P^2 - Av\{\rho(2 - \rho) + (1 - \rho)v - v^2/3\}]}}{(v + \rho)(2 - v - \rho)} \quad (17.12)$$

where:

$$A = \frac{2I}{\pi d \epsilon \mu} \quad (17.13)$$

$$\rho = \frac{a}{2d} \quad (17.14)$$

$$v = \frac{x}{d} \quad (17.15)$$

$$E_p = \frac{2V}{a \ln\left(\frac{4d}{a}\right)} \quad (17.16)$$

and E_p is the peak Laplacian field, v is the normalised distance between the point and the plane electrode, d is the gap between the point and plane electrodes, x is the distance from the point electrode along the inter-electrode gap, μ is the mobility of electrons, ϵ is the permittivity, I is the current, a is the radius of the point electrode and V is the voltage.

The volumetric space charge created in an electronegative gas by a negatively charged point electrode increases the breakdown voltage, this effect is significantly less pronounced in the case of positive energisation.

Townsend avalanches can develop into more filamentary, focused ‘streamers’. In non-uniform fields cathode and anode directed streamers are discussed in the next section.

Cathode Directed Streamers Discharge

An anode directed streamer discharge in a non-uniform field develops much like in a uniform field, initiating with an electron avalanche. However, cathode directed discharges, for example, a positive high voltage point, develop differently. The development of a positive streamer discharge from a high voltage anode is discussed in this section. Photoionisation mechanisms in the positive discharge will generate miniature electron avalanches which create the positive space charge [Haddad and Warne 2007]. The localised positive space charge forms ahead of the positive point electrode and creates an intensified local field at its tip. More electron avalanches are formed towards the tip of this space charge, and the positive space charge grows with the new positive ions. Figure 17.10 depicts a cathode directed streamer advancing as mini avalanches are absorbed into a positive column.

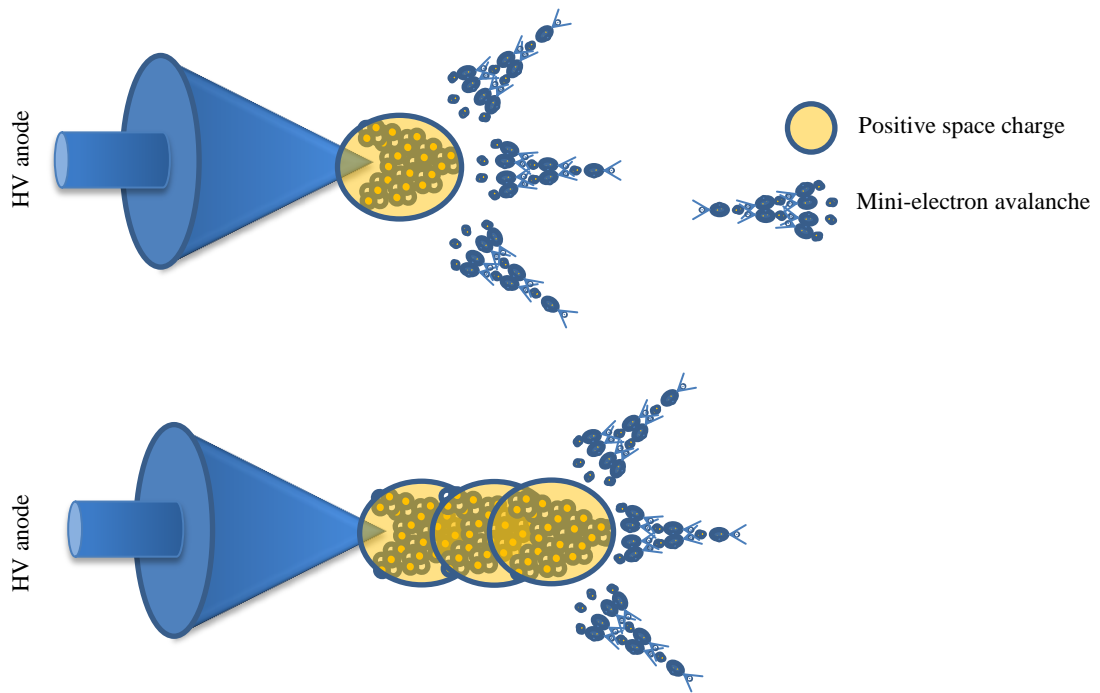


Figure 17.10 Cathode directed streamer.

The advancement of the cathode directed streamers is focused in the direction of the cathode and does not tend to expand out into the gap as much as the anode directed discharges. The advancement of the discharge is not affected nearly as much by the diffusions of electrons because the avalanches do not expand much before getting absorbed into the positive space charge and anode. This is known as a cathode directed streamer or positive streamer.

The positive energisation space charges occupy a smaller volume than negative space charge in the case of negative energisation. Thus, local positive space charge effects can aid the development of anode streamers, compared with the volumetric negative space charge which reduces the field due to screening effects. These increased screening effect in the case of negative energisation directly impacts on the breakdown voltage in the non-uniform topologies. The next section discusses the breakdown voltage of non-uniform topologies stressed with both positive and negative polarities.

Breakdown in Non-Uniform Electrode Topologies

When considering non-uniform electric field such as those created in point-plane and co-axial topologies, it is expected that the breakdown voltage will be higher for negative energisation of the HV electrode as compared with positive energisation. This is due to negative space charge effects ‘screening’ which are especially pronounced in electro-

negative gases; the electric field is reduced in the vicinity of the HV electrode by the volumetric space charge, thus an increased applied voltage is required in order to overcome this reduction in the field and to achieve the critical breakdown field value.

Early work in the field of non-uniform field breakdown in gas showed that there are combinations of thermodynamic and topological factors (first of all pressure and inter-electrode distance) at which this statement is not always true. Researchers such as Marx, Uhlmann, Stringel and Holzer have published data on breakdown voltages in non-uniform fields as far back as 1928 [Marx 1928] [Uhlmann 1929] [Stringel 1933 and 1939] [Holzer 1932]. Breakdown voltages in short gaps energised with both positive and negative polarities at low pressure (in the region of the Paschen minimum) and at higher pressures are available in the literature. Even though non-uniform field breakdown data does not conform to Paschen's law, it is often plotted as breakdown voltage against the product of pressure and distance in the manner of a Paschen's curve.

Positive breakdown voltages in the regions around Paschen minimum, have been shown to have values higher than the negative breakdown voltages at the same parameters in air which can be considered an electronegative gas due to containing ~21% oxygen [Meek 1953] [Huxley 1930 and 1928][Bruce 1930][Boulind 1934 and 1935]. Results from breakdown experiments in co-axial topologies have been shown to have a higher positive breakdown voltage than negative voltage for parameters which correspond to the region between Paschen minimum and some point on the right hand side at larger pd . The negative breakdown voltage increases at a steeper gradient and eventually crossed the positive breakdown curve.

Meek and Craggs presented data for different gases where breakdown voltages were higher for positive than negative energisation, but in the case of nitrogen (which is an electropositive non-attaching gas) the breakdown voltage for positive energisation remained higher than for negative energisation. This is probably due to the fact that nitrogen has no electron attachment affinity. Therefore, in the case of negative energisation less volumetric space charge is formed

Several researchers have also published data on breakdown voltages in point-plane topologies with short gaps (sub-mm to ~10 cm) at higher pressures, around atmospheric pressure and above [Marx 1928][Uhlmann 1929][Stringel 1933 and 1939][Holzer 1932]. Some of the breakdown tests were conducted in point-sphere topologies, but the breakdown

results are considered alongside point-plane because the differences are small. In some cases, the point electrode is either a cone or hemispherical tip to a rod.

Strigel reported breakdown voltages for gaps up to 10 mm, using sphere-sphere, point-sphere and point to point topologies [Strigel 1933 and 1939]. The point-sphere topology in Figure 17.11 is of interest, and it was shown that with a HV point cathode, the breakdown started below the voltages for a HV point anode but it increased at a steady rate almost linear with increasing gap. The HV point anode breakdown showed a complex curve when distance is increased which starts above the breakdown voltage for HV cathode point and eventually ends up lower when the gap is increased. Figure 17.11 shows Strigel's data for point-sphere in air.

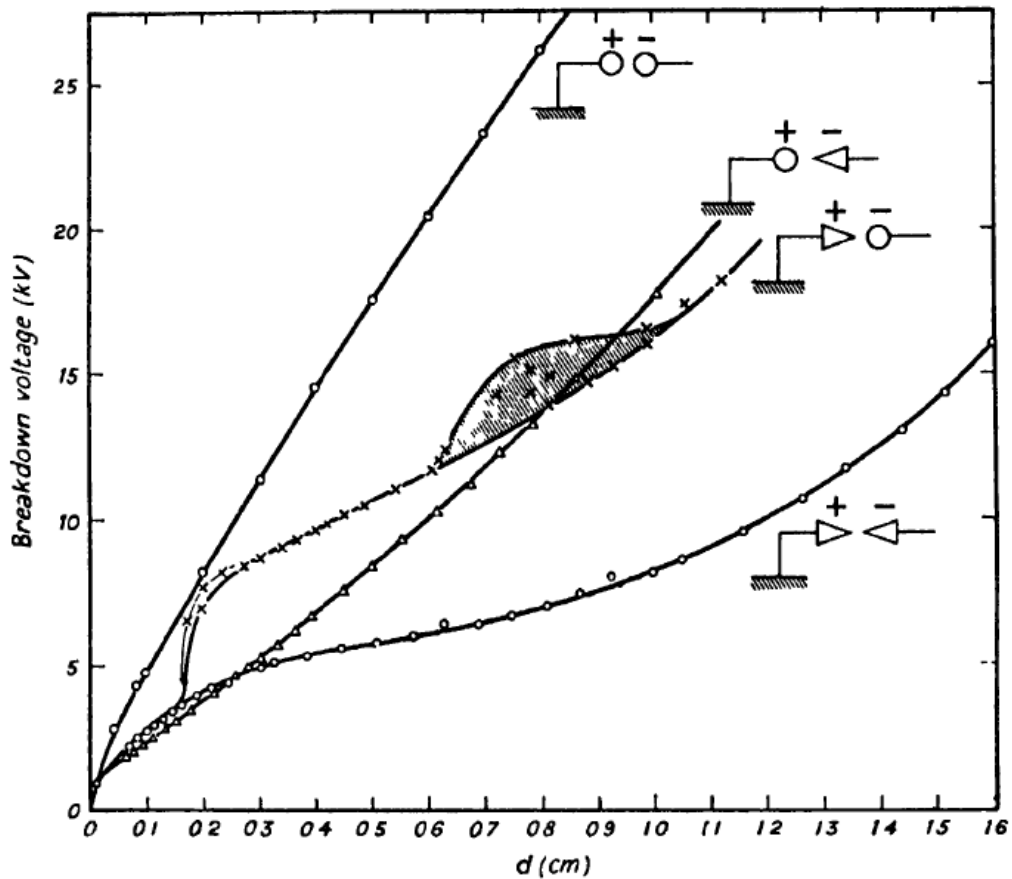


Figure 17.11 DC breakdown voltage curves in air for various combination of points and sphere electrodes. The sphere diameter is 5 cm [Strigel 1933 and 1939].

At larger gaps, 10 mm to 90 mm, Uhlmann shows that in a cone-plane gap (30° angle cone), the breakdown voltage for the HV anode cone is below that of the HV cathode cone [Uhlmann 1929]. The breakdown voltage for the HV cathode cone increase almost linearly

with an increase in distance, and the HV anode cone has a slight tendency to curve, increasing at a lower rate at larger gaps. However, Uhlmann's graph shows the data points converging around 1 mm and, if further data were collected in this regions, it is likely the HV anode cone breakdown would have a higher voltage than negative energisation. The best fit curves used in the graph cross at zero which is an assumption made by the researcher but may not be true considering that actual data points. This data further suggests the need to examine the short gap region. Figure 17.12 shows Uhlmann's data for cone-plane DC breakdown at increasing distances.

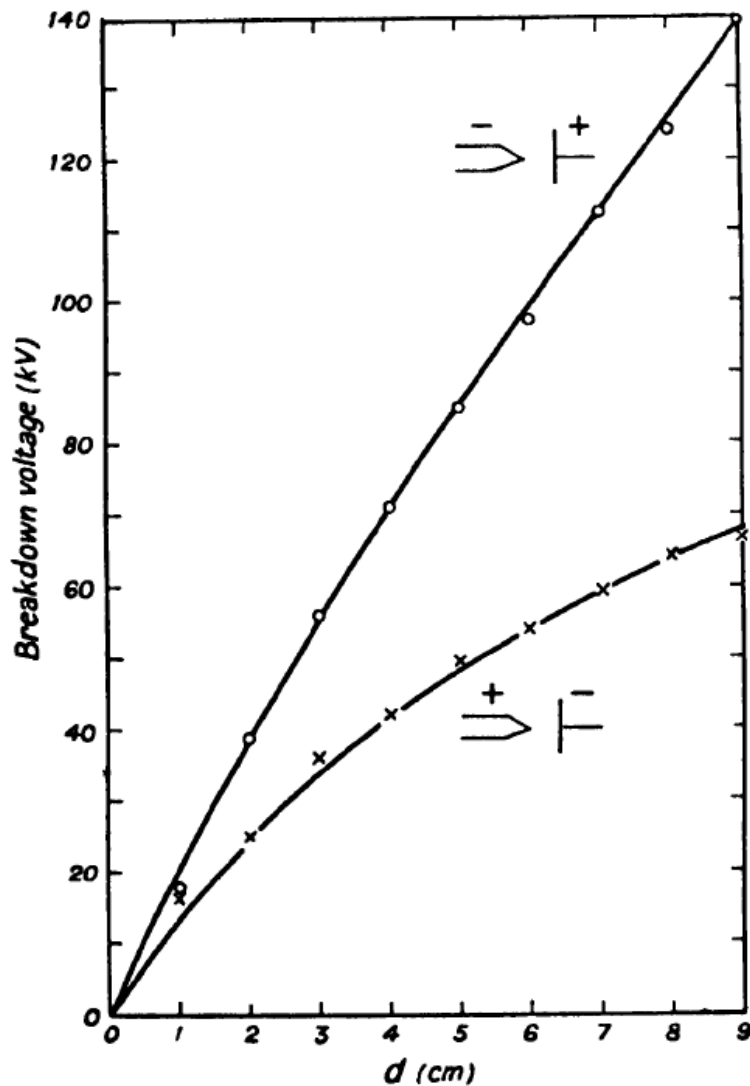


Figure 17.12 DC breakdown voltage curves for air between a 30° conical point and plane [Uhlmann 1929].

The same tendencies as those discussed for Uhlmann and Stigel are observed with the hemispherical point shown in Figure 17.13. The HV point anode breakdown voltage starts above the HV point cathode and ends up lower at the higher distances. However, the region at which the positive and negative breakdown voltages intersect is much larger ($\sim 20 - 30$ mm) which is likely to be due to the reduced electric field at the tip of the point. Figure 17.13 shows the data for the 2 mm hemispherical breakdown data from Meek and Craggs.

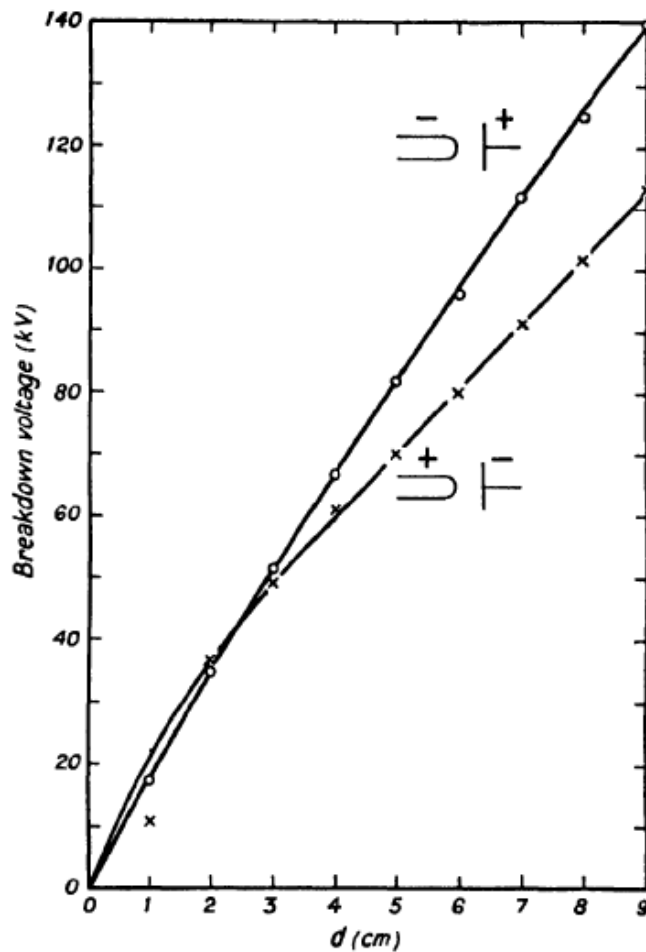


Figure 17.13 DC breakdown voltage curves for air between hemispherically-ended rod, of 0.4 cm diameter, and a plane [Meek 1953].

The electric field at the tip of a point electrode is dependent on the electrode gap and radius of the point as shown by Equation (2.7). This field modification by the space charge has a significant impact on the breakdown voltage behaviour, since positive energisation resulted in a higher breakdown voltage than negative energisation for much larger electrode gaps. This is likely due to positive space charge which is formed in the vicinity of the HV anode,

local positive space charge effects result in lower electric fields and higher breakdown voltages. The literature data presented and analysed here is particularly important and is used for analysis of original results obtained in this work and presented and discussed in Chapter 5.

Polarity Effects on Breakdown of Short Gaps in a Point-plane Topology in Air

M. G. Hogg, I. V. Timoshkin, S. J. McGregor, M. P. Wilson and M. J. Given

Department of Electronic and Electrical Engineering, University of Strathclyde
204 George Street, Glasgow, G1 1XW, UK

ABSTRACT

Electrical breakdown in air in a point-plane topology involves complex processes that are still not fully understood. Unlike uniform-field topologies, the highly-divergent fields produced by point-plane topologies create pre-breakdown corona with volumetric space charge. It is known that space charges developed by corona discharge have significant impacts on the breakdown voltage in non-uniform electrode topologies. With large inter-electrode gaps (>cm) the breakdown voltage for a HV point cathode in air at atmospheric pressure is noticeably larger than a HV point anode. However, this paper shows that in shorter point-plane gaps in air (less than ~10 mm), in the air pressure range 0.1-0.35 MPa, an HV point anode has a similar breakdown voltage which eventually is surpassed by the HV point cathode as the inter-electrode gap is increased. The inter-electrode gap at which the HV cathode has a higher hold-off voltage is found to be dependent on the gas pressure and radius of the point electrode.

Index Terms - Electrical breakdown, Corona discharge, Air-filled plasma-closing switch, Point-plane electrode topology.

1 INTRODUCTION

WITHIN the power and pulsed power industries there is a need for high voltage (HV) systems with a reduced footprint and, as such, it is useful to design and characterise compact gas-filled switches with short inter-electrode gaps. This paper investigates the effect of energisation polarity on the performance of a self-breakdown air-filled plasma closing switch with a point-plane electrode topology which is stressed with ramped voltage. Although electrical breakdown in air in point-plane electrode topologies has been under investigation for decades, further studies of the breakdown mechanisms and characteristics are required, as these topologies are widely used in practical applications in the power and pulsed power industries, [2-7]. In some cases, corona discharges are used for optimisation of switch operation characteristics and the present work investigates the effect of such pre-breakdown corona discharges of both polarities on the operation and performance of the air-filled plasma closing switch.

When dealing with highly non-uniform electric fields, corona discharges can be initiated before complete (spark) breakdown in the gap [1, 3, 4, 6, 7, 10]. Corona discharge is a self-sustained discharge, initiated in high-field regions if the field exceeds the threshold corona ignition value (~30 kV/cm for a spherically capped rod or pin HV

electrode in atmospheric air, [1]). The field magnitude reduces away from the sharp HV electrode, thus the ionisation zone of the corona discharge is defined by the critical ionisation field value, which is ~25-30 kV/cm for atmospheric air [1], ionisations stops as soon as the field reduces below this critical value.

Corona discharges can be classified according to the polarity of voltage which stresses the sharp electrode. Negative corona discharges in air initiate and sustain in accordance with the Townsend discharge mechanism, with primary electron avalanches emanating from the tip of the cathode into the ionisation zone. Much slower positive ions travelling in the opposite direction develop a cathode sheath which increases the field in close proximity to the sharp cathode. In the case of corona discharges in electronegative gases, negative ions are produced by attachment of electrons to electronegative molecules (molecules of oxygen in the case of air), these ions travel towards the anode through the transport zone where the electric field is lower than the critical ionisation field. These ions produce the negative volumetric space charge which results in the reduction of the space charge saturated electric field in the vicinity of the HV electrode as compared with the Laplacian electric field.

Positive corona initiates as a number of smaller-scale electron avalanches directed towards the sharp anode, and the secondary photoemission of electrons plays an important role in the development of this type of corona

discharge. The electrons are absorbed into the anode leaving behind positive ions resulting in development of the positive local charge in close proximity to the anode and a reduction of the field at the anode. Thus, the ignition voltage of positive corona discharges in atmospheric air is higher than the ignition voltage of negative ones, [10].

Positive ions travel to the cathode through the transport zone providing a current in the discharge circuit, however, the volumetric positive space charge does not modify the field as noticeably as in the case of the negative corona in an electronegative gas: the positive corona current and therefore the density of positive ions is significantly lower than the negative corona current for the same applied voltage.

With further increase in the applied voltage, a spark breakdown can be developed in the inter-electrode gap, resulting in gap closure. In non-uniform topologies in electronegative gases (including air), it is common to expect a higher breakdown voltage for a negatively-energised sharp HV electrode as compared with a positively-energised electrode, [11]. This is due to the development of negative volumetric space charge (as discussed above), which results in field screening in the vicinity of the sharp cathode, [1, 9]. The field in the inter-electrode gap is highly non-uniform: it reduces sharply from its maximum value near the cathode to a minimum value, then the field increases slightly toward the opposite plane electrode. For the point-plane electrode topology stressed with DC voltage in atmospheric air, the minimum value of the field is observed at distances $< 1\text{mm}$ away from the cathode, depending on the corona current, [12]. In the case of positive corona discharge, positive ions also modify the field distribution in the vicinity of the corona generating electrode (anode), however the degree of distortion of the field in the main gap is considered to be not so significant, [13].

Thus, for the longer inter-electrode distances which are sufficient for the development of noticeable space charges in the main inter-electrode space, the spark breakdown voltage in the case of negatively stressed high tension electrode can be higher than the breakdown voltage for a corresponding positively stressed electrode, [9, 14]. Therefore, higher DC or ramped switching voltages can be achieved using plasma closing switches with corona electrodes filled with electronegative gases, which is of significant importance to the pulsed power industry, [1, 8, 9, 18, 19].

However, over shorter inter-electrode distances, the complex processes in the vicinity of the high-tension electrode including development of plasma in the ionization zone, sheath formation, field screening and the space charges can result in less pronounced difference (or complete absence of this difference) in the positive and negative spark breakdown voltages, [2]. Therefore, it is expected that in the case of air-filled self-breakdown closing switch, a critical inter-electrode distance should exist: for inter-electrode gaps smaller than this critical distance, both positive and negative spark breakdown

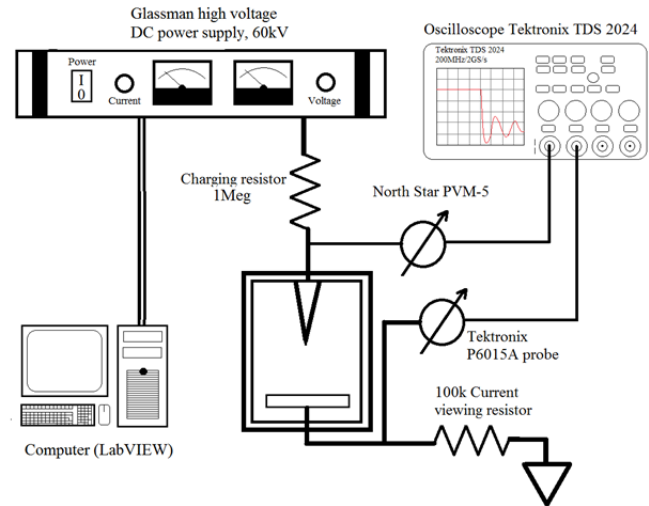
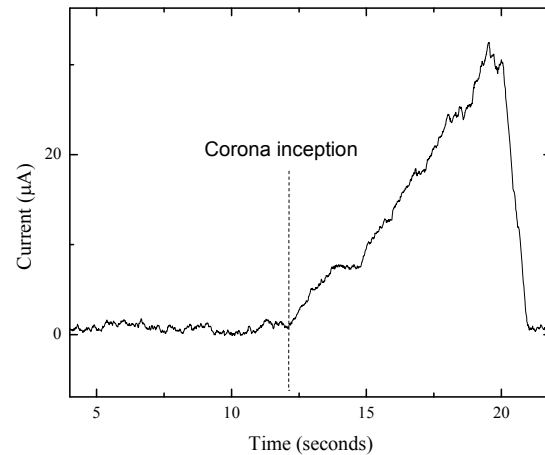
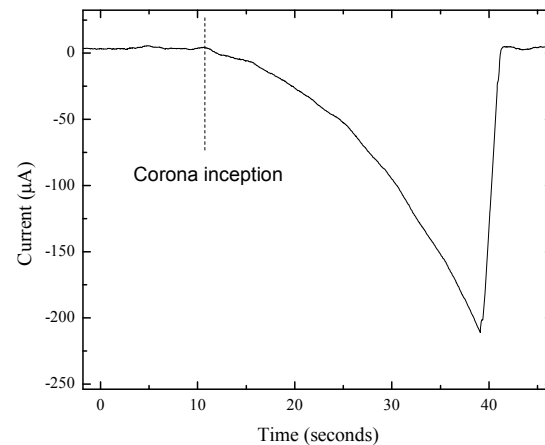


Figure 1. Experimental set up for measuring pre-breakdown corona current. Spark breakdown voltage was measured in the absence of 100 k Ω current viewing resistor.



(a) Positive energisation



(b) Negative energisation

Figure 2. Pre-breakdown corona current in the switch: (a) positive energisation, (b) negative energisation.

voltages will be almost the same, while for gaps larger than the critical distance, the negative spark breakdown voltage will be higher than the positive spark breakdown voltage. This behaviour can be used in practical plasma closing switches in order to provide operational performance independent of stress polarity.

In the present paper, the corona ignition voltage, spark breakdown voltage and pre-breakdown corona current have been measured in an air-filled plasma closing switch with a point-plane electrode configuration. Polarity effects on operational characteristics of this switch have been analysed.

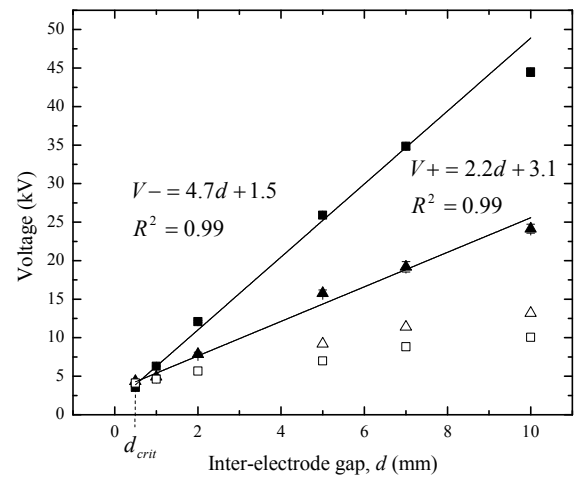
2 EXPERIMENTAL SET-UP

In order to investigate operational characteristics of the switch (breakdown voltages and corona discharge parameters), a dedicated experimental set-up has been developed and constructed. The spark breakdown voltage, corona ignition voltage and corona current were obtained for the switch filled with bottled compressed air (room temperature $\sim 20^{\circ}\text{C}$, 12.5%rh) in the range of pressures from 0.1 MPa to 0.35 MPa, for 8 inter-electrode gaps in the range between 0.5 mm and 14 mm.

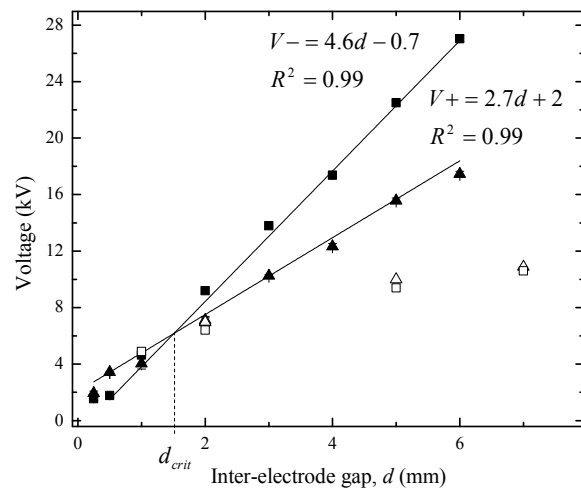
In these tests the point electrode was energised with steadily increasing voltage of both polarities until spark breakdown occurred. Figure 1 shows the experimental design where a Glassman HVDC power supply (EH series 0-60 kV) was used to provide up to 60 kV to the point electrode via a 1 M Ω charging resistor. The voltage increase was controlled via a LabVIEW program interfacing with a National Instruments DAQ (USB6008) providing a ramped voltage with a stepped rate of 370 V/150 ms. When measuring pre-breakdown corona discharge current the switch was grounded via a 100 k Ω shunt resistor, the voltage drop across this shunt resistor was measured using a Tektronix P6015A HV probe (1000:1), and a Tektronix TDS 2024 (200 MHz, 2 GS/s) oscilloscope, Figure 1. Corona inception voltage was determined as the voltage at which the corona current starts to show a clear tendency to increase (start to be above current noise fluctuations). Both positive and negative corona current waveforms were digitally filtered using adjacent-averaging procedure in Origin 8 software for clear identification of corona inception voltage.

The spark breakdown voltage was measured in a separate set of tests without the current viewing resistor, with the plane electrode of the switch directly connected to the ground. The breakdown voltage was identified at the moment of the collapse of voltage this voltage was measured using a North Star PVM-5 HV probe (1000:1) and a Tektronix TDS 2024 (200 MHz, 2 GS/s) oscilloscope.

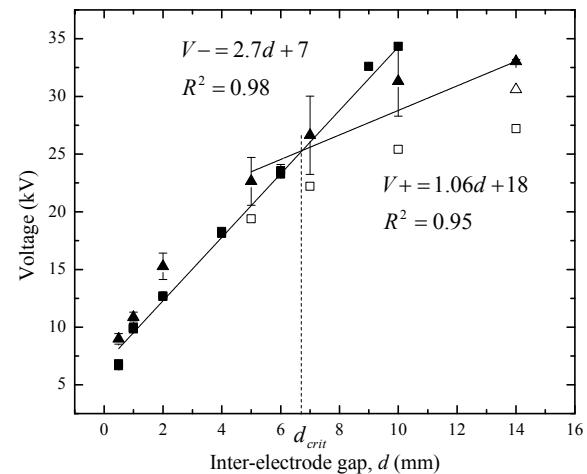
The localised field enhancement in the vicinity of the sharp high-tension electrode is strongly dependent on the radius of the point electrode, [15-18], and it is expected that the radius of the point electrode can affect the switching performance. Therefore, this paper investigates three



(a) Soft-tone gramophone needle, radius 0.036 mm



(b) Sharpened tungsten rod, radius 0.068 mm.



(c) Hemispherical tipped tungsten rod, radius 0.8 mm.

Figure 3. Self-breakdown voltage as a function of inter-electrode gap for point-plane topology. Comparing positive and negative energisation breakdown in air at 0.3 MPa for different radii of HV electrodes Squares – negative energisation; Triangles – positive energisation; Solid lines – best fitting line; Solid symbols – breakdown voltage; Open symbols – Corona inception voltages. Each point is an average value of 30 measurements, error bars represent standard deviation values.

different HV point electrodes: a tungsten rod with tip radius 0.068 mm; a tungsten rod with tip radius 0.8 mm; and a soft-tone gramophone needle with radius 0.036 mm, since it has a well-defined shape and is often used in the power and pulsed power industries as a high-tension point electrode, [20]. The sharp point tungsten electrode with radius of 0.068 mm was used to create a strong field enhancement. In contrast, the hemispherical tipped rod with radius 0.8 mm creates $\sim 7\times$ lower peak field, the peak field values in the point-plane topology have been calculated using the expression from [15]. Therefore, it is expected that for the larger radius electrode, corona current will be lower and space charge effects will be less pronounced. The ground plane electrode was a 50 mm diameter brass disk with rounded edges. A cylindrical switch body was made of black PVC.

The switch was set up with the desired point electrode and inter-electrode gap, and a rotary vacuum pump was used to evacuate the switch prior to filling with bottled air. The pressure in the switch was accurately set and controlled using a precision digital regulator Alicat PCD. The switch was evacuated every time when changing gas pressure, gap separation or electrode type.

Figure 2 shows typical pre-breakdown currents for positive and negative energisation of the point electrode, where the current waveform was obtained by division of the voltage measured across the shunt resistor by the nominal value of this resistor.

3 RESULTS AND DISCUSSION

Breakdown events were measured for all three point electrodes, with inter-electrode distances between 0.5 mm and 14 mm, and for air pressures between 0.1 MPa and 0.35 MPa. The point HV electrode was stressed with both positive and negative voltages and each breakdown measurement was repeated 30 times to allow statistical treatment of the results. Plotting the breakdown voltage as a function of inter-electrode gap shows the differences between breakdown voltages and corona characteristics for positive and negative energisation. These graphs have been plotted and analysed for all 7 pressures in 0.05 MPa increments. Figure 3 shows an example of the analysis conducted in the present study: this figure shows positive and negative corona ignition and breakdown voltages at 0.3 MPa for each of the point electrodes used. Images of the point HV electrodes were taken using an optical microscope with 1000X magnification: no visible change in point radius due to electrical erosion was visually observed after breakdown tests.

It was found that the positive corona ignition voltage was (slightly) higher than negative ignition voltage for all tested pressures, distances, and electrodes.

As can be seen in Figure 3, in the case of negative energisation, the spark breakdown voltage increases with an increase in the inter-electrode spacing. Experimental data on negative breakdown voltages as functions of the inter-electrode gaps were fitted with straight lines over the whole range of the tested inter-electrode distances and for all pressures used in this study. These lines are shown on Figure 3, together with the analytical coefficients and goodness of fitting (R^2) values: R^2 values of 0.98-0.99 are typical for all 3 points.

Positive breakdown voltages, V_{br} , also increase with an increase in the inter-electrode spacing, however positive V_{br} demonstrates more complex behaviour as compared with negative V_{br} . For sharper HV electrodes (0.036 mm and 0.068 mm radii electrodes, Figures 3a and 3b) experimental data on positive breakdown voltage also have been fitted with straight lines in the full range of the tested distances and pressures. However, the gradient of these lines is lower than that for the lines plotted through negative breakdown data. For example, in the case of 0.036 mm radius electrode (gramophone needle, Figure 3a, the gradient of the line of best fit is 2.24 kV/mm for positive breakdown voltages compared to 4.7 kV/mm for the negative breakdown data. The straight lines of best fit through the breakdown data for positive and negative energisation for 0.036 mm and 0.068 mm radius electrodes (Figures 3a and 3b) intersect indicating that there is a critical gap separation where the breakdown voltage is identical for both polarities of energisation. This gap length is referred to as d_{crit} in this paper. The low values of d_{crit} observed with tip radii of 0.036 mm and 0.068 mm (Figure 3a and b) mean that there is insufficient data to draw conclusions as to whether the positive and negative breakdown data follow an identical trend over a range of gap lengths below d_{crit} .

For the electrode with the largest tip diameter, the tungsten rod with a 0.8 mm radius tip, the positive breakdown voltage can't be fitted with a single straight line over the whole range of tested gap spacing's. For shorter distances, the values of the breakdown voltage for both polarities of applied voltage are broadly similar and the fitting line for negative voltages can also be used to describe the functional behaviour of the positive breakdown voltages. For larger gap distances the positive breakdown voltages are lower than the negative voltages and positive breakdown data in this range from 5 mm to 14 mm were fitted with a second straight line, Figure 3c. This line intersects the line of the best fit for negative breakdown data and the intersection point defines d_{crit} for this 0.8 mm radius electrode.

It was found that for the electrodes with smaller tip radii the standard deviation of positive breakdown voltage for all distances and pressures are significantly higher than those for negative energisation. This difference is even more marked in the case of the HV electrode with the largest tip radius (0.8 mm), where the standard deviation for positive breakdown voltage was an order of magnitude higher than for negative polarity, ± 5 kV and ± 0.5 kV, respectively. Potentially this effect (higher deviation in positive spark breakdown voltages) can be a result of different mechanisms of initiation and development of positive and negative corona discharges in air: in the case of increasing of HV stress, the development of positive corona discharges progresses through different stages including a highly unstable and volatile impulsive (flashing) corona stage, while the behaviour of the negative corona discharges is more predictable, typically negative corona current is a combination of DC component and Trichel impulses, [21].

As discussed in Introduction, the critical gap, d_{crit} , in air-filled gap is defined by complex processes in the ionisation and transport zones in the inter-electrode gap including sheath formation and space charge screening. In the present section the existence of the critical gap has been confirmed experimentally. It was shown that for shorter gaps ($d < d_{crit}$) there is no substantial difference in the positive and negative spark breakdown voltages (in such gaps positive and negative ions produce similar effect on the electric field). However, for larger gaps ($d > d_{crit}$), the corona discharge under negative energisation injects an order of magnitude higher current as compared with positive energisation which results in more pronounced space charge effects and higher negative spark breakdown voltage.

The observed values of the critical gap, d_{crit} depend on the pressure of the gas in the gap and the radius of the electrode tip. These critical distances have been plotted as functions of air pressure for all 3 electrodes, Figure 4. It can be seen that as the pressure is increased, d_{crit} becomes smaller. The critical gap for the 0.8 mm radius point electrode reduces from ~ 10 mm at atmospheric pressure down to ~ 8 mm at 0.15 MPa, a 20% reduction in critical gap with an increase of pressure of 0.05 MPa. However, with further increase in pressure up to 0.2 MPa, the reduction in d_{crit} is smaller, $\sim 2.5\%$. This trend continues and d_{crit} appears to reach a constant value for higher pressures, ~ 0.35 MPa. The critical gaps for the gramophone needle (0.036 mm radius) and tungsten point electrode (0.068 mm radius) were similar to each other and significantly smaller than the critical gap for the 0.8 mm radius point electrode. However, the same trend in reduction of the critical gap for both of these sharp electrodes was observed: for gramophone needles, the gap reduces by $\sim 51\%$, from

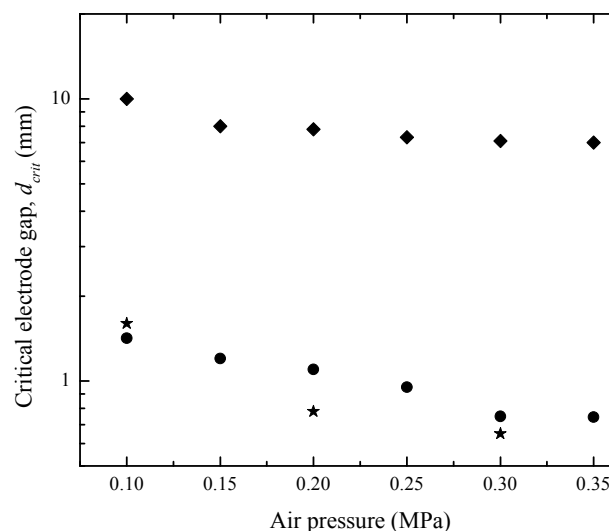


Figure 4. Critical inter-electrode gap at which positive energisation breakdown voltage reduced below negative energisation breakdown voltage as a function of pressure for 3 point electrodes in compressed air. Diamonds – hemispherical tipped tungsten rod, radius 0.8 mm; Stars – soft tone gramophone needle, radius 0.036 mm; Circles – sharpened tungsten rod, radius 0.068 mm.

1.6 mm to 0.78 mm, with an increase of air pressure from 0.1 MPa to 0.2 MPa.

It was found that the critical distance reduces as the radius of the electrode increases, which can be explained by in the lower geometrical field enhancement which results in reduced corona induced space charge screening. Lower field enhancement at the tip of the point electrode means larger gaps are required to initiate corona discharge prior to breakdown. As the breakdown voltage in large gaps is strongly dependent on corona discharge, the critical gap is larger with larger radius. It is expected that electrode material will not have a significant impact on the critical distance because corona ignition voltage is not strongly dependent on electrode material, [2].

The appearance of detectable pre-breakdown corona current was used to record the corresponding corona ignition voltage. Negative corona current increases very gradually starting from a few nA (which is the detection limit in the present set-up) to a few μ A as the voltage is increased. The negative corona discharge could start to impact the breakdown voltage from a low energisation level. In contrast, the positive corona current usually appears suddenly, transitioning from no detectable level to a few μ A, [5].

Examining the corona ignition voltage (indicated by open symbols in Figure 3) prior to complete spark breakdown shows that complete breakdown of the gap is not always preceded by intensive corona activity. The conditions where corona discharge occur prior to complete breakdown depend on applied voltage polarity, gas pressure and the radius of the point electrode, [22].

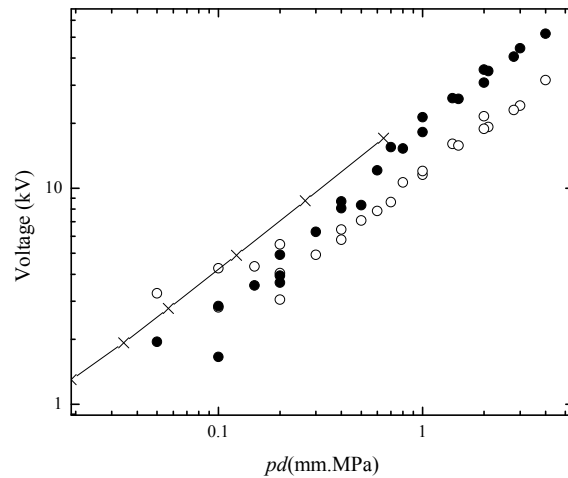
In these experiments, it was found that at shorter gaps (depending on pressure and electrode radius) there was no detectable pre-breakdown current that would be indicative of noticeable corona discharge for either positive or negative energisation. For example, in the case of the 0.036 mm radius HV electrode (Figure 3a), there was no corona discharge at 0.5 mm inter-electrode spacing for pressures equal to and below 0.2 MPa.

In the cases where corona discharges appeared prior to spark breakdown, it was observed that negative energisation would produce detectable corona discharge at smaller gap spacing, whereas positive energisation leads directly to spark breakdown under similar conditions. Figure 3a shows corona ignition voltages (open symbols) for negative energisation starting from 1 mm, however positive corona was not detected appearing until an inter-electrode spacing of 2 mm.

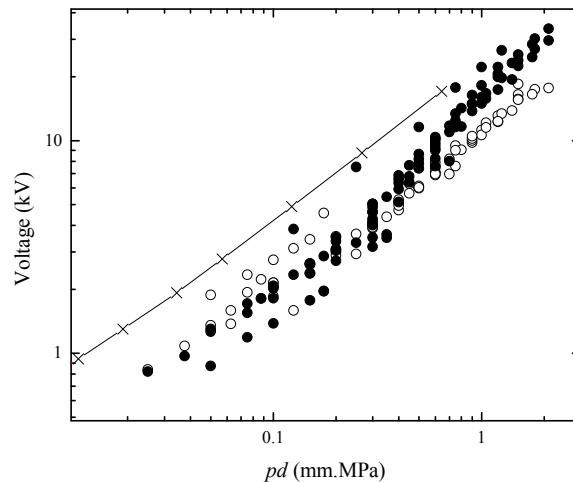
The probability of corona discharge appearing before complete breakdown was dependent on the air pressure in the switch. As pressure is increased, the probability that corona will precede spark breakdown increases for the sharp point electrodes. For example, at 0.1 MPa, using a 0.036 mm radius HV electrode, no corona was detected for 0.5 mm, 1 mm or 2 mm electrode gaps. At 0.35 MPa, negative corona discharges precede complete breakdown in all inter-electrode gaps; while corona activity starts at 2 mm for positive energisation.

The appearance of corona discharge before breakdown is also highly dependent on the radius of the point electrode. The sharper electrodes produced corona discharges prior to breakdown under both polarities of energisation for similar gap distances (1-4 mm). In the case of the 0.8 mm radius electrode, corona discharge before breakdown was observed for smaller gap distances (~5 mm) under negative energisation as compared with positive energisation (~10 mm). This can clearly be seen in Figure 3c where negative corona discharge is observed before breakdown for gaps greater than 5 mm while positive corona discharge is only observed for a gap of 14 mm.

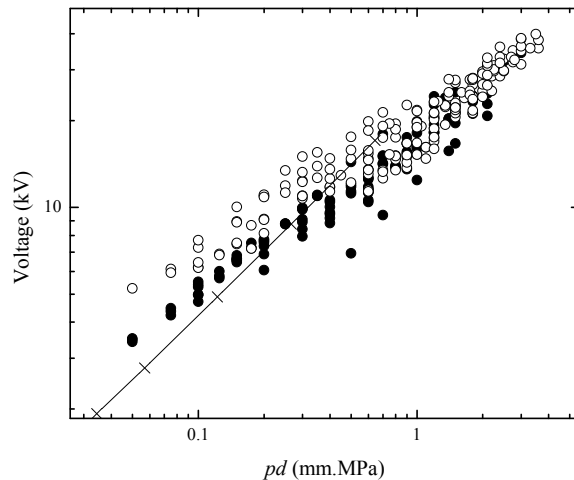
Comparison of positive and negative breakdown voltages shows the effect of such corona activity: due to the development of volumetric space charge the breakdown voltage is higher for negative energisation as compared with positive energisation in gaps greater than d_{crit} , and this difference increases with an increase in the inter-electrode spacing, Figure 3. For distances shorter than d_{crit} , the difference in the behaviour of the positive and negative breakdown voltages is not well pronounced; potentially this is a result of presence of the positive and negative charges which in short gaps produce comparable space charge effects. With an increase in the gap, the effects produced by the volumetric negative space charge continue to govern the negative breakdown voltage behaviour (almost linear increase in V_{br} with an increase in the gap spacing).



(a) Gramophone needle, radius 0.036 mm.



(b) Sharpened tungsten rod, radius 0.068 mm.



(c) Hemispherical tipped tungsten rod, radius 0.8 mm.

Figure 5. Self-breakdown voltage as a function of pressure and inter-electrode gap, pd for 3 different point electrodes along with a classic Paschen curve from literature [25]. Crosses with line – Paschen curve [25]; Black markers – negative energisation; White markers – positive energisation.

However, in the case of positive energisation the field screening effect produced by a weaker positive space charge is not so effective as the positive corona current for this range of distances and electrode radii is significantly lower than the negative current at the same level of the applied voltage. Thus, the rate of rise of the positive breakdown voltage with an inter-electrode distance decreases. In the case of 0.8 mm gap, no positive corona current was observed for gaps shorter than 14 mm which results in deviation of the positive breakdown voltages from the negative ones at longer inter-electrode gaps (larger critical distance, Figure 3c).

It is common to display breakdown voltages of gaseous dielectrics as a function of the product of gas pressure and inter-electrode separation, pd , [1, 2, 10, 23, 24]. The breakdown voltage of uniform topologies can be predicted given the inter-electrode gap and gas pressure using Paschen's law, [22, 23].

The breakdown voltages in non-uniform topologies obtained in the present study also have been plotted as $V_{br}(pd)$ functions for all pressures and electrode radii. Figure 5 shows the obtained breakdown voltages of each of the three electrodes as a function of the product of pressure and distance (pd) alongside the right branch of conventional Paschen breakdown curve (at values of pd above the Paschen minimum). Conventional Paschen data for air were taken from the literature, [25] in order to compare the results obtained in the present paper with already published $V_{br}(pd)$ data. Figure 5 shows that, the data obtained in the present work closely follows the conventional Paschen's law, and there is a strong scaling tendency for breakdown voltages in highly divergent electric fields which can be utilised in the design of plasma closing switches and other component parts of compact high-voltage systems.

4 CONCLUSION

In this paper, an air-filled plasma closing switch with a highly non-uniform and variable point-plane topology has been developed in order to investigate its performance under positive and negative ramp voltage stress. Corona ignition and spark breakdown voltage have been obtained for pressures in the range of 0.1-0.35 MPa, and the switch was energised using a computer-controlled high-voltage system until breakdown occurred. Three different point electrodes were used: tungsten rods with radii 0.068 mm and 0.8 mm, and a gramophone needle with radius 0.036 mm.

It was observed that negative breakdown voltage increases linearly with increasing inter-electrode gap throughout the range of gaps tested. At very short gaps (depending on radius of point electrode), positive breakdown voltage is comparable to negative breakdown voltage. For larger gaps, with an increase in intensity of pre-breakdown negative corona discharges, and as a result more pronounced negative space charge, the positive

breakdown voltage becomes lower than the negative breakdown voltage, and the rate of its increase with the distance reduces. The critical distance, d_{crit} , at which positive and negative breakdown voltages deviate from each other has been identified for all tested pressures and electrode topologies. The negative pre-breakdown corona discharges initiate at much smaller gaps than positive corona discharges, causing stabilisation in the switch operation at much smaller gaps, [2].

It was found that the critical distance is dependent on the HV point electrode radius and the gas pressure. With the larger radius needle, 0.8 mm, the critical distance at atmospheric pressure (0.1 MPa) is ~5-fold larger than the critical distance for the sharper electrodes. It was found that as the gas pressure is increased the critical distance reduces. This is likely due to the increased pre-breakdown corona activity at shorter gaps that is present at higher pressures. The critical distance and corresponding pressure can be used for identification of operational regimes in which corona stabilisation is necessary or vice versa – regimes when it is desirable to achieve the identical operational characteristics of the switch for both polarities, positive and negative. The results obtained and discussed in this paper aid in the design, development and optimisation of the performance of HV systems whether breakdown is desired or not: for example, plasma closing switches require breakdown at predictable levels, whereas designers of compact high-voltage/pulsed power systems require experimental data to ensure the avoidance of unwanted breakdown.

ACKNOWLEDGMENT

This research has been part-funded by a UK MoD research programme.

REFERENCES

- [1] E. Kuffel, W. S. Zaengl, and J. Kuffel, *High Voltage Engineering, Fundamentals*, Newnes Oxford, 2000.
- [2] J. M. Meek, and J. D. Craggs, *Electrical Breakdown of Gases*, John Wiley, New York, 1953.
- [3] A. Maglaras, and F. V. Topalis, "Influence of ground and corona currents on dielectric behavior of small air gaps", *IEEE Trans. Dielectr. Electr. Insul.*, Vol. 16, No. 1, pp. 32-41, 2009.
- [4] A. L. Maglaras, K. Giannakopoulou, T. G. Kousiouris, F. V. Topalis, D. S. Katsaros, and L. A. Maglaras, "Control and optimization of the Corona effects and breakdown of small rod-plate air gaps stressed by dc and impulse voltages", *IEEE Int'l. Conf. Solid Dielectr. (ICSD)*, pp. 160-165, 2013.
- [5] A. F. Kip, "Positive-Point-to-Plane Discharge in Air at Atmospheric Pressure", *Phys. Rev.*, Vol. 54, No. 2, pp.139-146, 1938.
- [6] M. Xiaobo, C. Changlong, and L. Wang, "Corona Charge Injection Prior to Sparkover in an Inversed Rod-Plane Gap Under Composite Voltages", *IEEE Trans. Power Delivery*, Vol. 27, No. 3, pp. 1442-1449, 2012.
- [7] L. K. Warne, R. E. Jorgenson, and E. E. Kunhardt, "Criterion for spark-breakdown in non-uniform fields", *J. Appl. Phys.*, Vol. 115, No. 14, pp. 143303, 2014.
- [8] J. R. Beveridge, S. J. MacGregor, M. J. Given, and I. V. Timoshkin, "A Corona-stabilised Plasma, Closing Switch," *IEEE Trans. Dielectr. Electr. Insul.*, Vol. 16, No. 4, pp. 948-955, 2009.

- [9] M. G. Hogg, I. V. Timoshkin, S. J. Macgregor, M. P. Wilson, M. J. Given, and T. Wang, "Electrical breakdown of short non-uniform air gaps", IEEE 19th Pulsed Power Conference (PPC), pp. 1-4, 2013.
- [10] D. S. Antao, D. A. Staack, A. Fridman, and B. Farouk, "Atmospheric Pressure DC Corona Discharges: Operating Regimes and Potential Applications", Plasma Sources Sci. Technol., Vol. 18, No. 3, pp. 35016, 2009.
- [11] P. Chowdhuri, A. K. Mishra and B. W. McConnell, "Volt-time characteristics of short air gaps under nonstandard lightning voltage waves", IEEE Trans. on Power Delivery, Vol. 12, No. 1, pp. 470-476, 1997.
- [12] Y. Akishev, M. Grushin, I. Kochetov, V. Karal'nik, A. Napartovich and N. Trushkin, "Negative corona, glow and spark discharges in ambient air and transitions between them", Plasma Sources Sci. Technol., Vol. 14, No. 2, pp. 18-25, 2005.
- [13] Th. Hinterholzer and W. Boeck, "Breakdown in SF₆ influenced by Corona-stabilisation", Int'l. Conf. Electr. Insul. Dielectr. Phenomena, pp. 413-416, 2000.
- [14] R. Sigmong, "Simple approximate treatment of unipolar space-charge-dominated coronas: The Warburg law and the saturation current", J. Appl. Phys., Vol. 53, No. 2, pp. 891-898, 1982.
- [15] R. Coelho, and J. Debeau, "Properties of the tip-plane configuration", J. Phys. D: Appl. Phys., Vol. 4, pp. 1266-1280, 1970.
- [16] K. Adamiak, V. Atrazhev, and P. Atten, "Corona discharge in the hyperbolic point-plane configuration: direct ionization criterion versus an approximate formulations", IEEE Trans. Dielectr. Electr. Insul., Vol. 12, No. 5, pp. 1015-1024, 2005.
- [17] I. V. Timoshkin, S. J. MacGregor, M. J. Given, J. R. Beveridge, and J. M. Lehr, "Dynamic Characteristics Of Corona Discharges In Point-Plane Electrode Topologies Influenced By Space Charge", IEEE Int'l. Power Modul. High Voltage Conf., pp. 495-498, 2008.
- [18] M. Hogg, I. Timoshkin, S. MacGregor, M. Given, M. Wilson, and T. Wang, "Performance of Air-Filled Plasma Closing Switch with Corona Pre-ionisation", XIX Int'l. Conf. Gas Discharges and Their Applications, pp. 504-507, 2012.
- [19] H. Bluhm, *Pulsed Power Systems: Principles and Applications* Springer, Berlin, 2006.
- [20] IEEE Standard Techniques for High-Voltage Testing (Revision of IEEE Std 4-1 978). IEEE Std 4- 1995: pp. i-129.
- [21] I. V. Timoshkin, M. Maclean, M. P. Wilson, M. J. Given, S. J. MacGregor, T. Wang and J. G Anderson, "Bactericidal Effect of Corona Discharges in Atmospheric Air", IEEE Trans. Plasma Sci., Vol. 40, No. 10, pp. 2322-2333, 2012.
- [22] F.W. Peek, *Dielectric Phenomena in High Voltage Engineering*, McGraw-Hill Book Company, London, 1915.
- [23] F. Paschen, "Ueber die zum Funkenübergang in Luft, Wasserstoff und Kohlensäure bei verschiedenen Drucken erforderliche Potentialdifferenz," Annalen der Physik, Vol. 273, No. 5, pp. 69 - 96, 1889.
- [24] L.B. Loeb, *Fundamental Processes of Electrical Discharge in Gases*, John Wiley and Sons, New York, 1939.
- [25] S.C. Brown, *Basic Data of Plasma Physics*, 1966.



Michael G Hogg is a Ph.D. degree student in the Department of Electronic and Electrical Engineering, University of Strathclyde, Glasgow. He received his B.Eng. (Hons) degree in Electronic and Electrical Engineering from the University of Strathclyde in 2010 and his M.Res. in 2011. His research interests include electrical breakdown in environmentally friendly gases, plasma closing switches, corona discharge and water as a dielectric insulator.



Igor V. Timoshkin (M'07-SM'14) received the degree in physics from the Moscow State University (Russia) in 1992, and the Diploma and the Ph.D. degree from the Imperial College of Science, Technology and Medicine, (London, UK) in 2001. After graduation from MSU he worked as a Researcher at Moscow State Agro-Engineering University, and then at the Institute for High Temperatures of Russian Academy of Sciences before moving to ICSTM in 1997. He joined the Department of Electronic and Electrical Engineering of the University of Strathclyde (Glasgow, UK) in 2001 as an Academic Visitor, where he became a Senior Lecturer in 2011. His research interests include properties of solid and liquid dielectric materials, electronics of plasma discharges in condensed media, practical applications of electro-hydraulic and high-power ultrasound pulses, bio-dielectrics and effects of electromagnetic fields on biological objects.



Scott J. MacGregor (M'95-SM'14) received the B.Sc. and Ph.D. degrees from the University of Strathclyde, Glasgow, U.K., in 1982 and 1986, respectively. He became a Pulsed Power Research Fellow in 1986 and a Lecturer in pulsed-power technology in 1989. In 1994, he became a Senior Lecturer, with a promotion to Reader and Professor of High Voltage Engineering, in 1999 and 2001, respectively. From 2010 he became the Dean of the Engineering Faculty of the University of Strathclyde. His research interests include high-voltage pulse generation, high-frequency diagnostics, high-power repetitive switching, high-speed switching, electronic methods for food pasteurization and sterilization, generation of high-power ultrasound (HPU), plasma channel drilling, pulsed-plasma cleaning of pipes, and stimulation of oil wells with HPU.



Mark P. Wilson (M'10) was born in Stranraer, Scotland, in 1982. He received the B.Eng. (with honours), M.Phil., and Ph.D. degrees in electronic and electrical engineering from the University of Strathclyde, Glasgow, U.K., in 2004, 2007, and 2011, respectively. He is presently working as a Teaching Associate at the University of Strathclyde, where he continues to investigate surface flashover of solids immersed in insulating oil. Mark is a member of the IEEE Nuclear and Plasma Sciences Society, from whom he received a Graduate Scholarship Award in 2011, the IEEE Dielectrics and Electrical Insulation Society, and the IET.



Martin J. Given (M'99-SM'11) is currently a Senior Lecturer in the Department of Electronic and Electrical Engineering at the University of Strathclyde. He received a degree in physics from the University of Sussex in 1981 and a PhD in electronic and electrical engineering from the University of Strathclyde in 1996. His research interests include, ageing processes and condition monitoring in solid and liquid insulation systems, high speed switching and pulse power applications.

PERFORMANCE OF AIR-FILLED PLASMA CLOSING SWITCH WITH CORONA PRE-IONISATION

M. HOGG, I. TIMOSHKIN, S. MACGREGOR, M. GIVEN, M. WILSON, T. WANG

University of Strathclyde, Glasgow
204 George Street, G1 1XW
United Kingdom

michael.hogg@eee.strath.ac.uk

ABSTRACT

Gas-filled plasma closing switches are widely used in pulsed power technology for generation of short high voltage impulses. There is a growing tendency to use environmentally friendly gases such as air, oxygen, nitrogen or their mixtures in such devices instead of the traditional insulating gaseous switching medium, sulphur hexafluoride, due to its high cost and the environmental issues associated with this gas.

The present study is focused on the analysis of performance of self-breakdown plasma closing switch with corona pre-ionisation electrodes. The following aspects of switch performance have been investigated: the self-breakdown voltage and its spread. This paper presents evidence that the use of a pre-ionisation electrode can reduce the voltage spread.

1. INTRODUCTION

Plasma closing switches are used in range of applications from the Z-R machine at Sandia National Laboratories in America [1], generating X-rays used in fusion and in devices such as the Linear Transformer Driver (LTD) in the Institute of High-current Electronics (IHCE) Tomsk, Russia [2]. The Z-pinch machine at Sandia National Laboratories has over 100,000 plasma closing switches [3] and therefore life time and running costs become important. The insulating

gas of choice for switching media has in the past been sulphur hexafluoride (SF_6) which is a greenhouse gas, posing a significant environmental issue. As a result research into plasma closing switches has been reignited with the aim of developing compact switches that operate with cheaper, more environmentally friendly gases such as oxygen, nitrogen and their mixtures.

Corona discharge electrodes have been used in plasma closing switches for stabilising the breakdown voltage in high frequency breakdown switches [4,5]. The corona delays the breakdown to allow impurities in the dielectric from previous breakdowns to disperse. This reduces the pre-fire rate which defines the number of early breakdowns. The same process may be used to stabilise the self-breakdown voltage and reduce the range of breakdowns [6].

The purpose of this research is to develop a compact self-triggering switch that operates at below 40kV in dry air. The parameters under investigation include the DC self-breakdown voltage and its spread with different electrode configurations. Comparisons are made between the switch before and after the inclusion of corona pre-ionisation electrodes at 0, 1 and 1.5bar (gauge).

There are 4 main switches currently in operation in LTD and high voltage/current machines [7].

The Institute of High Current Electronics in Russia, Sandia National Laboratories in America and Kinotech LLC have all produced switches. The switches differ in shape and size. Attempts to improve switching jitter, inductance, life time and pre-fire rates have led to the development of multi-stage electrode configurations and attempts to promote multi-channeling to reduce inductance during discharge.

All of the switches have been designed to use compressed air as the dielectric medium and the electrodes are machined out of copper-tungsten to withstand 10,000s of breakdowns. In this work the switch is being designed to operate at much lower voltage with far less corrosion to the electrodes. Therefore, the copper-tungsten alloy is not required in the initial testing stages.

2. EXPERIMENTAL SYSTEM

The experimental section of the present paper is focused on the investigation of self-breakdown parameters of dry air (1.5%, relative humidity) stressed with high voltage DC. Three electrode configurations (sphere-sphere, cone-plane, and plane-plane) were investigated with and without the addition of corona pre-ionisation electrodes.

The experimental procedure employed for this paper involved DC voltage applied to the one electrode and ramped up until spark breakdown occurs. In the cone-plane topology the voltage is applied to the cone electrode and the plane electrode is grounded. Where corona pins were used they were at the same polarity and potential as the HV electrode.

The breakdown procedure involved applying step-wise increasing voltage to the switch electrodes until breakdown occurred. Each voltage step has a magnitude of 66.7 V and duration of 10 ms, and this can be approximated by a ramped linear increased voltage stress with a rate of 667 V/s. The experimental set up consisted of a Glassman EH series HVDC power supply (0-60 kV) and a plasma closing switch containing the electrode topology and gas

insulator (dry bottled air 1.5%rh). A labVIEW program was used with a DAQmax (SBC 68) to control the output of the Glassman HVDC power supply and to record the self-breakdown voltage.

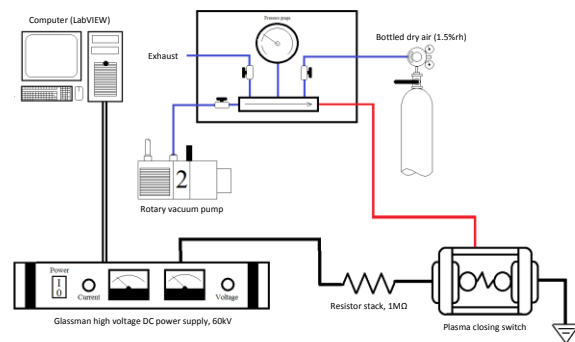


Fig. 1. Schematic diagram of the experimental system including power supply and control and pneumatic pressure control. Double line, two way communication; single black line, HV connections; grey line, pneumatic tubing.

The switch design was developed to minimize inductance, operate at pressure up to 2bar and self-breakdown at below 40 kV. The switch's brass end plates hold the electrodes which can be screwed out for easy changing. Each electrode is machined from brass and are designed such that when sealed the distance between the electrodes is 5 mm. The spheres used had a diameter of 19 mm, the plane electrodes are circular with 19 mm diameter and the tip of the cone has a diameter of 0.15 mm. The pre-ionisation electrodes are soft tone gramophone needles that sit 3 mm lower than the tip of the main electrode with a tip diameter of ~0.09 mm. The corona electrodes are positioned 8 mm out from the center of switch.

For each electrode configuration including the addition of corona pre-ionisation electrodes, positive and negative applied voltages were investigated with 50 measurements per configuration.

3. RESULTS AND DISCUSSION

Ramped voltage applied to the switch is increased until breakdown occurs. Both polarities of voltage were applied to a sphere-sphere, plane-plane and cone-plane electrode configurations.

Statistical analysis has been conducted using shots 21-50 as a result of a conditioning period in the first 20 shots. The voltage spread has been investigated using the standard deviation and visual analysis using normalized histograms. Fig. 2 and Fig. 3 show the positive and negative breakdown voltage standard deviation, σ , for each topology with and without corona pins with respect to pressure (bar gauge).

Fig. 2 and Fig. 3 show that the inclusion of corona pre-ionisation electrodes has an improvement on the voltage breakdown spread in dry air at atmospheric pressure. In most configurations of topology (cone-plane excluded) and polarity energisation at atmospheric pressure the inclusion of corona

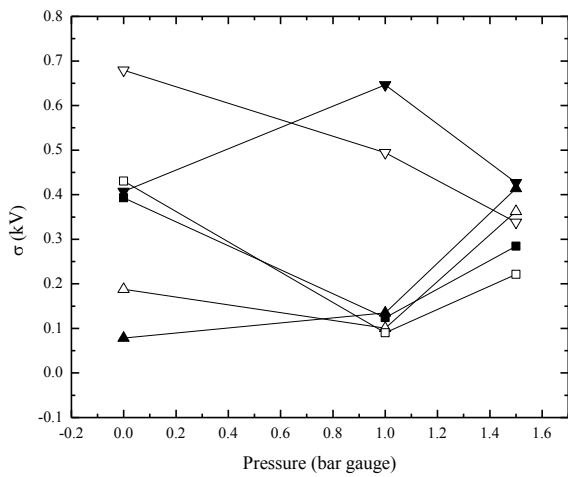


Fig. 2, Positive energisation DC breakdown voltage standard deviation, σ , of the sphere-sphere, plane-plane and cone plane topologies with respect to pressure. Sphere-sphere, up triangles; plane-plane, down triangles; and cone-plane, squares. Open symbols, no pre-ionisation; closing symbols, with pre-ionisation.

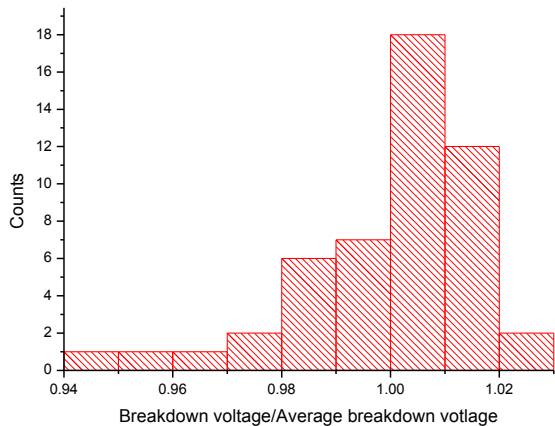


Fig. 4, Normalised histogram showing the negative energisation voltage breakdown spread on the sphere-sphere topology without pre-ionisation at atmospheric pressure. All 50 measurements were used.

pre-ionisation has reduced the standard deviation of self-breakdown voltage. Therefore, narrowing the self-breakdown voltage spread. Reducing the standard deviation is important because it is directly related to the breakdown jitter in triggered switching regimes.

The normalised histograms in Fig. 4 and Fig. 5 show how the spread of self-breakdown voltage has narrowed and a larger number of breakdowns are occurring closer to the mean breakdown voltage where the maximum range is reduced from 0.9 to 0.3 about the average breakdown voltage.

While the inclusion of pre-ionisation corona electrodes has shown to reduce the breakdown

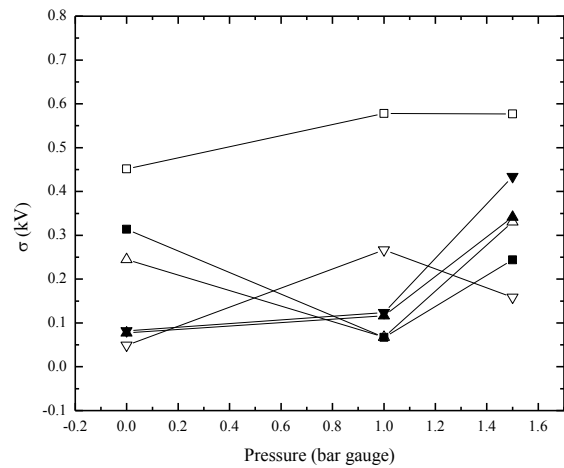


Fig. 3, Negative energisation DC breakdown voltage standard deviation, σ , of the sphere-sphere, plane-plane and cone plane topologies with respect to pressure. Sphere-sphere, up triangles; plane-plane, down triangles; and cone-plane, squares. Open symbols, no pre-ionisation; closing symbols, with pre-ionisation.

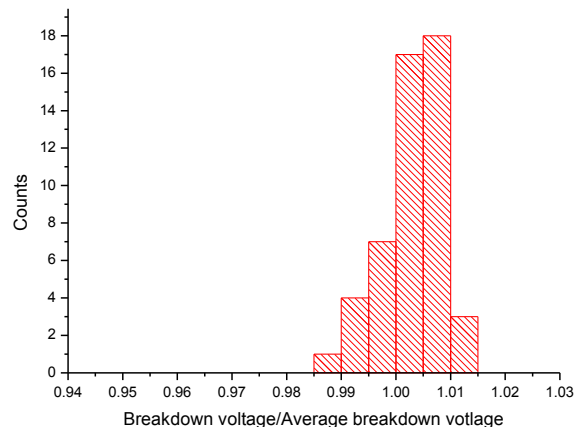


Fig. 5, Normalised histogram showing the negative energisation voltage breakdown spread on the sphere-sphere topology with pre-ionisation at atmospheric pressure. All 50 measurements were used.

voltage spread in most cases at atmospheric pressure, it has not been as consistent at higher pressures. At 1 bar (gauge) the standard deviations for most configurations, positive and negative, are ~ 0.1 kV. It was noticed that the standard deviation was overall best at pressure of 1 bar than at either 0 or 1.5 bar (gauge).

When examining the effects of corona using histograms it was noticeable that the best results were achieved using the sphere-sphere topology where the cone-plane and plane-plane topologies showed conditioning effects during the first 20 measurements.

4. CONCLUSION

Tests have been completed on three electrode configurations: sphere-sphere, plane-plane and cone-plane with and without corona pre-ionisation electrodes. Negative and positive energisation were used at pressure of 0, 1 and 1.5 bar gauge. Dry air was used as the switching medium. In the case of 0 bar pressure tests, the histograms and standard deviations of the self-breakdown voltage with the inclusion of corona electrodes showed a reduced voltage spread.

This is comparable to a similar investigation in SF₆ [5] where it is shown that improved self-breakdown voltage stabilisation can be achieved using corona pre-ionisation. At higher pressures it was found that corona pre-ionisation has a less desirable effect on the voltage spread.

However, the standard deviation converges around 0.1 kV at 1 bar pressure showing an improvement over 0 and 1 bar for most topologies. Pressures above (1.5 bar) and pressure below (0 bar) have larger spread out and higher standard deviations. This shows there may be an optimal pressure range for DC self-breakdown with regards to reducing voltage spread.

5. ACKNOWLEDGEMENTS

This work has been part-funded by a UK MoD Research Programme.

6. REFERENCES

- [1] J.M. Lehr, J.P. Corley, J.E. Elizondo, P. Corcoran, D.L. Johnson, J.M. Maenchen, M. Mazarakis, D.H. McDaniel, I.D. Smith, M. Kincy, D.L. Kitterman, P. Wakefield, K. Struve, "Multi-megavolt switching in water: Considerations for the Z-R machine", IEEE International Conference on Electrical Insulation and Dielectric Phenomena, pp. 554- 557, 2002.
- [2] J.R. Woodworth, J.A. Alexander, W.A. Stygar, L.F. Bennett, H.D. Anderson, M.J. Harden, J.R. Blickem, F.R. Gruner, R. White, "Low inductance switching studies for Linear Transformer Drivers", IEEE International Pulsed Power Conference, pp.250-254, 2009.
- [3] W. A. Stygar, M. E. Cuneo, D. I. Headley, H. C. Ives, R. J. Leeper, M. G. Mazarakis, C. L. Olson, J. L. Porter, T. C. Wagoner, and J. R. Woodworth, "Architecture of petawatt-class z-pinch accelerators", Phys. Rev. ST Accel. Beams, vol. 10(3), pp. 030401-030425, 2007.
- [4] J.R. Beveridge, S.J. MacGregor, I.V. Timoshkin, J.M. Lehr., "A Corona-Stabilised Plasma Closing Switch", IEEE International Power Modulators and High Voltage Conference, pp.487-490, 2008.
- [5] F.A. Tuema, S.J. MacGregor, J.A. Harrower, J. M. Koutsoubis, and O. Farish, "Corona stabilisation for high repetition rate plasma closing switches", 11th IEE International Symposium on High Voltage Engineering, vol. 3, pp. 280 – 284, 1999.
- [6] W. Frey, M. Sack, R. Wuestner, G. Mueller, "Gas-Insulated Self-Breakdown Spark on Low-Scattering and Long-Lifetime Switching", Acta Physica Polonica A, vol. 115, pp. 1016-1018, 2009.
- [7] J. Woodworth, J. Alexander, F. Gruner, J. Blickem, H. Anderson, M. Harden, "Low-Inductance Gas Switches for Linear Transformer Drivers," IEEE International Power Modulators and High Voltage Conference, pp. 201, 2008

ELECTRICAL BREAKDOWN OF SHORT NON-UNIFORM AIR GAPS

M. G. Hogg, I. V. Timoshkin, S. J. MacGregor, M. P. Wilson and M. J. Given, T. Wang

University of Strathclyde
204 George Street, Glasgow, G1 1XW, UK
michael.hogg@strath.ac.uk

Abstract

The breakdown voltage of air in highly divergent electric fields in not very short gaps (a few mm and above) is typically higher for negative energisation compared to positive energisation. Volumetric negative space charge, created by attachment of electrons to electro-negative molecules in the case of negative energisation, reduces the field in the vicinity of the sharp cathode, resulting in higher breakdown voltages. This paper investigates self-breakdown voltages in short, mm and sub-mm gaps formed by point and plane electrodes and filled with atmospheric air at pressures 0.5-3.5 atm (abs). It is expected that space charge effects will change self-breakdown voltages for positive and negative energisation modes resulting in their different functional behaviour as compared with larger inter-electrode gaps.

I. INTRODUCTION

The breakdown voltage of air in highly divergent electric fields in not very short gaps (a few mm and above) is typically higher for negative energisation compared to positive energisation [1]. In an electronegative gas a volumetric negative space charge develops between the electrodes, screening the electric field and increasing the hold-off voltage in the case of negative energisation. This is utilised in repetitive breakdown switching modes such as corona stabilised plasma closing switches [2] to increase the hold-off voltage and decrease time between impulses to full voltage recovery after previous breakdown.

In electronegative gases the electron attachment process results in the creation of negative ions that move slowly compared with electrons due to their significantly higher mass. In a highly diverging field, such as the field developed in a point-plane topology, negative ions are created in a localised region in front of the sharp electrode. This space charge screens the electric field and reduces the field at the point cathode. In the case of the positive energisation mode the effect of space charge is significantly reduced and, as the result, the required voltage to reach the breakdown is lower than in the case of negative energisation. This is accurate for most applications where the inter-electrode gap is relatively large, a

few mm and above. However, in the event of shorter gaps (~4 mm and below) it has been observed that the breakdown voltage is higher for positive energisation [3]. In this paper a comprehensive study of self-breakdown voltages in the point-plane topology stressed with a slowly rising voltage (230 V/s) has been conducted. Short inter-electrode gaps of 0.25 mm, 1.5 mm, 2 mm and 3 mm have been used. This research also compares breakdown voltages data for positive and negative energisation.

Breakdown voltage as a function of electrode separation, d , and gas pressure, p , is often displayed in the form of a Paschen curve. A Paschen curve shows the breakdown voltage against the product of pressure and inter-electrode distance, pd . First proposed by Friedrich Paschen in 1889 [4] using a uniform field with varying distances and pressures breakdown voltages can all fitted around one non-linear curve which exhibits a minimum in the breakdown voltage. Paschen curves have become a common method for displaying breakdown data for different gases [5]. Two branches of the Paschen curve (on the left and right hand sides from this minimum) shows that the breakdown voltage increases for larger and smaller values of pd . The Paschen curve shows the specific gap/pressure configuration to achieve breakdown at the minimum voltage [4]. At atmospheric pressure, the breakdown strength of air is ~30 kV/cm.

There are limitations to the conventional Paschen curve. The original curve is relevant for uniform fields achieved in simple topologies such as plane-plane and Rogowski profiles. Therefore, care must be taken when comparing the conventional Paschen curve [4] with any breakdown data collected from experiments with non-uniform fields. Literature also shows that when investigating very small inter-electrode air-filled gaps (below ~10 μm) the Paschen curve is not accurate and experimentally obtained breakdown voltage decreases with the decrease in pd at atmospheric pressure [6].

This research investigates an air-filled point-plane topology at a range of pressures (0.5 bar gauge to 3.5 atm abs) at gaps 3 mm, 2 mm, 1.5 mm and 0.25 mm. It is shown that in breakdown of short gaps positive energisation can have a higher breakdown voltage than negative energisation breakdowns. It is also shown that breakdown voltage changes linearly with air pressure and can be plotted near the right

hand side of the conventional Paschen curve for atmospheric air.

II. THE EXPERIMENT

This experiment required high voltage DC to energise a point-plane topology with a rate of 230 V/s until self-breakdown has occurred. The distance between the point electrode and the plane electrode is 3 mm, 2 mm, 1.5 mm and 0.25 mm and the pressure of the gaseous dielectric (bottled air) ranges from 0.5 atm (abs) to 3.5 atm (abs) in 0.5 atm increments. Bottled air was used for all experiments in this paper.

The experimental schematic can be seen in Figure 1 where a Glassman high voltage DC power supply (EH series, 0-60kV) energised the point electrode via a charging resistor (1M Ω). The voltage out of the HVDC power supply is controlled by a LabVIEW [7] program that interfaces with the power supply via a National Instruments DAQmax (SCB 68). The voltage across the switch is measured using a Tektronix HV probe (P6015A) and a Tektronix TDS 2024 oscilloscope (200 MHz, 2 GS/s). The breakdown voltage was measured as the highest value before the collapse of voltage.

The LabVIEW program is designed to increase the voltage across the switch with a stepwise increase of voltage ramping up from 0 V till breakdown occurs. A 0-10 V signal from the DAQmax proportionally outputs a 0-60 kV from the HVDC power supply. For this experiment the voltage is increased at a rate of 23 V every 10 ms which gives a smooth rise of 230 V/s. A feedback from the power supply allows the LabVIEW program to monitor the actual voltage outputted and when the voltage collapses the program identifies this as breakdown and stops the voltage increase.

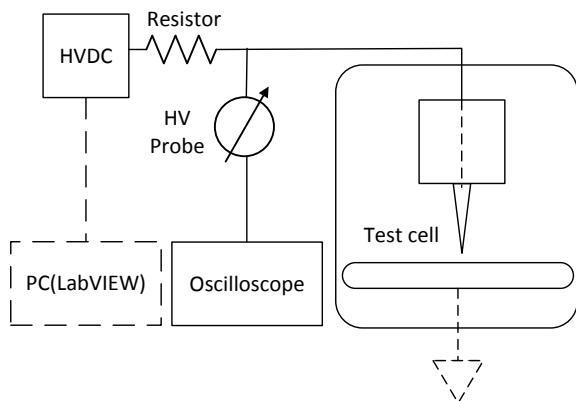


Figure 1. Experimental schematic.

The point-plane topology used in this experiment required a specifically designed test cell that could hold pressures up to 4 atm (abs) and set sub-mm inter-electrode gap spacing accurately. Therefore, a digital depth micrometer (RS, resolution 0.001 mm, accuracy ± 0.003 mm) was used to lower the electrode from a calibrated point. The control mechanism of

the depth gauge sat outside the test cell and the end, to which the HV point electrode was attached, was inside a pressurised chamber. The point electrode was tungsten rod with a hemispherical point (radius = 0.8 mm) and the plane electrode was a piece of machined brass with a diameter of 40 mm.

III. RESULTS AND DISCUSSION

Displaying the results has been broken down into different methods. The breakdown voltage as a function of pressure is discussed with respect to the linearity and energisation polarity. The results are compared with the conventional Paschen curve for atmospheric air [8]. Each data point is an average of 30 measurements; all figures were plotted using Origin Pro 8.6 graphing software.

A. Breakdown voltage as a function of pressure

Figure 2, Figure 3, Figure 4 and Figure 5 show the breakdown voltage as function of dielectric gas (bottled air) pressure with gaps 3 mm, 2 mm and 1.5 mm and 0.25 mm respectively. Self-breakdown for 3 mm, 2 mm, 1.5 mm and 0.25 mm all show positive energisation mode to have higher breakdown voltage. This has also been identified in other publications [9] where there are regions where positive is higher than negative on Paschen curves in similar experimental conditions. In larger gaps (above few mm) filled with an electronegative gas it is known that the breakdown strength for non-uniform electric fields is higher for negative energisation due to the development of a volumetric negative space charge. However, in this experiment the breakdown strength of air in the case of positive energisation is higher for almost every pressure and distance. Therefore it is expected that for larger gaps there will be a point at which the breakdown voltage curves for two energisation modes converge and cross over.

The breakdown voltage in the case of negative stress also has a much smaller standard deviation as compared with positive energisation. As mentioned above, each data point in the present work is an average of 30 measurements of breakdown voltage and from that the standard deviation has been calculated, the values of standard deviation for each breakdown voltage are shown in Figures 2-7 as vertical error bars.

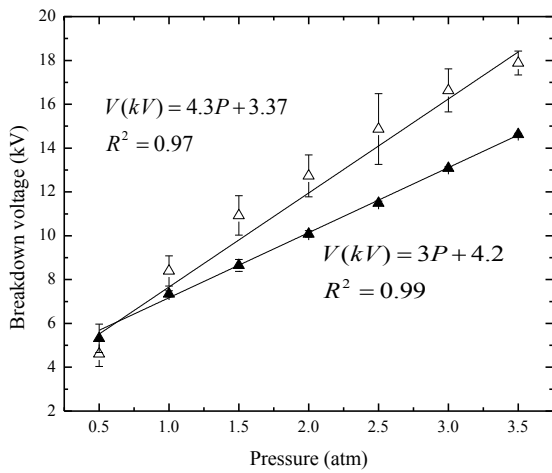


Figure 2. Breakdown voltage as a function of pressure for a 3 mm gap. Open symbols – positive, closed symbols – negative.

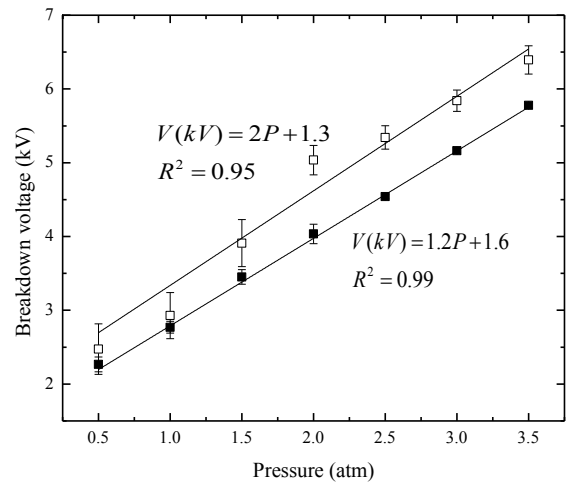


Figure 4. Breakdown voltage as a function of pressure for a 1.5 mm gap. Open symbols – positive, closed symbols – negative.

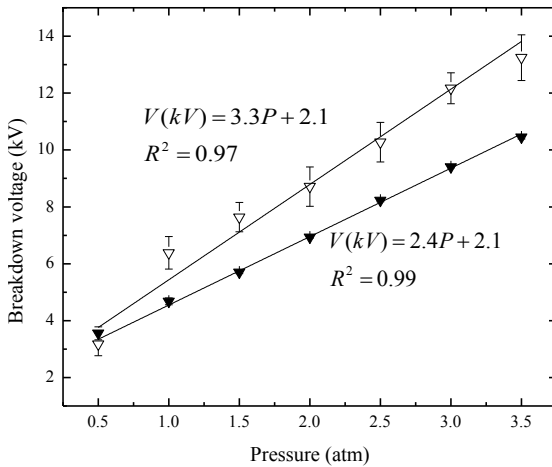


Figure 3. Breakdown voltage as a function of pressure for a 2 mm gap. Open symbols – positive, closed symbols – negative.

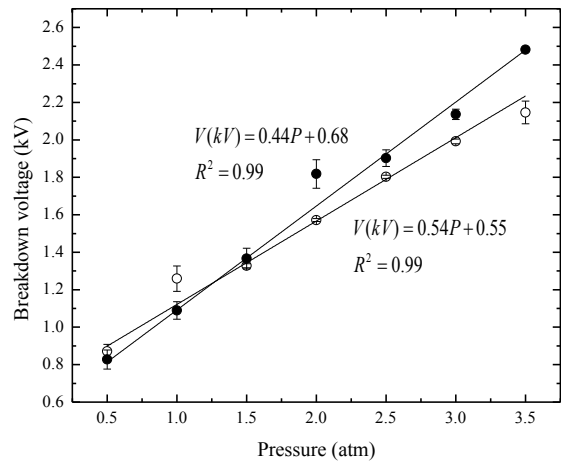


Figure 5. Breakdown voltage as a function of pressure for a 0.25 mm gap. Open symbols – positive, closed symbols – negative.

For negative energisation the standard deviation, σ , is quite consistent across all the pressures and distances with an average value of 0.1 kV (2.5%). This value is lower compared with an average standard deviation for positive energisation, 0.45 kV (6.1%). Standard deviation for positive energisation varies significantly between pressures and inter-electrode gaps. Therefore, it can be said that breakdown behaviour in the case of negative energisation is more predictable over a range of air pressures (0.5-3.5 atm): the breakdown voltage in the case of negative stress is much more consistent as compared with the positive energisation.

Paschen curve

Cumulative Figure 6 displays the breakdown data obtained in this study. The experimental points have been fitted with the analytical power fitting lines using Origin Pro 8.5 graphing software.

This graph shows breakdown voltage is proportional to $(pd)^n$, where $n=0.8$ for positive stress and $n=0.77$ for negative stress.

Figure 7 shows the comparison between the breakdown data obtained in the present study with the conventional Paschen data available from literature [8]. All of the results gathered in this experiment are positioned on the right hand side of the Paschen curve.

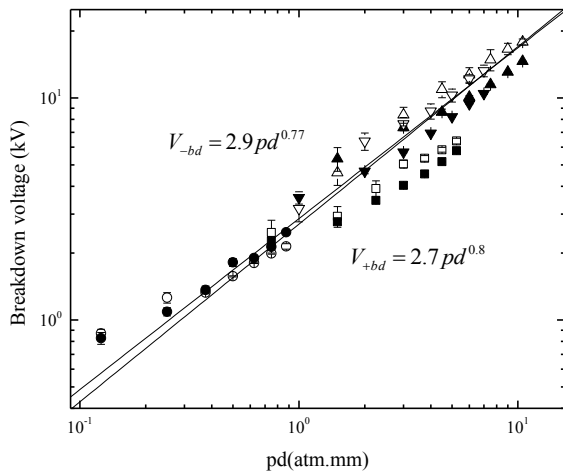


Figure 6. Experimental data plotted as a Paschen curve. up triangles – 3 mm gap, down triangles – 3 mm gap, squares – 1.5 mm gap, circles – 0.25 mm, open symbols – positive, closed symbols – negative.

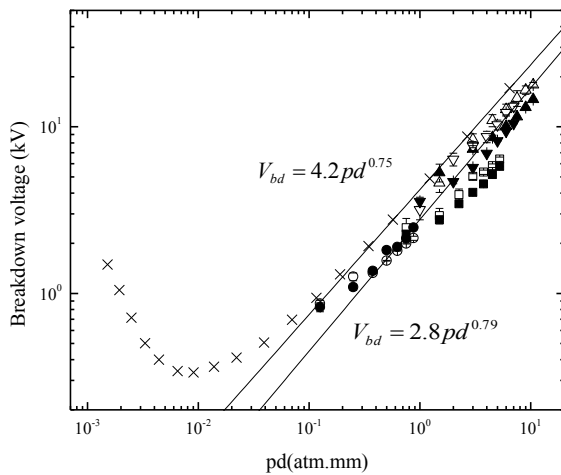


Figure 7. Experimental data plotted as a Paschen curve with a Paschen curve for uniform field from literature. up triangles – 3 mm gap, down triangles – 2 mm gap, squares – 1.5 mm gap, circles – 0.25 mm, open symbols – positive, closed symbols – negative. Crosses – Paschen from literature [8].

It can be seen that the experimental breakdown voltages obtained in the present work are located slightly below the conventional Paschen curve which potentially can be attributed to a highly non-uniform topology used in the present tests. However, the slope of the conventional Paschen curve is similar to the slope of the $V_{br}(pd)$ curves obtained in the present study.

IV. CONCLUSIONS

The self-breakdown voltages of bottled air in highly non-uniform electric field have been obtained for both, positive and negative energisation modes with varying electrode separations and gas pressures. It has been shown that for larger inter-electrode distances the difference between negative and positive breakdown voltages increases. For shorter distances the positive breakdown voltage can be higher than the negative breakdown voltage.

This paper has presented evidence that the negative energisation self-breakdown voltage is more stable than positive even in a pd region where the breakdown voltage is lower than the positive energisation. For positive energisation the self-breakdown standard deviation (average) is significantly higher at 6.1% of the breakdown voltage compared with 2.5% for negative energisation. It has also been shown that breakdown voltage increase with pressure almost linearly for the range of parameters used in the present paper. The breakdown voltage in the case of highly divergent electric field have been plotted as a Paschen curve and compared with a traditional $V_{bd}(pd)$ data for uniform electric fields. It has been also shown that the breakdown voltage as a function of pd can be fit with a power fit with coefficients 0.8 and 0.77 for positive and negative energisation modes respectively.

ACKNOWLEDGEMENTS

This work has been part-funded by a UK MoD Research Programme.

V. REFERENCES

- [1] A. Kara, O. Kalenderli, K. Mardikyan, "DC breakdown voltage characteristics of small air gaps with insulating barriers in non-uniform field," High Voltage Engineering and Application (ICHVE), pp. 425-428, 2010.
- [2] J. R. Beveridge, S. J. MacGregor, I. V. Timoshkin and J. M. Lehr, "A Corona-Stabilised Plasma Closing Switch," IEEE International Power Modulators and High Voltage Conference, pp.487-490, 2008.
- [3] I. Ye. Balygin "Electrical breakdown of Liquid dielectrics (Review)", Electrichestvo (Electricity), n.1, 1954, pp.89-92.
- [4] F. Paschen, "Ueber die zum Funkenübergang in Luft, Wasserstoff und Kohlensäure bei verschiedenen Drucken erforderliche Potentialdifferenz," Annalen der Physik. vol. 273 no. 5; pp. 69–75, 1889.
- [5] J. Kuffel, W. S. Zaengl and E. Kuffel, "High Voltage Engineering: Fundamentals," 2nd ed., Oxford; Boston: Butterworth-Heinemann, 2000.
- [6] E. Hourdakis, B. J. Simonds, N. M. Zimmerman, "Submicron gap capacitor for measurement of breakdown voltage in air," Review of Scientific Instruments , vol. 77, no. 3, pp. 034702-4, 2006.
- [7] J. Y. Beyon, "LabVIEW Programming, Data Acquisition and Analysis," Prentice Hall PTR, Upper Saddle River, NJ, 2001.
- [8] S. C. Brown Basic data of plasma physics, 1966
- [9] J. M. Meek and J. D. Craggs, "Electrical Breakdown of Gases," Wiley series in plasma physics, Chichester; New York: Wiley, 1978.

PERFORMANCE OF PLASMA CLOSING SWITCHES FILLED WITH AIR, NITROGEN AND A NITROGEN/OXYGEN MIXTURE

M. HOGG, I. TIMOSHKIN, S. MACGREGOR, M. GIVEN, M. WILSON, T. WANG

University of Strathclyde, Glasgow
204 George Street, G1 1XW
United Kingdom
michael.hogg@strath.ac.uk

ABSTRACT

This paper presents an experimental investigation into operation of a triggered, two electrode switch energised with a HV impulses superimposed over a DC charging voltage. A sphere-sphere topology with an electrode separation of 2 mm was DC energised to 6 kV, 7 kV and 8 kV and triggering impulses of varying dV/dt have been used. Breakdown voltage, time delay to breakdown and jitter have been measured for air, nitrogen and a 60% nitrogen/40% oxygen mixture. It is shown that higher dV/dt and higher DC energisation provide more stable and shorter time delays to breakdown.

1. INTRODUCTION

Plasma closing switches are widely used in the power and pulsed power industry because they can operate at high voltage and high current with fast closing times and low jitter. In recent times there has been a renewed interest in plasma closing switches with low jitter and low inductance filled with environmentally friendly gases, [1].

A gas which is traditionally used in high voltage and pulsed power engineering as an insulating or switching medium, sulphur hexafluoride (SF_6), is known to be a greenhouse gas, [2]. Also this gas is expensive to source and to reclaim. This research focuses on identifying environmentally friendly, low cost gases to replace SF_6 in plasma closing without detrimental effects to their performance. Many systems using plasma closing switches such as linear transformer drivers require rapid current rise after closure and therefore, therefore inductance of the switch and plasma channel should be minimised, [1]. This research introduces a new triggering

mechanism for plasma closing switches using a single gap switch.

Plasma closing switches can be subdivided according to their triggering modes of operation: self-breakdown, field distortion switches, trigatrons and laser triggered switches.

Self-breakdown switches only require 2 electrodes and operate when the breakdown strength of the electrode geometry is exceeded. The breakdown strength can be exceeded by different methods such as: reducing the inter-electrode gap by moving electrodes or by reducing the gas pressure inside the switch. Reducing the gas pressure to trigger a self-closing switch is commonly used to trigger pulsed power generators such as Marx generators.

Field distortion triggering requires a more complex circuit and switch than the basic two electrode switches. A third floating trigger electrode is positioned between the primary DC electrodes along the equipotential surfaces. A DC energised switch is triggered when a trigger pulse is applied to the trigger electrode, increasing the local field strength in the region on one of the primary electrodes, initiating a breakdown. This form of triggering is used in large pulsed generators such as linear transformer drivers where switches are charged to $\pm 100kV$ DC and as many as 100 000 switches are triggered at the same time, [1].

Trigatron switches also incorporate a third, trigger electrode and a triggering circuitry. A complete breakdown (switch closure) in a trigatron switch is initiated by creating a plasma channel between the triggering electrode and one of the primary electrodes. This initial plasma generates charge particles and UV photons which

lead to the switch closure (complete breakdown between the main electrodes). Trigratrons can operate in repetitive modes and are often used for high repetition triggering applications such as pulsed UV lamps, [3].

In laser triggered switches a laser impulse is used to form a plasma channel between two electrodes, For example, UV laser triggering is used for the 6MV multi-stage switch at Sandia National Laboratories, [4].

Each of the triggering mechanisms discussed have advantages and disadvantages. Laser triggering is very complex and costly and as such is not used often, multi-electrode switches complicate the switch adding inductance and creating issues with electrode erosion decreasing switch life time and performance. The self-breakdown switches are low effective devices which in main cases do not provide required degree of controllability over the switching operation.

This paper investigates operation characteristics of a DC energised two electrode switch which can be triggered by superimposing an impulse on top of the DC level to force a self-breakdown. In this work different environmentally friendly gases were used as switching media: air, nitrogen and a nitrogen/oxygen mixture (60%/40%) with a view to replace the SF₆ in plasma closing operations using the superimposed switching mechanism.

2. EXPERIMENT

The switch which consists of two spherical brass electrodes (9.5 mm diameter) is DC charged to a voltage which is lower than the static breakdown threshold. Then an impulse of the same (negative) polarity is superimposed on the DC level, resulting in switch closure by creating an overvoltage.

The switch was filled with air, nitrogen and a nitrogen/oxygen (60%/40%) mixture at atmospheric pressure. The breakdown voltage and time to breakdown were registered and the jitter and time to breakdown with respect to DC energisation level and impulse over voltage were analysed. The experimental set up is shown in Figure 1. The switch is pre-stressed with DC voltage through a charging resistor, a HV

impulse with a 270 ns duration is generated by a Blumlein pulsed power system.

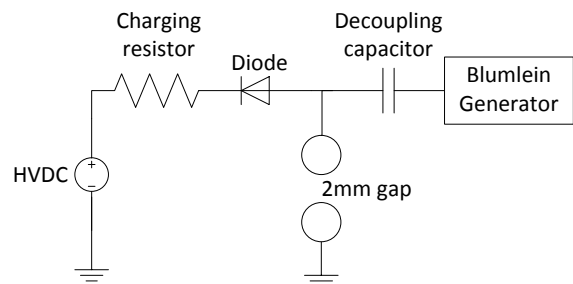


Figure 1. Experimental schematic.

The switch is energised to 6 kV, 7 kV and 8 kV DC using a Glassman EH series (0-60 kV) HVDC power supply via a 1 MΩ charging resistor. A double Blumlein charged from a Glassman EH series (0-100 kV) HVDC power supply provides an impulse of up to 55 kV with a rise time ~60 ns. The Blumlein is triggering by a trigatron (SAMTECH ltd) operated by a pulse generator. The Blumlein outputs a peak voltage ~1.33× the DC charging level. The rate of voltage rise and the peak voltage depends on the charging voltage of the Blumlein generator.

As shown in Figure 1, the triggering impulse circuit is connected to the switch via a decoupling 212 nF capacitor to allow the impulse to pass but block the flow of current from the DC energising circuit. The DC circuit is connect to the switch via a 6HV50k HV diode (HVCA.com) which blocks most of the energy from the impulse flowing into the DC energisation circuit for protection.

The switch used in this experiment is a simple compact design with two spherical electrodes placed 2 mm apart. The spheres are 9.5 mm radius brass spheres. A Tecktronix TDS 2024 (200MHz, 2GS/s) oscilloscope and Northstar PVM-6 high voltage probe were used to measure the charging voltage to the switch and to the Blumlien. The DC power supplies are left at the fixed voltage for the duration of the test to keep the conditions consistent.

3. RESULTS AND DISCUSSION

This experiment investigated triggered breakdown of a sphere-sphere topology switch filled with 3 different gases: air, nitrogen and a nitrogen/oxygen mixture (60% nitrogen/ 40% oxygen) at atmospheric pressure. To analyse

switch performance the time delay to breakdown results had to account for misfire (non-breakdowns). Misfires were assumed to have occurred because the impulse length was not long enough and it was assumed that the duration of the impulse (270 ns) provides a minimum value for pre-breakdown time delay in the case of misfires. 30 breakdown events were measured for each combination of DC and impulsive voltages.

The self-breakdown voltage level of the switch filled with air is 8.32 ± 0.09 kV. Initially the switch was filled with air, energised to 6 kV, 7 kV and 8 kV and then stressed with an impulse from the Blumlein generator. The Blumlein generator was charged to 19 kV, 25 kV and 35 kV, which resulted in the peak output voltage without breakdown of 25 kV, 35 kV and 55 kV respectively. The rate of rise (dV/dt) of the impulses changed from ~ 0.3 kV/ns at 19 kV charging voltage to ~ 0.7 kV/ns for 25 kV charging voltage and ~ 0.9 kV/ns for 35 kV charging voltage. The change in rate of rise had a significant impact on the misfires rate, the time delay to breakdown and the jitter of the switch. Figure 2 shows that the time delay to breakdown significantly reduces as the dV/dt (Blumlein charging voltage) is increased.

Impulses generated by the Blumlein generator charged to 19 kV were unable to cause breakdown at 6 kV DC stress level. When the Blumlein energisation level (and dV/dt) was increased the time delay to breakdown reduced and the switch operation became more stable. At 35 kV Blumlein charging voltage the time delay to breakdown converged for each DC charging level providing the most reliable operation and shortest time delay to breakdown, therefore 35 kV charging voltage was used in all further tests.

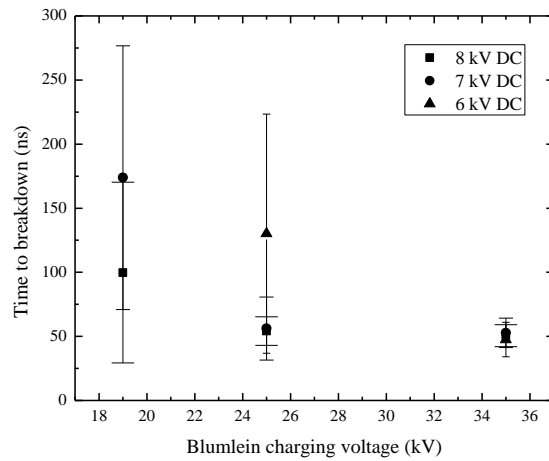


Figure 2. Time delay to breakdown in atmospheric pressure air as a function of Blumlein charging voltage (dV/dt).

Using the Blumlein charging voltage of 35 kV air, nitrogen and a nitrogen/oxygen mixture were investigated: time delay to breakdown, and jitter as a function of DC pre-energisation (6 kV, 7 kV and 8 kV) were obtained.

Figure 3 shows the time delay to breakdown as a function of DC pre-energisation level. Using the same Blumlein charging voltage (dV/dt) the time delay to breakdown for all gases reduces when the DC pre-energisation level was increased.

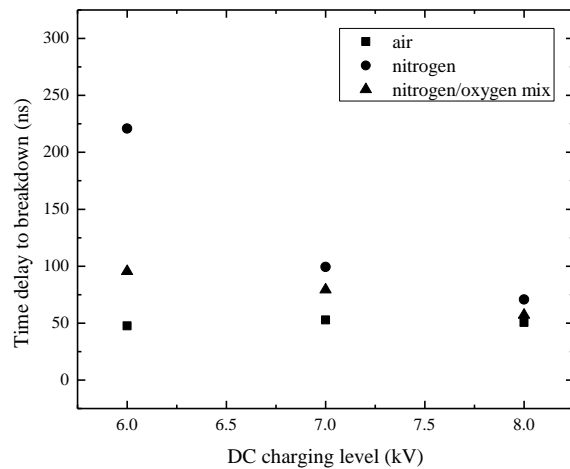


Figure 3. Time delay to breakdown in air, nitrogen and a 60% nitrogen/40% oxygen mixture as a function of DC charging voltage using a 35kV charged Blumlein triggering impulse.

It can also be seen that with all charging voltages air has the shortest time delay to breakdown at 8.6 ns when DC energised to 8 kV. Figure 5 displays the standard deviation of the time delay to breakdown data, showing stabilisation as the DC charging level is increased.

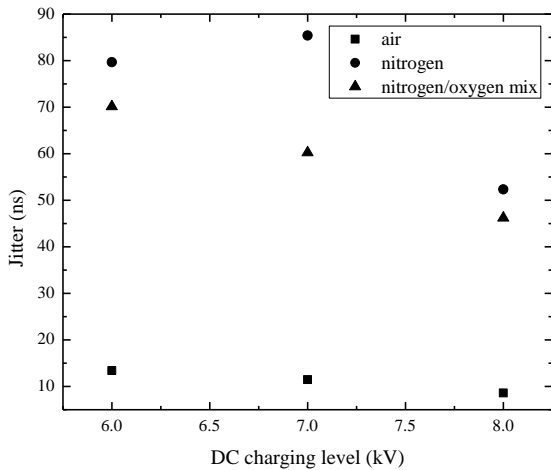


Figure 5. Standard deviation of time delay to breakdown for air, nitrogen and a 60% nitrogen/ 40% oxygen mixture as a function of DC charging voltage using a 35kV charged Blumlein triggering impulse.

Figure 5 shows jitter for all gas mixtures, the jitter decreases with an increase in DC pre-energisation indicating higher stability of switch operation at higher levels of DC stress. For air the jitter improves marginally however it is 83% lower than for nitrogen for 6 kV DC stress. The jitter for nitrogen and the nitrogen/oxygen mixture reduces significantly with increased DC energisation level, 34% reduction from 6 kV to 8 kV DC stress level.

4. CONCLUSIONS

This paper described experimental performance of a gas filled, two electrode switch, energised and triggered using a DC pre-stress and a short superimposed HV impulse. A sphere-sphere topology was used in the switch which was filled with air, nitrogen and a nitrogen/oxygen mixture (60% nitrogen/ 40% oxygen). Time delay to breakdown and jitter have been obtained for different levels of DC and impulsive stresses and all 3 gases.

It has been found that higher rates of voltage rise, dV/dt , for HV impulses provide the shortest time delay to breakdown and lowest jitter in the case of atmospheric air. It was found that charging the Blumlein generator to 35 kV (which produces HV impulses with a rate of rise ~ 0.9 kV/ns) results in the shortest time delay.

Using this Blumlein charging voltage and 6 kV DC pre-energisation it was shown that atmospheric air results in 83% lower jitter as compared with nitrogen at the same

(atmospheric) pressure. As DC switch pre-energisation is increased to 8 kV the time delay to breakdown reduces to ~ 50 -70 ns for all gases tested, a 68% reduction for nitrogen. The stability (jitter) of the switch, has been shown to be lowest for air and best for all gases at 8 kV DC pre-energisation.

It has been shown that using superimposed DC stress and HV impulses a two electrode switch can be used in the triggered regime. Higher rising rates of triggering HV impulses result in reduced time delay to breakdown and jitter. It has also been shown that the use of atmospheric air as a switching medium provides a lower time delay to breakdown and smaller jitter as compared with nitrogen or the 60% nitrogen/40% oxygen mixture. Jitter as low as 8 ns has been recorded using the superimposed triggering regime.

5. ACKNOWLEDGMENTS

This work has been part-funded by a UK MoD Research Programme.

REFERENCES

- [1] J. R. Woodworth, J. A. Alexander, F. R. Gruner, W. A. Stygar, M. J. Harden, J. R. Blickem, G. J. Dension, F. E. White, L. M. Lucero, H. D. Anderson, L. F. Bennett, S. F. Glover, D. Van De Valde, and M. G. Mazarakis, "Low-inductance gas switches for linear transformer drivers", *Phys. Rev. ST Accel. Beams*, 12 (6), 060401, 2009.
- [2] P. Bullock, J.R. Evans, K. Goulding, P.G. Jarvis, I.R. Noble, Australia; M. Rounsevell, UK; T.D. Sharkey, "The Science of Climate Change: Summary for Policymakers and Technical Summary of the Working Group I Report", *Climate Change*, page 22, 1995.
- [3] M. Maclean, J. G. Anderson, S. J. MacGregor, and J. W. Mackersie, "The development of a pulsed UV-light air disinfection system and its application in university lecture theatres", *Power Modulator Symposium*, 630-633, 2004.
- [4] D. R. Humphreys, J. K. Penn, J. S. Cap, R. G. Adams, J. F. Seaman, B. N. Turman, "Rimfire: A six megavolt laser-triggered gas-filled switch for PBFA 2", *5th IEEE Pulsed Power Conf.*, 262-265, 1985.

Simulation of spark dynamic plasma resistance and inductance using PSpice

M. Hogg, I. Timoshkin, S. MacGregor, M. Given, M. Wilson, T. Wang

Department of Electronic and Electrical Engineering
University of Strathclyde, Glasgow
204 George Street, G1 1XW
United Kingdom
michael.hogg@strath.ac.uk

ABSTRACT

This paper presents the results of analyses of the transient resistance and inductance of spark plasma, parameters which have been obtained using the hydrodynamic approach described in [2], and a new model for plasma resistance. A lumped RLC model to represent the transient process in the spark-discharge plasma has been built and solved using PSpice simulation software. The dynamic plasma resistance, $R(t)$, and inductance, $L(t)$, have been used in the lumped-element circuit.

Index terms – Plasma, dynamic, resistance, inductance, hydrodynamic, PSpice.

1 INTRODUCTION

This paper presents a PSpice-based solution of the hydrodynamic equations which describe the dynamic electrical properties of spark-discharge plasma. The properties of spark-discharge plasma have been under investigation for over a century [1]. The transient resistance and inductance of plasma in the first quarter-cycle of the current wave-form (rise to peak current) is of particular interest in the pulsed-power community, for applications such as linear transformer drivers (LTDs) where current magnitude and rise-time are critical. Designers of LTDs seek maximum current magnitude and the fastest possible rise-time, both of which are directly affected by the plasma resistance and inductance.

This paper presents the results of analyses of the transient resistance and inductance of spark plasma, parameters which have been obtained using the hydrodynamic approach described in [2], and a new model for plasma resistance. A lumped RLC model to represent the transient process in the spark-discharge plasma has been built and solved using PSpice simulation software. The dynamic plasma resistance, $R(t)$, and inductance, $L(t)$, have been used in the lumped-element circuit. PSpice solves the time-dependant circuit equations and allows a transient solution to be obtained for complex spark-plasma models. Different equations which describe $R(t)$ and $L(t)$ for spark-plasmas have been obtained from the literature [1-8] for use in the present analysis, and these equations have been solved and compared with experimental data.

Using PSpice simulations and experimental results, an advanced model of spark-plasma parameters has been

developed. This model will aid further analysis of the transient processes in spark-discharge plasmas.

2 PLASMA RESISTANCE MODELS

There are several models for the simulation of plasma resistance, by Toepler [1], Braginskii [3], Rompe and Weizel [4], Barannik *et al.* [5], Popovic *et al.* [6], Demenik *et al.* and Kushner *et al.* [8]. In this paper, models by Toepler, Braginskii, Rompe and Weizel, and Barannik are considered. The equations for channel resistance considered in this paper have been derived from the energy balance equation and in some cases theoretical reasoning supporting their choice of coefficients has been provided [4]. In the models proposed by Toepler, Rompe and Weizel, and Barannik, the spark resistance is inversely proportional to the integral of the current that flows in the channel. The Braginskii model uses the plasma channel radius, $a(t)$.

Braginskii's hydrodynamic equation for plasma radius is also used by other authors and has been proved to provide a reasonable fit to experimental data [3, 5, 9, 10]. For the purpose of continuity and comparison with literature results, equation (1) is also used in this paper:

$$a^2(t) = \left(\frac{4}{\pi^2 \rho_0 \zeta \sigma} \right)^{1/3} \int_0^t i^{2/3} dt [\mu\text{m}] \quad (1)$$

where $a(t)$ is the plasma channel radius, i is the channel current, t is time, ρ_0 is the initial gas density, σ is the conductivity, and ζ is a constant.

In the literature, plasma-resistance models have been reviewed and compared using a numerical method deriving circuit equations without the use of PSpice [2].

For this purpose, it is necessary to use simple RLC circuits to simulate plasma properties, as circuit equations have to be derived. The approach in this paper can use complex circuits attached to plasma RLC models, which would be unrealistic to derive by hand, because PSpice solves the circuit equations.

3 PLASMA MODELLING USING PSpICE

3.1 PLASMA RLC MODEL

Plasma is modelled using an *RLC* lumped-element model, representing the plasma resistance, inductance and capacitance. An *RLC* model is the standard approach to modelling plasma. By adding in a basic pulsed-power circuit to this model, a transient analysis of plasma can be conducted. Figure 1 shows the basic *RLC* plasma model, the closure of the switch (U1) initiates the plasma breakdown.

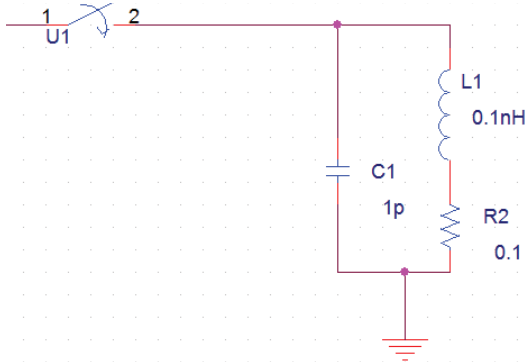


Figure 1. RLC lumped element plasma model. *C1*, *L1* and *R2* represent the plasma capacitance, inductance and resistance respectively.

In this paper, the resistor *R2* in Figure 1 will be replaced by a dynamic resistance that is dependent on the current, by solving hydrodynamic equations for plasma resistance. Ultimately this paper will show that the plasma inductance can also be simulated simultaneously with resistance.

3.2 DYNAMIC PLASMA RESISTANCE

In this paper, a time-varying dynamic plasma resistance which is controlled by hydrodynamic models for resistance is used. Voltage-controlled current sources are used to represent a plasma resistance. Using the analogue behaviour modelling (ABM) package in PSpice, the hydrodynamic equations are solved, to control the voltage-controlled current source configured to represent a dynamic resistance. Figure 2 shows how a voltage-controlled current source is configured to represent a dynamic resistance.

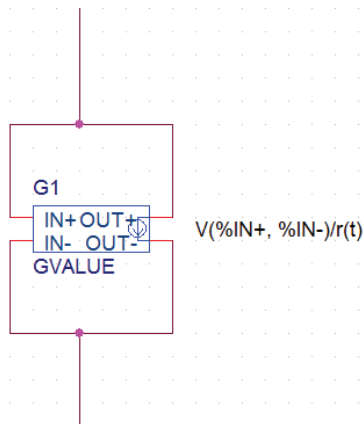


Figure 2. Voltage-controlled current source representing a dynamic resistance, *R(t)*, controlled by function *r(t)*.

Including the dynamic resistor (Figure 2) as the resistive component of plasma in the *RLC* model, time-varying plasma resistance is considered. Where the resistance model uses current to calculate resistance, *R(t)*, the current-controlled voltage source is used to provide a signal representing time-dependent resistance in this calculation. This method was used to simulate the hydrodynamic models mentioned in Section 2 [1, 3-5].

3.3 DYNAMIC PLASMA INDUCTANCE

This paper also presents a model for simulating the dynamic plasma resistance and inductance using PSpice. Using the ABM package, equation (1) for plasma channel radius can be used to calculate inductance. By assuming that the inductance of a filamentary plasma channel is similar to that of a conductive wire, the inductance can be calculated [11]:

$$L(t) = 2d \left[\ln \left(\frac{2d}{a(t)} \right) - 0.75 \right] [nH] \quad (2)$$

where: *L(t)* is the time-varying plasma inductance, *d* is the discharge length and *a(t)* is the time-varying plasma channel radius. The inductive voltage drop is obtained as:

$$V_L = \frac{d[L(t)i(t)]}{dt} = L(t) \frac{di(t)}{dt} + i(t) \frac{dL(t)}{dt} \quad (3)$$

where *L(t)* is the inductance and *i* is the circuit current. The ABM package is used to solve equations (1-3) and the inductance is implemented as a voltage-controlled voltage source. A model, which includes both dynamic inductance and resistance, has been solved (Figure 4).

4 RESULTS AND DISCUSSION

This paper presents PSpice solutions to hydrodynamic models of plasma resistance and as such the resistance curves are compared against the other models and experimental data taken from literature [3, 10]. For this comparison, the inductance is assumed to be a fixed value of 10 nH. To create a voltage impulse, an 80 nF capacitor was charged in parallel with a 120 kV DC voltage source. The output current pulse has been manipulated, by introducing circuit inductance (1 μH), to be similar to that of Akiyama *et al.* (peak current of ~20 kA and rise time of ~0.5 μs).

The equation coefficients have been selected from Engel *et al.* [2] for comparison with their simulations and to compare with the experimental data from Akiyama *et al.* [9]. Engel *et al.* normalised the resistance curves to be equal to the measured curve at time *t*=0.5 μs. Braginskii's model was not solved by Engel *et al.*, but similar experimental parameters were used in this paper. The integrator in the model by Rompe and Weizel required an initial condition which was set to 1×10^{-6} . Figure 3 shows the resistance curves for each model alongside an experimental curve.

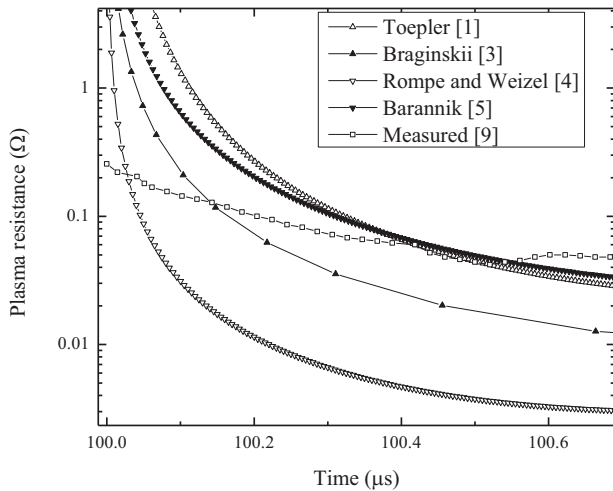


Figure 3. Plasma resistance taken from PSpice simulated hydrodynamic equations for resistance.

Shown in Figure 3, the plasma resistance curves for Toepler, Braginskii, Rompe and Weizel, and Barannik are compared against experimental data. Figure 3 shows that PSpice can be used to solve hydrodynamic equations for plasma resistance in a self-consistent model. The results are similar to the measured resistance at $t=0.5\mu\text{s}$ for the models by Toepler and Barannik *et al.* However, the model by Rompe and Weizel was an order of magnitude different. The results for Toepler and Barannik models are similar to the results shown by Engel *et al.*, confirming the PSpice approach with traditional approaches to solving plasma resistance.

Using PSpice has the advantage that it could allow for much more complex pulsed power circuits which include the dynamic plasma resistance to be modelled. Performance of large advanced systems such as LTD's can be affected by plasma-resistance and high precision models which included plasma resistance would be useful for optimisation of characteristics of such systems.

Using the method described in Section 3.3, the dynamic inductance of plasma is included in Braginskii's model alongside the dynamic plasma resistance. Figure 4 shows the plasma-resistance curve alongside the voltage and current wave-forms for Braginskii's equation for plasma resistance [3].

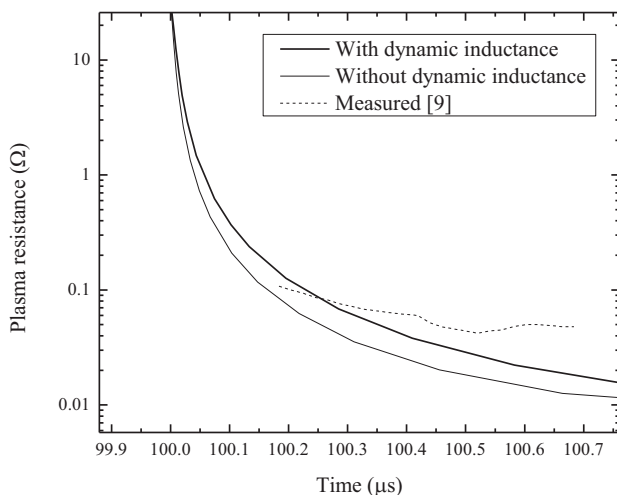


Figure 4. Comparison of plasma resistance from Braginskii's model [3] with and without dynamic inductance.

Using the dynamic plasma resistance and inductance, Figure 4 shows the plasma resistance with and without time-varying dynamic inductance alongside the measured plasma curve. This simulation shows that the dynamic resistance and inductance properties of plasma can be simulated simultaneously. The plasma-resistance curve from the model with dynamic inductance is closer to the measured plasma resistance.

5 CONCLUSION

In this paper, the plasma-resistance models in literature have been simulated using PSpice utilising the analogue behavioural modelling (ABM) package. It has been shown how dynamic resistance and inductance of a plasma channel can be simulated using voltage-controlled current sources and voltage-controlled voltage sources. Various models from the literature have been implemented using the PSpice approach. The results have been compared to determine which model provides the closest fit to an experimental curve taken from the literature.

The results of the PSpice simulations have been compared with different approaches to modelling the same hydrodynamic models and it has been shown that the PSpice model provides similar results and can be assumed to be a viable method for simulating plasma resistance.

An advanced model for simulating plasma properties was developed with dynamic resistance and inductance simulated simultaneously. Comparing Braginskii's model for plasma resistance with a fixed inductance and with a dynamic inductance showed that using time-varying inductance can increase the accuracy of plasma-resistance simulations.

Future work in this area will include further investigation of different plasma-resistance models in literature, dynamic inductance included in all models, comparison between the advanced models with dynamic inductance and fixed inductance, and comparison with previously published results. A new model for plasma resistance could be developed using new experimental data and the results from the PSpice simulations.

ACKNOWLEDGEMENTS

This research has been part-funded by a UK MoD research programme.

REFERENCES

- [1] M. Toepler, "Zur kenntnis der gesetz der gleitfunkenbildung," Ann. Phys. D., 4 folge, bd. 21, pp. 193-222, 1906.
- [2] T. G. Engel, A. L. Donaldson and M. Kristiansen, "The Pulsed Discharge Arc Resistance and its Functional Behaviour," IEEE Trans. Plasma Sci. vol. 17, 2, 1989.
- [3] S. I. Braginskii, "Theory of the development of a spark channel," Sov. Phys. -JETP 34, 7, 1068, 1958.
- [4] R. Rompe and W. Weizel, "Über das Toeplesche funkengastz," Z. Phys. Rev. 122, 636, 1944.
- [5] S. I. Barannik *et al.*, "Resistance and inductance of a gas arc," Sov.Phys.-Tech. Phys. vol. 19, pp. 1449-1453, 1975.
- [6] M. M. Popovic *et al.*, "Investigation of the beginning of high current discharges in pulsed arcs," in Proc. Int. Conf, Gaseous Discharges, p.32-36, 1974.
- [7] I. V. Demenik *et al.*, "Resistance of a xenon plasma in a large flash lamp," Sov. Phys.-Tech Phys. 13, pp. 829-832, 1968.
- [8] M. J. Kushner *et al.*, "Arc resistance of laser triggered spark gaps,"

- J. Appl. Phys. 58, 1744-1751, 1985.
- [9] H. Akiyama et al., "Current voltage characteristics of high-current pulsed discharge in air," IEEE Trans. Plasma. Sci., vol. 16, pp. 312-316, 1988.
 - [10] B. L. Maas, "Arc current, voltage, and resistance in high energy, gas-filled spark gap," Master's thesis, Texas University, Lub-bock, TX, May 1985, p. 45.
 - [11] F. Grover, "Inductance calculations: Working Formulas and Tables", Dover Publications, NY, 1962.